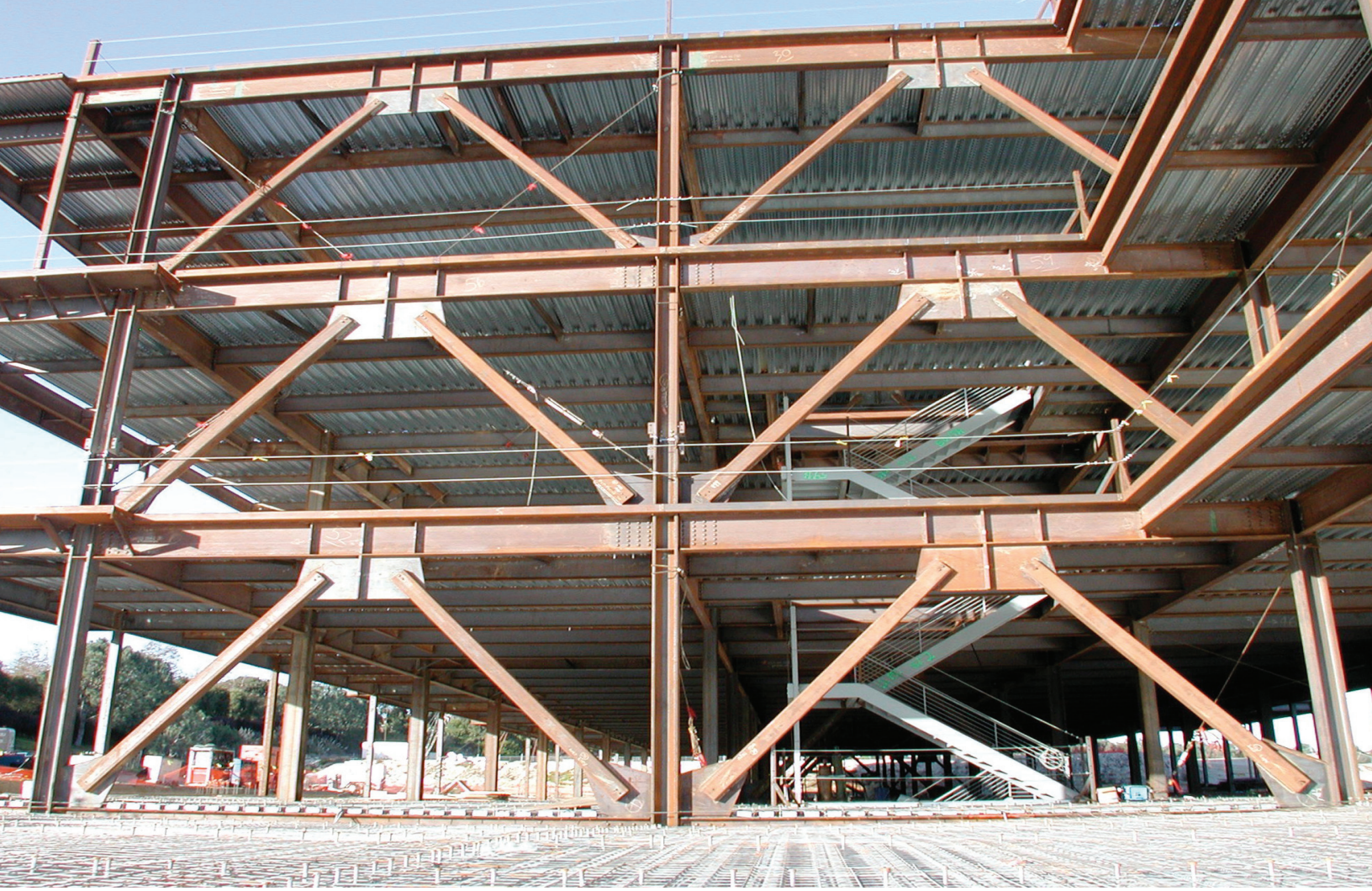

Short-Period Building Collapse Performance and Recommendations for Improving Seismic Design

Volume 4 – Study of One-to-Four Story Steel Special Concentrically Braced Frame Buildings

FEMA P-2139-4 / October 2020

FEMA

nehrp

Short-Period Building Collapse Performance and Recommendations for Improving Seismic Design

Volume 4 – Study of One-to-Four Story Steel Special Concentrically Braced Frame Buildings

Prepared by

APPLIED TECHNOLOGY COUNCIL
201 Redwood Shores Parkway, Suite 240
Redwood City, California 94065
www.ATCouncil.org

Prepared for

FEDERAL EMERGENCY MANAGEMENT AGENCY
Mai (Mike) Tong, Project Officer
Robert D. Hanson, Technical Advisor
Washington, D.C.

APPLIED TECHNOLOGY COUNCIL
Jon A. Heintz, Project Executive
Justin Moresco, Project Manager
Scott D. Schiff, Associate Project Manager

PROJECT TECHNICAL COMMITTEE
Charles A. Kircher (Project Tech. Director)
Jeffrey W. Berman
Kelly Cobeen
J. Daniel Dolan
Andre Filiatrault
James R. Harris
Gregory Kingsley
Dawn Lehman
Weichiang Pang
P. Benson Shing

SOIL-STRUCTURE INTERACTION WORKING GROUP
Lisa Star
Jonathan P. Stewart

PROJECT REVIEW PANEL
Anthony Court*
William T. Holmes
Larry Kruth
Onder Kustu
James O. Malley
Steve Pryor

STEEL WORKING GROUP
Alex Stone
Sarah Wichman

*ATC Board Representative

FEMA

nehrp

Notice

Any opinions, findings, conclusions, or recommendations expressed in this publication do not necessarily reflect the views of the Applied Technology Council (ATC), the Department of Homeland Security (DHS), or the Federal Emergency Management Agency (FEMA). Additionally, neither ATC, DHS, FEMA, nor any of their employees, makes any warranty, expressed or implied, nor assumes any legal liability or responsibility for the accuracy, completeness, or usefulness of any information, product, or process included in this publication. Users of information from this publication assume all liability arising from such use.

Cover photograph – Three-story steel special concentrically braced frame system (credit: C-M. Uang, UCSD).

Foreword

Most buildings in the United States are less than five stories tall. These low-rise buildings typically possess fundamental periods less than one-half second and thus are referred to as short-period buildings. Many commonly used analytical models have predicted that short-period buildings designed to current building codes are likely to suffer severe damage or collapse during design-level earthquakes. However, post-earthquake field investigations have not confirmed these predictions. Since this uncertainty is found across all types of building structures and construction materials permitted by current building codes and standards, it decreases confidence in the earthquake resilience of such code-compliant buildings. This technical resource series provides the findings and conclusions related to this issue and recommendations for improving seismic design of short-period buildings.

The National Earthquake Hazards Reduction Program (NEHRP) at the Federal Emergency Management Agency (FEMA) has a responsibility to help translate and implement new knowledge and research results to increase earthquake resilience nationwide. This FEMA-supported multi-year project series has successfully applied new analytical modeling techniques to investigate the long-standing problem of short-period building seismic collapse performance. This report is the fourth volume of the series, and it summarizes a study on one-to-four story steel special concentrically braced frame buildings designed in accordance with the ASCE/SEI 7-10 standard for high-seismic regions. The study has examined various contributing factors to the uncertainty. Through advanced modeling and parametric evaluation, the study has shown that the uncertainty can be resolved and further improvements to seismic design of steel braced frame buildings can be achieved.

FEMA is grateful to the Applied Technology Council (ATC) for managing this sophisticated multi-year project series to a successful completion, to the Project Technical Committee and the Project Review Panel for their dedicated effort leading to invaluable technical findings and recommendations. FEMA is also thankful to the project workshop participants for their scrutiny and valuable comments. Resolving the uncertainty in short-period building seismic collapse performance will strengthen confidence in seismic building codes. This project series will also contribute to improving seismic design and predicting collapse potential of short-period buildings in high-seismic communities in the nation.

Federal Emergency Management Agency

Preface

Recent analytical studies investigating a wide range of modern seismic-force-resisting systems have predicted collapse rates for short-period buildings that are significantly larger than those observed in earthquakes during the past 50 years. This gap between analytically predicted and historically observed collapse rates is known as the *short-period building seismic performance paradox*. Analytically predicted collapse rates for short-period buildings are also generally larger than maximum collapse rates used in national model codes and standards to establish seismic design requirements. If these analytical predictions are accurate, it means that the goal of acceptable collapse performance for all seismic-force-resisting systems at all building periods is not being achieved.

In 2013, the Applied Technology Council (ATC) was awarded the first in a series of task orders under contracts HSFE60-12-D-0242 and HSFE60-17-D-0002 with the Federal Emergency Management Agency (FEMA) to investigate "Solutions to the Issue of Short Period Building Performance," designated the ATC-116 Project series. The purpose of this series of projects was to investigate the response behavior and collapse performance of different structural systems and to identify causes and develop solutions for the short-period building seismic performance paradox. Studies investigated three structural systems: wood light-frame, special reinforced masonry shear wall, and steel special concentrically braced frame (SCBF) systems.

This report, which focuses on the investigation of steel SCBF systems, is one of four principal products of the ATC-116 series of projects:

- FEMA 2139-1, *Short-Period Building Collapse Performance and Recommendations for Improving Seismic Design, Volume 1 – Overarching Findings, Conclusions, and Recommendations*
- FEMA 2139-2, *Short-Period Building Collapse Performance and Recommendations for Improving Seismic Design, Volume 2 – Study of One-to-Four Story Wood Light-Frame Buildings*
- FEMA 2139-3, *Short-Period Building Collapse Performance and Recommendations for Improving Seismic Design, Volume 3 – Study of One-to-Four Story Special Reinforced Masonry Shear Wall Buildings*

- FEMA 2139-4, *Short-Period Building Collapse Performance and Recommendations for Improving Seismic Design, Volume 4 – Study of One-to-Four Story Steel Special Concentrically Braced Frame Buildings*

These reports are the result of a collaborative effort of more than 30 individuals tasked with the design of archetypes, development of numerical models, and interpretation of results across all three structural systems, in addition to the many others who participated in review workshops where draft versions of the reports were presented and discussed. ATC is indebted to the leadership of Charlie Kircher, Project Technical Director, and to the other members of the ATC-116 project team for their efforts in developing these reports. The Project Technical Committee, consisting of Jeff Berman, Kelly Cobeen, Dan Dolan, Andre Filiatrault, Jim Harris, Greg Kingsley, Dawn Lehman, Weichiang Pang, and Benson Shing, managed and performed the technical development effort.

Alex Stone assisted in the development of the design of the steel archetypes, and Sarah Wichman assisted in the steel numerical modeling. Lisa Star provided technical guidance on the development of the steel soil-structure interaction and foundation flexibility parametric study. The Project Review Panel, consisting of Tony Court, Bill Holmes, Larry Kruth, Onder Kustu, Jim Malley, and Steve Pryor, provided technical review and advice at key stages of the work.

ATC also gratefully acknowledges Mike Tong (FEMA Project Officer) and Bob Hanson (FEMA Technical Advisor) for their input and guidance in the preparation of this report, Scott Schiff who assisted in ATC project management, and Carrie J. Perna who provided ATC report production services. The names and affiliations of all who contributed to this report, including those who participated in the review workshop focused on steel SCBF systems, are provided in the list of Project Participants at the end of this report.

Justin Moresco
ATC Director of Projects

Jon A. Heintz
ATC Executive Director

Table of Contents

List of Figures

List of Tables

Chapter 1
Introduction

This report describes the approach, analyses, findings, conclusions, and recommendations for one in a series of studies on the gap between analytically predicted and historically observed earthquake-induced collapse rates for short-period buildings. It presents work focused on steel special concentrically braced frame (SCBF) systems. The Applied Technology Council (ATC) was commissioned by the Federal Emergency Management Agency (FEMA) to conduct these studies as part of the ATC-116 Project series, "Solutions to the Issue of Short Period Building Performance."

Short-period buildings, such as low-rise residential and commercial buildings, comprise a major portion of the building stock in U.S. communities with high-seismic hazard. The gap between analytically predicted and historically observed collapse rates for short-period buildings exists across many seismic-force-resisting systems and construction materials. As a result, it is believed that the seismic collapse performance for short-period buildings is not accurately predicted by current analytical models. Based on a review of previous studies and available research and data, three seismic-force-resisting systems were selected for investigation: wood light-frame, special reinforced masonry shear wall, and steel SCBF systems.

The subject of this report is commercial buildings constructed using steel SCBF systems. Studies on buildings constructed using wood light-frame or special reinforced masonry shear wall systems are described in separate reports. An additional report compares results from all three studies to identify commonalities for the possible extension of the findings, conclusions, and recommendations to other seismic-force-resisting systems and construction materials. The FEMA P-2139 series of reports include the following:

- FEMA P-2139-1, *Short-Period Building Collapse Performance and Recommendations for Improving Seismic Design, Volume 1 – Overarching Findings, Conclusions, and Recommendations*
- FEMA P-2139-2, *Short-Period Building Collapse Performance and Recommendations for Improving Seismic Design, Volume 2 – Study of One-to-Four Story Wood Light-Frame Buildings*

- FEMA P-2139-3, *Short-Period Building Collapse Performance and Recommendations for Improving Seismic Design, Volume 3 – Study of One-to-Four Story Special Reinforced Masonry Shear Wall Buildings*
- FEMA P-2139-4, *Short-Period Building Collapse Performance and Recommendations for Improving Seismic Design, Volume 4 – Study of One-to-Four Story Steel Special Concentrically Braced Frame Buildings*

1.1 Background and Purpose

At the time this study began, commercial buildings were designed in accordance with ASCE/SEI 7-10, *Minimum Design Loads for Buildings and Other Structures* (ASCE, 2010), which was adopted by reference in the 2015 edition of the *International Building Code* (IBC) (ICC, 2015). Design seismic loads in ASCE/SEI 7-10 are based on risk-targeted maximum considered earthquake (MCE_R) ground motions, which were introduced in FEMA P-750, *NEHRP Recommended Seismic Provisions for New Buildings and Other Structures* (FEMA, 2009a). Buildings designed and constructed in accordance with national model codes and seismic design standards (e.g., ASCE/SEI 7-10) are expected to meet general seismic performance targets, which are described in terms of not exceeding a specified probability of collapse given MCE_R ground motions. For reference, a collapse probability of no more than 10 percent, given MCE_R ground motions, is the anticipated "reliability" in ASCE/SEI 7-10 (Table C1.3.1b) for Risk Category II buildings, which constitute the vast majority of all buildings. Further, the use of MCE_R ground motions in building design is intended to provide a reasonable assurance of seismic performance for all buildings—regardless of building period, seismic-force-resisting system, or other characteristic—designed in accordance with the governing building code.

Studies conducted prior to the ATC-116 Project series have used the methodology described in FEMA P-695, *Quantification of Building Seismic Performance Factors* (FEMA, 2009b), to evaluate the collapse performance of common code-permitted seismic-force-resisting systems. For example, one widely cited previous collapse performance study is described in NIST GCR 12-917-20, *Tentative Framework for Development of Advanced Seismic Design Criteria for New Buildings* (NIST, 2012a). This and other similar studies have shown that many seismic-force-resisting systems achieve the collapse performance target (i.e., less than a 10 percent probability of collapse given MCE_R ground motions). However, these studies have also found that shorter-period buildings have calculated probabilities of collapse that exceed those of longer-period buildings, and generally exceed the 10 percent target for acceptable collapse performance.

This can be observed in Figure 1-1, taken from NIST GCR 12-917-20. The figure plots the calculated collapse probabilities for groups of structural systems, as identified in Table 12.2-1 of ASCE/SEI 7-10, over a range of periods. Bearing wall systems (diamonds) include special reinforced masonry shear walls (A.7), ordinary reinforced masonry shear walls (A.9) and light-frame (wood) walls with wood structural panel sheathing (A.15). Building frame systems (squares) include steel special concentrically braced frames (B.2), which are the focus of this report, special reinforced concrete shear walls (B.4), ordinary reinforced concrete shear walls (B.5), and steel buckling-restrained braced frames (B.25). Moment frame systems (triangles) include steel special moment frames (C.1), special reinforced concrete moment frames (C.5), and ordinary reinforced concrete moment frames (C.7)

In the figure, FEMA P-695 collapse performance studies on a variety of structural systems over a range of periods suggest that, for systems with design periods less than about 0.5 seconds, the probability of collapse given MCE_R ground motions increases significantly as the design period decreases. If these analytical predictions are accurate, then the goal of acceptable collapse performance for all seismic-force-resisting systems at all building periods is not being achieved, and short-period buildings are exceeding the 10 percent collapse performance target of ASCE/SEI 7.

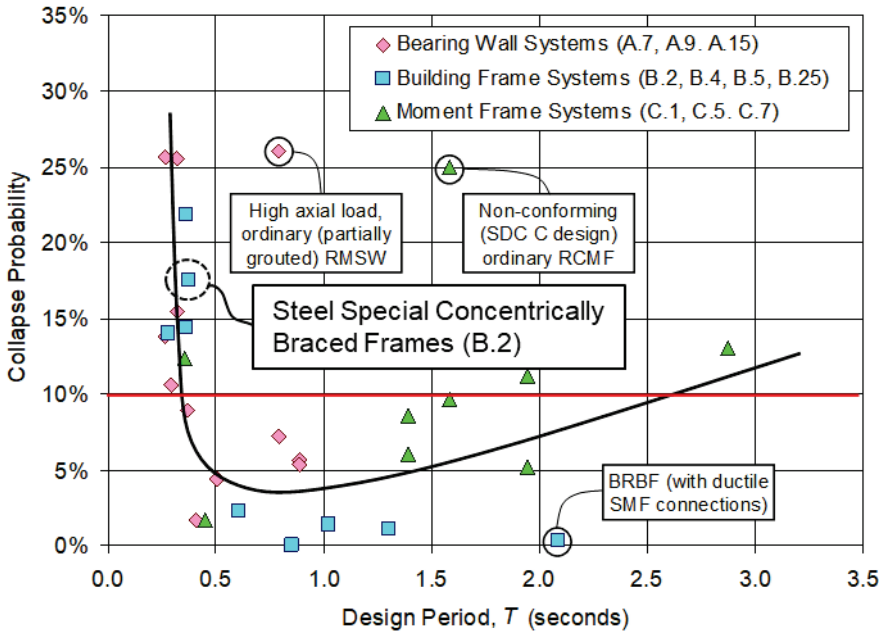

Figure 1-1 Trends in the probability of collapse of selected systems as a function of design period (adapted from NIST, 2012a).

The importance of building period on the calculation of peak response of inelastic systems dates back to studies of response and design spectra in the 1960s and 1970s by Veletsos, Newmark, and others (e.g., Veletsos and Newmark, 1960). These studies found that the ratio of inelastic displacement to elastic displacement of simple single-degree-of-freedom numerical models was period dependent and increased as the periods of the numerical models decreased, implying worse collapse performance for shorter-period buildings.

Findings from other numerical studies of earthquake response and collapse performance are consistent and suggest that seismic design coefficients (e.g., R) could be period dependent or more stringent for shorter-period buildings (e.g., Miranda and Bertero, 1994). Although ASCE/SEI 7 does not include period-dependent seismic modification factors, the underlying concepts can be found in other seismic codes. For example, Section 5.2.3 of Eurocode 8 (CEN, 2004) increases inelastic seismic demands as a function of period for detailing of reinforced-concrete elements in areas of plastic hinging when the building period is relatively short (i.e., T less than T_s, where T_s is the code-defined transition period between spectral response domains of constant acceleration and constant velocity). Explicit incorporation of period-dependent properties can also be found in the "coefficient method" of ASCE/SEI 41-17, *Seismic Evaluation and Retrofit of Existing Buildings* (ASCE, 2017).

Trends in observed earthquake damage of short-period buildings, however, do not support the high collapse probabilities shown in Figure 1-1. Analysis of available historical data on short-period building performance is described in Chapter 2. For example, very few steel buildings were severely damaged and none collapsed in the 1994 Northridge earthquake, which suggests that collapse risk for this class of short-period buildings is not elevated. This observation is contrary to the results of analytical studies used to predict collapse probabilities. Because observed damage in short-period buildings is less than what is implied by the body of analytical results available in the literature, the opinion of many structural engineers suggests that numerical models overestimate the actual collapse risk of short-period buildings.

The apparent discrepancy between analytical prediction of collapse performance and the opinions and observations of structural engineers has been designated the *short-period building seismic performance paradox*. With the standardized collapse evaluation methodology of FEMA P-695, additional testing of structural elements and assemblies, and the evolution of high-speed computer processing, we now have the capability to effectively investigate and resolve this paradox.

Given this context, the purpose of the ATC-116 Project series was to investigate the response behavior and collapse performance of different short-period structural systems. The results of this work are intended to:

- Identify the causes of the short-period building seismic performance paradox, quantify factors contributing to short-period building performance, and develop solution concepts.
- Improve and validate numerical modeling methods for short-period buildings to more accurately capture response behavior and collapse performance characteristics.
- Improve code seismic design methods and engineering practices for short-period buildings so that seismic performance targets are achieved across all seismic-force-resisting systems and all design periods.
- Inform future research so that better data and improved numerical modeling can be used in the development of more efficient and effective structural systems, seismic assessment methodologies, and engineering design procedures.

1.2 Approach and Scope

A phased approach for investigation was developed and presented in the ATC-116 report, *Roadmap for Solutions to the Issue of Short Period Building Performance* (ATC, 2015). Many factors are thought to contribute to the apparent discrepancy between analyzed and observed seismic performance of short-period buildings. Reasons for the paradox could include an underestimation of the peak strength and post-peak capacity of short-period buildings, an overestimation of the demands on short-period buildings, or a combination of both. Possible causes include building configuration issues (e.g., incorporation of all structural and nonstructural components, including interior and exterior wall finishes, that contribute to building strength and stiffness), hysteretic response backbone curve issues (e.g., realistic characterization of peak strength and collapse displacement capacity), and other factors (e.g., soil-structure interaction and foundation flexibility) that affect building response behavior and collapse performance.

Overall, the approach was to: (1) establish benchmarks for the historically observed performance of short-period buildings; (2) conduct parametric analytical studies on archetypical short-period buildings using advanced numerical models and the latest available research and test data; and (3) identify modeling parameters or building characteristics that provide the best match between the simulated and benchmark performance.

Although there are a number of parameters by which seismic performance can be measured, these studies were primarily interested in collapse performance as measured by the conditional probability of collapse given a ground motion intensity (e.g., MCE_R ground motions), based on observations from historical earthquake data, as described in Chapter 2, or collapse statistics obtained from Incremental Dynamic Analysis (IDA), as described in Chapter 5.

For the purpose of these studies, short-period buildings were defined as buildings with first-mode periods less than about 0.5 seconds. Studies investigated different systems, configurations, and materials commonly used in the United States for design and construction of new short-period buildings in regions of high and very high seismicity.

To study steel SCBF systems, a suite of archetypes, with variations in height and seismic-design level, were selected. Archetypes were intended to represent code-compliant modern construction for commercial office occupancies (COM) classified under Risk Category II. Other occupancies, like residential or industrial, were not studied because occupancy is not believed to have a significant effect on the layout or design of steel SCBF systems. Archetypes included one-story, two-story, and four-story buildings, all with fundamental periods below 0.5 seconds. The key configuration and seismic-design criteria for the steel SCBF archetypes are provided in Table 1-1, where the design period ($T = C_u T_a$) and the seismic response coefficient (C_s) were calculated in accordance with Section 12.8.2 and Section 12.8.1.1 of ASCE/SEI 7-10, respectively. The development of the steel SCBF archetypes is described in detail in Chapter 3.

Archetype design methods and details represented typical modern practice exercised in areas of significant seismicity based on the usual and customary standard of care. In contrast with prior FEMA P-695 collapse studies, archetype configurations for each occupancy were selected to be realistic and representative of actual buildings in terms of size and proportion. They were designed to meet code-minimum base shear strength requirements, but were not biased with overstrength through deliberate conservatism in the design or understrength caused by the use of member sizes that would be considered unrealistic based on gravity load or architectural considerations.

Archetypes were designed for a range of seismic ground-motion levels. "High-seismic" archetypes were designed for a value of short-period MCE_R spectral response acceleration adjusted for site class effects (S_{MS}) of 1.5g, and "very high-seismic" archetypes were designed for an S_{MS} of 2.25g. This highest value of S_{MS} is not required by FEMA P-695 (e.g., for evaluation of a

new seismic-force-resisting system proposed for ASCE/SEI 7) but was used in this study to investigate the collapse performance of short-period buildings for MCE_R ground motions that are unlikely but could occur in regions of very high seismicity (e.g., at sites located relatively close to fault rupture).

Table 1-1 Key Configuration and Seismic Design Criteria for Steel SCBF Archetypes

Archetype ID	No. of Stories	Seismic Design Criteria				
		Design Period* $T = C_u T_a$ (sec)	Seismic Design Category (SDC)	MCE_R Design Parameter, S_{MS} (g)	Response Modification Coefficient (R)	Seismic Response Coefficient, C_s (g)
Commercial Buildings: High Seismic						
COM1	1	0.25	D	1.5	6	0.167
COM2	2	0.34	D	1.5	6	0.167
COM3	4	0.57	D	1.5	6	0.167
Commercial Buildings: Very High Seismic						
COM4	1	0.25	E	2.25	6	0.25
COM5	2	0.34	E	2.25	6	0.25
COM6	4	0.57	E	2.25	6	0.25

* The design period is defined as $T = C_u T_a \geq 0.25$ seconds, in accordance with the requirements of FEMA P-695, where the values of the parameters C_u and T_a are specified by ASCE/SEI 7-10.

Archetype designs provided the basis for advanced numerical models. Using FEMA P-695 procedures, IDA results provided collapse performance metrics in terms of the conditional probability of collapse given MCE_R ground-motion levels.

To investigate the apparent discrepancy between analyzed and observed seismic performance of steel SCBF systems, five parametric studies were performed. These included: (1) baseline configuration; (2) brace configuration; (3) no redundancy; (4) soil-structure interaction (SSI) and foundation flexibility; and (5) no reserve moment frame. Parametric studies are described in detail in Chapter 4 and summarized below:

Baseline Configuration Parametric Study: investigated variation in the response behavior and collapse performance of short-period steel SCBF buildings. The study considered differences in archetype configurations compared with those of previous FEMA P-695 collapse evaluations and compared modeled "baseline" collapse performance to observed earthquake data. Baseline models considered the results of other parametric studies and incorporated a best estimate for each parameter to provide an overall best estimate of the simulated response of short-period steel SCBF buildings.

Brace Configuration Parametric Study: investigated the effects of different types of brace configurations on response behavior and collapse performance. Steel SCBF buildings can be designed with different brace configurations for a given bay of bracing, including diagonal bracing, chevron bracing, and double-story X-bracing. Comparison of response and collapse results of archetype models with chevron bracing to the results of corresponding baseline archetype models with double-story X-bracing (two-story and four-story archetypes) provided the basis for evaluating the effects of brace configuration.

No Redundancy Parametric Study: investigated the effects of redundancy on response behavior and collapse performance. Section 12.3.4 of ASCE/SEI 7-10 requires a redundancy factor (ρ) to be assigned to the seismic-force-resisting system in each of the two orthogonal directions based on the configuration of the system and system-specific redundancy criteria. The redundancy factor increases horizontal seismic loads required for design of members of structures not meeting the redundancy criteria. Comparison of response and collapse results of archetype models designed to be code compliant assuming the redundancy criteria were not met (i.e., ρ is 1.3) to the results of corresponding baseline archetype models designed to be code compliant where the redundancy criteria were met (i.e., ρ is 1.0) provided the basis for evaluating the effects of redundancy.

Soil-Structure Interaction (SSI) and Foundation Flexibility Parametric Study: investigated SSI inertial and kinematic effects and foundation flexibility for two soil conditions (stiff and soft sites) on response behavior and collapse performance. SSI inertial effects were modeled with a distributed set of discrete nonlinear soil springs and dashpots below flexible foundation elements. SSI kinematic effects were evaluated by modifying the frequency content of ground motion records (filtered records) used for response history analysis. Comparison of response and collapse results of archetype models with nonlinear soil springs, dashpots, and flexible foundation elements analyzed using filtered records to the results of corresponding baseline archetype models on fixed bases (i.e., rigid foundations) analyzed using unfiltered records provided the basis for evaluating the effects of SSI and foundation flexibility.

No Reserve Moment Frame Parametric Study: investigated the effects of the reserve moment-frame action within the braced frames on response behavior and collapse performance. After brace fracture occurs on a given story, lateral resistance is still provided by reserve moment-frame action within the braced frames resulting from the presence of the gusset plate connections at beam-to-column connections and the column bases.

Comparison of response and collapse results of archetype models that removed the reserve moment-frame action within the braced frames to the results of corresponding baseline archetype models that preserved the reserve moment-frame action within the braced frames provided the basis for evaluating the effects of the reserve moment frame.

Due to budget and time constraints, not all steel SCBF archetype buildings were designed, modeled, and analyzed. Table 1-2 lists the names of the archetype designs and numerical models for which parametric studies were completed. A total of 14 models were developed for the five parametric studies (each archetype analyzed as part of the SSI and foundation flexibility parametric study had two variations—one located at a site with soft soil and one located at a site with stiff soil). In general, the high-seismic ground-motion level was prioritized over the very high-seismic ground-motion level because high-seismic ground motions best represent strong ground motions in major earthquakes at sites not close to fault rupture.

Table 1-2 Steel SCBF Building Archetypes Developed for the Parametric Studies

Archetype ID	No. of Stories	(1) Baseline Configuration	(2) Brace Configuration	(3) No Redundancy	(4) Soil-Structure Interaction (SSI) and Foundation Flexibility	(5) No Reserve Moment Frame
Commercial Buildings: High Seismic						
COM1	1	COM1B	-	-	-	-
COM2	2	COM2B	COM2B-BC	COM2B-NR	COM2B-SS	COM2B-NMF
COM3	4	COM3B	COM3B-BC	-	COM3B-SS	-
Commercial Buildings: Very High Seismic						
COM4	1	COM4B	-	-	-	-
COM5	2	COM5B	-	-	-	-
COM6	4	COM6B	-	-	-	-

1.3 Organization and Content

This report describes an investigation of the response behavior and collapse performance of short-period steel SCBF buildings. It presents historical data on earthquake performance, typical configurations of steel SCBF construction, development of archetype designs and numerical models, results from parametric analytical studies, solutions to the short-period building seismic performance paradox, and recommendations for seismic design, engineering practice, and future research.

Chapter 2 identifies potential sources of earthquake data, describes methods for evaluation of response behavior and collapse performance using these data, presents observations of short-period building steel SCBF building performance in past earthquakes, and establishes benchmarks of collapse performance for comparison with parametric study results.

Chapter 3 discusses factors influencing the performance of short-period steel SCBF buildings, identifies common building types in terms of use (occupancy) and structural configuration, defines representative commercial building archetypes and their associated design criteria, and describes the design of these archetypes.

Chapter 4 describes the methods used to develop numerical models of short-period steel SCBF archetypes, including their calibration and validation with experimental data, and provides a detailed description of the five parametric studies.

Chapter 5 summarizes the analytical results for each of the five parametric studies on short-period steel SCBF buildings.

Chapter 6 presents key findings, conclusions, and recommendations related to short-period steel SCBF buildings.

Appendix A provides additional archetype design details that are not included in Chapter 3.

Appendix B presents a brief introduction of SSI theory followed by a detailed description of the means and methods used in modeling the effects of SSI and foundation flexibility for this study.

Appendix C describes the organization and content of peak response quantities from each archetype that have been archived for further study and future use.

References and a list of project participants are provided at the end of this report.

Chapter 2
Observed Response and Performance Benchmarks

2.1 Introduction

This chapter summarizes the observed damage and collapse of modern short-period steel SCBF buildings in past earthquakes and presents the performance benchmarks used in this study for comparison to baseline archetype model results.

2.2 Observed Damage and Collapse of Modern Short-Period Steel SCBF Buildings in Past Earthquakes

The literature on the performance of modern short-period steel SCBF buildings in earthquakes is limited and not sufficient to develop a quantitative measure of collapse failure rates. This is due, in part, to the relatively small population of all short-period buildings that are constructed with steel SCBFs and to the relatively good performance of modern steel SCBF buildings in past earthquakes. A notable exception is the large number of steel braced frame buildings with severe or collapse damage in the 1995 Kobe (Hyogo-ken Nanbu), Japan earthquake, although most of these buildings are not representative of modern steel SCBF buildings. Nonetheless, observed damage and collapse of these buildings provides valuable information, since the 1995 Kobe earthquake exposed these buildings to very strong (e.g., MCE_R or greater) ground motions.

Table 2-1 taken from Simpson et al. (2017) summarizes the types of damage observed to steel braced-frame buildings in four earthquakes: (1) the 1971 San Fernando earthquake; (2) the 1978 Miyagi-ken Oki, Japan earthquake; (3) the 1994 Northridge earthquake; and (4) the 1995 Kobe earthquake. These four earthquakes were selected for this summary since damage data for these events were available in the literature. Notably missing from this set of earthquakes is the 1989 Loma Prieta earthquake, for which there is only anecdotal accounts of damage to steel braced frames (e.g., brace buckling) in a few buildings. The steel braced-frame buildings damaged in the older (pre-1981) 1971 San Fernando and 1978 Miyagi-ken earthquakes are not representative of modern steel braced-frame buildings and are expected to have more damage and collapses than newer construction. A summary of steel braced-frame damage and collapse statistics (where available) from the four earthquakes follows.

Table 2-1 Description of Braced Frame Damage in Past Earthquakes

Year	Location	Magnitude	Description of Damage
1971	San Fernando, California	M6.6	Buckling and fracture of bar and double-angle braces
1978	Miyagi-ken Oki, Japan	M7.4	Buckling and fracture of bar and double-angle braces Premature connection failures
1994	Northridge, California	M6.7	Local buckling and fracture of bracing members Premature connection failure Deformation of beam Uplift of column base Weak-story behavior
1995	Kobe, Japan	M7.2	Local buckling and fracture of small- and large-section braces Premature connection failure Distortion of beam near connections Significant yielding of beams

Note: Information in this table is based on Simpson et al., 2017.

2.2.1 Steel Braced-Frame Building Damage in the 1971 San Fernando Earthquake

Although moderate in energy release (magnitude 6.6), the San Fernando earthquake of February 9, 1971, caused significant damage and led to detailed post-earthquake case studies of damaged buildings (NOAA, 1973). These case studies included 38 "earthquake-resistant" buildings: (1) 17 low-rise industrial and commercial buildings; (2) 9 hospital and medical facilities; and (3) 12 high-rise buildings. The case studies also included 6 "non-earthquake-resistant" buildings (i.e., unreinforced masonry and non-ductile reinforced concrete). Buildings were selected for study because they had sustained significant damage and, in some cases, had collapsed (e.g., Olive View Hospital). Only 1 of the buildings studied, the two-story Foothill Medical Center, was a steel building with braced frames (single-story, double-angle X-braces). Principal structural damage to this building was at the base of a column, which was severely bent due to brace eccentricity. Although some braces failed, leading to glass and partition damage, the building did not collapse and was repaired.

Although most of the damage after the San Fernando earthquake was reported in reinforced-concrete structures, there were a few observed cases of brace buckling and rupture (Simpson et al., 2017). One case was of flat-bar braces in a temporary wall in a mixed-use construction building. The other case was of buckling of steel double-angle X-bracing damage in a three-story metal-skin building.

2.2.2 Steel Braced-Frame Building Damage in the 1978 Miyagi-ken Oki Earthquake

The Miyagi-ken Oki earthquake of June 12, 1978, was a magnitude 7.4 event that occurred offshore of Sendai City, Japan, and generated peak ground accelerations of 1/5g, 1/4g, and 1/3g in areas surrounding the city (EERI, 1978). The majority of the steel buildings were relatively new braced frames typically consisting of bar or double-angle braces with bolted gusset-plate connections. The gusset connections were usually welded to the beams and columns. Braced frames were commonly found in long-span structures, such as factories, warehouses, or gymnasiums (Simpson et al., 2017).

Following the earthquake, a team of Japanese researchers performed field investigations of damaged buildings in a 4 km-by-4 km (2.5 mile-by-2.5 mile) area east of old Sendai City that had a relatively large number of commercial and industrial steel buildings. The investigations included: (1) 861 one-story steel buildings; (2) 412 steel buildings of two stories or more; and (3) 150 light-gauge steel buildings (Tanaka et al., 1980). Except long-span buildings (e.g., industrial structures and sports arenas), one-story steel buildings had limited structural damage, and the field investigations focused on steel buildings two stories and taller. Surveyed steel buildings included both moment-resisting frames and braced frames, although only a few moment frames had structural damage.

Of the 454 steel buildings of two stories or more investigated, only 6 buildings (1.3 percent) collapsed and only 13 buildings (2.8 percent) had significant structural damage with residual displacements of at least 1/30 relative story-drift angle. Fracture of jointed brace connections was observed in the 6 buildings that collapsed, with collapse damage attributed to "fatal" defects (Kato et al., 1980). In response to the Miyagi-ken Oki Earthquake, the Ministry of Construction in Japan recommended earthquake design lateral force be increased by a factor of 1.5 for braced frames and that connection forces be 1.2 times larger than the yield strength of the braces designed for those lateral forces.

2.2.3 Steel Braced-Frame Building Damage in the 1994 Northridge Earthquake

The Northridge earthquake of January 17, 1994, was a magnitude 6.7 event that affected the greater Los Angeles metropolitan area, causing 51 deaths (26 due to building collapse) and more than $40 billion of economic loss (OES, 1995; OES, 1997). The damage observed after the 1994 Northridge earthquake highlighted a variety of unexpected damage states in steel structural systems (Simpson et al., 2017), but none resulting in building

collapse (Krawinkler et al., 1996). Observed structural damage to 10 steel concentrically braced frame (CBF) buildings is summarized in Table 2-2, where MRF indicates that moment-resisting frames were present in one direction of the building.

Table 2-2 Summary of Observed Structural Damage to Steel Braced-Frame Buildings in the 1994 Northridge Earthquake

Structure	Type	Structural Damage
Kaiser Permanente Hospital penthouse	CBF	Buckling of bracing members: excessive sway
Two-story First Interstate Bank Building in Northridge	CBF	Buckling of brace connecting plates; possible yielding of anchor bolts
Four-story Student Union Building, California State University at Northridge	CBF	No structural damage observed
Roof structure for the bleachers of the football field	Other	Failure of anchor bolts (uplift)
Four-story Oviatt Library, California State University at Northridge	CBF	Failure of brace connecting plates; cracking of baseplates; yielding of anchor bolts
Three-story building under construction in Van Nuys	CBF, MRF	Buckling of bracing members
Four-story No. 2 Brew-house, Anheuser-Busch Co. Inc.	CBF	Buckling of bracing members
Department of Water and Power San Fernando Generating Station	CBF	No structural damage observed
Four-story commercial office structure	CBF	Buckling and failure of brace-welded connections; failure of beam-column moment connections
Two-story fashion plaza	CBF, MRF	Cracking in floor slab; buckling of bracing members

Note: Information in this table is based on Tremblay et al., 1995.

Many post-earthquake safety assessments use the guidelines provided in ATC-20, *Procedures for Postearthquake Safety Evaluation of Buildings* (ATC, 1989; 2005). The ATC-20 safety assessment procedure is a rapid evaluation tool that focuses on the integrity of the structural system. Inspectors are instructed to affix a placard (colored tag) on an inspected structure, according to the following guidelines:

- **Inspected Placard (green tag).** No apparent hazard found, although repairs may be required. Original lateral load capacity not significantly decreased. No restriction on use or occupancy.
- **Restricted Use Placard (yellow tag).** Dangerous condition believed to be present. Entry by owner permitted only for emergency purposes and

only at own risk. No usage on a continuous basis. Entry by public not permitted. Possible major aftershock hazard.

- **Unsafe Placard (red tag).** Extreme hazard, may collapse. Imminent danger of collapse from aftershock. Unsafe for occupancy or entry, except by authorities.

The 10 steel buildings listed in Table 2-2 represent a small fraction of all of the steel CBF buildings in the area of strongest ground motions, although the total number of steel CBF buildings is not known. For reference, post-earthquake safety evaluations of 114,039 potentially damaged buildings included 10,393 commercial and industrial buildings, of which 637 (6.1 percent) were deemed unsafe and assigned red tags (OES, 1995). Those safety inspections included 189 "steel frame" buildings, of which 10 (5.3 percent) were assigned red tags (OES, 1995), where "steel frame" does not distinguish between braced-frame and moment-frame construction. Only a fraction of all buildings was safety inspected, and red tag percentages based on the number of inspected buildings, rather than the total number of buildings in the affected area, represents an upper bound on observed damage rates.

More meaningful estimates of red tag percentages are shown in Figure 2-1 for wood buildings and for other (non-wood) buildings for each of five Modified Mercalli Intensity (MMI) regions (V through IX). Here, the red tag percentage is the ratio of the number of buildings assigned a red tag (OES, 1995) to the number of buildings in the MMI region of interest (Kircher et al., 2006). Red tag percentages are plotted as a function of the average value of 0.3-second response spectral acceleration of the MMI region of interest (Kircher et al., 2006). Non-wood buildings include three primary construction classes: (1) steel frame; (2) concrete frame; and (3) brick, block, or poured-in-place concrete (e.g., tilt-up construction). Non-wood construction classes are grouped together since the red tag percentages could not be reliably estimated for individual construction classes (other than wood). For example, steel-frame buildings represent less than 0.1 percent of all buildings in Los Angeles County (OES, 1995).

Figure 2-1 Percentage of wood and non-wood buildings assigned a red tag as a function of 0.3-second response spectral acceleration for five MMI regions (V–IX) based on post-earthquake safety inspections following the 1994 Northridge earthquake.

As shown in Figure 2-1, red tag percentages are quite low, less than 1.0 percent, even for the MMI IX region (e.g., average 0.3-second response spectral acceleration of 1.35g). The number of buildings assigned a red tag is shown in the figure for MMI regions VII, VIII and IX. For example, only 25 of the 313 non-wood buildings assigned a red tag are in the MMI IX region, none of which is steel-frame construction. That is, qualitatively, non-wood buildings have similar trends and values of red tag percentages as wood buildings (e.g., about 1.0 percent for the MMI IX region) and steel frame construction appears to perform somewhat better, on average, than wood and other construction classes (although the paucity of data precludes reliable quantification of this observation).

2.2.4 Steel Braced-Frame Building Damage in the 1995 Kobe Earthquake

The M6.8 Kobe earthquake of January 17, 1995, is one of the most significant events to affect an urban region of modern construction and, other than the 2012 Tohoku tsunami, the most devastating earthquake to hit Japan since 1923, when the Great Kanto earthquake destroyed Tokyo and Yokohama. Severe ground shaking was felt throughout Kobe and other nearby cities of the Hyogo Prefecture that were located close to fault rupture. Figure 2-2 is a map of the southern portion of the Hyogo Prefecture and neighboring areas of the Osaka Prefecture showing Kobe City and other nearby cities of the region affected by the 1995 Kobe earthquake (i.e., the near-fault zone identifies areas within 5 km, or 3.1 miles, of fault rupture).

Figure 2-2 Southern portion of Hyogo Prefecture and neighboring areas of the Osaka Prefecture showing Kobe City and other nearby cities of the region affected by the 1995 Kobe earthquake (figure credit: Risk Management Solution, Inc.).

The 1995 Kobe earthquake caused the death of 6,434 people, approximately 4,600 of whom were from Kobe, and serious injury to more than 25,000 people, and forced as many as 300,000 people to seek temporary shelter. Lifeline systems were severely damaged, in particular highway and railway lifelines and port facilities. The Port of Kobe, which was the third largest container cargo port in Japan before the earthquake, was completely closed. Structures near the shoreline and on man-made Port and Rocco Islands, unless supported by deep foundations, were severely damaged by liquefaction.

The earthquake caused approximately $100 billion in damage, 2.5 percent of the gross domestic product of Japan at the time of the earthquake, of which an estimated $80 billion was due to building damage. Of the $80 billion in direct losses to buildings, about 10 percent was due to fire. Building damage due to ground shaking was the primary cause of loss of life and serious injury, as well as direct and indirect economic losses.

The region affected by the 1995 Kobe earthquake included Kobe City and other nearby cities with a total population of about 4 million people (based on Japanese census data), and an estimated 800,000 buildings (assuming five people per building, on average), as summarized in Table 2-3.

Table 2-3 Approximate Populations and Estimated Number of Buildings in Areas Affected by the 1995 Kobe Earthquake

Area Affected by Earthquake	Population (× 1 Million)	Number of Buildings
Hyogo Prefecture:		
Kobe	1.5	300,000
Other Cities	2.0	400,000
Total	3.5	700,000
Other Prefectures	0.5	100,000
Total (All Areas)	4.0	800,000

Based on post-earthquake damage surveys by the Architectural Institute of Japan (AIJ) through April of 1995, more than 150,000 of the estimated 800,000 buildings in the affected region had either severe structural damage or had collapsed, as summarized in Table 2-4.

Table 2-4 Collapse Damage, Severe Damage, or Fire Damage of Buildings Affected by the 1995 Kobe Earthquake

Area Affected by Earthquake	Collapse Damage	Severe Damage	Fire Damage
Hyogo Prefecture:			
Kobe	54,949	31,783	7,733
Other Cities	26,257	31,043	79
Total	81,206	62,826	7,456
Other Prefectures	885	5,217	0
Total (All Areas)	82,091	68,043	7,456

Note: Information in this table is based on AIJ, 1995a.

Building damage varied greatly from one neighborhood to another influenced by local site conditions and other factors. In general, however, buildings in areas close to fault rupture were much more likely to have sustained collapse or severe structural damage. This is illustrated in Table 2-5, which shows the number of buildings with severe or collapse damage (referred to as "complete damage" in the table) for all areas of Hyogo Prefecture affected by the earthquake (144,032 buildings) and the number of buildings with severe or collapse damage for those areas within 5 km of fault rupture (131,355). That is, more than 90 percent of the buildings that suffered severe damage or had collapsed were located within 5 km of fault rupture. Table 2-5 also shows the approximate number of buildings located within 5 km of fault rupture (375,000, or about one-half of all Hyogo Prefecture buildings in the affected region). Approximately 21 percent (i.e., 77,259 / 375,000) of the buildings located within 5 km of fault rupture had collapse damage, whereas only about 1.2 percent (i.e., (81,206 – 77,259) / (700,000 – 375,000)) of the buildings located farther than 5 km from fault rupture had such damage.

Table 2-5 Number of Buildings that Collapsed or Suffered Severe Damage in Areas Affected by the 1995 Kobe Earthquake

Area Affected by Earthquake	Number of Buildings	Collapse Damage	Severe Damage
All Wards/Cities	700,000	81,206	62,826
Within 5 km of Fault	375,000	77,259	54,096
Complete Damage (All Areas)		144,032 (~20%)	
Complete Damage (within 5 km of Fault)		131,355 (~35%)	

Building damage summarized in Table 2-5 includes all building types (structural systems), occupancies (building use), and design vintages. In Kobe City, building use can be divided crudely into: (1) low-rise residential buildings; (2) smaller commercial and mixed-use buildings; (3) mid-rise residential and commercial buildings; and (4) high-rise (>60 m, or 197 feet) buildings. Short-period, low-rise residential and smaller commercial and mixed-use buildings were by far the most common types of buildings (roughly 90 percent of all buildings) and were also the most likely building types to be damaged in the 1995 Kobe earthquake.

The very high rate of collapse of short-period low-rise residential and smaller commercial and mixed-use buildings (i.e., greater than 20 percent in areas within 5 km of fault rupture) in the 1995 Kobe earthquake was largely due to the vulnerability of older construction built prior to the enforcement of the Japanese Building Standard Law (1981), but was also due to the intensity of the ground motions, particularly at sites near fault rupture. Although the buildings are essentially of the same construction both near and farther from the fault rupture, the collapse rate was only about 1 percent in areas farther than 5 km from fault rupture.

The preliminary earthquake reconnaissance report of the Architectural Institute of Japan (AIJ, 1995a), which provides the basis for the overall damage data reported in Table 2-4, also provides summaries of damage by building location and structure type. A total of 1,776 steel buildings were investigated, of which 457 (26 percent) were collapsed or had suffered severe damage. The relatively high percentage of steel building collapses (26 percent) is consistent with collapse percentage for all buildings located within 5 km of fault rupture (21 percent). The 1,776 steel buildings surveyed included steel buildings of all vintages and construction type.

A more focused and in-depth reconnaissance of observed damage to 988 "modern" steel buildings was performed by The Steel Committee of Kinki Branch of the AIJ (AIJ, 1995b). Older steel buildings with light-gauge columns were omitted from the survey. The steel buildings surveyed included

three structure types: (1) moment frames (370 buildings); (2) braced frames in one direction and moment frames in the other (123 buildings); and (3) braced frames in both directions (26 buildings), with 469 buildings of unknown structure type. Of the 988 steel buildings surveyed, 90 buildings (9.1 percent) were rated as collapsed, and of the 149 buildings with braced frames in one or both directions, 10 buildings (6.7 percent) were rated as collapsed.

Damage was associated with the bracing type (where bracing type was known), distinguishing between rods, angles, and flat bars ("smaller" braces) and round tubes, wide flanges, square tubes, and channels ("larger" braces). Of the 165 steel buildings with "smaller" braces, 14 (8.5 percent) were rated as collapsed, and of the 60 steel buildings with "larger" braces, none (0 percent) was rated as collapsed (Tremblay et al., 1996). Of the 227 steel buildings of unknown bracing type, 15 (6.6 percent) were rated as collapsed. The "larger" brace types (e.g., tubes) are representative of steel SCBFs used in the United States; the "smaller" brace types (e.g., rods and flat bars) are not (i.e., tension-only bracing is not permitted in regions of high seismicity by U.S. building codes). Although there are no reported collapses of steel buildings with "larger" brace types, some of the 15 steel buildings of unknown bracing type that were rated as collapsed could have had such bracing.

2.3 Benchmark Target Collapse Rates of Steel SCBF Buildings

Observations of steel SCBF building performance in past earthquakes is limited and not sufficient to develop a quantitative measure of collapse failure rates. Qualitatively, however, collapse performance of modern short-period steel SCBF buildings appears to be similar to that of wood buildings.

As shown in Figure 2-1, non-wood building red tag damage data are sparse, but evidence from other events (e.g., the 1995 Kobe earthquake) for which data are more reliable for generating collapse statistics suggests that steel braced frame buildings have collapse rates that are no larger than that of wood buildings. Hence, for the purposes of this study, benchmark target collapse rates for modeled performance of steel SCBF buildings are assumed to be the following:

- **One-Story Buildings.** 1 percent (0 percent to 2 percent) probability of collapse given MCE_R ground motions of S_{MS} = 1.5g; and
- **Two-or-More-Story Buildings.** 2.5 percent (0 percent to 5 percent) probability of collapse given MCE_R ground motions of S_{MS} = 1.5g.

Benchmark MCE_R collapse probabilities represent building collapse that includes both partial collapse and full collapse of the building structure, consistent with the ASCE/SEI 7-10 and FEMA P-695 definition of collapse. The higher benchmark MCE_R collapse probabilities for buildings two stories or more in height are based on an observed first-story failure mechanism of wood light-frame buildings and may not be applicable to other collapse failure modes (e.g., foundation rocking) of steel SCBF buildings, which have not been observed.

Chapter 3

Development of Building Archetype Configurations and Designs

3.1 Introduction

The archetype buildings selected for this study were intended to represent code-compliant modern construction for common occupancies that routinely adopt a steel structural system with lateral loads carried by special concentrically braced frames (SCBF). Design methods and details chosen were not intended to represent special or innovative designs, but rather typical practice exercised with the normal standard of care in the design of routine buildings.

The first consideration in the design of the archetype buildings was to establish the age and historic design approach appropriate for the study. The variation in steel SCBF building design among the stock of existing buildings in earthquake-prone regions in the United States is broad, due in large part to the continuing evolution of seismic-design philosophy for braced frames over the past four decades. It was determined that the objectives of the study could be achieved more efficiently by selecting archetype buildings designed according to current codes rather than selecting archetypes that reflected variations in past seismic-design practice. The information presented in this chapter, in conjunction with additional design details provided in Appendix A, provides the basis for the numerical models described in Chapter 4.

3.2 Factors Influencing Building Performance

This section presents factors that are expected to influence the seismic response and performance of short-period steel SCBF buildings, and thus were considered in the selection and design of the study's archetypes.

3.2.1 Seismic Design Level

This study focused on the performance of short-period steel SCBF buildings in regions of high seismicity. This study defined "high-seismic" demand to be a location where the MCE_R ground motion is characterized by a mapped

short-period spectral response acceleration (S_S) of 1.5g. For ordinary soil profiles, this corresponded to a short-period MCE_R spectral response acceleration adjusted for site class effects (S_{MS}) of 1.5g. This level of seismicity places ordinary occupancy buildings in Seismic Design Category (SDC) D in the 2015 IBC and ASCE/SEI 7-10.

To capture more severe seismic hazard levels (such as sites located relatively close to a fault), archetype designs were also prepared for 150 percent of the high-seismic short-period MCE_R spectral response acceleration. Termed "very high seismic" in this study, S_{MS} = 2.25g is high enough that the mapped one-second MCE_R spectral response acceleration, S_1, will often place the building into SDC E. For the archetypes, $S_1 = 0.9 > 0.75$, so the design rules for Seismic Design Category E were applied in the "very high-seismic" designs in this study.

3.2.2 Occupancy and Architectural Influence on Structure Configuration

Steel is a versatile and widely used structural material in different building types and occupancies. However, for steel buildings, the occupancy is unlikely to significantly affect the layout and design of the seismic-force-resisting system. As a result, the steel SCBF building type was sufficiently represented by a single occupancy that is common nationwide: commercial office occupancies (with archetypes designated as "COM"). For commercial occupancies, a Risk Category II was considered appropriate, requiring a seismic importance factor of 1.0.

In keeping with the common characteristics of economically designed commercial office buildings, all the archetypes in this study shared a symmetrical rectangular plan, 90 feet × 150 feet, with a regular grid of 30-feet × 30-feet bays. The gravity-load-resisting system included beams spaced 10-feet apart, framing to 30-foot girders. Other grid spacings are common in steel buildings. For example, it is generally economical to choose rectangular bays with longer beams framing to shorter girders, which would result in some shorter braced bays. However, it was determined that maintaining bi-directional symmetry was sufficiently representative of common practice and simplified the numerical modeling.

All baseline archetypes had two braced bays on each exterior face of the building. The braces occupied entire 30-foot bays and were continuous from roof to foundation. To limit brace lengths, all braces were in a chevron form or a super-X (mirrored chevron braces from one level to the next).

Finally, building height was an important parameter. This study looked at archetypes of one story, two stories, and four stories, but not taller because the scope was limited to short-period structures.

3.2.3 *Steel Concentrically Braced Frame Design and Construction Practice*

The history of steel concentrically braced frame (CBF) construction over the last 100 years has included considerable evolution of design and construction practice. An investigation of archaic design practice was beyond the scope of this study, so all archetypes were designed according to current American Institute of Steel Construction (AISC) specifications for SCBFs.

Steel concentrically braced frames are composed of braces and gusset plates connected to beams and columns. The centerlines of the braces, beams, and columns join at a single, concentric, or nearly concentric, point. In addition to the braces, seismic response of CBFs also includes significant participation of the beams and columns through moment-resisting frame action, whether or not the frame has been designed to be moment resistant.

Although a wide variety of cross-sectional shapes have historically been used for braces, current designs typically use square or round hollow structural sections (HSS) or wide-flange sections. Welded or bolted connections are used to connect the brace to the gusset plate and the gusset plate to the beams and columns.

Many bracing configurations exist. Figure 3-1 illustrates the more typical configurations, including: single diagonal braced bay; opposing paired braces in single-story X; multi-story X; and inverted V (or chevron).

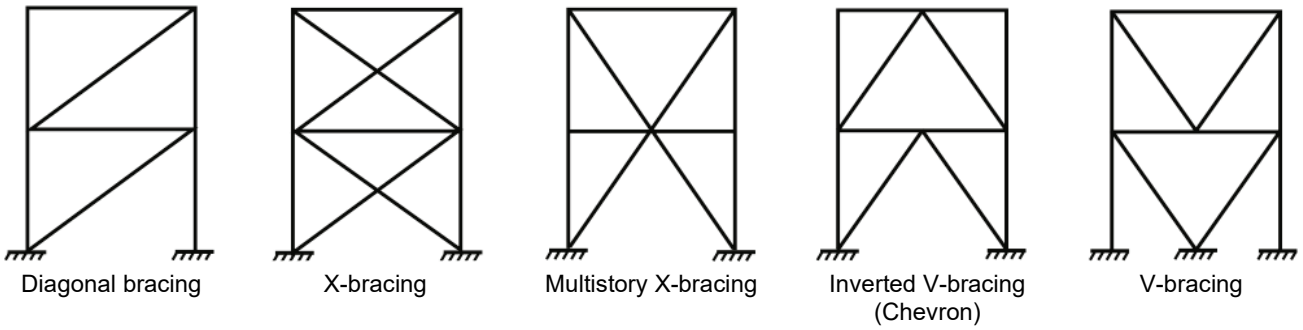

Figure 3-1 Typical CBF configurations (Sabelli et al., 2013).

Prior to publication of the 1988 version of the *Uniform Building Code* (UBC) (ICBO, 1988), building codes required that braces and other framing elements be designed for a specified lateral force without consideration of failure hierarchy or mode. Nonlinear behavior of many of these frames was controlled by failure of the brace-to-gusset plate or gusset plate-to-frame

connection. The 1988 UBC introduced significant changes in seismic design, including capacity-design principles intended to provide CBF components of sufficient strength to ensure that braces could yield in tension and buckle in compression without failure of other framing elements. These capacity-design requirements continued to evolve over the period 1988–1994, when the concept of SCBFs was first introduced and differentiated from other CBFs, classified as "ordinary." Today the building code recognizes three types of CBFs: "Special," "Ordinary," and "Systems not Specifically Detailed for Seismic Resistance." SCBFs are designed with full consideration of capacity-design principles. Important components of these capacity-design principles are summarized in the following list:

- limiting bracing configurations to complete concentric systems
- where chevron pattern braces are used, ensuring that beams at the apex of the braces are capable of resisting the unbalanced loading that occurs after buckling of the compression brace
- ensuring that columns in CBFs have adequate axial capacity to resist the imposed forces from the braces
- ensuring that the portion of lateral resistance provided by braces in compression is similar to that provided by braces in tension
- limiting member and cross-sectional slenderness ratios for braces and framing members to ensure ductile behavior
- requiring connections to develop the expected brace capacity and to accommodate end rotation of the brace
- requiring demand-critical welds for yielding elements

One of the more important requirements to ensure that post-elastic CBF behavior is possible is to design end connections of braces to develop the strength of the brace in both compression and tension. By following AISC design recommendations for SCBFs, the archetype designs were expected to have brace-end connections capable of developing the brace strengths to accommodate rotations associated with brace buckling.

3.2.4 Site Class and Foundation Systems

This study investigated the effects of soil-structure interaction and foundation flexibility, comparing building response and collapse performance on sites with stiff and soft soils. Unique designs were prepared for each site using different allowable soil bearing pressures and moduli of subgrade reaction. Both sites were characterized as Site Class D.

There is often an association between site characteristics and foundation type. Typically, piles or caissons are used with soft soil, whereas shallow spread footings are used with firmer sites. Exceptions include "poor" sites with soft soils, liquefaction potential, or expansive soil. For the purposes of this study, a shallow spread-footing foundation with a slab-on-grade was selected. Interior columns were supported on isolated spread footings, and exterior walls were supported on continuous stem walls supported on continuous strip footings. A slab-on-grade at the ground level was located above the interior isolated footings and inside the exterior stem walls. The selected foundation system was considered representative of typical systems and appropriate for studying the inclusion or exclusion of foundation flexibility in response prediction.

3.2.5 Architectural and Nonstructural Components

In the context of this study, "architectural and nonstructural components" are intended to include light-framed partition walls, building envelope systems, drywall, stucco, and other similar lightweight finishes. The effects of architectural and nonstructural components on the behavior of steel-braced frame buildings were assumed to be small because the mass and stiffness of these components are usually small relative to the properties of the structure itself and because architectural systems tend to be connected to the structure through light, flexible connections. The influence of architectural and nonstructural components on the seismic response of the archetypes was not included in this study.

3.3 Previous Studies Including Braced-Frame Archetypes

Archetype configurations were selected to be consistent with, but not necessarily identical to, those used in previous studies. The following sections describe selected previous reports that included braced-frame archetypes and that informed the archetype configurations of this study.

3.3.1 FEMA Model Building Types

FEMA Model Building Types (MBTs) define different types of structural systems in terms that are believed useful for characterizing seismic performance. These designations have been used extensively in FEMA publications, such as FEMA 547, *Techniques for the Seismic Rehabilitation of Existing Buildings* (FEMA, 2006), and FEMA P-154, *Rapid Visual Screening of Buildings for Potential Seismic Hazards: A Handbook* (FEMA, 2015a).

A list of FEMA MBTs from FEMA P-154 is shown in Table 3-1. Steel braced frames are designated S2 and illustrated in Figure 3-2. The

archetypes in this study were consistent with the FEMA MBTs described in FEMA 547 and FEMA P-154.

Table 3-1 FEMA Model Building Types

Designation	Description
W1	Light wood frame single- or multiple-family dwellings of one or more stories in height
W1A	Light wood frame multi-unit, multi-story residential buildings with plan areas on each floor of greater than 3,000 square feet
W2	Wood frame commercial and industrial buildings with a floor area larger than 5,000 square feet
S1	Steel moment-resisting frame
S2	Braced steel frame
S3	Light metal frame
S4	Steel frame with cast-in-place concrete shear walls
S5	Steel frame with unreinforced masonry infill walls
C1	Concrete moment-resisting frame
C2	Concrete shear wall
C3	Concrete frame with unreinforced masonry infill walls
PC1	Tilt-up construction
PC2	Precast concrete frames
RM1	Reinforced masonry with flexible floor and roof diaphragms
RM2	Reinforced masonry with rigid floor and roof diaphragms
URM	Unreinforced masonry bearing-wall buildings
MH	Manufactured housing

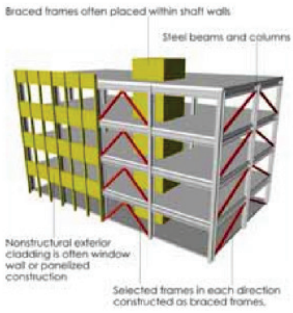

S2/S2A: Steel Braced Frames

Building Type **S2** consists of a frame assembly of steel beams and columns. Lateral forces are resisted by diagonal steel members placed in selected bays. Floors are cast-in-place concrete slabs or metal decks infilled with concrete. Building Type **S2A** is similar but has floors and roofs that act as flexible diaphragms such as wood or untopped metal deck.

Figure 3-2 Steel braced frame archetype (S2) from FEMA 547.

3.3.2 NIST GCR 10-917-8 Evaluation of the FEMA P-695 Methodology for Quantification of Building Seismic Performance Factors

NIST GCR 10-917-8, *Evaluation of the FEMA P-695 Methodology for Quantification of Building Seismic Performance Factors* (NIST, 2010), established model building types used for evaluation of collapse probability using the FEMA P-695 methodology. Braced-frame archetypes from NIST GCR 10-917-8 are illustrated in Figure 3-3 and Figure 3-4. The archetypes in this study were consistent with the short-period two-story and three-story building types described in NIST GCR 10-917-8. However, archetypes in this study had plan dimensions that were one 30-foot bay less in each direction, and building heights were limited to four stories or less to keep periods of vibration in the short-period range. The baseline archetypes in this study included two braced bays instead of one on each face of the building.

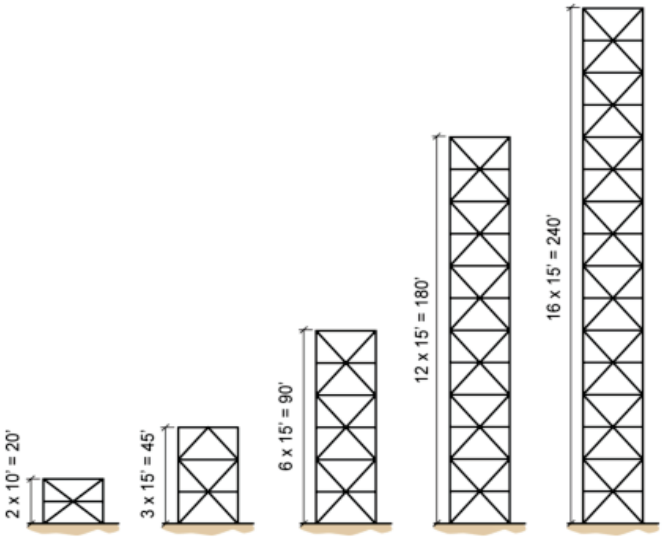

Figure 3-3 Braced-frame archetype elevations from NIST GCR 10-917-8.

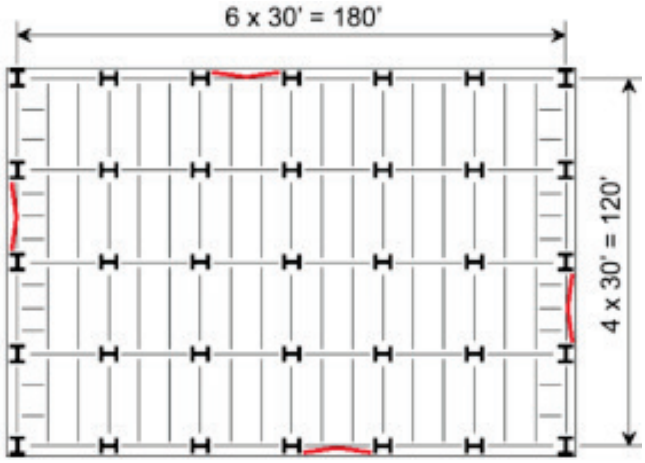

Figure 3-4 Braced-frame archetype plan from NIST GCR 10-917-8.

3.4 Archetype Design Criteria

This section documents the basic design criteria for the archetype SCBF steel buildings that were used in this study. Detailed documentation of the designs for each archetype is provided in Appendix A.

3.4.1 Applicable Codes and Standards

The codes and standards referenced for the design of the SCBF archetypes were:

- IBC 2015,
- ASCE/SEI 7-10,
- AISC *Steel Construction Manual*, 14th Ed. (AISC, 2011),
- ANSI/AISC 360-10, *Specification for Structural Steel Buildings* (AISC, 2010a), and
- ANSI/AISC 341-10, *Seismic Provisions for Structural Steel Buildings* (AISC, 2010b).

For the design of the steel superstructure of all archetypes, ASCE/SEI 7-10 Section 12.4 strength-level load combinations were used, including the vertical component, E_v. The steel members were designed for the governing limit states and requirements of both ANSI/AISC 360-10 and ANSI/AISC 341-10, using the load-and-resistance-factor-design (LRFD) method.

3.4.2 Gravity Loads

Gravity loads assumed for the archetype designs are summarized in Table 3-2 and in Appendix A

Table 3-2 Gravity Loads used for Design of Steel SCBF Archetypes

Building Type	Floor Live Load (psf)	Partition Load (psf)	Floor Dead Load (psf)	Roof Dead Load (psf)	Exterior Wall Dead Load (psf)
COM	50	15	81	25	10

3.4.3 Seismic Loads and Design Criteria

Archetype designs were developed for two different seismic criteria summarized in Table 3-3. These criteria followed the seismic-design loading requirements of Section 5.2.2 of FEMA P-695 considering typical intensities of MCE_R ground motions in regions of high seismicity.

Table 3-3 Seismic Loads Used for Design of Steel SCBF Archetypes

Seismic Design Level	Seismic Design Category (SDC)	MCE_R Ground Motion Definition				
		S_1 (g)	S_S (g)	F_a	S_{MS} (g)	S_{DS} (g)
Very High	E	0.90	2.25	1.0	2.25	1.5
High	D	0.60	1.50	1.0	1.50	1.0

Seismic design criteria were established by ASCE/SEI 7-10 requirements for the equivalent-lateral-force (ELF) method. The design coefficients and factors for the seismic-force-resisting system are given in Table 12.2-1 of ASCE/SEI 7-10 as:

- $R = 6$,
- $\Omega_0 = 2$, and
- $C_d = 5$.

Table 3-4 summarizes the basic seismic design criteria used for the archetype designs.

Table 3-4 Seismic Design Criteria used for Design of Steel SCBF Archetypes

Archetype ID	No. of Stories	Seismic Design Criteria				
		SDC	S_{MS} (g)	T^* (sec)	ρ	C_s (g)
COM1B	1	D	1.5	0.25	1.0	0.167
COM2B	2	D	1.5	0.34	1.0	0.167
COM3B	4	D	1.5	0.57	1.0	0.167
COM4B	1	E	2.25	0.25	1.0	0.250
COM5B	2	E	2.25	0.34	1.0	0.250
COM6B	4	E	2.25	0.57	1.0	0.250
COM2B-BC	2	D	1.5	0.34	1.0	0.167
COM3B-BC	4	D	1.5	0.57	1.0	0.167
COM2B-NR	2	D	1.5	0.34	1.3	0.167
COM2B-SS	2	D	1.5	0.34	1.0	0.167
COM3B-SS	4	D	1.5	0.57	1.0	0.167
COM2B-NMF	2	D	1.5	0.34	1.0	0.167

* The design period is defined as $T = C_u T_a \geq 0.25$ seconds, in accordance with the requirements of FEMA P-695, where the values of the parameters C_u and T_a are specified by ASCE/SEI 7-10. $T = C_u T_a = 0.2$ seconds for COM1B and COM4B but was taken as 0.25 seconds for design per the requirements of FEMA P-695.

3.4.4 Foundation Design Criteria

Soil properties were assumed to represent typical West Coast sites as described in Appendix B and summarized in Table 3-5. Assumed site-specific properties of soils used for foundation design are summarized in Table 3-6. The foundations for the baseline archetypes were designed for stiff soils (3000 psf allowable bearing pressure). The soil-structure interaction and foundation flexibility parametric study investigated the performance of archetypes designed for stiff and soft soils, where the stiff soils were assumed to have a 3,000 psf allowable bearing pressure, and the softs soils were assumed to have a 1,500 psf allowable bearing pressure. Both stiff and soft sites were characterized as Site Class D.

Table 3-5 Site Characteristics for Soil-Structure Interaction and Foundation Flexibility Parametric Study

Site	Site Class	Near Surface Soil	V_{s30} (m/s)	V_s (m/s)	Other
Soft	D	Unsaturated clay	183	~100	S_u=32 kPa
Stiff	D	Dense sand	354	~295	$\Phi' = 40^o$

Table 3-6 Foundation Criteria used for Design of Steel SCBF Archetypes

Material	Properties
Site class	D
Allowable soil bearing pressure (stiff soil)	3000 psf
Allowable soil bearing pressure (soft soil)	1500 psf
Modulus of subgrade reaction (stiff soil)	129 kip / cu ft
Modulus of subgrade reaction (soft soil)	60 kip / cu ft
Minimum footing depth	12 in

3.5 Archetype Configurations and Designs

This section describes the archetype configurations and designs, which were meant to broadly represent common steel braced-frame buildings routinely encountered in practice. Table 3-7 lists the archetypes described in the following sections. Any cell without a unique identifier indicates that the archetype was not included in the study.

Table 3-7 Steel SCBF Baseline and Variant Archetypes

No. of Stories	SDC	Baseline Configuration	Brace Configuration	No Redundancy	Soil-Structure Interaction and Foundation Flexibility	No Reserve Moment Frame
Commercial Buildings: High Seismic						
1	D	COM1B	-	-	-	-
2	D	COM2B	COM2B-BC	COM2B-NR	COM2B-SS	COM2B-NMF
4	D	COM3B	COM3B-BC	-	COM3B-SS	-
Commercial Buildings: Very High Seismic						
1	E	COM4B	-	-	-	-
2	E	COM5B	-	-	-	-
4	E	COM6B	-	-	-	-

3.5.1 Baseline Configurations

Basic Geometry and Materials

The baseline configurations represent the best estimates for response behavior and collapse performance of steel SCBF buildings. The baseline designs also formed the basis of comparison to variant archetypes summarized in Table 3-7.

The conceptual layout of the building plan is shown in Figure 3-5. The plans for *all* archetypes in the study shared the following characteristics:

- Rectangular plan: 90 feet × 150 feet.
- Grid spacing: 30 feet × 30 feet.
- Floor-to-floor height: 14 feet.
- Structurally symmetrical in each plan direction.
- Seismic-force-resisting system on the building faces.
- Floors: 3-inch normal-weight concrete over 2-inch, 18-gauge composite deck supported on composite wide-flange beams at 10-feet on center.
- Roof: 3-inch roof deck over wide-flange beams at 10-feet on center. One full bay at the center of the building was assumed to have a concrete deck and mechanical loading.

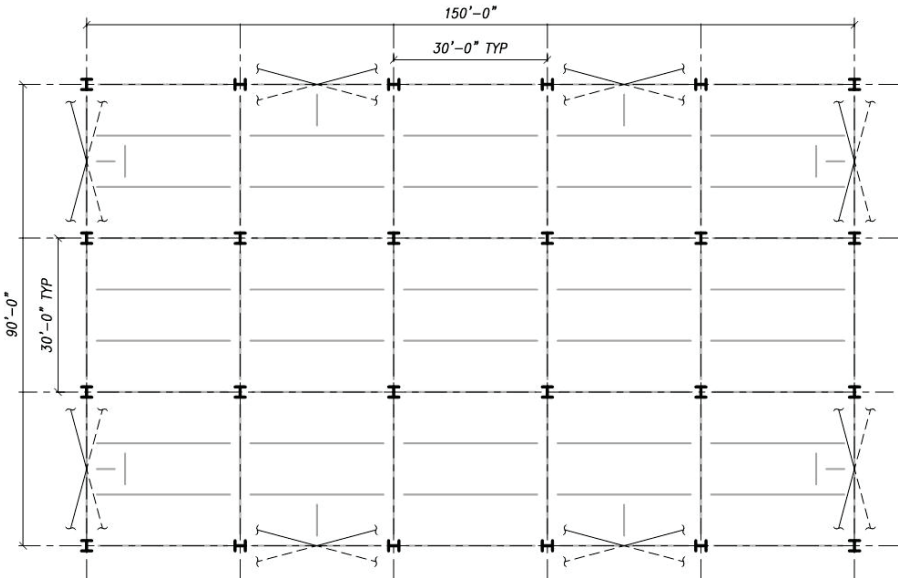

Figure 3-5 Plan configuration of all baseline archetypes.

In elevation, the baseline archetypes included three heights (one story, two stories, and four stories) with brace configurations as illustrated in Figure 3-6.

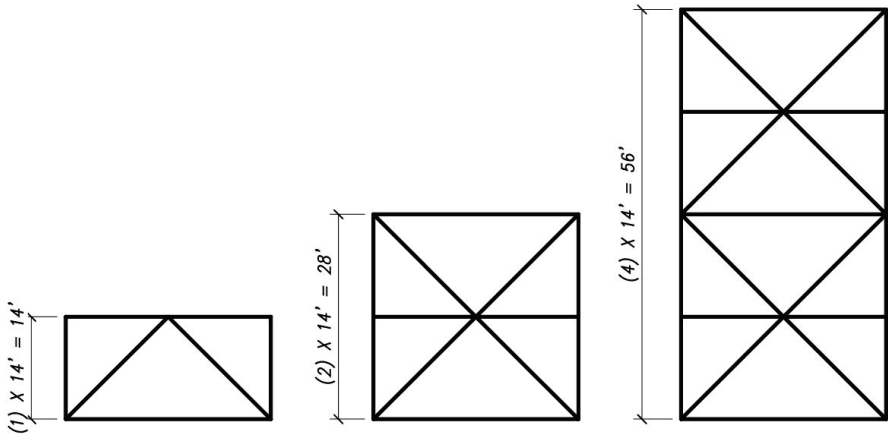

Figure 3-6 Brace elevations.

The three high-seismic baseline archetypes are illustrated in isometrics in Figure 3-7, Figure 3-8, and Figure 3-9. The isometrics for the very high-seismic archetypes, which are not shown, are nearly identical to those of the high-seismic archetypes, with differences being in relative sizes of foundations, braces, and other structural elements.

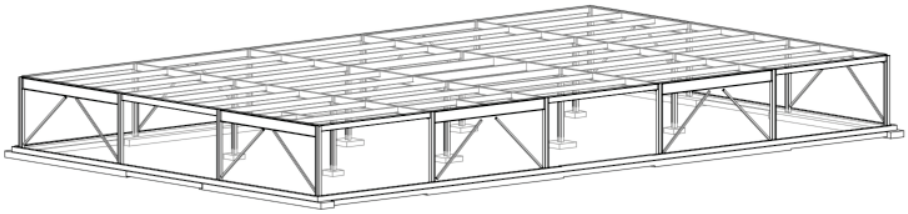

Figure 3-7 COM1B: one-story baseline archetype.

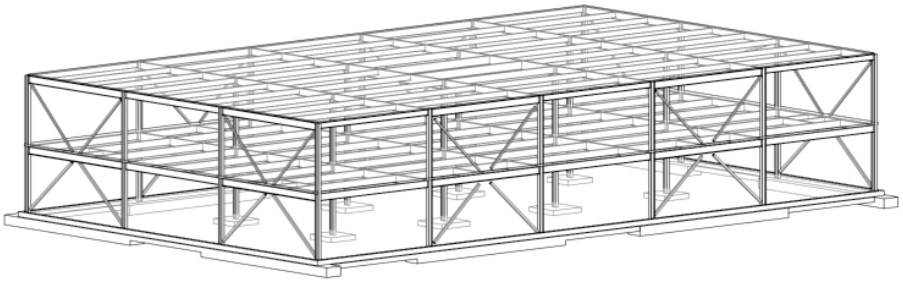

Figure 3-8 COM2B: two-story baseline archetype.

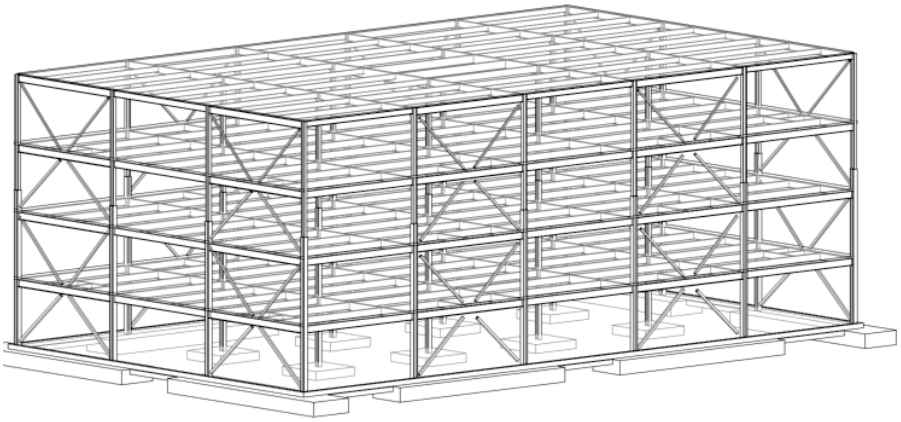

Figure 3-9 COM3B: four-story baseline archetype.

Braced-Frame Design

In practice, many different brace shapes—including wide flange, square, rectangular and round HSS—and sizes can be selected to satisfy project requirements. For this study, square HSS was chosen to represent a common choice for low-rise building SCBF braces. Square HSS had the additional benefit that the shape has been widely used in research. All HSS shapes were selected to meet the width-to-thickness ratio (b/t) requirements of ANSI/AISC 341-10.

Braces were designed assuming that forces were equally distributed between tension and compression braces, with the compression limit state governing the designs. Brace sizes were selected to produce a design demand-to-design capacity ratio (D/C) closest to 1.0 (D/C ratios for all designs can be found in Appendix A). This included using HSS shapes that are allowed by code but

that may not be readily available or used commonly in practice, including HSS 3 1/2×3 1/2, HSS 4 1/2×4 1/2, and HSS 5 1/2×5 1/2.

The details for the anchorage of columns and braces to foundations can vary widely in practice. For this study, tension anchor rods were used to resist uplift, and lap plates and embed plates were used to transfer shear. Anchorage was designed assuming the full yielded capacity of the anchor rods would be reached before concrete breakout. Anchor rods were sized to develop the strength of the yielded tension braces according to ANSI/AISC 341-10 Section D2.6.

Necessarily, a number of decisions were made in the archetype designs in this study that can vary in practice from one engineer or locality to another. For example, the material grade for the braced-frame gusset plates was selected to be A36, but it could have been A572 Gr. 50. In this study, such choices were evaluated based on the most common approach for the element and on the likely impact of the design choice on the collapse probability analysis. In the case of the gusset yield strength, for example, it was determined that the difference would not materially affect the analysis results.

Foundation Design

The general approach to the foundation design was to use a continuous shallow footing across the width of the braced frames, sized to satisfy stability from overturning and allowable soil bearing pressures. The stability of the system from overturning used ASCE/SEI 7 Section 12.4 strength-level load combinations, including vertical load effects, E_v. A 25 percent reduction in overturning moment was applied in accordance with ASCE/SEI 7 Section 12.13.4. To satisfy allowable bearing pressures, the design of the continuous footings at the braced frames used ASCE/SEI 7 Section 12.4 service-level load combinations, including vertical load effects, E_v. A 25 percent reduction in overturning moment was applied in accordance with ASCE/SEI 7 Section 12.13.4. Refer to Appendix A for more information on archetype foundation design.

3.5.2 Parametric Studies

Having established the baseline archetypes, four parametric studies were conducted to examine the influence of common variations on observed behavior and collapse performance:

1. Brace Configuration Parametric Study: Structures with chevron brace configurations instead of super-X configurations.

2. No Redundancy Parametric Study: Structures with a single, non-redundant braced bay on each face.
3. Soil-Structure Interaction and Foundation Flexibility Parametric Study: Structures with foundations analyzed including the effects of soil-structure interaction and foundation flexibility.
4. No Reserve Moment Frame Parametric Study: Structures with the reserve moment-frame action within the braced frames removed.

Brace Configuration Parametric Study

The influence of brace configuration on behavior and collapse probability was investigated for the two-story and four-story high-seismic archetypes (Figure 3-10 and Figure 3-11). In the baseline archetypes, the two-story and four-story braces had super-X configurations. In the parametric variations, a chevron-type brace elevation was adopted. (Note that for the one-story baseline archetype, the brace configuration was necessarily a chevron configuration as well.) Details of the designs are presented in Appendix A.

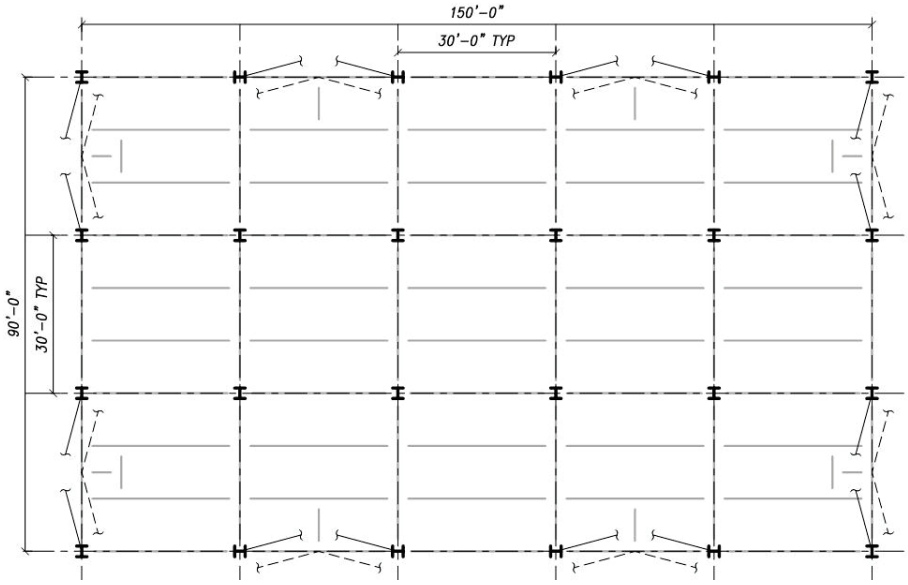

Figure 3-10 Plan configuration of COM2B-BC and COM3B-BC for the brace configuration parametric study (identical to COM2B and COM3B).

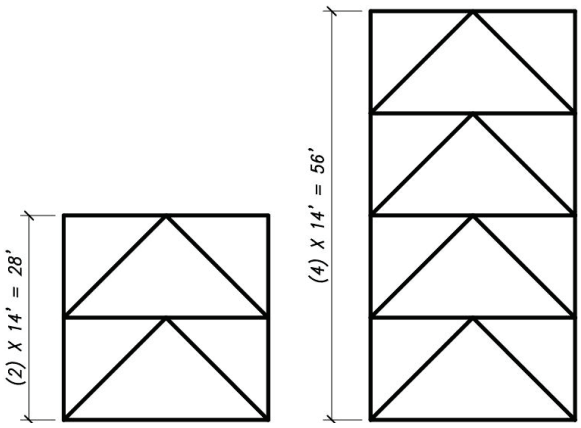

Figure 3-11 Typical two- and four-story brace elevation configurations of COM2B-BC and COM3B-BC, respectively, for the brace configuration parametric study.

No Redundancy Parametric Study

The influence of brace redundancy on behavior and collapse probability was investigated for the two-story high-seismic archetype (Figure 3-12 and Figure 3-13). For the baseline archetypes, the redundancy factor (ρ), as defined in ASCE 7-10 Section 12.3.4.2, had a value of 1.0. For the parametric variation, the number of braced bays on each face was reduced from two to one, and the redundancy factor was set as equal to 1.3. Details of the design are presented in Appendix A.

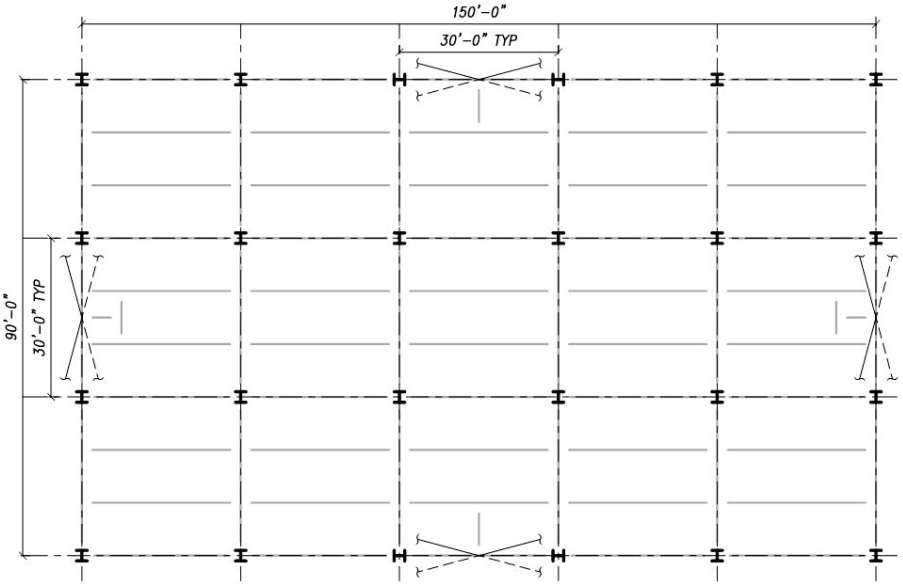

Figure 3-12 Plan configuration of COM2B-NR for the no redundancy parametric study.

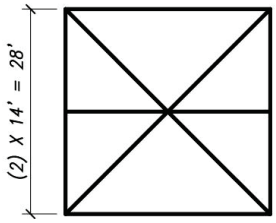

Figure 3-13 Typical brace elevation configuration of COM2B-NR for the no redundancy parametric study (identical to COM2B).

Soil-Structure Interaction and Foundation Flexibility Parametric Study

The influence of soil-structure interaction (SSI) and foundation flexibility on behavior and collapse probability was investigated for the two-story and four-story high-seismic archetypes (Figure 3-14 and Figure 3-15). Details of the foundation designs are presented in Appendix A.

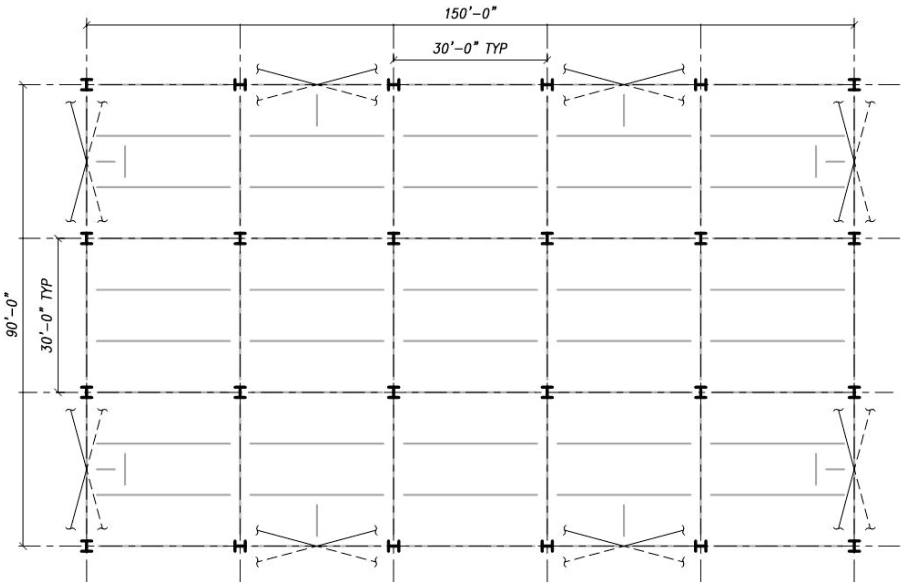

Figure 3-14 Plan configuration of COM2B-SS and COM3B-SS for the SSI parametric study (identical to COM2B and COM3B).

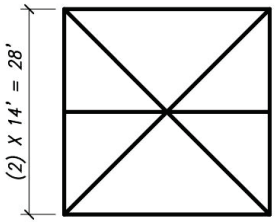

Figure 3-15 Typical brace elevation configuration of COM2B-SS for the SSI parametric study (identical to COM2B).

No Reserve Moment Frame Parametric Study

The influence of the removal of the reserve moment frame within the braced frames on behavior and collapse probability was investigated for the two-story high-seismic archetype. The design for the COM2B-NMF archetype was the same as that for the COM2B archetype, so no additional design information is provided. However, changes were made to modeling assumptions for the purposes of the parametric study, as described in Chapter 4.

Chapter 4

Numerical Modeling for Parametric Studies

4.1 Introduction

Steel concentrically braced frames (CBFs) are composed of braces, gusset plates, beams, and columns. The centerlines of the braces, beams, and columns join at a single concentric point. Key components include diagonal braces, typically hollow structural sections (HSS) or wide-flange sections (although other sections may be used); gusset plates; columns; and beams (the latter are sometimes referred to as framing elements). Figure 4-1 shows a typical braced frame with these key components highlighted.

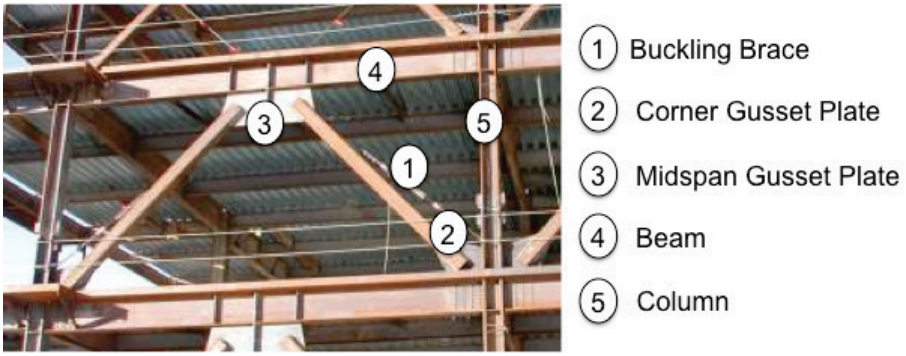

Figure 4-1 Components of a CBF.

The braces are the primary source of lateral resistance in CBFs. For buckling braces, opposing brace pairs are used to provide symmetrical resistance, and configurations include a single diagonal braced bay and opposing paired braces arranged in a single-story X, multi-story X, or chevron (i.e., inverted V).

Figure 4-2 shows the idealized cyclic response of paired buckling braces. Under compressive loading, the brace buckles and a "plastic hinge" forms at the center of the brace. Figure 4-3 shows photos of an HSS brace undergoing cyclic compressive and tensile loading. As the buckled brace is subjected to tension forces, the brace straightens and yields. Ultimately, the brace fractures in tension following development of local buckling and large local deformations in compression. As Figure 4-2a indicates, the tensile and compressive capacities of buckling braces are different; placing the braces in pairs results in symmetric behavior, as shown in Figure 4-2c. Notably in

Figure 4-2c, the total cyclic response of the braced frame is due to both the braces and the surrounding frame.

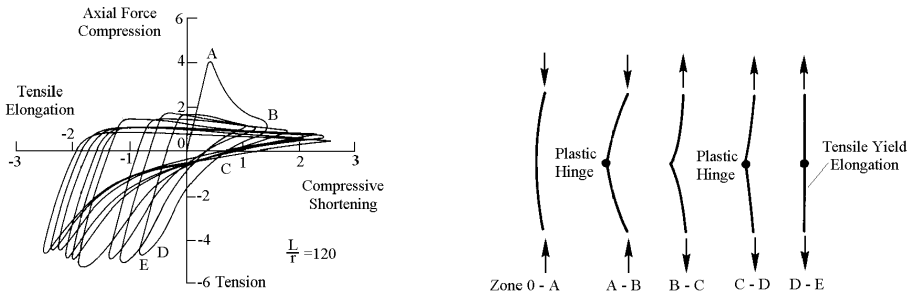

(a) Brace axial force-deflection hysteresis (b) Zones of behavior

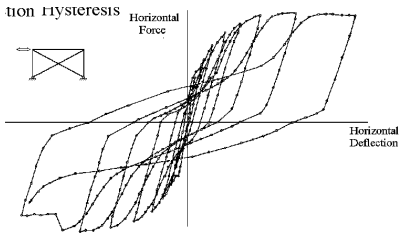

(c) Resulting frame lateral load-deflection hysteresis

Figure 4-2 Cyclic response of CBF with opposing braces (Bruneau et al., 2015).

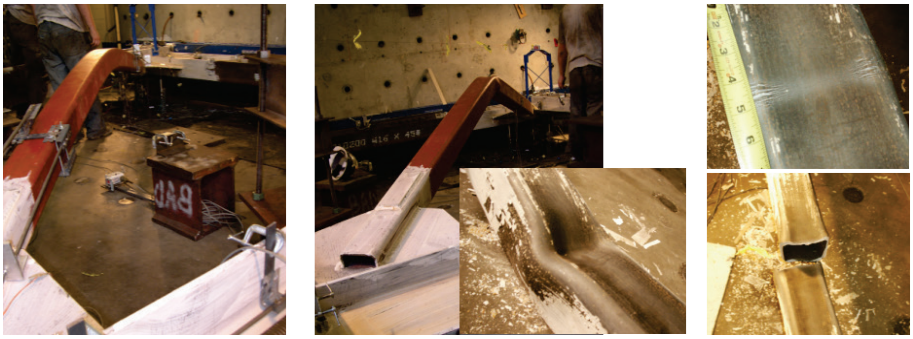

(a) Out-of-plane movement (b) Cupping at apex (c) Initial tearing and fracture

Figure 4-3 Progressive failure of a buckled brace from inelastic cyclic loading (adapted from Roeder et al., 2011).

In modern CBFs designed for regions of moderate-to-high seismicity, ANSI/AISC 341 provides design specifications for special concentrically braced frames (SCBFs) to ensure ductile response and an appropriate hierarchy of yield and failure modes. Ductile response is achieved by designing the braces for the calculated seismic loads, per ASCE/SEI 7, satisfying width-to-thickness ratio limits, and designing the connections, beams, and columns to develop the expected capacity of the braces.

Figure 4-4 illustrates the possible yield mechanisms and failure modes in CBFs. Capacity design of SCBFs eliminates several of the less desirable response modes from occurring. The anticipated hierarchy of yield mechanisms and failure modes for a modern SCBF is: (1) compressive-brace buckling (often inelastic buckling); (2) tensile-brace yielding; (3) yielding of beams or columns or both adjacent to gusset-plate connections; (4) yielding of gravity-frame-connection components; (5) brace fracture; (6) full development of plastic hinges in frame members adjacent to gusset plates; and (7) gravity-frame-connection failure, which typically requires pullout of bolts from shear tab beam-to-column connections (Roeder et al., 2011). This behavior might then be followed by sidesway collapse of the frame over a single story or multiple stories. Braced frames are susceptible to soft-story collapse modes because the story drifts can concentrate at the levels where brace deterioration occurs most rapidly.

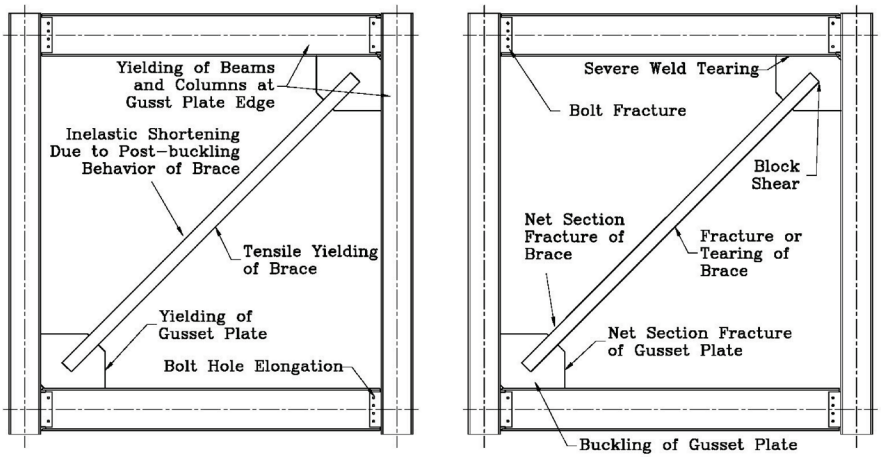

Figure 4-4 Possible yield mechanisms and failure modes for CBFs (adapted from Roeder et al., 2012).

The seismic response of modern SCBFs not only depends on the braces but also on the frame members and connections. These components provide additional strength and stiffness that becomes particularly important following brace fracture. However, the frame members and their connections typically undergo inelastic deformations at large story drifts. Thus, in order to study the response of SCBFs through collapse, it is necessary to consider the responses of the braces, connections, and frame members (Hsiao et al., 2012).

In some SCBFs that have foundations that consist of footings under the braced frames rather than a basement or deeper foundation, it is possible that the footings will uplift and rock prior to brace yielding, and the sequence of yield and failure modes described above may change. The archetypes in this

study included footings, and the effect of footing rocking on the collapse of short-period SCBFs was investigated. Models that included the potential for footing rocking were included in the soil-structure interaction (SSI) and foundation flexibility parametric study.

The archetypes described in Chapter 3 included two common brace configurations: multistory-X (sometimes called super-X) and chevron (inverted-V). They were designed in accordance with ANSI/AISC 341-10 and ASCE/SEI 7-10, hence it was necessary to consider the inelastic behavior of the braces, frame members, and connections in the modeling. Section 4.2 describes the modeling approach for the archetypes in this study. Section 4.3 provides an overview of the parametric studies. Section 4.4 describes additional modeling conducted to include the effects of SSI and foundation flexibility in the analysis of selected archetypes, and Section 4.5 discusses the analysis methods used.

4.2 Nonlinear Analyses Modeling

4.2.1 Modeling Approach

The archetypes were modeled in three dimensions using the nonlinear structural analysis program OpenSees (Mazzoni et al., 2006). Recent research on simulating the nonlinear seismic response of SCBFs (such as by Uriz et al., 2008; Hsiao et al., 2012; Hsiao et al., 2013a; and Sen et al., 2019) was drawn upon to develop the component behaviors that were included in the models. An illustration of a complete three-dimensional (3D) building model for the baseline COM2B archetype is shown in Figure 4-5. The key components of the model are described in the following sections.

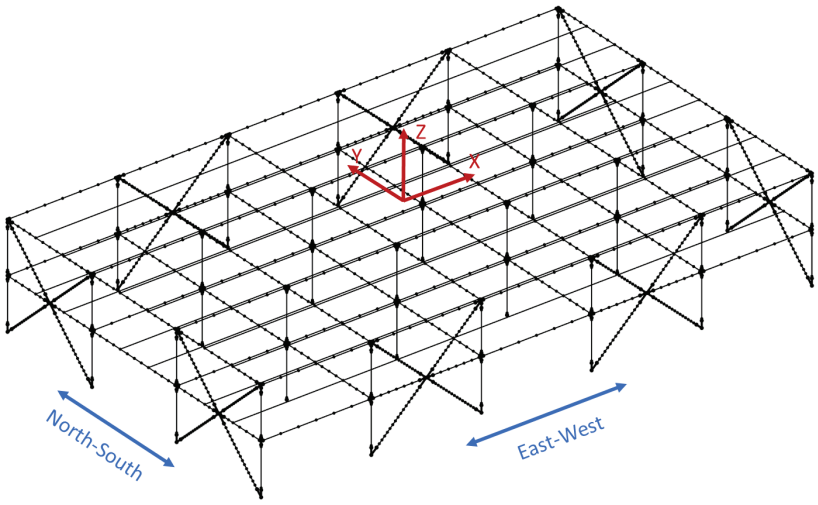

Figure 4-5 Example 3D frame model of steel SCBF archetypes.

To account for the contribution of the gravity frame to system response, all gravity frame members were included. Gravity frame members were modeled using the same method as the beams and columns within the braced frame as described below, and the nonlinear behavior of the beam-to-column connections were included. Corotational element formulations were used in OpenSees to account for nonlinear geometric effects.

The braced frames were modeled considering the nonlinear behavior of the braces, beams, columns, and connections. Figure 4-6 shows an annotated close-up of one of the SCBFs with callouts to the component models described in the sections below.

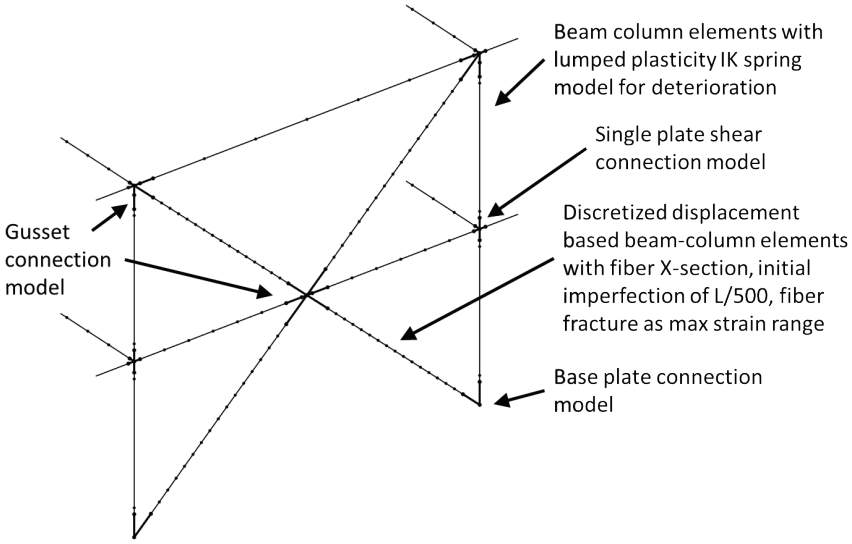

Figure 4-6 Annotated SCBF model with callouts for component models.

The diaphragms for all levels of the archetypes were modeled as rigid following a small study of the impact of modeling diaphragm flexibility on collapse probability. It was found that considering diaphragm flexibility resulted in negligible changes in the median spectral acceleration at collapse for the COM2B baseline archetype but did significantly increase computational time. Although the diaphragm flexibility was not found to meaningfully affect collapse performance, it might affect other aspects of building performance that were not the focus of this study. It was assumed that collector connections were able to consistently transfer loads from the floors to the braced frames. As is common in braced frames, the lateral forces are transferred through a combination of shear studs attached to the beams of the braced frames and the connections of the braced frames to adjacent bays of gravity framing. Since these connections and configurations vary widely and conservative assumptions are often used for determining collector forces, their potential for nonlinear behavior was not considered.

Both gravity loads and seismic mass were included in all models and were calculated using the load combination of $1.05D + 0.25L$, where D and L are the dead and live loads, respectively, as recommended in FEMA P-695. Seismic mass was assigned to only the horizontal displacement degrees of freedom. As noted in Section 4.3, the models that included SSI and foundation flexibility resulted in the braced frames rocking on their footings. Including vertical mass would have provided additional resistance to overturning. Therefore, to be conservative, vertical mass was not included in the models, resulting in somewhat higher estimates of collapse capacity than would have been calculated had vertical mass been included. The inclusion of the seismic weight, and the corotational geometric transformation used for the columns, ensured that P-delta effects were included. Since the diaphragms were modeled as rigid, both mass and gravity loads were applied at the columns using tributary area concepts. Within braced frames, mass and gravity loads were placed at brace-beam intersection points within the beam spans, again calculated based on tributary areas so that the braces were initially compressed.

4.2.2 Brace Model

The brace model was based upon research by Hsiao et al. (2012) that has been extended recently by Sen et al. (2019). All braces considered in this study were square HSS, and all were assumed to yield in tension and buckle in compression. They buckled out of plane because they were connected to the frame with gusset plates. The brace model used 16 displacement-based distributed plasticity beam-column elements with fiber cross sections per brace. The cross section was discretized with 128 total fibers and an initial imperfection of $L/500$ (where L is the brace length) in the out-of-plane direction. Figure 4-7 illustrates the brace model.

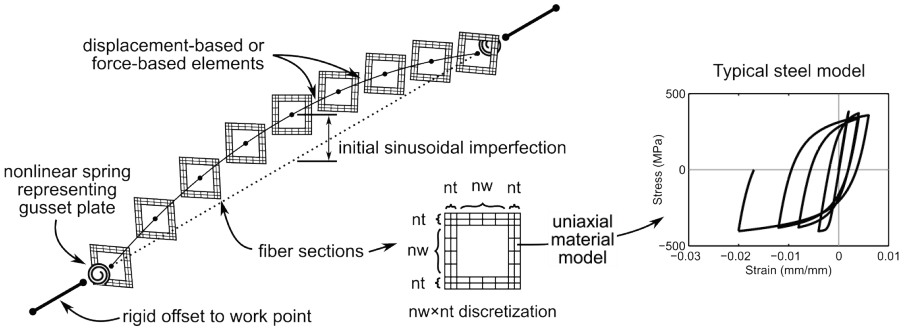

Figure 4-7 HSS brace model (Hsiao et al., 2013a).

The steel material model (Steel02) assigned to the brace fibers was a Giuffre-Menegotto-Pinto stress-strain model available in OpenSees and is illustrated in Figure 4-7. Fracture of the brace was simulated with a material wrapper

that uses the strain range of the fiber (i.e., the maximum range of strain from compression to tension for the fiber). When the strain range reaches a maximum strain range (MSR) calibrated from test results on HSS braces, fracture of the fiber occurs, and the fiber stress and modulus were assigned near zero values. Figure 4-8 illustrates the MSR concept, where the maximum tensile and compressive strains for a particular fiber are tracked, and upon reaching the MSR value, the fiber fractures (i.e., has negligible strength and stiffness).

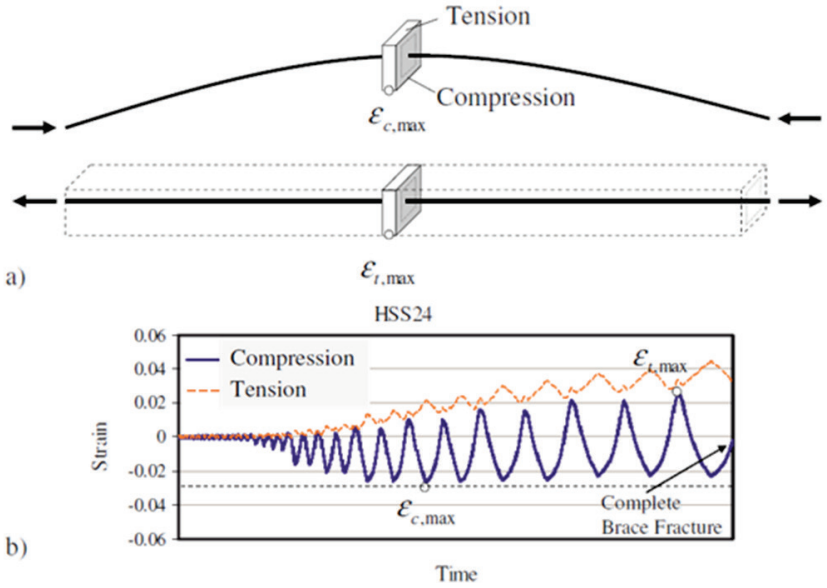

Figure 4-8 Illustration of the MSR model for brace fiber fracture (adapted from Hsiao et al., 2013a).

Sen et al. (2019) calibrated the MSR at fracture for more than 60 tests on HSS braces. The key parameters in determining the MSR at fracture, MSR_f, were found to be brace local slenderness (b/t, where b is the brace width and t is the wall thickness), brace global slenderness (L_c/r, where L_c is the clear length of the brace and r is the radius of gyration), ratio of the brace modulus of elasticity to the brace yield stress (E/F_y), and the ratio of maximum compressive brace deformation to tensile brace deformation ($\delta_{c,max}/\delta_{t,max}$). These parameters were combined into an equation to predict MSR_f:

$$MSR_f = 0.554\left(\frac{b}{t}\right)^{-0.75}\left(\frac{L_c}{r}\right)^{-0.47}\left(\frac{E}{F_y}\right)^{0.21}\left(\frac{\delta_{c,max}}{\delta_{t,max}}\right)^{0.068} \quad (4\text{-}1)$$

To apply this model both the fiber strains and the maximum brace deformations were tracked as history variables within the material wrapper for the steel fiber. Sen et al. (2019) found the model was capable of predicting brace fracture from the experimental database with an R^2 of 0.72, indicating a good correlation for a range of brace sizes and load histories.

Figure 4-9 shows the resulting brace behavior, through brace fracture, using the complete brace model described above compared with experimental results from Sen et al. (2019).

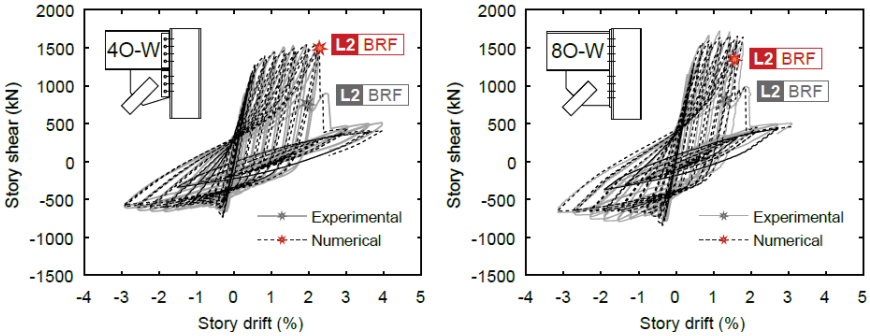

Figure 4-9 Comparison of numerical and experimental brace behavior (adapted from Sen et al., 2019).

4.2.3 Brace Connection Model

The square HSS braces of the archetypes were connected to the beams and columns with gusset plates and thus buckled out of the plane of the SCBF. The gusset plates were designed to have appropriate clearances between the brace ends and the beams and columns—a straight-line clearance of two times the gusset plate thickness—such that the gusset plates had out-of-plane flexibility and the brace ends could rotate out-of-plane during brace buckling. However, the out-of-plane restraint provided at the ends of the braces was not negligible (i.e., was not a pinned condition). As Hsaio et al. (2012) found, to model the buckling and post-buckling behavior of an SCBF assembly, it is necessary to approximate the end conditions for the braces as something other than pinned or fully restrained.

Here, the recommendations of Hsaio et al. (2012) were used to simulate the out-of-plane rotational response of the gusset plates and to simulate the impact of the gusset plate on beam-to-column connection stiffness and yield mechanisms. This modeling approach is shown schematically in Figure 4-10. A rotational spring with nonlinear behavior was used for the out-of-plane rotational strength and stiffness of the gusset plates, and rigid elements were used to represent the beams and columns along the attachment of the gusset plates. The out-of-plane rotational stiffness and moment strength of the gusset plates are given by:

$$K_{cal}^{rotational} = \frac{E}{L_{ave}}\left(\frac{W_w t^3}{12}\right) \tag{4-2}$$

$$M_p = \left(\frac{W_w t_p}{6}\right) F_{y,gusset} \tag{4-3}$$

where E is the elastic modulus of the gusset plate, t is the depth of the section that is bending the gusset plate out of plane, $F_{y,gusset}$ is the gusset yield stress, W_w is the Whitmore width computed with a 45-degree angle, L_{ave} is the average of L_1, L_2, and L_3 shown in Figure 4-10, and t_p is the thickness of the gusset plate. This configuration allows the brace to buckle and then results in inelastic deformation of the frame members just outside the edges of the gusset plate, which is the behavior that has been observed in numerous experiments.

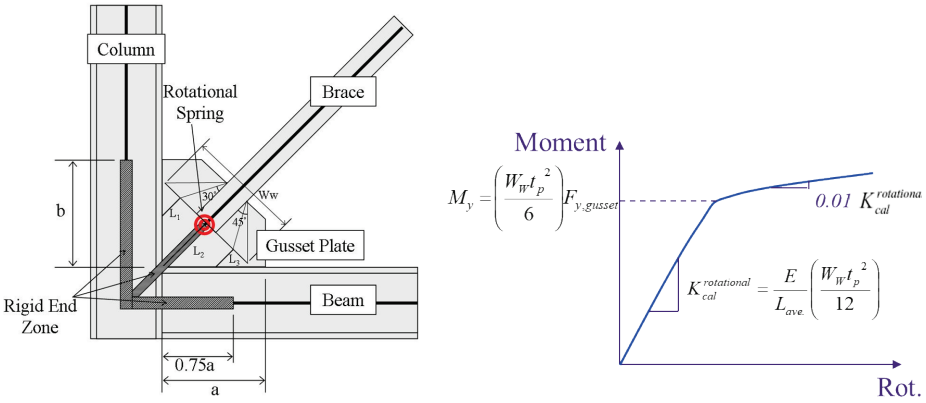

Figure 4-10 Gusset plate modeling approach and out-of-plane gusset plate moment-rotation behavior (adapted from Hsiao et al., 2012).

Figure 4-11 shows a comparison from Hsiao et al. (2012) of single diagonal SCBF response with three different models, as illustrated with experimental results from cyclic testing. Apart from the connections, the braces, beams, and columns were modeled using a similar approach to that used in this study. As shown, the model—including rotational springs at the brace ends and considering the regions of the beams and columns adjacent to the braced frame as rigid—provided the best approximation of the actual behavior in terms of strength, stiffness, and post-buckling behavior. Hsiao et al. (2012) provided these comparisons for a range of gusset-plate configurations, where the clearance, gusset thickness, and gusset geometry were varied, and all were shown to be best simulated with the model illustrated in Figure 4-9 and used here.

The behavior of the gusset plates, especially at collapse, is relatively independent of material specification for typical plate materials. For the archetype designs described in Chapter 3, the gusset plates were specified to be A36. As noted above, all materials were modeled using their expected stress, R_yF_y, which for A36 plate steel is 46.8 ksi, where R_y is the ratio of the expected yield stress to the specified minimum yield stress and F_y is the specified minimum steel stress. Had A572 grade 50 steel been specified, the yield stress used in the models would have been 55 ksi. This difference in

gusset-plate material yield stress would not have impacted the collapse capacity of the frames in a significant way because it was only used to determine the out-of-plane bending resistance of the gusset plates.

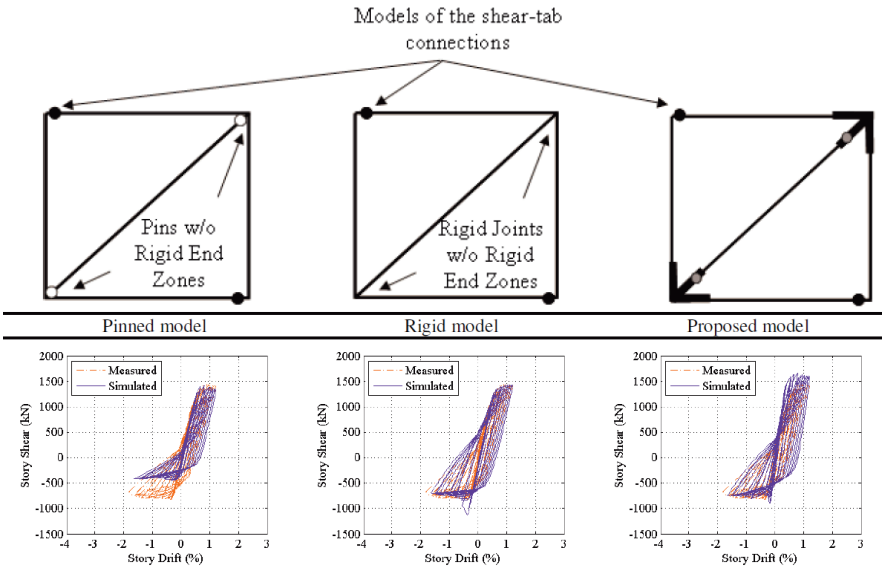

Figure 4-11 Comparison of modeling approaches for brace-to-gusset plate connections (adapted from Hsiao et al., 2012).

4.2.4 Beam Model

Beams were modeled with displacement-based nonlinear beam-column elements with distributed plasticity and fiber discretized cross sections. This approach accounted for the interaction between axial force and flexure. Similar to the brace, a Giuffré-Menegotto-Pinto model was used for the steel material behavior. The beams within a braced frame were discretized into five elements, each with five integration points, and the beams of the gravity frames were modeled with a single element over the entire bay width. For beams, the strength and stiffness provided by the composite slab at the floors was neglected. Additionally, because all beams met seismic compactness requirements, deterioration of their flexural and axial strength was neglected.

4.2.5 Column Model

Columns, in both the braced frames and the gravity framing, were modeled with elastic beam-column elements with discrete nonlinear rotational springs at each end to represent the nonlinear behavior of the columns in both the strong-axis and weak-axis bending directions, including deterioration. The springs were located at the gusset-plate edges where gusset plates were present (a dimension *b*, as shown in Figure 4-10, from the centerline intersections of the beams and columns or the column bases), or were located

a distance of one half of the column depth from column ends or beam-and-column intersections where gusset plates were not present.

The nonlinear behavior assigned to each rotational spring in each axis of bending was derived from the recommendations in NIST GCR 17-917-46v2, *Guidelines for Nonlinear Structural Analysis for Design of Buildings: Part IIa-Steel Moment Frames* (NIST, 2017), and in Lignos et al. (2019) for hinge models of wide-flange columns. The rotational spring model used was the modified Ibarra-Medina-Krawinkler (IK) phenomenological component model, a peak-oriented multi-linear model with cyclic deterioration available in OpenSees. The peak and post capping strengths were reduced for the effect of axial load according to the recommendations in NIST (2017), where the axial load was assumed to be the gravity load only and was assumed to be constant. This assumption is appropriate for modeling braced frames to collapse after the braces fracture, leaving only gravity loads and a small additional amount of axial load from frame action at large story drifts where the column rotation demand is largest. Further, in cases where foundation rocking occurs, there is little flexural demand on the columns, and they remain essentially elastic. Cyclic deterioration in flexural strength in the columns was modeled using the deterioration parameters in the IK material model with values based on the recommendations from Lignos et al. (2019). The cyclic deterioration parameters are primarily a function of the column width-to-thickness ratio and were recalculated for each different column section.

4.2.6 Single Shear-Plate Connection Model

The moment-rotation behavior of the single shear plate beam-to-column connections within the gravity framing and at locations in the braced frames where gusset plates are not present was based on the recommendations in NIST (2017), which were largely based on the recommendations in Liu and Astaneh-Asl (2004). Connections were modeled with a zero-length rotational spring, applied only to the strong-axis rotation direction of the beams, where the nonlinear moment-rotation behavior is illustrated in Figure 4-12, with small differences as described below. As shown, the behavior is pinched, deteriorates with increasing rotation, and does not have symmetric strength. This behavior is consistent with the effects of accumulating bearing deformations at bolt holes (creating pinching and deterioration) and the presence of a composite floor slab (creating asymmetric strength). Liu and Astaneh-Asl (2004) provide comparisons of the model with test results.

There were two deviations from the recommendations in NIST (2017) and Liu and Astaneh-Asl (2004). First, the shear tab connections were assumed

to deteriorate as shown in Figure 4-12 until they reached 50 percent of the peak strength in a given direction of loading. Then, they were assumed to maintain that capacity indefinitely, whereas Liu and Astaneh-Asl (2004) recommended that the connections be modeled to fail at a rotation of g/d_c, where g is the gap between the beam-and-column flanges and d_c is the distance from the mid-height of the shear plate to the flange of the beam in compression. This failure was neglected because: (1) modern single shear-plate connections were designed for bolt bearing to control over bolt fracture, where several of the tests used to calibrate the model by Liu and Astaneh-Asl (2004) were simulating older connections where bolt fracture occurred; and (2) in practice, there is evidence of large variability in the gaps between the beam-and-column flanges in gravity frames. Second, the connection model was applied to connections where more than two columns of bolts were present, whereas all tests used to calibrate the Liu and Astaneh-Asl (2004) model had only a single column of bolts. This difference was implemented because the deformation modes were expected to be similar, and there is no experimental data to inform a different model.

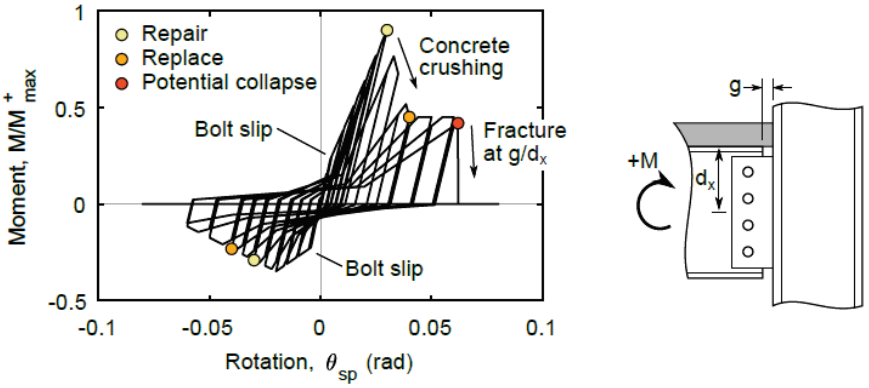

(a) Moment-rotation behavior with annotated damage and performance states

(b) Bolted shear plate configuration

Figure 4-12 Example moment-rotation behavior for representing single-plate shear connections (adapted from Sen et al., 2019).

4.2.7 Column Base Model

Column base nonlinearity (e.g., yielding of anchor rods) in low-rise steel frames may occur due to tension demands, moment demands, or a combination of both. In braced frames, the maximum tension and moment do not occur at the same point in the load history, and generally when the tension force is high, the moment demand is low, and vice-versa. This is due to brace buckling and fracture, which occurs at small drifts (approximately 2 percent to 3 percent). When the braces are intact, the overturning moments and tension in the columns is maximum, but the drifts and corresponding moments at the bases of the columns are small. Similarly, once the braces

buckle and fracture, the overturning moments and column tension are reduced significantly, and the drifts and moment demand at the column bases become larger. Thus, for simplicity, the axial force (i.e., vertical force) and moment behavior of the column-base connections in the braced frames were modeled as uncoupled. A typical column base detail for the COM2B baseline archetype is shown in Figure 4-13.

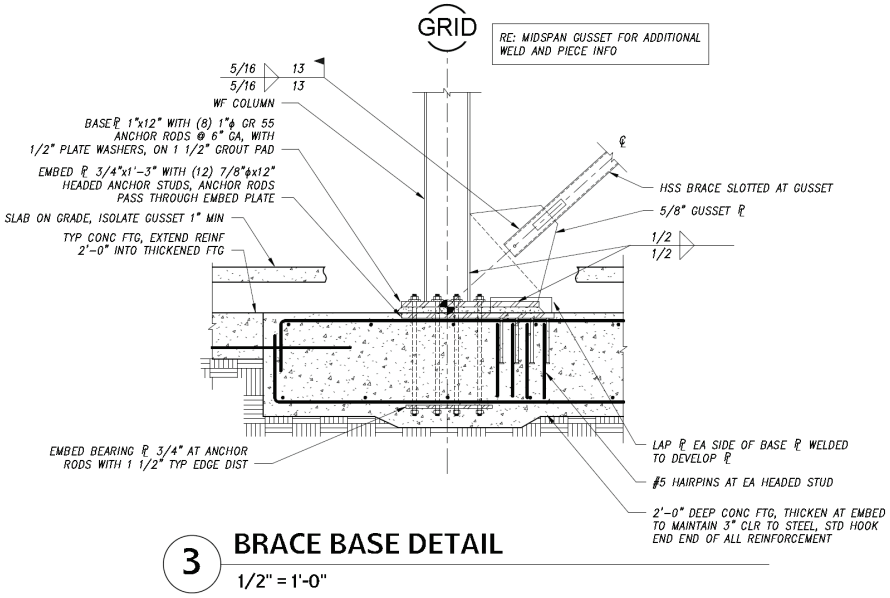

Figure 4-13 Typical column base detail.

To evaluate the need to model nonlinearity in the vertical force responses of the column bases, the maximum reaction forces from all archetype models were established using pushover analyses. The tension capacities of the column-base designs were then compared to demands from pushover analyses, and it was determined that in most cases the connections remained elastic. In the few cases where anchor rod yielding was noted, small adjustments to the design, such as specifying 1/8-inch larger diameter rods, were found to mitigate the yielding and were considered well within the range of acceptable designs for these archetypes. Further, as noted in the sections that follow, the braced frames were found to rock on their footings when SSI and foundation flexibility were considered. Modeling anchor rod yielding or pull out would have caused the frames to rock at the column-base interfaces and would have resulted in all models experiencing rocking. Since in many cases the vertical forces were small enough that the base connections could remain elastic, and it was desirable to have braced-frame models that did not rock (since rocking would be addressed at the foundation as described later in the report), yielding caused by vertical forces at the column bases was not modeled.

At large story drift, the flexural behavior of column base-plate connections can be important, especially for columns within braced frames where gusset plates are present at the column bases. However, there is limited data in the literature to guide the nonlinear moment-rotation responses of these connections. Thus, simple mechanics was used to approximate the nonlinear response. As shown in Figure 4-14, the tension in the anchor bolts is balanced by compression under the base plate provided by the footing. When the compression is under the portion of the base plate where the gusset plate is present (positive moment in the figure), it is generally large enough to yield all the anchor bolts. For moment in the opposite direction (negative moment in the figure), the compression zone is smaller and not all of the anchor bolts yield. This and the difference in the moment arm between the illustrated positive and negative moment directions results in significantly different moment strengths for the connection for each direction. The strengths were computed using expected material strengths for the anchor bolts and the footing, and 5 percent strain hardening was assumed for the anchor bolts. Since the anchor bolts yield and elongate permanently, the hysteretic behavior was assumed to be pinched, as shown in Figure 4-15. The axial-force interaction was neglected because the column axial forces are small when the moment is large, as discussed above. The anchor bolts were assumed to be partially debonded, which ensured that they had the strain capacity to reach rotations beyond those required for the collapse analyses, and therefore strength deterioration of these connections was not simulated.

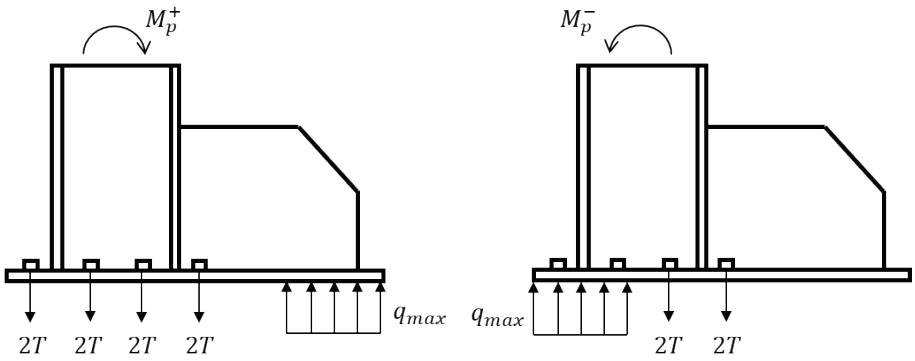

Figure 4-14 Assumed connection forces due to column bending moments.

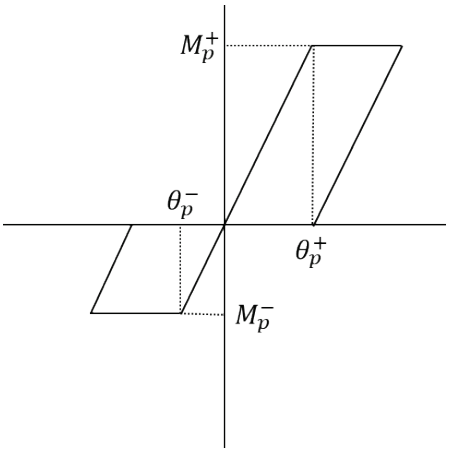

Figure 4-15 Assumed column base-plate connection response for in-plane moment.

4.2.8 Comparison of Model Behavior with Experiments

Experiments on braced-frame systems have been conducted and then modeled in previous research using component models described above, with the exception of the column base model, which was added for this study. Sen et al. (2019) and Hsiao et al. (2013b) modeled two-story and three-story braced frames in chevron and super-X configurations, respectively, where the experiments themselves are detailed in Sen et al. (2016) and Lumpkin et al. (2012), respectively. Both sets of experiments were quasi-static cyclic tests of full-scale braced frames with partially composite floor slabs that were loaded at the upper levels only. The brace sizes were the same over all stories. The numerical modeling of the experiments showed that the complete system behavior of the braced frames is captured well by the modeling approach. Both compared global response quantities (e.g., base shear and story drift) and local quantities (e.g., out-of-plane brace deformation and story drift at brace fracture). An example comparison between the experimental and numerical responses is shown in Figure 4-16, which compares both the base shear versus first-story drift and the drift at which brace fracture occurs (points labeled L2BRF). As shown, both the global and local response quantities are predicted well with the model, including the cycle of loading during which brace fracture occurs.

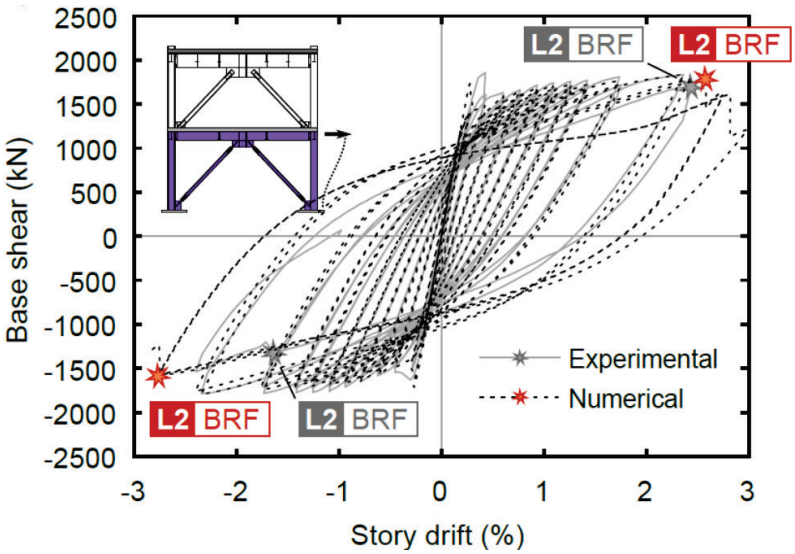

Figure 4-16 Comparison of experimental and numerical braced-frame responses (adapted from Sen et al., 2019).

4.2.9 *Damping*

Damping is necessary for nonlinear response history analysis. Hysteretic damping was provided by the nonlinear behavior of the elements within the model. Additional damping was specified to represent inherent damping due to nonstructural components, friction, and other difficult-to-quantify sources. Often the Rayleigh damping model is used for this purpose. However, recent research by Chopra and McKenna (2015) found that application of the Rayleigh damping model in nonlinear response history analysis can lead to the presence of "spurious" damping forces and inaccurate response results. Instead, they suggested the use of a viscous damping matrix that is constructed using the superposition of modal damping matrices. Known as "modal damping," this model is available in OpenSees and was employed for this study. A 2 percent modal damping ratio was applied to the first six elastic modes for all archetype models.

4.3 Parametric Studies and Building Archetypes

4.3.1 *Overview*

This study investigated the collapse probability of short-period SCBF archetypes using detailed modeling approaches and considering a range of variations in building design and analysis that may affect collapse probability. Five parametric studies using the archetype buildings presented in Chapter 3 were used. These parametric studies included: (1) baseline configuration; (2) brace configuration; (3) no redundancy of braced frames; (4) soil-structure interaction (SSI) and foundation flexibility; and (5) no

reserve moment frame. These are briefly described below, and Table 4-1 lists the names of the archetype models. Table 4-2 summarizes the key seismic design criteria for each baseline configuration.

Table 4-1 Baseline and Variant Numerical Models for the Parametric Studies

No. of Stories	Baseline Configuration	Brace Configuration	No Redundancy	SSI and Foundation Flexibility	No Reserve Moment Frame	No. of Models
Commercial Buildings: High Seismic						
1	COM1B	-	-	-	-	1
2	COM2B	COM2B-BC	COM2B-NR	COM2B-SS(1,2) and -Unfiltered	COM 2B-NMF	6
4	COM3B	COM3B-BC	-	COM3B-SS(1,2)	-	4
Commercial Buildings: Very High Seismic						
1	COM4B	-	-	-	-	1
2	COM5B	-	-	-	-	1
4	COM4B	-	-	-	-	1

Table 4-2 Seismic Design Criteria for the Baseline Archetypes

Baseline Configuration	No. of Stories	W (kips)	SDC	R	T_a (sec)	$T = C_u T_a$* (sec)	C_s	S_{MS} (g)
COM1B	1	495	D	6	0.14	0.25	0.167	1.5
COM2B	2	1868	D	6	0.24	0.34	0.167	1.5
COM3B	4	4646	D	6	0.41	0.57	0.167	1.5
COM4B	1	495	E	6	0.14	0.25	0.250	2.25
COM5B	2	1868	E	6	0.24	0.34	0.250	2.25
COM4B	4	4646	E	6	0.41	0.57	0.250	2.25

* The design period is defined as $T = C_u T_a \geq 0.25$ seconds, in accordance with the requirements of FEMA P-695, where the values of the parameters C_u and T_a are specified by ASCE/SEI 7-10. $T = C_u T_a = 0.2$ seconds for COM1B and COM4B. Consistent with FEMA P-695, COM1B and COM4B were designed for $T = 0.25$ seconds. However, the ground motions used for IDA for COM1B and COM4B were scaled using the median spectral acceleration of the ground-motion set at a period $T = 0.2$ seconds.

4.3.2 Baseline Configuration Parametric Study

Baseline archetypes of one, two, and four stories were designed with a commercial building geometry with four braced frames in each direction of loading, placed symmetrically at the exterior walls. Braced frames in the two-story and four-story designs had super-X configurations, whereas the one-story baseline had a chevron configuration. The baseline archetypes were modeled assuming fixed bases. Number of stories, and correspondingly the fundamental period, and the design base shear were the primary variables in the baseline configuration parametric study.

4.3.3 Brace Configuration Parametric Study

The behavior of braced frames in super-X configurations differs from that of braced frames in chevron configurations. Because braces degrade quickly following buckling, there is significant flexural demand placed on the beams in chevron configurations due to differences in forces in the tension and compression braces. This is considered in design, and large beams are specified to resist this demand. Additionally, chevron configurations result in gusset plates at all beam-to-column connections except the roof, potentially providing additional strength and stiffness to the lower stories following brace fracture. Therefore, a parametric study on braced-frame configuration was conducted for the two-story and four-story archetypes. Each was designed and modeled with a super-X configuration (COM2B and COM3B) and a chevron configuration (COM2B-BC and COM3B-BC).

4.3.4 No Redundancy Parametric Study

It is possible, and sometimes economical, to design building systems with braced-frame layouts that have fewer bays of braced frames and larger braces in each bay than the baseline configuration. In ASCE/SEI 7-10, this reduction in redundancy is sometimes penalized with the redundancy factor, $\rho = 1.3$, which results in 30 percent larger design brace forces from earthquake loads than it would be for systems conforming to the redundancy requirements. This reduction in redundancy and increase in brace size may impact the collapse performance of braced-frame systems. Therefore, a parametric study on braced-frame redundancy was conducted, where the two-story archetype was designed meeting the requirements for $\rho = 1.0$ with four braced frames in each direction of loading (COM2B) and designed with only two frames in each direction and the resultant $\rho = 1.3$ penalty (COM2B-NR).

4.3.5 Soil-Structure Interaction and Foundation Flexibility Parametric Study

SSI and foundation flexibility are typically not considered when analyzing the collapse capacity of structural systems. SSI can reduce the effective ground motions through kinematic interaction (which includes the effects of base-slab averaging), and the foundation-soil system provides a flexible layer where the foundations can move vertically and horizontally and rotate. Braced frames have significant overstrength that is not considered in current practice for foundation design, which can lead to uplift of strip footings underneath braced frames and a rocking behavior. Therefore, a parametric study on the impact of modeling both SSI and foundation flexibility was conducted. Two baseline configurations were modeled considering the effects of SSI and foundation flexibility for a stiff soil site (COM2B-SS1 and

COM3B-SS1) and a soft soil site (COM2B-SS2 and COM3B-SS2). Additionally, the COM2B-SS1 and COM2B-SS2 models were run with the original ground motions, unfiltered for kinematic interaction, to investigate the impact of ground motion modification on collapse probability. These analyses are denoted COM2B-SS1-Unfiltered and COM2B-SS2-Unfiltered, respectively, and otherwise use the COM2B-SS1 and COM2B-SS2 models exactly. Additional modeling considerations for including these effects are described in Section 4.4.

4.3.6 No Reserve Moment Frame Parametric Study

After brace fracture occurs for both braces on a given story, lateral resistance is provided by two mechanisms: (1) the gravity framing; and (2) moment-frame action within the braced frames resulting from the presence of the gusset-plate connections at beam-to-column connections and the column bases. To examine whether these effects might play a significant role in collapse probability of the archetypes, pushover analyses were performed for COM2B for cases where: (1) the gravity frame beam-to-column connections were assumed to have zero moment capacity; and (2) the beam elements where gusset plates are located within the braced frame and the column bases within the braced frames were assumed to have zero moment capacity, as illustrated in Figure 4-17. As shown in Figure 4-18 and Figure 4-19, relative to the COM2B case, the pushover response for the braced frames is similar (6 percent maximum difference in base shear strength) if the gravity connections are assumed to be pinned but is significantly different (17 percent maximum difference in base shear strength) when the braced-frame members are assumed to be pinned at the gusset-plate ends and column bases.

Subsequent pushover analyses found that the braced-frame archetypes had significant capacity above their design demands due to several factors, including available brace sizes and the difference between the tension and compression strengths of the selected braces. This caused the relative contribution of the gravity frames to the lateral resistance to be small, since the braced frames were considerably stronger than design lateral-force demands. In contrast, the removal of the reserve moment-frame capacity within the braced frames had a larger impact on the system's strength. Based on the pushover analysis results, a variant was studied for COM2B where the moment capacity of the beams at gusset-plate edges were assumed to be zero, and the column bases within the braced frames were assumed to have zero moment strength. This variant where the reserve moment frame is removed is denoted COM2B-NMF. The gravity framing in COM2B-NMF was modeled identically to COM2B.

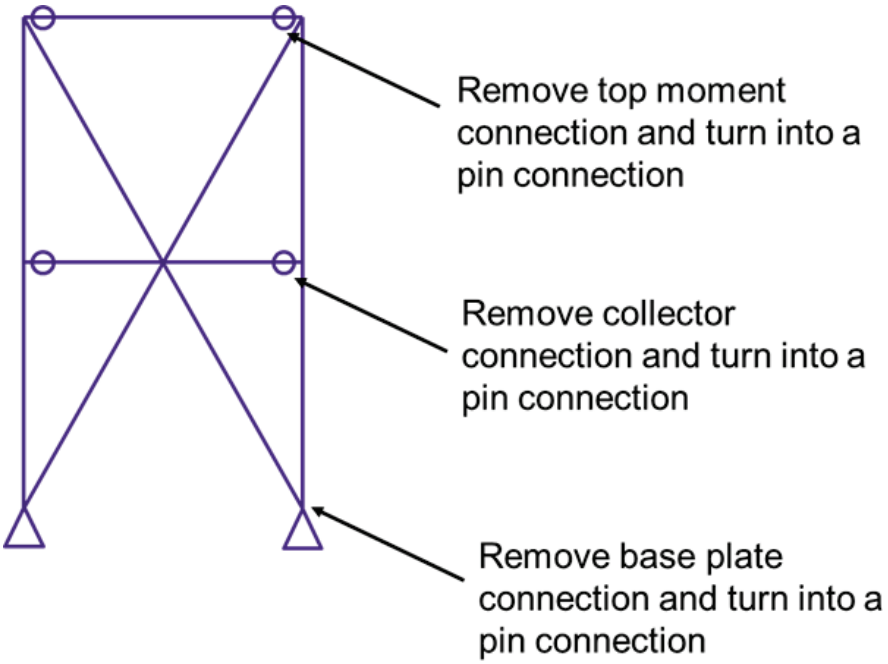

Figure 4-17 Schematic of model changes for COM2B-NMF.

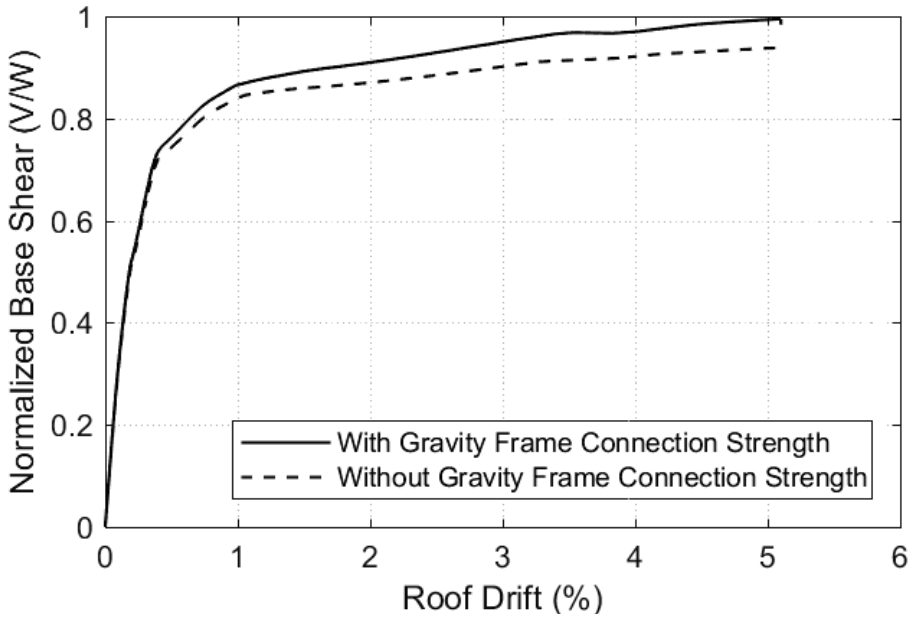

Figure 4-18 Comparison of pushover analyses for COM2B with and without moment capacity at the beam-to-column connections in the gravity framing.

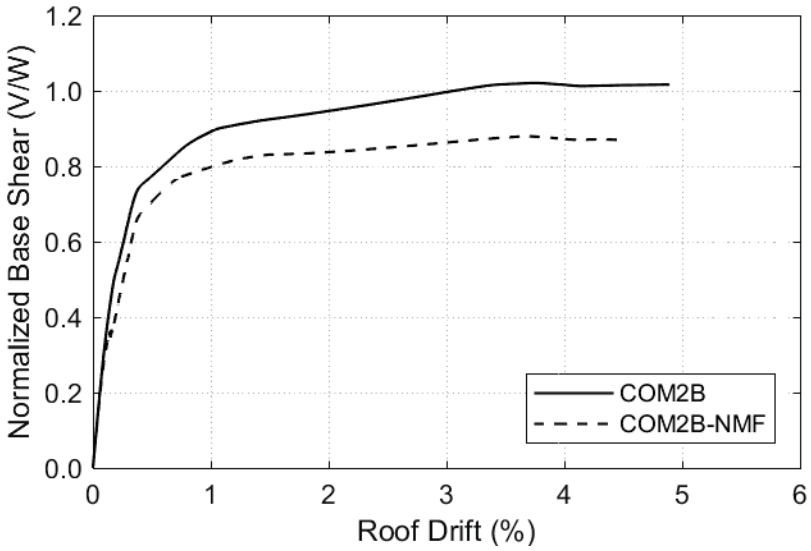

Figure 4-19 Comparison of pushover analyses for COM2B with and without moment capacity at the beam-to-column connections and at the column bases in the braced frames.

4.4 Modeling Soil-Structure Interaction and Foundation Flexibility

One parametric study investigated the effects of SSI and foundation flexibility on the collapse behavior of short-period braced frames. The intent was to simulate: (1) soil deformation; (2) foundation sliding; (3) foundation uplift and rotation; and (4) the impact of kinematic interaction in ground-motion input. Foundation systems for the archetypes are described in Chapter 3 and generally consist of strip footings underneath braced frames and isolated footings under gravity-frame columns. Where SSI is considered in the analyses, the footings under the braced frames were modeled explicitly using the lumped-plasticity nonlinear beam elements (beam with hinges in OpenSees), and the behavior of the soil, including damping, was simulated for all six degrees of freedom using a series of nonlinear spring and damper elements. To include the effects of kinematic interaction, which reduces ground motion, the process outlined in NIST GCR 12-917-21, *Soil-Structure Interaction for Building Structures* (NIST, 2012b), was used and is detailed in Appendix B.

Figure 4-20 shows a plan view of the COM2B-SS model at the foundation level. As shown, the footings were connected to each other and to the gravity column footings with pin-ended struts that represented the grade beams and the slab-on-grade. As reinforcement in those elements was light (only supplied for temperature and shrinkage), their flexural and tensile strengths were neglected, and they only transferred loads between footings through compression.

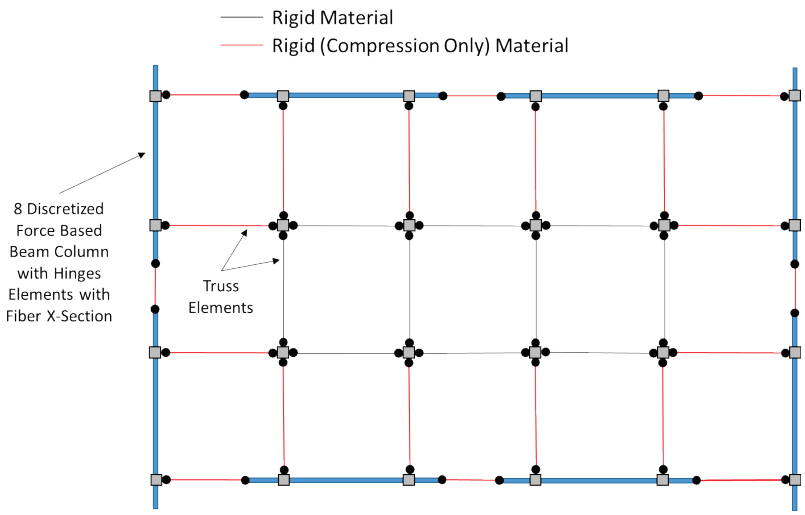

Figure 4-20 Plan view of foundation level of the COM2B-SS model.

Figure 4-21 shows a schematic of the model of the footings and soil springs under the braced frames. The footings were discretized into eight beam-with-hinges elements per footing for the two-story buildings, where the footings are isolated to each braced frame. The plastic hinge length for the beam-with-hinges elements was specified as six inches for all elements due to the section depth and light transverse reinforcement. Where the footings were continuous around the perimeter of the building (only for COM3B-SS on the softer soil profile discussed below), they were discretized similarly around the entire perimeter of the building. A small refinement study was performed using pushover analysis to determine the impact of the discretization of the footings where the mesh size was reduced by half. It was found that the discretization of eight elements per footing was adequate.

Two sites (soft and stiff) were selected with different target values of time-averaged shear wave velocity to a depth of 30 m (V_{s30}), with the intent of capturing potentially variable levels of SSI effects. The soft and stiff sites were targeted to be near the site class D/E boundary (V_{s30} = 180 m/s) and near the site class C/D boundary (V_{s30} = 360 m/s), respectively. The soft site was taken as the Imperial Valley Wildlife Liquefaction site. The shear-wave velocity profile compiled from multiple sources by Star et al. (2015) has V_{s30} = 183 m/s. The stiff site was taken as the Cholame Parkfield 12W site. The shear-wave velocity profile from Thompson et al. (2010) has V_{s30} = 354 m/s. Complete site profiles, not just V_{s30} values, were needed for the parametric study because the process of evaluating soil properties for the analysis of foundation impedance depends on the details of the profile closer to the surface. Moreover, soil shear strength was required for limiting spring capacities, which requires attributes of a specific site to be evaluated in a meaningful way. Calculation of these properties is discussed in Appendix B.

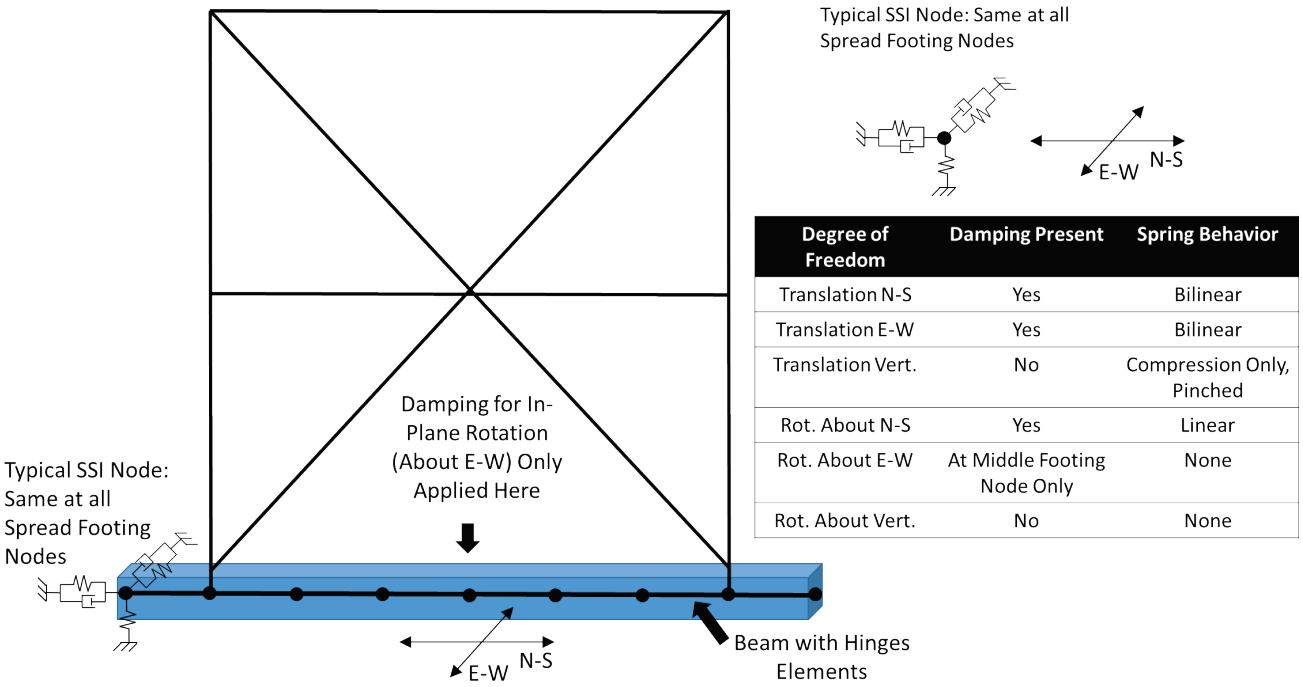

Degree of Freedom	Damping Present	Spring Behavior
Translation N-S	Yes	Bilinear
Translation E-W	Yes	Bilinear
Translation Vert.	No	Compression Only, Pinched
Rot. About N-S	Yes	Linear
Rot. About E-W	At Middle Footing Node Only	None
Rot. About Vert.	No	None

Figure 4-21 Schematic of spread footing and SSI springs and dampers.

The soil was modeled with springs and dampers at each node along the footings of the braced frame and at the single nodes representing the footing-soil interfaces under the gravity frame columns. For the soil supporting the gravity frame columns, which are all on isolated footings, springs and dampers were applied for all degrees of freedom except the rotations about the vertical axes. Values for the sliding resistance, bearing capacity, and stiffness for all gravity frame soil springs are shown Appendix B. There were two gravity-frame footing sizes and gravity-load demands due to the zone designated for equipment, so each archetype had two gravity-frame-footing soil spring and damper properties.

As illustrated in Figure 4-21, soil springs were applied in the three translational directions and the out-of-plane rotation at each footing node in the braced-frame footings. Additionally, there was no in-plane rotational spring applied at each node because resistance to overturning resulted from the springs in the vertical direction. A small in-plane rotational damper was used at the middle of the footing to include a small amount of damping from the soil when the footings rocked. For sliding translations, the soil behavior was modeled as bilinear to simulate the elastic sliding soil deformation and the friction between the soil and footing. In the vertical direction, the soil was assumed to be bilinear in compression, yielding at the soil's bearing capacity. The compressive hysteretic behavior of the vertical springs was pinched to reflect the permanent compression deformation of the soil after

the bearing capacity was reached. As illustrated in Figure 4-21, the vertical spring had zero tension stiffness, which allowed foundation uplift. For all translational springs, after reaching the sliding capacity or bearing capacity, the stiffness was assumed to be 15 percent of the initial stiffness. For the out-of-plane rotation for each strip footing, the soil behavior was assumed to be linear. Soil damping for sliding translations and out-of-plane rotation was included at each node of the braced-frame footings with dampers. Appendix B reports the spring and damper properties for the braced-frame footings for both soil types and for the COM2B-SS1, COM2B-SS2, COM3B-SS1, and COM3B-SS2 archetypes.

4.5 Analysis Methods and Data Analysis

4.5.1 Overview

The following analysis methods were conducted for each archetype configuration:

- free vibration analyses,
- nonlinear static pushover analyses, and
- nonlinear incremental dynamic analyses (IDAs) according to the FEMA P-695 methodology.

4.5.2 Free Vibration Analyses

Free vibration (eigenvalues and eigenvectors) analyses were conducted in OpenSees on the complete models to determine the initial fundamental periods of vibration, T_1, and mode shapes in each orthogonal direction of each archetype model.

4.5.3 Nonlinear Static Pushover Analyses

Pushover analyses were conducted on each archetype model in each orthogonal direction to determine the overall backbone base shear versus roof displacement (or drift) response and extract parameters needed for the FEMA P-695 evaluation procedure. The load distribution for the pushover analyses was consistent with the vertical distribution of base shear per ASCE/SEI 7-10 for each structure and is similar to the first mode distribution of forces. Nonlinear geometric effects were included, and the analyses were run until collapse or convergence failure.

The data obtained from the nonlinear static analyses were the maximum base shear strength (which is used to calculate the overstrength) and the ductility, which is needed in the FEMA P-695 methodology to calculate the spectral shape factor (*SSF*). Figure 4-22, adapted from FEMA P-695, illustrates how

the maximum base shear strength, V_{max}, effective yield displacement, $\Delta_{y,eff}$, the displacement after 20 percent degradation from peak strength, $\Delta_{u,80}$, and the ultimate displacement, $\Delta_{u,max}$, are calculated from the pushover curve resulting from a nonlinear static analysis (the displacements are typically expressed as drift ratios throughout this report). The overstrength factor, Ω, is then V_{max}/V_{design}, where V_{design} is the design base shear for the archetype, and the period-based ductility, μ_T, is $\Delta_{u,80}/\Delta_{y,eff}$.

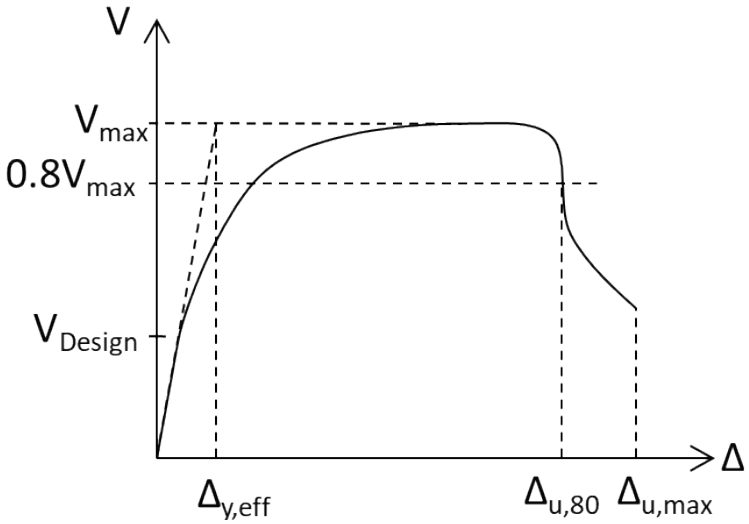

Figure 4-22 Idealized nonlinear static pushover curve and identification of V_{max}, $\Delta_{y,eff}$, $\Delta_{u,80}$, and $\Delta_{u,max}$.

In the nonlinear static analyses of the braced-frame archetypes where brace buckling and brace fracture occurred, which was for all archetypes except those where SSI and foundation flexibility were modeled, convergence failure occurred at brace fracture, and the analyses could not proceed past that point. This is attributed to the large and sudden change in stiffness and strength at brace fracture and the lack of numerical damping in nonlinear static analysis. The analysis results were interrogated at the point of nonconvergence and it was verified, based on the maximum strain range criteria described above, that the tension braces in the direction of loading were indeed fracturing at the point of non-convergence. Since the tension braces resist considerably more than 50 percent of the base shear (often closer to 85 percent), this point of nonconvergence was taken as both $\Delta_{u,80}$ and $\Delta_{u,max}$ (i.e., it was assumed that the lateral strength would degrade more than 20 percent). Notably, nonlinear dynamic analyses were able to converge beyond brace fracture. Also, $\Delta_{u,max}$ is not used in the computation of the collapse probability.

When SSI and foundation flexibility were modeled, the braced frames remained largely elastic and the footings underneath rocked on the

supporting soil below. At large displacements in these models, when P-delta effects exceeded the lateral capacity of the gravity systems, the analyses again failed to converge in static pushover analysis (larger displacements were achieved prior to convergence failure in the dynamic analyses). At this point, it was assumed that the strength degradation exceeded 20 percent, and this point was taken as both $\Delta_{u,80}$ and $\Delta_{u,\max}$.

4.5.4 Incremental Dynamic Analyses and Collapse Evaluation

IDAs were conducted on all archetype models listed in Table 4-1 per the FEMA P-695 procedure using OpenSees as the nonlinear analysis engine. The set of 22 FEMA P-695 far-field, two-component ground motions were used and were scaled to specific intensities (denoted intensity stripes). Figure 4-23 shows the response spectra for the FEMA far-field set normalized to MCE_R spectra at $T = 0.25$ seconds. The normalized record set was scaled at increments of 0.1g, starting at 0.1g, based on the median spectral intensity of the set (S_T) at the ASCE/SEI 7-10 period, $T = C_u T_a$, of the archetype models given in Table 4-2. The variation in period was small, and all periods aligned with the plateau of the median response spectra in Figure 4-23, so differences in ground-motion scaling between archetypes was small.

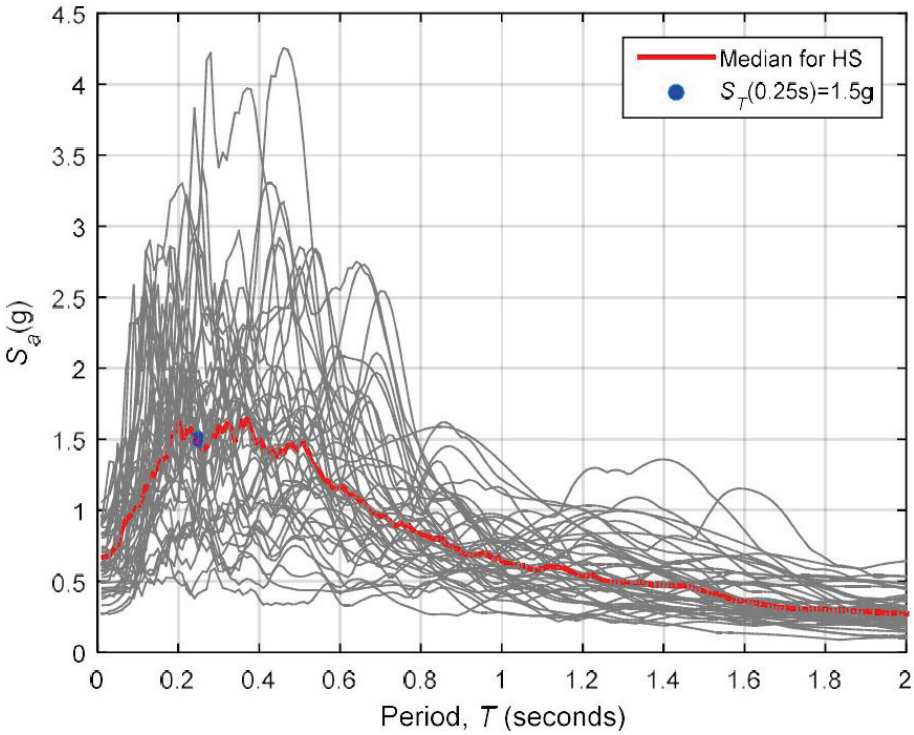

Figure 4-23 FEMA P-695 ground motion set scaled to the MCE_R (SDC D_{max} from FEMA P-695) spectra at $T = 0.25$ seconds.

For each archetype, the analyses were run by applying the two record components simultaneously in the orthogonal directions of the models and then rotating the motions 90 degrees and repeating the analyses. Thus, at each intensity stripe, there were 44 individual nonlinear response history analyses used to compute the collapse statistics and other response quantities.

Previous studies have shown that the median collapse intensity resulting from three-dimensional analyses is on average approximately 20 percent less than the median collapse intensity resulting from two-dimensional analyses (FEMA, 2009b). The application of pairs of ground motion records in three-dimensional analyses introduces a conservative bias as compared to results from two-dimensional analyses. Three-dimensional IDAs were conducted in this study, and to achieve parity with previous two-dimensional analyses, the calculated median collapse intensities were multiplied by a factor of 1.2 per the FEMA P-695 methodology.

In this study, the FEMA P-695 analysis methods were used to calculate the probability of collapse. FEMA P-695 defines the collapse margin ratio, *CMR*, as the ratio of the median 5 percent-damped spectral acceleration of the collapse-level ground motions to the 5 percent-damped spectral acceleration of the MCE_R ground motions at the fundamental period of the seismic-force-resisting system. The adjusted collapse margin ratio, *ACMR*, is obtained by correcting the collapse margin ratio by the *SSF* value defined above.

Figure 4-24 shows resulting IDA curves for the 44 ground motions for the COM2B archetype, where the IDA is plotted as the median spectral acceleration of the ground-motion set at the period of the archetype versus the maximum story drift obtained in the analysis. For most of the archetypes, the maximum story drift occurred on the first floor; however, in some cases, the maximum story drift occurred elsewhere. Collapse was determined to occur when an individual IDA curve for a particular ground motion reached a horizontal plateau (i.e., zero slope in the S_1(g) versus maximum story drift curve) or when convergence failure occurred. All cases of nonconvergence were investigated, and in all cases it was found that sidesway collapse was occurring for the ground motion at that scale factor. Nonsimulated collapse modes were not considered in the post-processing because most of the deterioration mechanisms were included in the numerical models.

Figure 4-24 shows the median drift at incipient collapse. This was calculated by determining the drift at the last converged point for each ground motion and then assuming a lognormal distribution of the drift values. In the data reported in Chapter 5, the drift in each building direction at incipient collapse was computed separately.

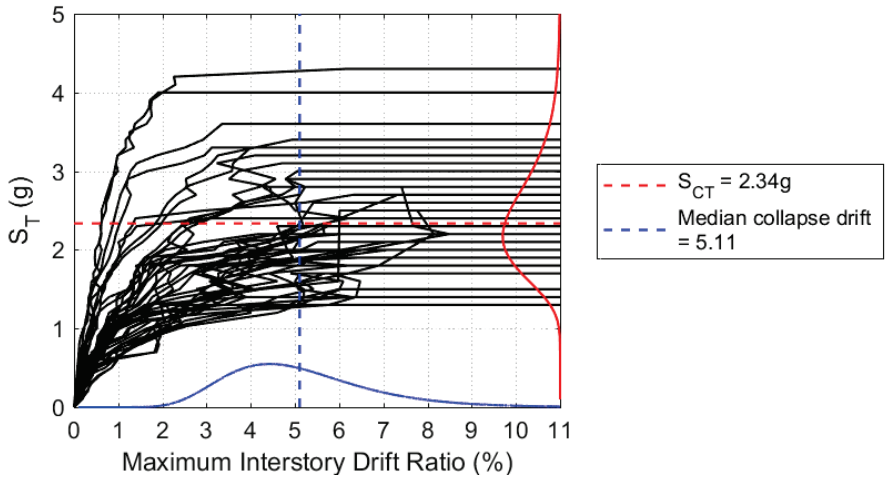

Figure 4-24 IDA results for a notional archetype with median spectral acceleration at collapse at the ASCE/SEI 7-10 period of the structure of 0.25 seconds.

The median collapse spectral acceleration, S_{CT}, was calculated from the IDA data assuming a lognormal distribution. Then, the median spectral acceleration was multiplied by 1.2 to account for the fact that S_{CT} was determined from 3D analysis and by the *SSF* from the FEMA P-695 methodology, which is a function of the archetype period and μ_T. The *SSF* factor is intended to account for the observation that the shape of the response spectra of rare ground motions in California, such as the MCE_R ground motions, is more favorable (i.e., less damageable) to ductile structures, which is not necessarily reflected in the record sets.

Figure 4-25 illustrates the calculation of the collapse rates (collapse fraction) determined from the IDA data for the COM2B archetype and the application of the FEMA P-695 methodology. The collapse fraction is the number of ground motions that caused collapse at a given S_T divided by the number of ground motions used (i.e., 44 here). In Figure 4-25, the x-axis for the collapse fraction data is the median spectral acceleration of the record set at the period of the archetype (S_T) increased by the 3D factor of 1.2. Figure 4-25 also shows the resulting collapse fragility curve (lognormal distribution) for collapse probability versus spectral acceleration. In this case, the median collapse spectral acceleration was multiplied by both the 1.2 3D factor and the *SSF*. Additionally, the dispersion (or lognormal standard deviation), β, has been applied, as discussed below.

In order to consider all sources of uncertainty beyond the record-to-record uncertainty captured in the IDAs, a dispersion factor (standard deviation of the logarithmic values of collapse statistics) $\beta = 0.50$ was used to define all adjusted collapse fragility curves.

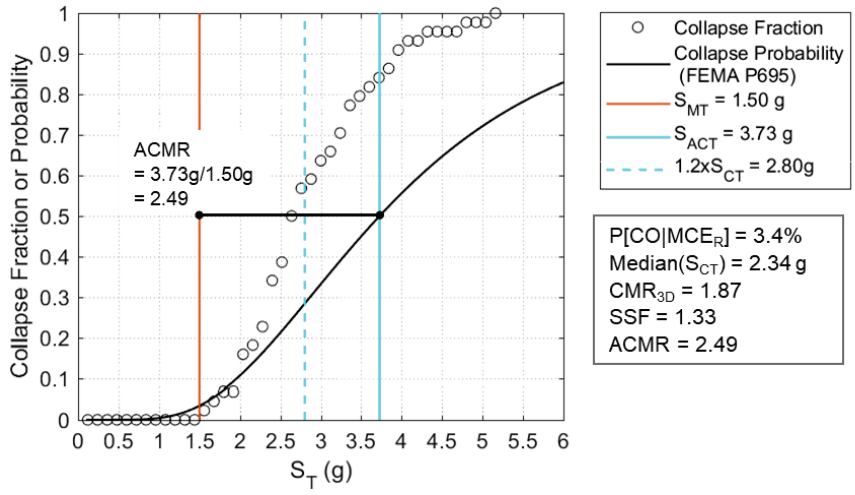

Figure 4-25 Collapse rates and collapse probability for COM2B.

The probability of collapse as a function of ground-motion intensity (at the period, T, of the archetype model) is assumed to be lognormally distributed with an adjusted median, S_{ACT} (i.e., $ACMR \times S_{MT}$), and a lognormal standard deviation, β_{TOT}, that accounts for total collapse uncertainty related to: (1) record-to-record variability; (2) design requirements (for the SFRS of interest); (3) test data (used to establish nonlinear properties); and (4) modeling methods, as described in Section 7.3 of FEMA P-695. Table 7-2a through Table 7-2d of FEMA P-695 specify values of β_{TOT} based on subjective evaluation of the "quality" of the design requirements, test data, and modeling methods, respectively. Reasonably well-defined archetype models have total collapse uncertainty values of β_{TOT} ranging between 0.50 and 0.60. For reference, Section 21.2.1.2 (Method 2) of ASCE/SEI 7-10 specifies a lognormal standard deviation value of 0.6 for development of site-specific probabilistic MCE_R ground motions (i.e., the value used by the USGS to develop the MCE_R ground motion maps of Chapter 22 of ASCE/SEI 7-10). In order to consider all sources of uncertainty beyond the record-to-record uncertainty captured in the IDAs, $\beta = 0.50$ was used to define all adjusted collapse fragility curves.

Using the factored median collapse spectral acceleration and the dispersion, the FEMA P-695 methodology was used to determine the collapse margin ratio (CMR_{3D}) and adjusted collapse margin ratio ($ACMR$), as illustrated in Figure 4-25. The probability of collapse at the MCE_R ground-motion intensity P[C|MCE_R] was determined directly from the collapse fragility curves.

Beyond the FEMA P-695 data, Chapter 5 also reports results from the raw IDA data (i.e., not factored by either the 3D factor or the SSF). These data include the number of instances of collapse at the MCE_R spectral acceleration

for each archetype and the mean peak drift in each building direction for the ground-motion set scaled to one-half of MCE_R and MCE_R.

4.5.5 Peak Response Calculations from IDA Analyses

Response parameters of interest were post-processed and archived at each intensity stripe. Table 4-3 lists the stripe data and corresponding statistics that were calculated from the IDA analyses. For each archetype, an Excel spreadsheet containing these response parameters for each IDA and all intensity stripes was generated and archived (See Appendix C).

Table 4-3 Description of Stripe Statistics Archived for Each Orthogonal Direction (EW and NS) of the Archetype Models

Statistic Type	Response Parameters	Statistical Values
Peak Relative Displacement	Peak Roof Drift Peak Story Drift at Each Story Maximum Peak Story Drift	Median [1] Mean of Survivors [2] Overall Mean [3] Overall Beta [4] Minimum Maximum
Peak Relative Velocity	Peak Relative Velocity at All Levels	
Peak Absolute Acceleration	Peak Absolute Acceleration at All Levels	
Residual Relative Drift	Residual Roof Drift Ratio Residual Story Drift Ratio for Each Story Maximum Residual Story Drift	
Collapse	All Records Collapse Cases	Percentage
	Individual Record Collapse Cases	Peak Roof Displacement at Last Surviving Intensity, Floor Level Initiating Collapse, and Collapse Direction

[1] Median from fitted lognormal distribution based on all 2 × 22 earthquake record sets; for nonsurviving records (i.e., records causing collapse), they are calculated with the last values.

[2] Mean value for surviving earthquake records (i.e., records not causing collapse).

[3] Mean value for all 2 × 22 earthquake record sets; calculated with the last values for nonsurviving records.

[4] The lognormal standard deviation for all 2 × 22 earthquake record sets; calculated with the last values for nonsurviving records.

Chapter 5

Numerical Results of Parametric Studies

5.1 Overview

This chapter presents the results of the parametric studies of short-period steel SCBF archetypes described in the previous chapters. All archetypes were numerically modeled and analyzed using OpenSees and the methods described in Chapter 4.

For each archetype, the results of free vibration analyses, nonlinear static analyses, and IDAs are presented, along with a discussion of key behaviors. Free vibration analysis returns the natural periods and mode shapes, nonlinear static pushover analysis provides estimates of peak strength and ductility, and the IDA results are used to compute collapse probabilities consistent with the FEMA P-695 methodology.

5.2 Baseline Configuration Study

5.2.1 Baseline Archetypes

This section compares the numerical analysis results for the baseline models. These differ in height and seismic design level. COM1B, COM2B, and COM3B (the "high-seismic" baseline archetypes) are one story, two stories and four stories, respectively, and were all designed for MCE_R ground motions with a short-period spectral acceleration of 1.5g. COM4B, COM5B, and COM6B (the "very high-seismic" baseline archetypes) are one story, two stories and four stories, respectively, and were all designed for MCE_R ground motions with a short-period spectral acceleration of 2.25g. All had the same plan, layout of braced frames, and gravity loads per story and at the roof. All were modeled using the methods described in Chapter 4, with the effects of soil-structure interaction and foundation flexibility neglected and thus are representative of buildings with fixed bases.

5.2.2 Numerical Results

The first-mode periods in each building direction are shown in Table 5-1 for all baseline archetypes. All buildings have first-mode periods that are less than 0.5 seconds, indicating that they can be considered short-period

buildings in this study. The mode shapes are consistent with expectations for a regular and reasonably symmetric building.

Results of nonlinear static pushover analyses following the nonlinear static analysis procedure in ASCE/SEI 41-06, *Seismic Rehabilitation of Existing Buildings* (ASCE, 2007), are shown in Figure 5-1. Table 5-1 presents the values of major parameters characterizing the normalized pushover curves in each building direction. In general, results in the North-South (N-S) and East-West (E-W) directions are similar.

Table 5-1 Modal and Pushover Results of Baseline Archetype Models in the N-S and E-W Directions of Response

Archetype ID	North-South Direction				East-West Direction			
	T_1 (sec)	V_{max}/W	$\Delta_{U,80}$ (in/in)	$\Delta_{U,max}$ (in/in)	T_1 (sec)	V_{max}/W	$\Delta_{U,80}$ (in/in)	$\Delta_{U,max}$ (in/in)
Commercial Buildings: High Seismic								
COM1B	0.16	2.00	0.07	0.07	0.17	1.84	0.07	0.07
COM2B	0.27	1.02	0.05	0.05	0.27	0.99	0.05	0.05
COM3B	0.46	0.66	0.01	0.01	0.47	0.66	0.02	0.02
Commercial Buildings: Very High Seismic								
COM4B	0.15	2.43	0.06	0.06	0.16	2.26	0.06	0.06
COM5B	0.25	1.14	0.04	0.04	0.25	1.06	0.04	0.04
COM6B	0.44	0.75	0.03	0.03	0.44	0.73	0.03	0.03

As described in Figure 4-22, V_{max} is the maximum base shear strength developed in each direction of the building, $\Delta_{u,80}$ is the roof drift ratio (roof displacement divided by the building height) at which the lateral resistance drops to 80 percent of the maximum, and $\Delta_{u,max}$ is the maximum roof drift ratio at collapse. As previously noted, the nonlinear static analyses typically failed to converge at tension-brace fracture resulting in the same values for $\Delta_{u,80}$ and $\Delta_{u,max}$. V_{max}/W is the maximum base shear of the pushover curve normalized by building weight (referred to herein as the "normalized pushover strength"), provided in Table 5-1 in the N-S and E-W directions.

Figure 5-1 shows normalized base shear (V/W) plotted versus roof drift for all baseline archetypes. Whereas the very high-seismic archetypes are designed for seismic demands 50 percent greater than those used for the high-seismic archetypes (i.e., 2.25g/1.5g = 1.5), the very high-seismic archetypes are less than 50 percent stronger, in terms of their normalized pushover strengths (V_{max}/W), than the high-seismic archetypes. This is due to the availability of brace sizes that meet the local slenderness requirements for steel SCBFs. For example, the same brace size (HSS 6×6×1/2) is used for

the bottom story of both four-story archetypes, COM3B and COM6B. This brace is the most efficient selection meeting slenderness requirements for a compressive force in the range of 200 kips to 300 kips. The result is lower overstrength factors (Ω) for the archetypes designed for very high-seismic demands, as presented in Table 5-2.

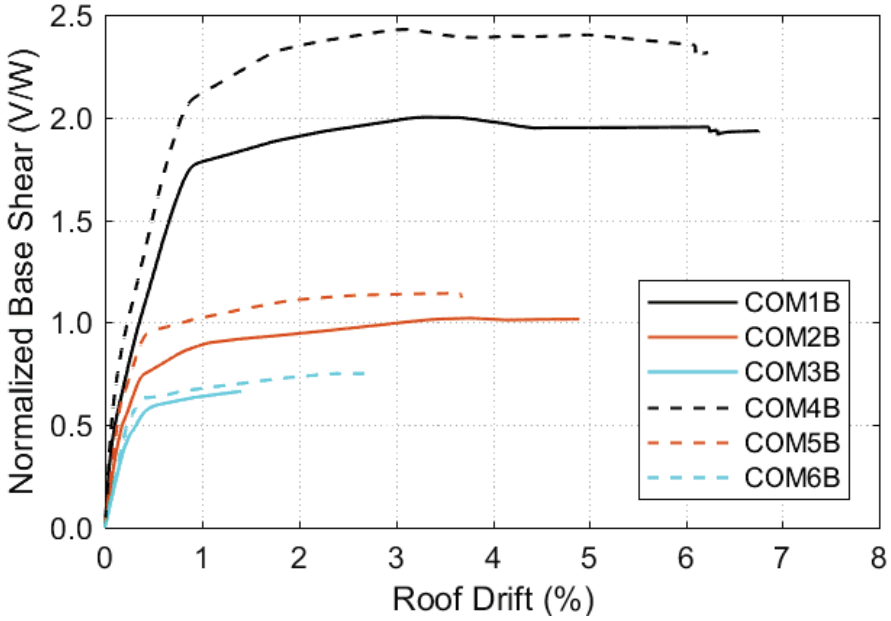

Figure 5-1 Pushover curves for baseline building archetype models with loading in the N-S direction normalized by total building seismic weight and roof height.

Figure 5-2 shows the results of the IDAs for the baseline archetypes. The analyses indicate that the sequence of yielding and failure modes was typically as follows: (1) brace buckling; (2) brace yielding; (3) yielding of the columns at their bases; (4) yielding of shear-plate connections; (5) deterioration in strength of all yielded components; (6) brace fracture; (7) sidesway collapse as the P-delta loads exceed the deteriorated column flexural strength and the deteriorated gravity frame and collector connection strengths. The dots in Figure 5-2 represent the collapse fraction from the IDAs at each increment, or stripe, of the IDA (i.e., the number of collapse occurrences divided by the 44 analyses) versus S_T, the median spectral acceleration of the record set for that stripe multiplied by the 3D analysis factor of 1.2. As shown, the collapse fraction is higher for the taller structures (COM3B and COM6B) at all values of S_T. The collapse fraction is also higher for the very high-seismic archetypes (COM4B, COM5B, and COM6B) relative to the corresponding high-seismic archetypes. Figure 5-2 also shows the smooth collapse fragility curves anchored at a median S_T that is the median from the IDAs, S_{CT}, multiplied by both the 3D analysis factor and the *SSF*, and assuming $\beta = 0.5$.

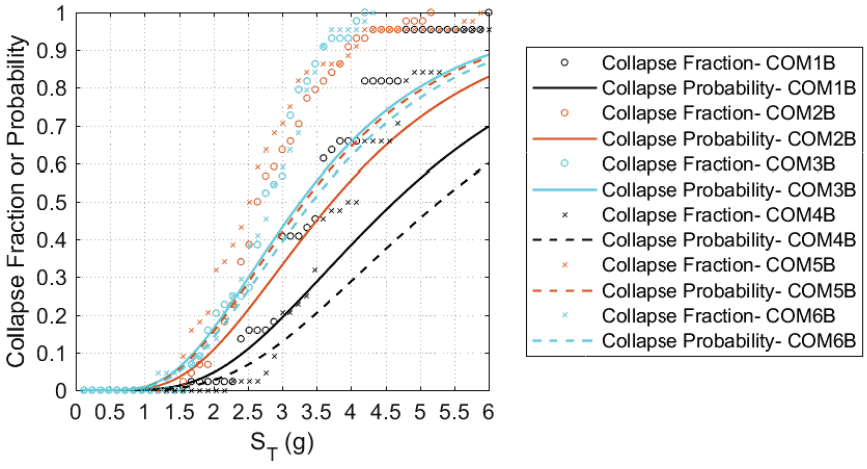

Figure 5-2 Collapse fraction versus S_T (including the 3D analysis factor) from the IDA analyses, and the collapse fragility curves versus S_T (including both the 3D analysis factor and the *SSF*) for the baseline archetypes.

Table 5-2 shows the values of additional parameters calculated with the pushover analyses results per the FEMA P-695 methodology. In this table, the value of $V_{max,av}$ is the average of the values for the two orthogonal directions of the building, Ω is the overstrength factor computed using the minimum lateral strength from the two building directions, and μ_T is the period-based ductility, which is taken as the minimum of the values calculated for the two building directions. Although μ_T and Ω are the minimum values taken from the two orthogonal directions, the values computed for each direction are generally within 10 percent of each other, and the reported values can be considered equivalent to the averages.

Table 5-2 Pushover and Collapse Analysis Results of Baseline Archetype Models

Archetype ID	Pushover Analysis[1]			Collapse Analysis				
	$V_{max,av}/W$	Ω	μ_T	S_{CT}[2] (g)	CMR_{3D}	SSF	ACMR	P[CO|MCE$_R$]
Commercial Buildings: High Seismic								
COM1B	1.92	11	14.04	2.90	2.32	1.33	3.09	1.2%
COM2B	1.01	6.0	10.01	2.34	1.87	1.33	2.49	3.4%
COM3B	0.66	3.9	3.15	2.29	1.83	1.19	2.18	6.0%
Commercial Buildings: Very High Seismic								
COM4B	2.34	9.0	10.67	3.31	1.77	1.33	2.35	4.0%
COM5B	1.10	4.2	6.80	2.13	1.14	1.30	1.48	20%
COM6B	0.74	2.9	5.38	2.27	1.21	1.26	1.53	19%

[1] Pushover analysis results represent the minimum responses in the North-South and East-West directions, but in all cases the minimum values were within 10% of the average of the two directions.

[2] Does not include the 3D analysis factor.

Importantly, the overstrength of the archetypes is large. The overstrength is largest for the shorter buildings but is still close to 4 for the four-story high-seismic archetype, COM3B. For the single-story building, the overstrength is more than 10. Overstrength in braced frames results from: (1) a limited selection of available HSS brace sizes that meet the requirements for seismic compactness in ANSI/AISC 341; (2) selection of brace sizes based on the compressive resistance of braces (where the design story shear is assumed to be equally distributed between the tension and compression braces, but the compressive capacity governs member design), and the difference between tensile and compressive brace strengths, especially for slender braces, which are used to resist smaller loads; and (3) the contribution of the gravity frames and moment-frame action within the braced frames, which is neglected in typical design.

Table 5-2 shows the collapse margin ratio (CMR_{3D}) computed as the ratio of the S_{CT} factored by the 1.2 3D analysis factor (i.e., $1.2S_{CT}$) to the MCE_R spectral acceleration used for design (1.5g for the high-seismic archetypes and 2.25g for the very high-seismic archetypes). The table also shows the *SSF* computed per FEMA P-695 and the adjusted collapse margin ratio (*ACMR*) taken as the $SSF \times CMR_{3D}$. Finally, Table 5-2 shows the probability of collapse for each of the baseline archetypes at the MCE_R spectral acceleration computed using smooth fragility curves in Figure 5-2. As shown, the probability of collapse at the MCE_R ground motion is lower for the one-story and two-story archetypes than it is for the four-story archetypes. Additionally, the collapse probabilities are larger for the archetypes designed for the very high-seismic demand than for the archetypes designed for the high-seismic demand. This is due to: (1) the archetypes designed for the very high-seismic demand having lower overstrength, as discussed above; and (2) the collapse mechanisms being lateral sway after brace fracture for both frames, which depends primarily on the gravity systems and the beams and columns of the braced frames, all of which are similar for both high-seismic and very high-seismic designs. Given these factors, and the fact that the MCE_R spectral acceleration is 50 percent larger for the very high-seismic archetypes, it is reasonable that the very high-seismic archetypes have larger probabilities of collapse at MCE_R.

Table 5-3 shows the median roof and first-story drifts at incipient collapse and the lognormal standard deviations (β) for the baseline models. As expected, first floor drifts at incipient collapse are larger than roof drifts, indicating first-story collapse mechanisms. The ratio of first-story drift to roof drift is largest for the four-story archetypes, indicating more severe first-story collapse mechanisms for those archetypes. Also, the first-story drifts at incipient collapse for COM3B and COM6B are similar, as are their normalized pushover strengths from Table 5-2 ($V_{max,av}/W$), yet the MCE_R spectral acceleration for COM6B is 50 percent larger. Thus, it is clear why the collapse probability is larger for COM6B.

Table 5-3 Median and Lognormal Standard Deviation (β) Values of Peak Drift Ratio and Response Spectral Acceleration at Incipient Collapse of Baseline Archetype Models

Archetype ID	Peak Drift Ratio at Incipient Collapse				Response Spectral Acceleration at Incipient Collapse S_T (g)	
	Roof		First Story			
	Median	β	Median	β	Median	β
Commercial Buildings: High Seismic						
COM1B	0.030	0.68	0.030	0.68	2.90	0.27
COM2B	0.033	0.34	0.051	0.32	2.34	0.27
COM3B	0.032	0.29	0.065	0.47	2.29	0.25
Commercial Buildings: Very High Seismic						
COM4B	0.058	0.85	0.058	0.85	3.31	0.24
COM5B	0.021	0.37	0.035	0.39	2.13	0.35
COM6B	0.034	0.43	0.075	0.49	2.27	0.29

Table 5-4 shows mean peak first-story drift ratios in each building direction at intensities of 0.5 × MCE_R and MCE_R. These values are from the raw data (i.e., prior to application of the 1.2 3D factor and the *SSF*). As shown, the mean peak first-story drift ratios are reasonably small at 0.5 × MCE_R. However, high collapse rates and large mean peak first-story drifts are observed for the archetypes designed for the very high-seismic demand due to the reasons noted above. For the high-seismic archetypes, the mean peak first-story drifts are generally less than 3 percent at MCE_R.

Table 5-4 Collapse Rates and Mean Peak First-Story Drift Ratios of Baseline Archetype Models in N-S and E-W Directions of Survivors at 50 Percent-of-MCE_R and at MCE_R Ground-Motion Intensities

Archetype ID	Collapse Rate at MCE_R (out of 44)		Mean Peak First-Story Drift Ratio of Survivors (%)			
			0.5 × MCE_R		MCE_R	
	0.5 × MCE_R	MCE_R	North-South Direction	East-West Direction	North-South Direction	East-West Direction
Commercial Buildings: High Seismic						
COM1B	0	0	0.39	0.27	0.99	0.85
COM2B	0	0	0.49	0.50	1.76	1.85
COM3B	0	0	0.35	0.33	1.63	1.23
Commercial Buildings: Very High Seismic						
COM4B	0	1	0.45	0.34	1.62	1.17
COM5B	0	17	0.74	0.82	1.57	1.58
COM6B	0	11	1.34	1.27	3.69	3.99

5.2.3 *Summary of Results*

Figure 5-3 shows the collapse probability at the MCE_R spectral intensity, $P[C|MCE_R]$, versus the normalized pushover strength, $V_{max,av}/W$, which is a proxy for overstrength. As shown, the collapse probability decreases with increasing normalized pushover strength. Increasing building height was correlated with decreasing overstrength, and the collapse probability is also observed to decrease with decreasing building height. This trend is affirmed in Figure 5-4, which shows $P[C|MCE_R]$ versus building period, where the collapse probability decreases with decreasing building period (or increases with increasing building period). The figures also show that the collapse probabilities for the very high-seismic archetypes are larger than those for the high-seismic archetypes.

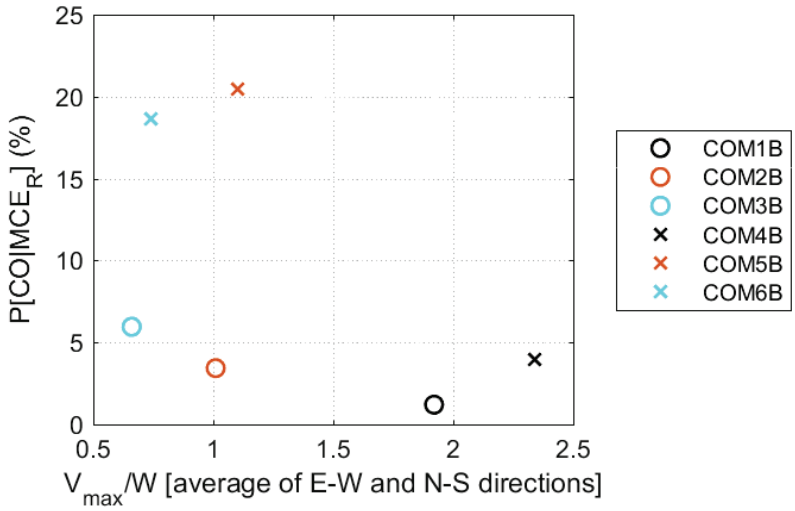

Figure 5-3 MCE_R collapse probability versus $V_{max,av}/W$ for the baseline steel SCBF building archetype models.

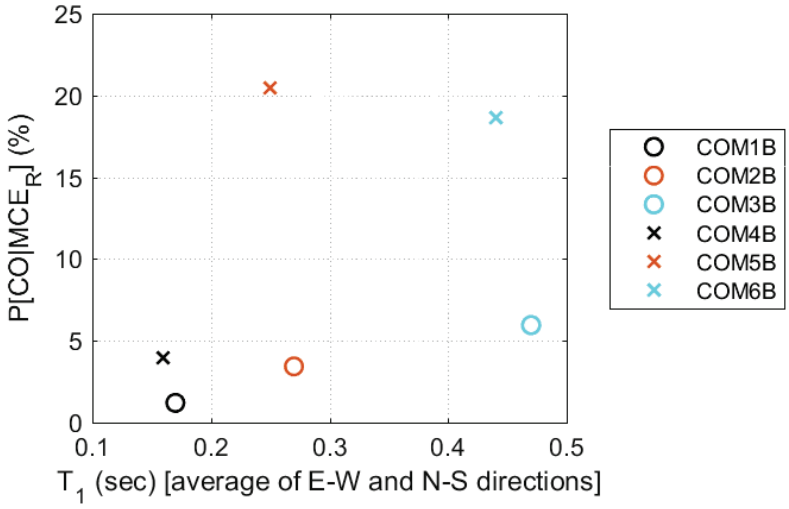

Figure 5-4 MCE_R collapse probability versus fundamental period (T_1) for the baseline steel SCBF building archetype models.

5.3 Brace Configuration Parametric Study

5.3.1 Brace Configuration Archetypes

This section compares the analysis results for archetypes with super-X and chevron (or inverted-V) braced-frame configurations. The performance of the baseline COM2B and COM3B archetypes having super-X configurations are compared to COM2B-BC and COM3B-BC archetypes with chevron configurations.

5.3.2 Numerical Results

The first-mode periods in both building directions are shown in Table 5-5 and demonstrate that the elastic behaviors of the baseline (super-X) and chevron archetypes are similar. Figure 5-5 compares the nonlinear static pushover analysis results in the N-S directions for the baseline and chevron-configured SCBF archetypes. As shown, the chevron configurations have slightly larger lateral strengths and reduced displacement capacities at brace fracture. The larger strength can be attributed to: (1) shorter brace lengths due to the deep beams required to resist the unbalanced load as required by ANSI/AISC 341; and (2) increased resistance from moment-frame action within the braced frames due to the presence of gusset-plate connections at all levels except the roof and deeper-beam sections. The reduced maximum interstory drift at brace fracture is also attributed to the reduced brace length (the maximum strain range at brace fracture decreases with decreasing brace global slenderness) and a more severe concentration of story drift at the first story.

This latter point is illustrated in Figure 5-6, which shows the displaced shapes at peak interstory drifts from a single dynamic analysis, scaled to MCE_R ground-motion intensity, for COM2B and COM2B-BC. The figure shows there is a concentration of drift in the first story in both cases, as is typical of braced frames, but it is somewhat more severe in COM2B-BC. The gusset plates at the beam-to-column connections at the first level in COM2B-BC cause plastic hinges to form in the columns at the top of the first story, which ultimately results in larger first-story drifts. Figure 5-6 also shows that the beam in the chevron configuration deflects slightly down due to the unbalanced forces in the tension and compression braces. It was found that the beams remained essentially elastic, and the vertical displacements were small.

Table 5-5 **Modal and Pushover Results of Brace Configuration Parametric Study Archetype Models in the N-S and E-W Directions of Response**

Archetype ID	North-South Direction				East-West Direction			
	T_1 (sec)	V_{max}/W	$\Delta_{U,80}$ (in/in)	$\Delta_{U,max}$ (in/in)	T_1 (sec)	V_{max}/W	$\Delta_{U,80}$ (in/in)	$\Delta_{U,max}$ (in/in)
Commercial Buildings: High Seismic								
COM2B	0.27	1.02	0.05	0.05	0.27	0.99	0.05	0.05
COM2B-BC	0.27	0.98	0.03	0.03	0.28	0.88	0.03	0.03
COM3B	0.46	0.66	0.01	0.01	0.47	0.66	0.02	0.02
COM3B-BC	0.43	0.82	0.02	0.02	0.44	0.77	0.02	0.02

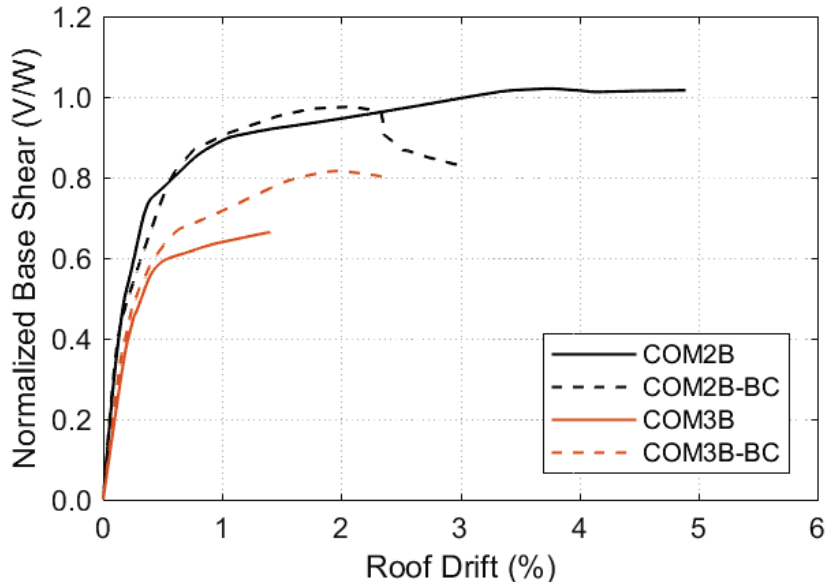

Figure 5-5 N-S direction pushover curves for baseline (super-X) archetypes (COM2B and COM3B) and chevron archetypes (COM2B-BC and COM3B-BC) normalized by total building seismic weight and roof height.

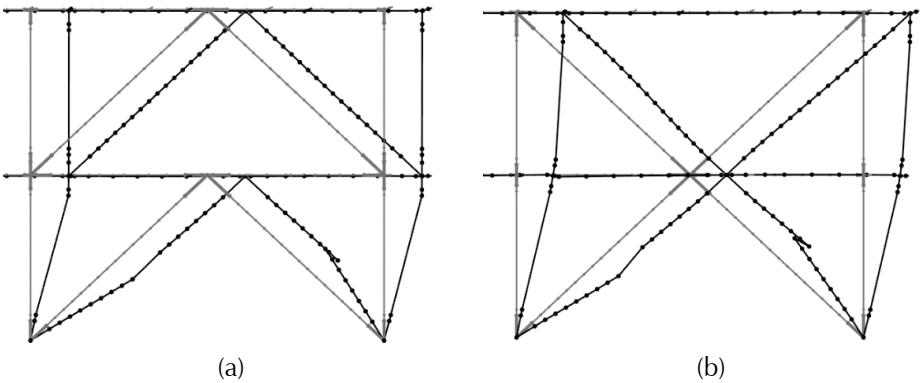

(a) (b)

Figure 5-6 Comparison of displaced shapes at peak interstory drift from a single MCE_R ground motion for (a) COM2B-BC and (b) COM2B.

Table 5-6 reports the overstrength and period-based ductility for the archetypes as determined from the nonlinear static pushover analyses. As shown, the results are similar for both the baseline (super-X) and chevron systems, and in both cases the overstrength and ductility decrease with building height.

Table 5-6 Pushover and Collapse Analysis Results of Brace Configuration Parametric Study Archetype Models

Archetype ID	Pushover Analysis			Collapse Analysis				
	$V_{max,av}/W$	Ω	μ_T	S_{CT}* (g)	CMR_{3D}	SSF	ACMR	$P[CO\|MCE_R]$
Commercial Buildings: High Seismic								
COM2B	1.01	6.0	10.01	2.34	1.87	1.33	2.49	3.4%
COM2B-BC	0.93	5.3	6.41	1.94	1.55	1.29	2.00	8.3%
COM3B	0.66	3.9	3.15	2.29	1.83	1.19	2.18	6.0%
COM3B-BC	0.79	4.6	3.52	1.56	1.25	1.20	1.50	21%

* Does not include the 3D analysis factor.

Figure 5-7 compares the collapse fraction and resulting collapse fragility curves for the baseline (super-X) and chevron systems consistent with the previous figure for the baseline archetypes. As shown, the chevron configurations (COM2B-BC and COM3B-BC) have reduced collapse capacities (increased probability of collapse at a given spectral acceleration). The four-story chevron braced-frame archetype (COM3B-BC) has a probability of collapse that exceeds 10 percent for the MCE_R spectral acceleration of 1.5g. It is the only instance of the collapse probability exceeding 10 percent for the MCE_R ground motion. In general, the behavior of the chevron frames was similar to that described for the baseline configuration with the exception of the formation of plastic hinges and subsequent deterioration at the tops of the first-story columns. It is this concentrated damage at the top of the first-story columns that decreases the collapse capacity of the chevron braced frames. Notably, recent research, such as Roeder et al. (2019) and Roeder et al. (in press), have demonstrated that improved seismic performance of chevron braced frames can be obtained if the chevron beams are designed to be smaller than currently required by ANSI/AISC 341. Doing this has benefits in increasing the drift at which brace fracture occurs and reducing the demands on the braced-frame columns. The current research demonstrates that such designs have improved collapse probability and reduced concentration of drift demand and damage on the first stories.

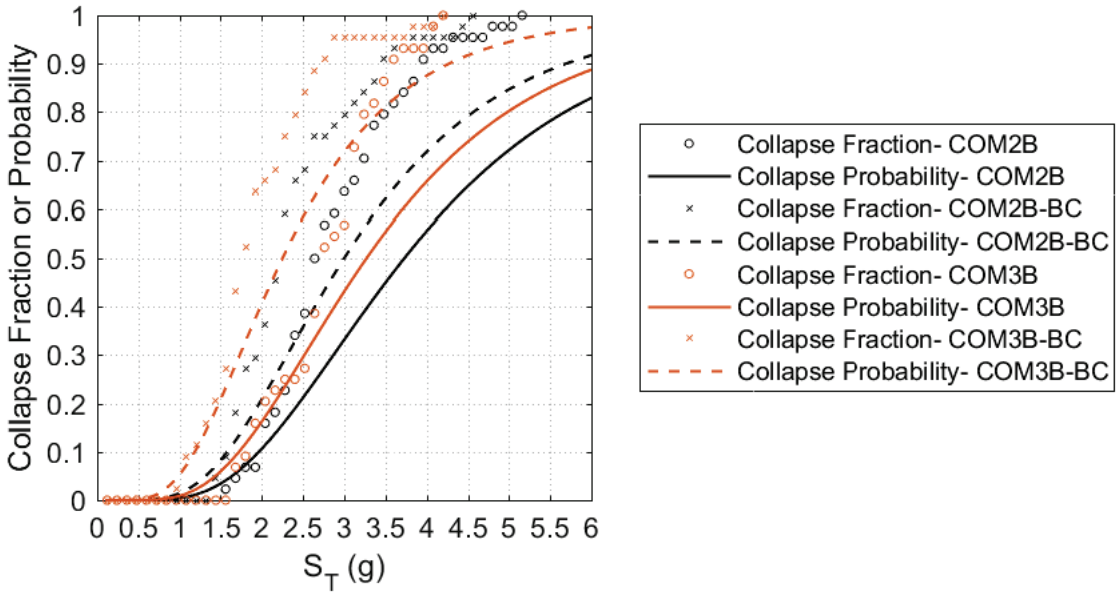

Figure 5-7 Collapse fraction versus S_T (including the 3D analysis factor) from the IDA analyses and the collapse fragility curves versus S_T (including both the 3D analysis factor and the *SSF*) for baseline (super-X) and chevron steel SCBF archetype models.

Table 5-6 shows the CMR_{3D} and collapse probability at the MCE_R ground-motion intensity for the baseline (super-X) and chevron configuration archetypes, computed as described above. As shown, the chevron configuration has a somewhat increased probability of collapse at the MCE_R ground-motion intensity, which is due to the development of more severe rotation demands at the plastic hinges forming at the top of the first-floor columns in the chevron braced frames because of the large beams. Again, in both the baseline (super-X) and chevron configurations, the collapse probability is found to decrease with building height. In all cases except the four-story chevron archetype, COM3B-BC, the collapse probability of the archetypes at the MCE_R ground motion intensity is less than 10 percent.

Table 5-7 shows the median and β values for peak roof and first-story drift for the brace configuration parametric study models. As shown, the roof drift at collapse is smallest for COM3B-BC, and that model also has the largest ratio of first-story drift at incipient collapse to roof drift at incipient collapse, indicating that the drift in that archetype is concentrated more in the first floor than it is in other archetypes. These factors combine with the somewhat reduced overstrength for COM3B-BC to result in the larger collapse probability at MCE_R (Table 5-8).

Table 5-8 shows mean peak first-story drift ratios in each building direction at intensities of $0.5 \times MCE_R$ and MCE_R. These values are from the raw data (i.e., prior to application of the 1.2 3D factor and the *SSF*). As shown, the

mean peak first-story drift ratios are reasonably small at 0.5 × MCE_R, are generally less than 3 percent at MCE_R, and are similar for the baseline (super-X) and chevron configurations.

Table 5-7 Median and Lognormal Standard Deviation (β) Values of Peak Drift Ratio and Response Spectral Acceleration at Incipient Collapse of Brace Configuration Parametric Study Archetype Models

Archetype ID	Peak Drift Ratio at Incipient Collapse				Response Spectral Acceleration at Incipient Collapse S_T (g)	
	Roof		First Story			
	Median	β	Median	β	Median	β
Commercial Buildings: High Seismic						
COM2B	0.033	0.34	0.051	0.32	2.34	0.27
COM2B-BC	0.022	0.28	0.042	0.30	1.94	0.29
COM3B	0.032	0.29	0.065	0.47	2.29	0.25
COM3B-BC	0.013	0.18	0.037	0.28	1.56	0.32

Table 5-8 Collapse Rates and Mean Peak First-Story Drift Ratios of Brace Configuration Parametric Study Archetype Models in the N-S and E-W Directions of Survivors at 50 Percent-of-MCE_R and at MCE_R Ground-Motion Intensities

Archetype ID	Collapse Rate at MCE_R (out of 44)		Mean Peak First-Story Drift Ratio of Survivors (%)			
			0.5 × MCE_R		MCE_R	
	0.5 × MCE_R	MCE_R	North-South Direction	East-West Direction	North-South Direction	East-West Direction
Commercial Buildings: High Seismic						
COM2B	0	0	0.49	0.50	1.76	1.85
COM2B-BC	0	2	0.54	0.59	1.67	1.55
COM3B	0	0	0.35	0.33	1.63	1.23
COM3B-BC	0	9	0.84	0.57	1.62	2.07

5.3.3 Summary of Results

Figure 5-8 shows the collapse probability at the MCE_R spectral intensity, P[C|MCE_R], versus the normalized pushover strength, $V_{max,av}/W$, which is a proxy for overstrength. Again, the collapse probability decreases with increasing lateral strength for both configurations. Figure 5-9 shows P[C|MCE_R] versus building period for the baseline (super-X) and chevron configuration archetypes, demonstrating that in both cases the collapse probability decreases with decreasing building period (or increases with increasing building period).

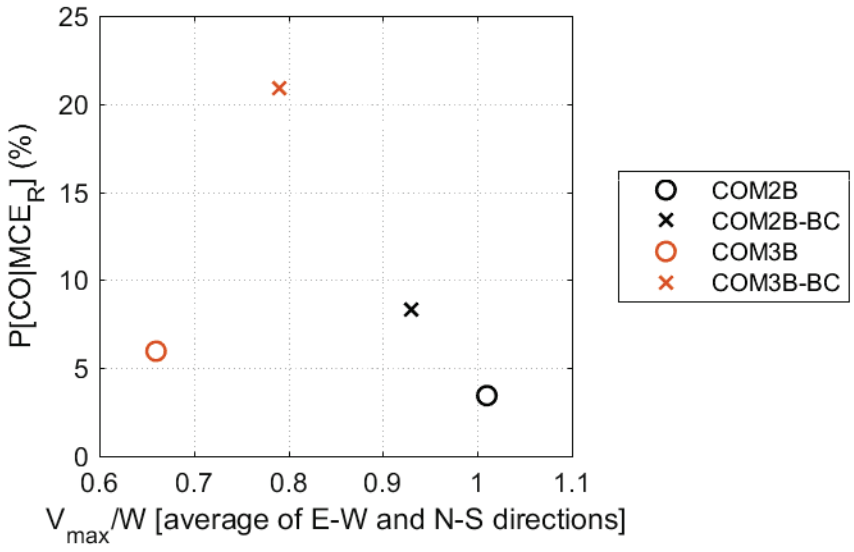

Figure 5-8 MCE_R collapse probability versus $V_{max,av}/W$ for the baseline (super-X) and chevron steel SCBF archetype models.

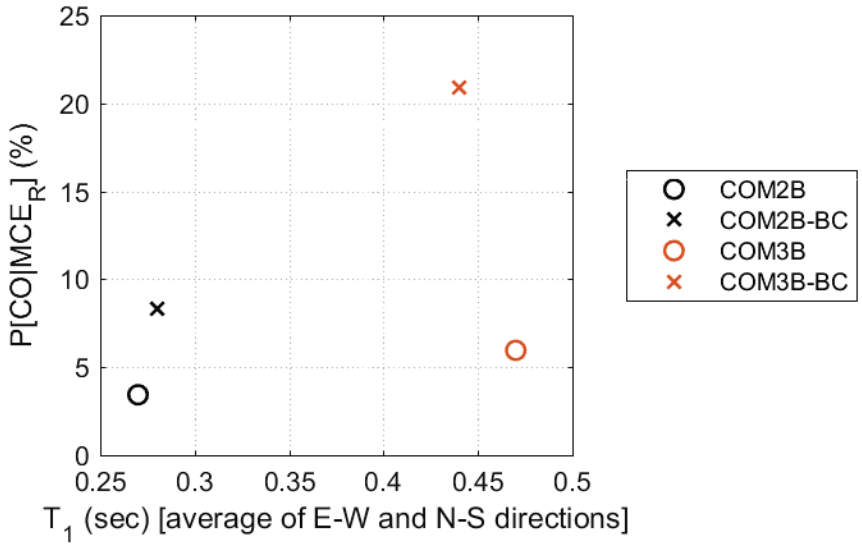

Figure 5-9 MCE_R collapse probability versus fundamental period (T_1) for the baseline (super-X) and chevron steel SCBF archetype models.

5.4 No Redundancy Parametric Study

5.4.1 No Redundancy Archetypes

This section compares the analysis results for archetypes that satisfy and do not satisfy the redundancy requirements in ASCE/SEI 7-10. The performance of the baseline COM2B archetype, which satisfies the redundancy requirements, is compared with an archetype, COM2B-NR, that has only two braced frames in each building direction, requiring the use of the redundancy factor (ρ) equal to 1.3, resulting in 30 percent larger design brace forces from earthquake loads.

5.4.2 Numerical Results

The first-mode periods in both building directions are shown in Table 5-9. As indicated, the first-mode period for COM2B-NR is nearly 20 percent longer than that for COM2B, indicating a difference in elastic response. Figure 5-10 compares the nonlinear static pushover analysis results in the N-S directions for COM2B and COM2B-NR, Table 5-9 shows the resulting peak lateral force and displacements, and Table 5-10 shows the resulting overstrength and period-based ductility. The system designed with redundancy (COM2B) has larger overstrength and stiffness than the system designed with less redundancy (COM2B-NR). The overstrength factor in Table 5-10 is computed using the same design base shear for both structures because the MCE_R demand for the two archetypes is the same. The decrease in both overstrength and stiffness of COM2B-NR is due to the realities of design. Because the brace forces are a bit larger, there are more HSS shapes available, and the capacity of the braces is closer to the brace demand (i.e., the design is more efficient in terms of brace size). Also, increased brace design forces requires the use of HSS shapes with larger cross sections and smaller global slenderness, resulting in braces that have compression capacities that are closer to their tension capacities, which reduces the overstrength. Further, the use of only two braced frames in each direction decreases the contribution of moment-frame action within the braced frames due to the gusset-plate connections and column-base fixity. Aside from the difference in stiffness and overstrength, the behavior of the two archetypes is similar in terms of yield progression and failure modes.

Notably, the difference in the ratio of V_{max}/W for COM2B and COMB2B-NR is explained almost entirely by the difference in the number of braced brays and the selected braces. Considering only the contribution of the braces to the lateral strength of a single braced frame for COM2B and assuming that the tension brace is at its expected yield capacity and that the compression brace has degraded to 0.5 of its expected compression strength, the lateral strength would be computed to be 218 kips. Similarly, the lateral strength of one braced frame from COM2B-NR would be 296 kips. Because there are four braced frames in each direction in COM2B and two in COM2B-NR, their ratio of expected strengths (COM2B over COM2B-NR) would be 1.47, which is nearly identical to the ratio of V_{max}/W for COM2B over V_{max}/W for COM2B-NR, which is 1.46.

Table 5-9 **Modal and Pushover Results of No Redundancy Parametric Study Archetype Models in the N-S and E-W Directions of Response**

Archetype ID	North-South Direction				East-West Direction			
	T_1 (sec)	V_{max}/W	$\Delta_{U,80}$ (in/in)	$\Delta_{U,max}$ (in/in)	T_1 (sec)	V_{max}/W	$\Delta_{U,80}$ (in/in)	$\Delta_{U,max}$ (in/in)
Commercial Buildings: High Seismic								
COM2B	0.27	1.02	0.05	0.05	0.27	0.99	0.05	0.05
COM2B-NR	0.32	0.74	0.05	0.05	0.34	0.63	0.03	0.03

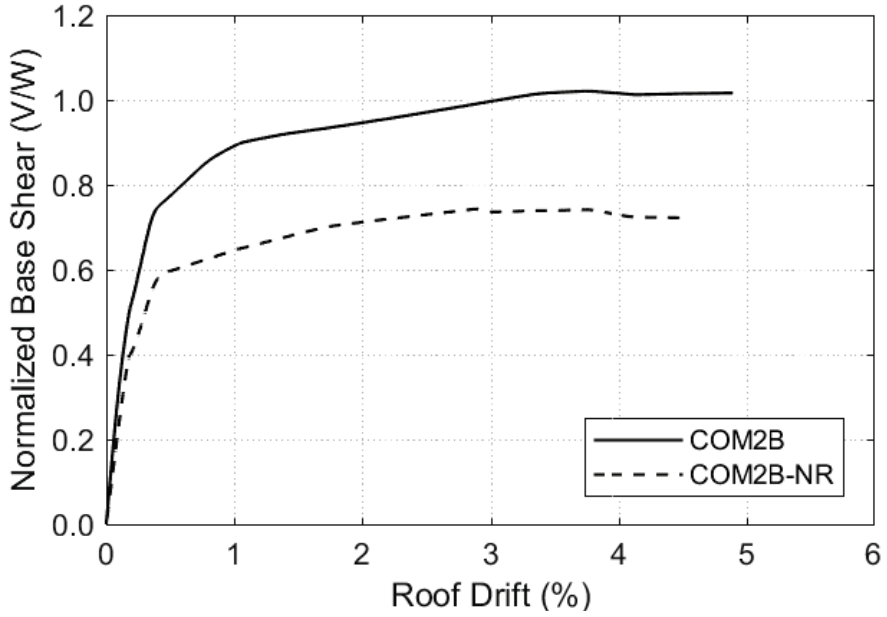

Figure 5-10 N-S direction pushover curves for steel SCBF models with (COM2B) and without (COM2B-NR) lateral system redundancy normalized by total building seismic weight and roof height.

Table 5-10 **Pushover and Collapse Analysis Results of No Redundancy Parametric Study Archetype Models**

Archetype ID	Pushover Analysis			Collapse Analysis				
	$V_{max,av}/W$	Ω	μ_T	S_{CT}* (g)	CMR_{3D}	SSF	ACMR	$P[CO \mid MCE_R]$
Commercial Buildings: High Seismic								
COM2B	1.01	6.0	10.01	2.34	1.87	1.33	2.49	3.4%
COM2B-NR	0.69	3.8	10.79	1.73	1.39	1.33	1.84	11%

* Does not include the 3D analysis factor.

Figure 5-11 compares the collapse fraction and resulting collapse fragility curves for COM2B and COM2B-NR in a manner consistent with the similar previous figures. As shown, COM2B-NR has a reduced collapse capacity, which is expected given its lower overstrength and similar ductility relative to COM2B. The results indicate that the collapse probability in the MCE_R

ground motion is larger than 10 percent for COM2B-NR. The analyses indicated that the yielding and failure sequence leading to collapse is the same for the two frames and that ultimately a sidesway collapse mode of the first story occurs when the gravity frame and braced frames without braces are no longer able to support the P-delta loads.

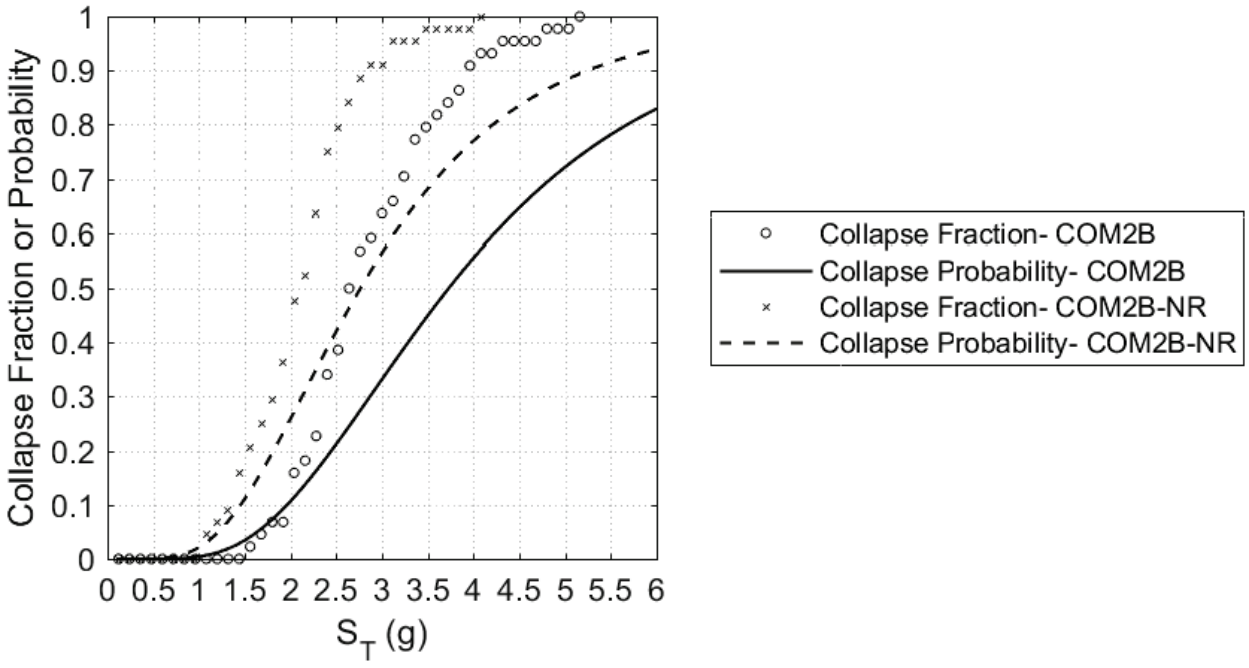

Figure 5-11 Collapse fraction versus S_T (including the 3D analysis factor) from the IDA analyses and the collapse fragility curves versus S_T (including both the 3D analysis factor and the *SSF*) for systems with (COM2B) and without (COM2B-NR) lateral system redundancy.

Table 5-10 shows the collapse margin ratios and collapse probabilities at the MCE_R ground-motion intensity for the COM2B and COM2B-NR archetypes, computed as described above. As shown, COM2B-NR has a larger probability of collapse at the MCE_R ground-motion intensity (~11 percent) versus less than 4 percent for COM2B. Again, this result is largely due to the decrease in brace ductility when the brace global slenderness decreases and to the lower overstrength of the non-redundant system. The difference in collapse probabilities is large enough to indicate that seismic-force-resisting system redundancy plays a role in the seismic behavior and impacted the collapse probability of the two-story steel braced-frame archetype.

Table 5-11 shows the median and β values for peak roof and first-story drift for the redundancy parametric study models. As shown, the roof drift and first-story drifts at collapse are similar for the two archetypes, with the values being somewhat smaller for the design without redundancy (COM2B-NR).

Table 5-12 shows mean peak first-story drift ratios in each building direction at intensities of 0.5 × MCE_R and MCE_R. These values are from the raw data (i.e., prior to application of the 1.2 3D factor and the *SSF*). As shown, the mean peak first-story drift ratios are reasonably small at 0.5 × MCE_R, are generally less than 3 percent at MCE_R, and are similar for COM2B and COM2B-NR.

Table 5-11 Median and Lognormal Standard Deviation (β) Values of Peak Drift Ratio and Response Spectral Acceleration at Incipient Collapse of the No Redundancy Parametric Study Archetype Models

Archetype ID	Peak Drift Ratio at Incipient Collapse				Response Spectral Acceleration at Incipient Collapse S_T (g)	
	Roof		First Story			
	Median	β	Median	β	Median	β
Commercial Buildings: High Seismic						
COM2B	0.033	0.34	0.051	0.32	2.34	0.27
COM2B-NR	0.027	0.46	0.045	0.34	1.73	0.29

Table 5-12 Collapse Rates and Mean Peak First-Story Drift Ratios of No Redundancy Parametric Study Archetype Models in the N-S and E-W Directions of Survivors at 50 Percent-of-MCE_R and at MCE_R Ground-Motion Intensities

Archetype ID	Collapse Rate at MCE_R (out of 44)		Mean Peak First-Story Drift Ratio of Survivors (%)			
			0.5 × MCE_R		MCE_R	
	0.5 × MCE_R	MCE_R	North-South Direction	East-West Direction	North-South Direction	East-West Direction
Commercial Buildings: High Seismic						
COM2B	0	0	0.49	0.50	1.76	1.85
COM2B-NR	0	7	0.68	0.84	2.44	2.53

5.4.3 Summary of Results

Figure 5-12 shows the collapse probability at the MCE_R spectral intensity, P[C|MCE_R], versus the normalized pushover strength, $V_{max,av}/W$, which is a proxy for overstrength. Again, the collapse probability decreases with increasing lateral strength (i.e., COM2B has a smaller collapse probability than COM2B-NR). Figure 5-13 shows P[C|MCE_R] versus building period for COM2B and COM2B-NR, and again it is clear that the collapse probability decreases with decreasing building period, although in this case the difference in collapse capacity is largely attributable to the larger overstrength of COM2B.

Only a single archetype was studied, which makes arriving at conclusions difficult. However, this one study provides an example of a less redundant system, designed for 30 percent larger brace forces from earthquake loads, having a significantly larger collapse risk than the redundant baseline system.

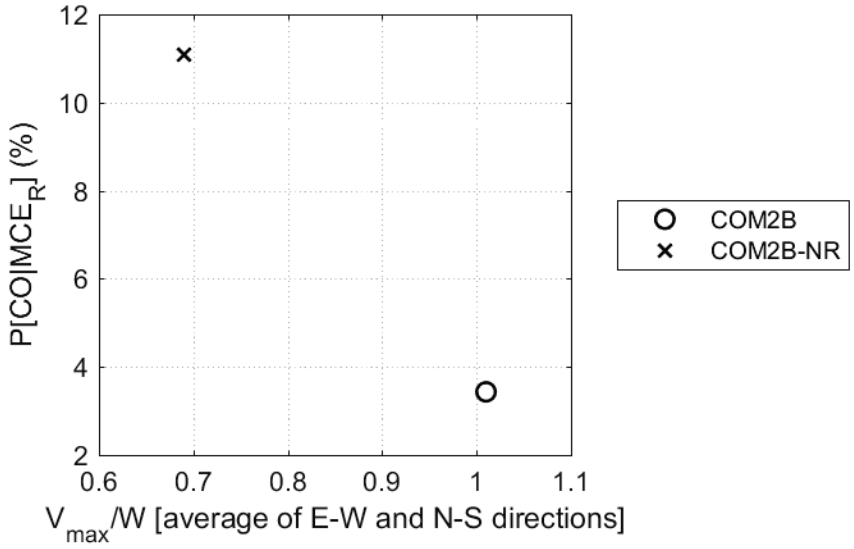

Figure 5-12 MCE_R collapse probability versus $V_{max,av}/W$ for redundant and non-redundant steel SCBF archetype models.

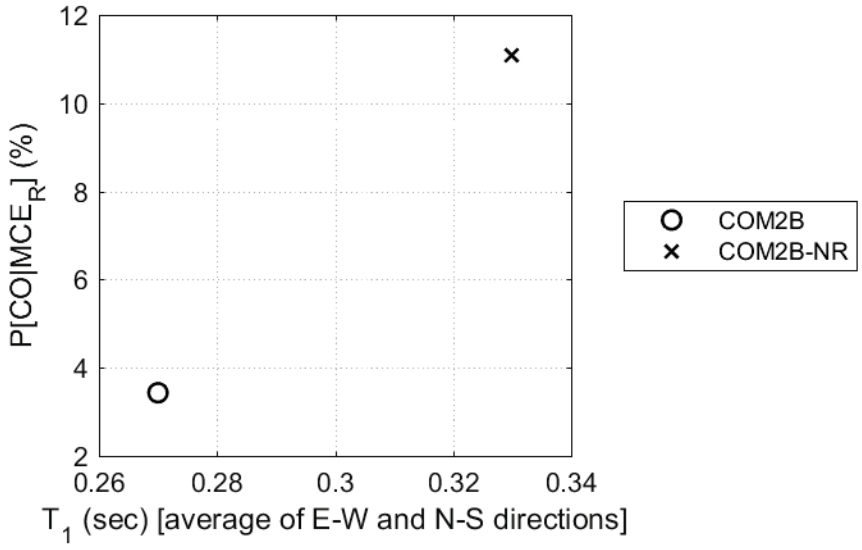

Figure 5-13 MCE_R collapse probability versus fundamental period (T_1) for redundant and non-redundant steel SCBF archetype models.

5.5 Soil-Structure Interaction and Foundation Flexibility Parametric Study

5.5.1 Soil-Structure Interaction and Foundation Flexibility Archetypes

This section compares the analysis results for archetypes with no ground-motion reduction and fixed bases to archetypes that incorporate soil-structure interaction (SSI) and foundation flexibility. COM2B and COM3B were modeled with SSI and foundation flexibility to simulate foundation sliding, foundation uplift, and the impact of kinematic interaction in ground-motion

input. This was done for two different soil profiles: a stiff soil near the site class C/D boundary, resulting in archetype models COM2B-SS1 and COM3B-SS1, and a soft soil near the site class D/E boundary, resulting in archetype models COM2B-SS2 and COM3B-SS2. This section compares the analysis results for baseline and SSI and foundation flexibility models to investigate the impact of SSI and foundation flexibility on collapse capacity. Additionally, to investigate the impacts of kinematic interaction, the two-story models for both the stiffer and softer soils were run with the unfiltered ground motions (i.e., without kinematic interaction). These analyses are denoted COM2B-SS1-Unfiltered and COMB2B-SS2-Unfiltered for the stiff and soft soil models, respectively.

5.5.2 Numerical Results

The first-mode periods in both building directions are shown in Table 5-10. As indicated, the first-mode periods when SSI and foundation flexibility is included in the numerical models are much longer than for the baseline models, especially for the models using the softer soil SSI parameters (COM2B-SS2 and COM3B-SS2). This is due to soil flexibility for foundation sliding and overturning.

Table 5-13 Modal and Pushover Results of SSI and Foundation Flexibility Parametric Study Archetype Models in the N-S and E-W Directions of Response

Archetype ID	North-South Direction				East-West Direction			
	T_1 (sec)	V_{max}/W	$\Delta_{U,80}$ (in/in)	$\Delta_{U,max}$ (in/in)	T_1 (sec)	V_{max}/W	$\Delta_{U,80}$ (in/in)	$\Delta_{U,max}$ (in/in)
Commercial Buildings: High Seismic								
COM2B	0.27	1.02	0.05	0.05	0.27	0.99	0.05	0.05
COM2B-SS1	0.31	0.40	0.10	0.10	0.32	0.40	0.06	0.06
COM2B-SS2	0.77	0.39	0.10	0.10	1.00	0.39	0.06	0.06
COM3B	0.46	0.66	0.01	0.01	0.47	0.66	0.02	0.02
COM3B-SS1	0.65	0.22	0.10	0.10	0.67	0.23	0.05	0.05
COM3B-SS2	1.11	0.26	0.08	0.08	1.26	0.25	0.04	0.04

Figure 5-14 compares the nonlinear static pushover analysis results in the N-S directions for archetypes with and without SSI and foundation flexibility, Table 5-13 shows the resulting peak lateral force and displacements, and Table 5-14 shows the resulting overstrength and period-based ductility. As shown, the lateral strength of the models that consider SSI and foundation flexibility is much smaller than the strength of the models that do not consider SSI and foundation flexibility. Additionally, the roof drift at collapse of the models that consider SSI and foundation

flexibility is much larger than the models that do not consider SSI and foundation flexibility. These results are due to a shift in behavior from a typical braced-fame response to one where the braced frames remain essentially elastic while their footings uplift and rock on the soil below.

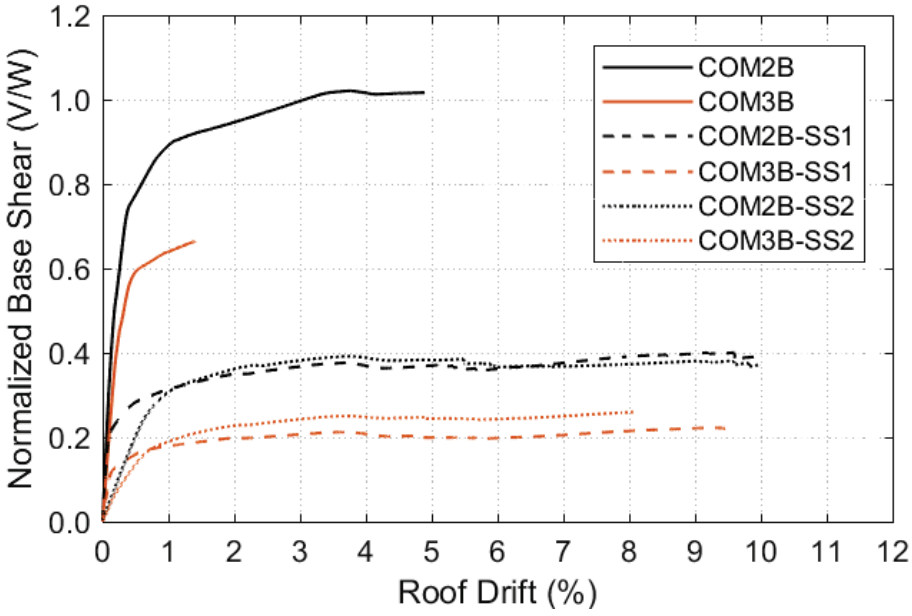

Figure 5-14 Pushover curves for archetype models with and without SSI and foundation flexibility normalized by total building seismic weight and roof height.

Table 5-14 Pushover and Collapse Analysis Results of SSI and Foundation Flexibility Parametric Study Archetype Models

Archetype ID	Pushover Analysis			Collapse Analysis				
	$V_{max,av}/W$	Ω	μ_T	S_{CT}* (g)	CMR_{3D}	SSF	ACMR	P[CO|MCE_R]
Commercial Buildings: High Seismic								
COM2B	1.01	6.0	10.01	2.34	1.87	1.33	2.49	3.4%
COM2B-SS1	0.40	2.4	32.61	2.90	2.32	1.33	3.08	1.2%
COM2B-SS2	0.39	2.3	3.67	2.68	2.15	1.27	2.72	2.3%
COM3B	0.66	3.9	3.15	2.29	1.83	1.19	2.18	6.0%
COM3B-SS1	0.23	1.3	30.07	2.65	2.12	1.35	2.86	1.8%
COM3B-SS2	0.26	1.5	4.96	2.77	2.22	1.29	2.86	1.8%

* Does not include the 3D analysis factor.

Figure 5-15 shows a comparison of the displaced shapes of COM2B and COM2B-SS2 at peak lateral displacement from a single response history analysis for an earthquake record scaled to the MCE_R. As shown, the braced frame in COM2B is undergoing brace deformation and fracture while the braced frame in COM2B-SS2 is uplifting with its footing pulling away from

and rocking on the soil. This damages the footing, as there are plastic hinges forming there, and the footing is only lightly reinforced. Deterioration of the footing flexural capacity was considered in the modeling, but the damage to the footing did not limit the ductility of the rocking system. Rocking is expected for these braced frames due to the large overstrength in the baseline models. Modern foundation design does not consider overstrength in the structure above the foundation to determine the foundation demands, instead using an allowable stress design approach for the base shear and overturning moments directly from ASCE/SEI 7-10. A simple calculation of the expected lateral capacity of the braced frames relative to the overturning resistance of the footing and gravity loads indicates footing rocking is expected.

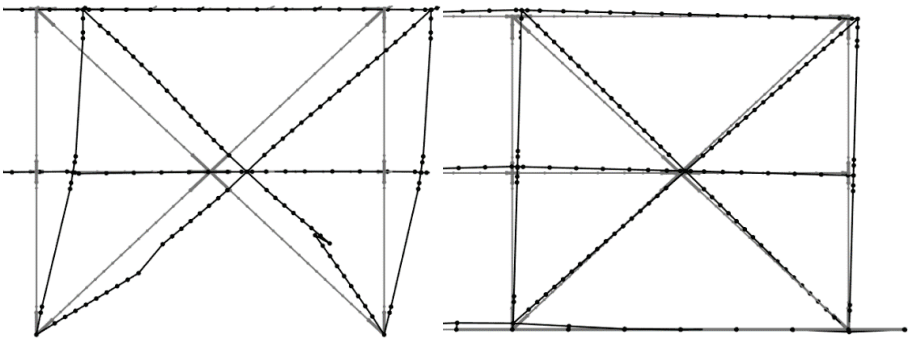

(a) (b)

Figure 5-15 Comparison of displaced shapes at peak interstory drift from a single MCE_R ground motion for (a) COM2B and (b) COM2B-SS2.

Table 5-14 shows that all archetypes where SSI and foundation flexibility were modeled exhibited the rocking behavior described above and illustrated in Figure 5-15. In the models with softer soil (COM2B-SS2 and COM3B-SS2), a smaller initial stiffness was observed, as shown in Figure 5-14. This is due to both vertical compression of the soil and foundation sliding. The smaller initial stiffnesses for the models on the softer soil also increases their first-mode periods and their effective yield displacements, which in turn decreases their period-based ductilities relative to the models on stiffer soils, as the values in Table 5-14 indicate.

Figure 5-16 compares the collapse fraction and resulting collapse fragility curves for the baseline and SSI and foundation flexibility models in a manner consistent with the similar previous figures. Table 5-14 shows the collapse margin ratios and collapse probabilities at the MCE_R ground-motion intensity for archetype models with and without modeling SSI and foundation flexibility, computed as described above. The ground-motion records used were filtered for kinematic interaction, as described in Appendix B. However, the x-axis in Figure 5-16 uses the median spectral acceleration of the

unmodified record set. As Figure 5-17 and Table 5-14 show, the reduction of strength but increase in ductility and flexibility of the models that consider SSI and foundation flexibility results in similar or slightly better collapse performance relative to the baseline models. The analyses indicate that the behavior is different when the braced frames rock on their foundations. The braced frames remain essentially elastic, and collapse results from overturning as the resistance of the gravity frames to P-delta is overcome. The failure mode was P-delta collapse for all of the SSI and foundation flexibility models. The gravity frame and collector connections influence the displacement at collapse for both the baseline and SSI and foundation flexibility models, indicating their importance to providing collapse resistance.

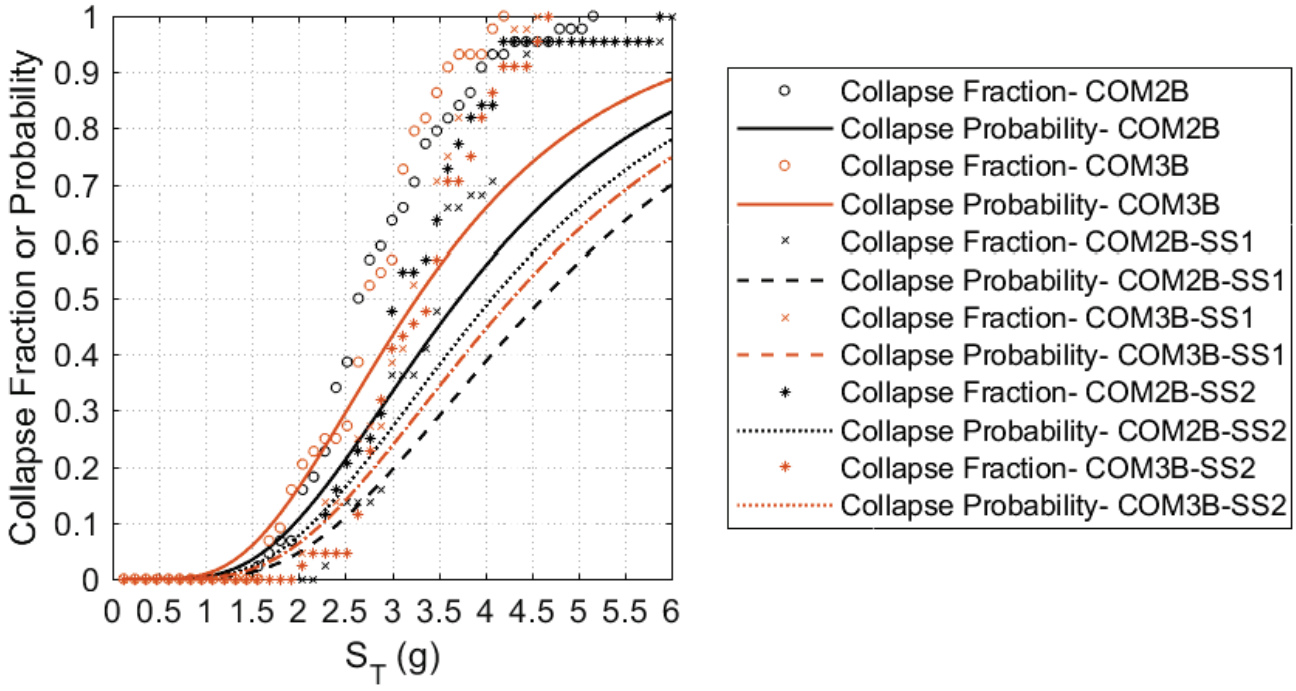

Figure 5-16 Collapse fraction versus S_T (including the 3D analysis factor) from the IDA analyses and the collapse fragility curves versus S_T (including both the 3D analysis factor and the *SSF*) for models with and without SSI and foundation flexibility.

Table 5-15 shows the median and β values for peak roof and first-story drift for the SSI and foundation flexibility parametric study models. As shown, for all SSI and foundation flexibility models, the roof drift and first-story drift at incipient collapse are similar, indicating that the rocking mechanism essentially eliminates the concentration of drift on the first story observed for all other models. Additionally, the roof drift at incipient collapse is significantly larger for the SSI and foundation flexibility models than it is for the baseline models. These findings help explain the lower collapse probabilities calculated for the models with SSI and foundation flexibility.

Table 5-15 Median and Lognormal Standard Deviation (β) Values of Peak Drift Ratio and Response Spectral Acceleration at Incipient Collapse of the SSI and Foundation Flexibility Parametric Study Models

Archetype ID	Peak Drift Ratio at Incipient Collapse				Response Spectral Acceleration at Incipient Collapse S_T (g)	
	Roof		First Story			
	Median	β	Median	β	Median	β
Commercial Buildings: High Seismic						
COM2B	0.033	0.34	0.051	0.32	2.34	0.27
COM2B-SS1	0.083	0.24	0.083	0.23	2.90	0.23
COM2B-SS2	0.091	0.25	0.096	0.25	2.68	0.24
COM3B	0.032	0.29	0.065	0.47	2.29	0.25
COM3B-SS1	0.086	0.32	0.086	0.32	2.65	0.21
COM3B-SS2	0.094	0.30	0.092	0.28	2.77	0.20

Table 5-16 shows mean peak first-story drift ratios in each building direction at intensities of $0.5 \times MCE_R$ and MCE_R. These values are from the raw data (i.e., prior to application of the 1.2 3D factor and the *SSF*). As shown, the mean peak first-story drift ratios are much larger for the SSI and foundation flexibility models at both $0.5 \times MCE_R$ and MCE_R. This indicates that braced-frame systems with footings that rock on soil may suffer more nonstructural damage than those with foundations that do not rock.

Table 5-16 Collapse Rates and Mean Peak First-Story Drift Ratios of SSI and Foundation Flexibility Parametric Study Archetype Models in the N-S and E-W Directions of Survivors at 50 Percent-of-MCE_R and at MCE_R Ground-Motion Intensities

Archetype ID	Collapse Rate at MCE_R (out of 44)		Mean Peak First-Story Drift Ratio of Survivors (%)			
			$0.5 \times MCE_R$		MCE_R	
	$0.5 \times MCE_R$	MCE_R	North-South Direction	East-West Direction	North-South Direction	East-West Direction
Commercial Buildings: High Seismic						
COM2B	0	0	0.49	0.50	1.76	1.85
COM2B-SS1	0	0	0.98	0.96	2.78	2.78
COM2B-SS2	0	0	0.95	1.04	3.00	3.04
COM3B	0	0	0.35	0.33	1.63	1.23
COM3B-SS1	0	0	1.26	1.27	3.27	3.18
COM3B-SS2	0	0	1.17	1.26	3.01	3.00

The effects of kinematic interaction on collapse are shown in Figure 5-17, Table 5-17, Table 5-18, and Table 5-19. As shown, the collapse fragility curves and collapse probabilities at MCE_R for the analyses incorporating the impacts of kinematic interaction on ground motions and the original ground motions are essentially the same for both the COM2B-SS1 and COM2B-SS2 models. The pushover responses for COM2B-SS1 and COM2B-SS2 still apply for the models subjected to unfiltered ground motions in the dynamic analyses because the models themselves are unchanged.

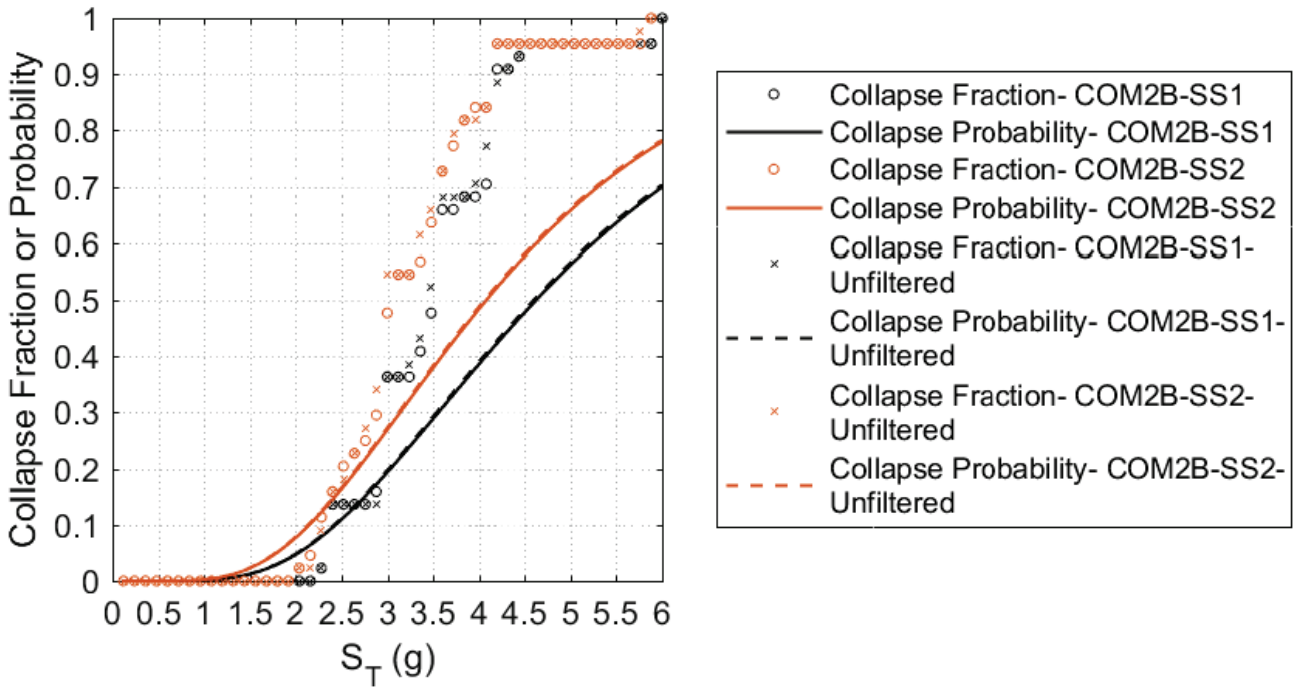

Figure 5-17 Collapse fraction versus S_T (including the 3D analysis factor) from the IDA analyses and the collapse fragility curves versus S_T (including both the 3D analysis factor and the *SSF*) for two-story SSI and foundation flexibility models subjected to ground motions with and without kinematic interaction.

Table 5-17 Pushover and Collapse Analysis Results of Two-Story SSI and Foundation Flexibility Archetype Models Analyzed Using Ground Motions with and without Kinematic Interaction

Archetype ID	Pushover Analysis			Collapse Analysis				
	$V_{max,av}/W$	Ω	μ_T	S_{CT}* (g)	CMR_{3D}	SSF	ACMR	P[CO|MCE_R]
Commercial Buildings: High Seismic								
COM2B-SS1	0.40	2.38	32.61	2.90	2.32	1.33	3.08	1.2%
COM2B-SS2	0.39	2.32	3.67	2.68	2.14	1.27	2.72	2.3%
COM2B-SS1-unfiltered	0.40	2.4	13.13	2.88	2.30	1.33	3.06	1.3%
COM2B-SS2-unfiltered	0.39	2.3	3.67	2.66	2.13	1.27	2.71	2.3%

* Does not include the 3D analysis factor.

Table 5-18 Median and Lognormal Standard Deviation (β) Values of Peak Drift Ratio and Response Spectral Acceleration at Incipient Collapse of Two-Story SSI and Foundation Flexibility Archetype Models Analyzed Using Ground Motions with and without Kinematic Interaction

Archetype ID	Peak Drift Ratio at Incipient Collapse				Response Spectral Acceleration at Incipient Collapse S_T (g)	
	Roof		First Story			
	Median	β	Median	β	Median	β
Commercial Buildings: High Seismic						
COM2B-SS1	0.083	0.24	0.083	0.23	2.90	0.23
COM2B-SS2	0.091	0.25	0.096	0.25	2.68	0.24
COM2B-SS1-unfiltered	0.082	0.23	0.083	0.22	2.88	0.22
COM2B-SS2-unfiltered	0.092	0.24	0.097	0.24	2.66	0.23

Table 5-19 Collapse Rates and Mean Peak First-Story Drift Ratios of Two-Story SSI and Foundation Flexibility Archetype Models Analyzed Using Ground Motions with and without Kinematic Interaction in the N-S and E-W Directions of Survivors at 50 Percent-of-MCE_R and at MCE_R Ground-Motion Intensities

Archetype ID	Collapse Rate at MCE_R (out of 44)		Mean Peak First-Story Drift Ratio of Survivors (%)			
			$0.5 \times MCE_R$		MCE_R	
	$0.5 \times MCE_R$	MCE_R	North-South Direction	East-West Direction	North-South Direction	East-West Direction
Commercial Buildings: High Seismic						
COM2B-SS1	0	0	0.98	0.96	2.78	2.78
COM2B-SS2	0	0	0.95	1.04	3.00	3.04
COM2B-SS1-unfiltered	0	0	0.97	0.94	2.80	2.79
COM2B-SS2-unfiltered	0	0	1.00	1.08	3.10	3.16

5.5.3 Summary of Results

Figure 5-18 shows the collapse probability at the MCE_R spectral intensity, $P[C|MCE_R]$, versus the normalized pushover strength, $V_{max,av}/W$, which is a proxy for overstrength. Here the previously identified trend of decreasing collapse probability with increasing strength does not hold due to the large increase in ductility of the models with SSI and foundation flexibility. However, the results show that the models with SSI and foundation flexibility have a lower collapse probability at MCE_R intensity. Figure 5-19 shows $P[C|MCE_R]$ versus building period for the models with and without SSI and foundation flexibility, demonstrating that the collapse probability decreases with decreasing building period when comparing models that incorporate SSI and foundation flexibility (i.e., COM2B-SS1 vs. COM3B-SS1). However, when comparing the collapse probability for the same

building height but different SSI parameters, the collapse probabilities do not vary significantly (i.e., COM3B-SS1 vs. COM3B-SS2).

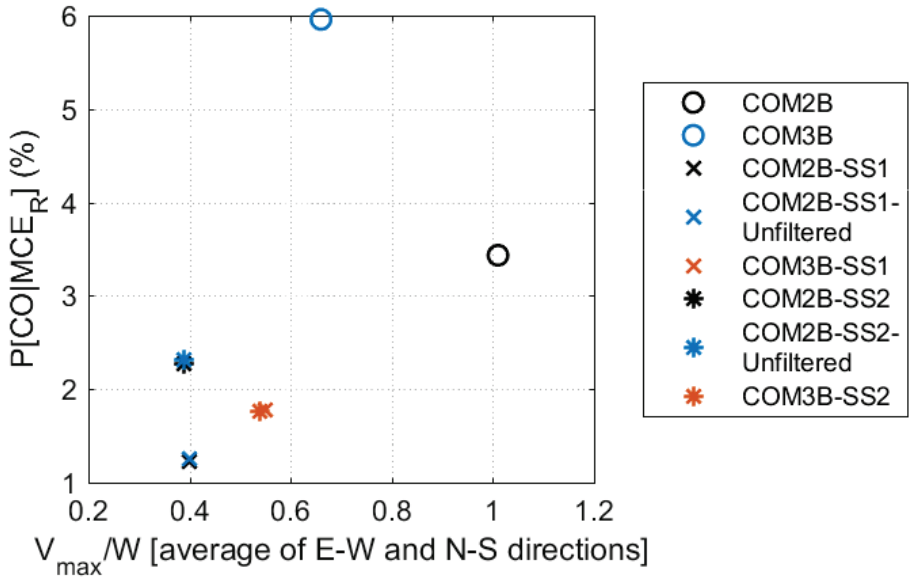

Figure 5-18 MCE_R collapse probability versus $V_{max,av}/W$ for steel SCBF models with and without SSI and foundation flexibility and with and without kinematic interaction.

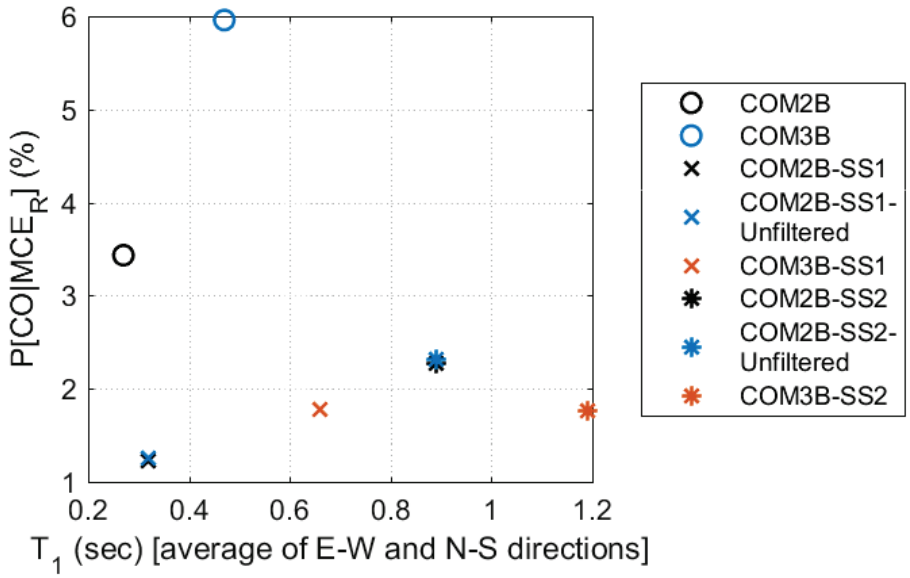

Figure 5-19 MCE_R collapse probability versus fundamental period (T_1) for steel SCBF models with and without SSI and foundation flexibility and with and without kinematic interaction.

5.6 No Reserve Moment Frame Parametric Study

5.6.1 No Reserve Moment Frame Archetypes

This section compares the analysis results for archetypes with and without the reserve moment frames within the braced frames. The reserve moment frame capacity of the braced frames (i.e., the moment frame provided by the presence of gusset plates at the beam-to-column and column-base connections) provides significant lateral-force capacity. The impact of removing that reserve capacity is investigated using a modified version of the COM2B model, denoted COM2B-NMF, by eliminating the moment capacity of the beams at the gusset-plate edges, the collector connections within the braced frames, and the column-base connections within the braced frames. The gravity frame in COM2B-NMF is modeled identically to that for COM2B, in order to focus on the impact of the reserve moment frame within the braced frames.

5.6.2 Numerical Results

The first-mode periods in both building directions are shown in Table 5-20. As shown, the first-mode period does not change significantly when the reserve moment-frame capacity is removed because the initial stiffness is still dominated by the braces.

Table 5-20 Modal and Pushover Results for Two-Story Archetype Models with and without Reserve Moment-Frame Capacity in the N-S and E-W Directions of Response

Archetype ID	North-South Direction				East-West Direction			
	T_1 (sec)	V_{max}/W	$\Delta_{U,80}$ (in/in)	$\Delta_{U,max}$ (in/in)	T_1 (sec)	V_{max}/W	$\Delta_{U,80}$ (in/in)	$\Delta_{U,max}$ (in/in)
Commercial Buildings: High Seismic								
COM2B	0.27	1.02	0.05	0.05	0.27	0.99	0.05	0.05
COM2B-NMF	0.27	0.85	0.05	0.05	0.28	0.88	0.04	0.04

Figure 5-20 compares the nonlinear static pushover analysis results in the N-S directions for the COM2B and COMB2B-NMF models, Table 5-20 shows the resulting peak lateral force and displacements, and Table 5-21 shows the resulting overstrength and period-based ductility. As shown, there is about a 15 percent reduction in peak lateral strength when the reserve moment frame is removed, but the period-based ductility is largely unchanged.

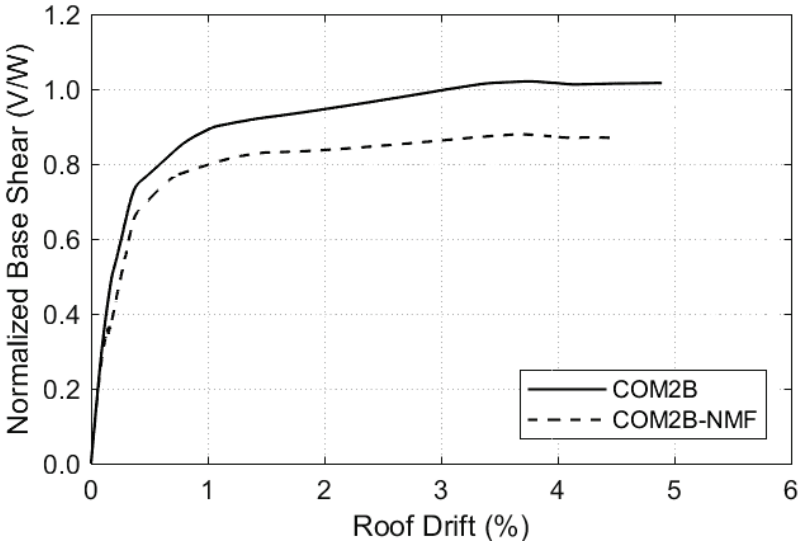

Figure 5-20 Pushover curves for two-story archetype models with and without reserve moment-frame capacity normalized by total building seismic weight and roof height.

Table 5-21 Pushover and Collapse Analysis Results for Two-Story Archetype Models with and without Reserve Moment-Frame Capacity

Archetype ID	Pushover Analysis			Collapse Analysis				
	$V_{max,av}/W$	Ω	μ_T	S_{CT}* (g)	CMR_{3D}	SSF	ACMR	$P[CO\|MCE_R]$
Commercial Buildings: High Seismic								
COM2B	1.01	6.0	10.01	2.34	1.87	1.33	2.49	3.4
COM2B-NMF	0.86	5.1	11.08	2.24	1.80	1.33	2.39	4.1

* Does not include the 3D analysis factor.

Figure 5-21 compares the collapse fraction and resulting collapse fragility curves for COM2B and COM2B-NMF in a manner consistent with the similar previous figures. Table 5-21 shows the collapse margin ratios and collapse probabilities at the MCE_R ground-motion intensity for the two-story archetype models with and without reserve moment-frame capacity. As shown, despite the 15 percent reduction in lateral strength, the collapse probability for the baseline and COM2B-NMF archetypes are largely the same, and the collapse fragility curves are nearly identical.

The dispersion of the raw data used to generate Figure 5-21 indicates that there is more variability in the collapse data for COM2B-NMF. When the reserve capacity of the moment frame is removed, the building relies only on the braces, and brace fracture is inherently more variable and more dependent on the input motion than moment-frame action. These results indicate that reserve moment-frame capacity does play a role in the collapse fragility for steel SCBFs.

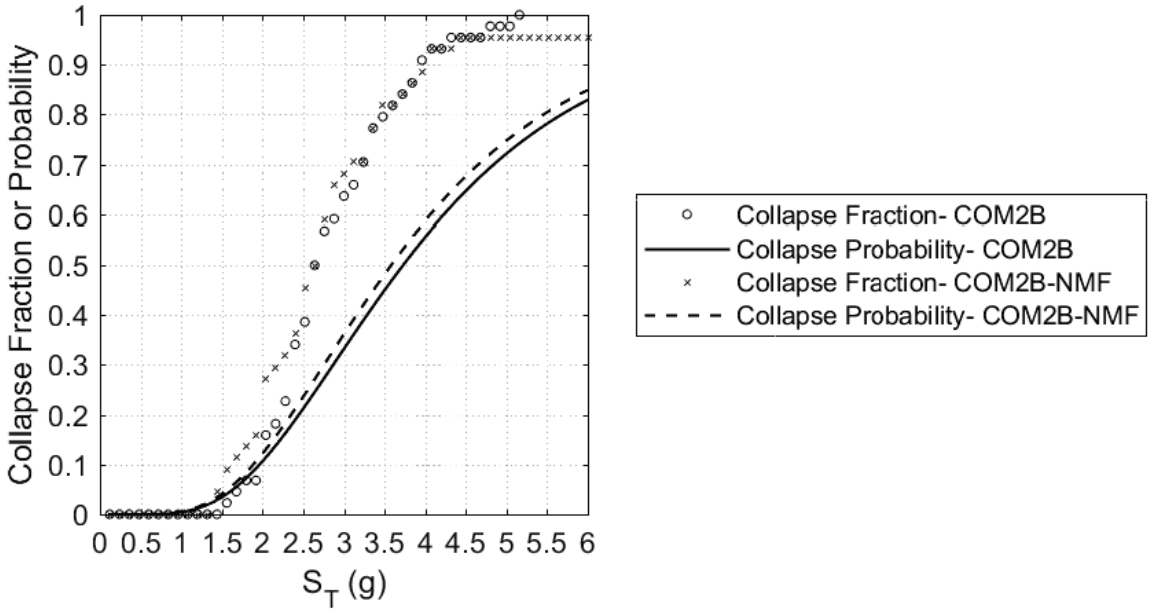

Figure 5-21 Collapse fraction versus S_T (including the 3D analysis factor) from the IDA analyses and the collapse fragility curves versus S_T (including both the 3D analysis factor and the *SSF*) for two-story archetype models with and without reserve moment-frame capacity.

Table 5-22 shows the median and β values for roof and first-story drift ratio at incipient collapse for COM2B and COM2B-NMF. As shown, drift demand appears to be more evenly distributed between the stories in COM2B-NMF. This is due to a reduction in stiffness of the second story, where a gusset plate connects the beam and column and is modeled as fully restrained in the COM2B model and pinned in the COM2B-NMF model. This reduced second-story stiffness in COM2B-NMF results in larger second-story drifts and more uniform drifts overall. Notably, the first-story drift at incipient collapse for the two frames is similar, with COM2B-NMF having a slightly smaller median value.

Table 5-22 Median and Lognormal Standard Deviation (β) Values of Peak Drift Ratio and Response Spectral Acceleration at Incipient Collapse for Two-Story Archetype Models with and without Reserve Moment-Frame Capacity

Archetype ID	Peak Drift Ratio at Incipient Collapse				Response Spectral Acceleration at Incipient Collapse S_T (g)	
	Roof		First Story			
	Median	β	Median	β	Median	β
Commercial Buildings: High Seismic						
COM2B	0.033	0.34	0.051	0.32	2.34	0.27
COM2B-NMF	0.043	0.38	0.047	0.33	2.24	0.35

Table 5-23 shows mean peak first-story drift ratios in each building direction at intensities of 0.5 × MCE_R and MCE_R. These values are from the raw data (i.e., prior to application of the 1.2 3D factor and the *SSF*). As shown, the mean peak first-story drift ratios are larger for COM2B-NMF at both 0.5 × MCE_R and MCE_R. This indicates that the reserve moment frame also helps to limit drifts in large earthquakes and potentially serves a purpose at demands less than MCE_R.

Table 5-23 Collapse Rates and Mean Peak First-Story Drift Ratios of Two-Story Archetype Models with and without Reserve Moment-Frame Capacity at 50 Percent-of-MCE_R and at MCE_R Ground-Motion Intensities

Archetype ID	Collapse Rate at MCE_R (out of 44)		Mean Peak First-Story Drift Ratio of Survivors (%)			
			0.5 × MCE_R		MCE_R	
	0.5 × MCE_R	MCE_R	North-South Direction	East-West Direction	North-South Direction	East-West Direction
Commercial Buildings: High Seismic						
COM2B	0	0	0.49	0.50	1.76	1.85
COM2B-NMF	0	2	0.70	0.74	1.98	2.02

5.6.3 Summary of Results

Figure 5-22 shows the collapse probabilities at the MCE_R spectral intensity, P[C|MCE_R], versus the normalized pushover strength, $V_{max,av}/W$, which is a proxy for overstrength. The previously identified trend of decreasing collapse probability with increasing strength is apparent, albeit with small differences in collapse probability. Figure 5-23 shows P[C|MCE_R] versus building period for the two-story archetype models with and without reserve moment-frame capacity.

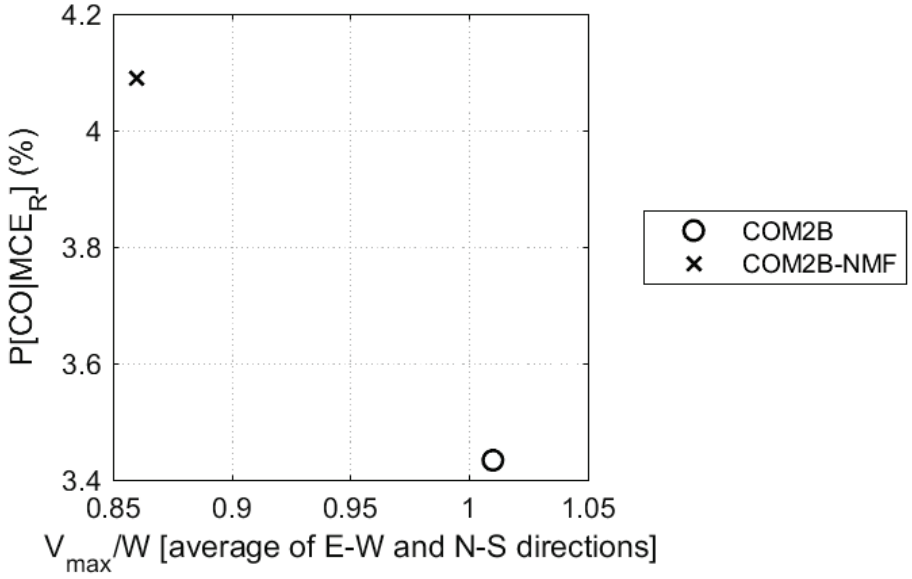

Figure 5-22 MCE_R collapse probability versus $V_{max,av}/W$ for two-story archetype models with and without reserve moment-frame capacity.

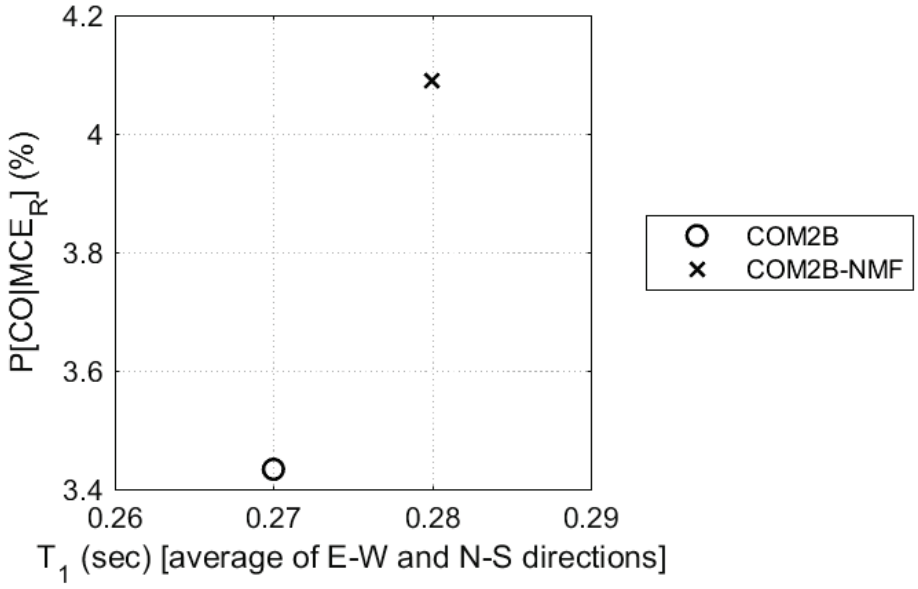

Figure 5-23 MCE_R collapse probability versus fundamental period (T_1) for two-story archetype models with and without reserve moment-frame capacity.

Chapter 6
Findings, Conclusions, and Recommendations

6.1 Introduction

This chapter summarizes key findings, conclusions, and recommendations arising from the parametric studies conducted on steel SCBF building archetypes. In preceding chapters, the following topics were addressed:

- establishing target collapse performance benchmarks for the numerical models of steel SCBF buildings based on observations of collapse performance in past earthquakes (Chapter 2);
- identifying representative building archetypes and developing detailed designs of these building archetypes according to current seismic-code requirements (Chapter 3);
- transforming the archetype designs into advanced nonlinear numerical models, including variations on selected parameters in the models (Chapter 4); and
- conducting nonlinear pushover and incremental dynamic analyses with these numerical models to evaluate the relative importance of the modeling assumptions and parametric variations on the reliable calculation of response behavior and collapse performance (Chapter 5).

6.2 Key Findings of the Parametric Studies

Key findings of the parametric studies are summarized and discussed in the following sections. A table is provided with each parametric study, summarizing key archetype model properties (e.g., number of stories; first-mode period, T_1; overstrength, Ω; and normalized pushover strength, V_{max}/W) and key collapse results (e.g., first-story and roof drift ratios at the point of incipient collapse; the collapse margin ratio, CMR_{3D}; and the probability of collapse given MCE_R ground motions). The target range of benchmark collapse probabilities are also provided for comparison with the collapse probabilities of archetype models designed for high-seismic loads (S_{MS} = 1.5g). Values of first-mode period, overstrength, and normalized pushover strength in the tables represent the average values of these parameters in the two horizontal directions of response.

6.2.1 Baseline Configuration Parametric Study

This study investigated the response behavior and collapse performance of six commercial steel SCBF baseline archetype configurations. The baseline archetypes included variations in height (one story, two stories, and four stories) and seismic design level (high seismic, where S_{MS} = 1.5g, and very high seismic, where S_{MS} = 2.25g). Baseline archetypes designed for the moderate seismic design level were not investigated. Based on previous FEMA P-695 studies, steel SCBF archetypes designed for the moderate seismic design level are expected to have equal, or better, collapse performance than that of the steel SCBF archetypes designed for the high-seismic or very high-seismic design levels, all else being equal.

Baseline archetype models considered the results of other parametric studies and incorporated a best estimate for each parameter to provide an overall best estimate of the simulated response of short-period steel SCBF buildings. Table 6-1 summarizes key model properties and collapse results for each of the baseline archetypes.

Baseline archetypes were designed with conventional shallow spread-footing foundations below braced frames but modeled with fixed bases representative of steel SCBF buildings on mat foundations or having basements. Baseline archetype models implicitly assume that collapse performance is governed by brace failure, which is typical of the type of damage observed to steel braced-frame buildings in past earthquakes. For this and other reasons, the baseline models did not include SSI or foundation flexibility. However, baseline archetypes representative of steel SCBF buildings on shallow spread-footing foundations were investigated as part of the soil-structure interaction (SSI) and foundation flexibility parametric study.

Table 6-1 Summary of Key Properties and Collapse Results of Baseline Archetype Models

Archetype ID	Model Properties				Collapse Results				Benchmark Collapse Probability (%)
	No. of Stories	T_1 (sec)	Strength		Drift Ratio*		CMR_{3D}	P[COL | MCE_R] (%)	
			Ω	V_{max}/W	Roof	First Story			
High-Seismic (S_{MS} = 1.5g) Baseline Archetype Models									
COM1B	1	0.16	11	2.00	0.030	0.030	2.32	1.2	0 to 2
COM2B	2	0.27	6.0	1.02	0.033	0.051	1.87	3.4	0 to 5
COM3B	4	0.46	3.9	0.66	0.032	0.065	1.83	6.0	0 to 5
Very High-Seismic (S_{MS} = 2.25g) Baseline Archetype Models									
COM4B	1	0.15	9.0	2.43	0.058	0.058	1.77	4.0	NA
COM5B	2	0.25	4.2	1.14	0.021	0.035	1.14	20	NA
COM6B	4	0.44	2.9	0.75	0.034	0.075	1.21	19	NA

* Median drift ratio at incipient collapse.

The overall findings of the baseline parametric study include the following:

1. **Collapse Failure Mode.** Simulated (computed) collapse of all baseline building archetypes was due to sidesway failure of the first story.

2. **Collapse Probabilities.** The MCE_R collapse probabilities calculated for high-seismic one-story (COM1B), two-story (COM2B) and four-story (COM3B) baseline archetypes are consistent with benchmark collapse rates, as shown in Table 6-1.

   The MCE_R collapse probabilities calculated for very high-seismic two-story (COMB5B) and four-story (COM6B) archetypes exceed the 10 percent collapse-safety objective of ASCE/SEI 7-10 by a factor of about two.

3. **Collapse Trend with Building Period.** In general, the probability of collapse was found to increase with archetype model period, T_1, all else being equal, as illustrated in Figure 6-1. This trend is most likely due to differences in archetype normalized pushover strength (V_{max}/W), which tends to decrease with height, and P-delta collapse of the first story, which becomes more critical with height (number of stories).

   For comparison purposes, horizontal lines are included in Figure 6-1 (and subsequent figures of this chapter that show the probability of collapse as a function of an archetype model parameter) to indicate: (1) the 2 percent benchmark collapse probability for one-story high-seismic archetypes; (2) the 5 percent benchmark collapse probability for two-story-and-taller high-seismic archetypes; and (3) the 10 percent collapse-safety objective of ASCE/SEI 7-10.

4. **Strength.** In general, collapse probability is strongly influenced by the archetype normalized pushover strength (V_{max}/W), where the stronger the archetype model, the better the collapse performance, all else being equal. The same trend is seen where collapse probability is expressed as a function of archetype overstrength (Ω), which is the maximum base shear strength (V_{max}) of the model relative to the design base shear (V_{design}). Figure 6-2 shows MCE_R collapse probabilities of the baseline archetypes plotted as a function of building archetype overstrength (Ω), indicating the general trend of lower MCE_R collapse probability with increased archetype overstrength.

5. **P-Delta Effects.** In general, collapse was found to be strongly influenced by P-delta effects. In general, the taller (and heavier) the archetype, the more P-delta detrimentally affects collapse performance, all else being equal.

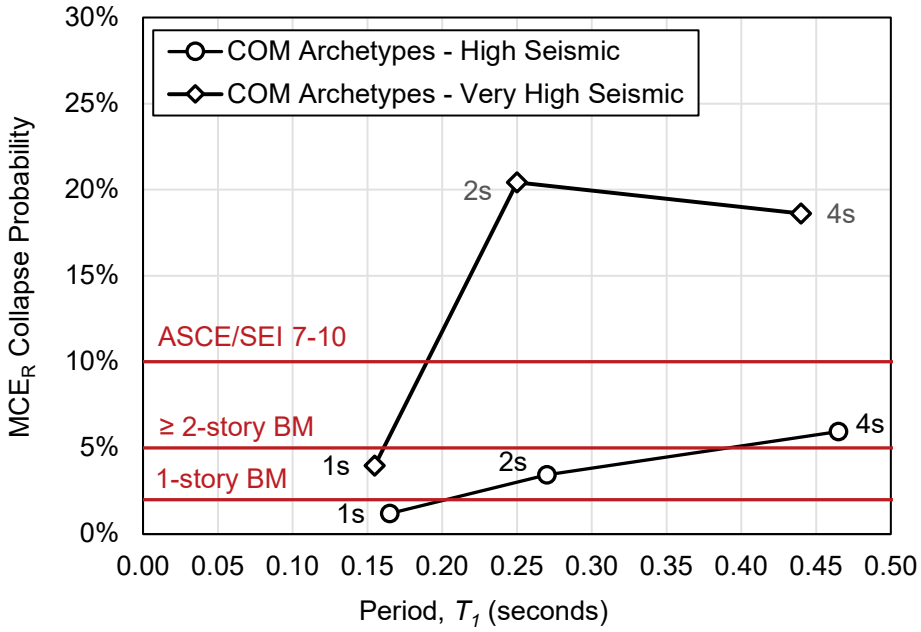

Figure 6-1 MCE_R collapse probability of baseline archetype models plotted as a function of archetype model period (T_1), and benchmark (BM) values of high-seismic MCE_R collapse probability and the MCE_R collapse-safety objective of ASCE/SEI 7-10.

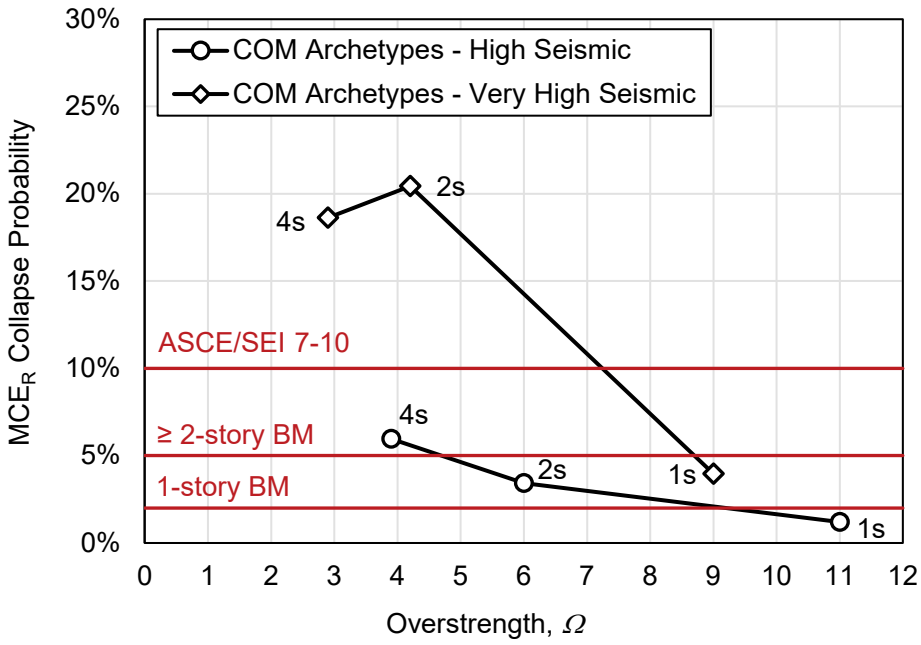

Figure 6-2 MCE_R collapse probabilities of steel SCBF baseline archetype models plotted as a function of archetype model overstrength (Ω), and benchmark (BM) values of MCE_R collapse probability and the MCE_R collapse-safety objective of ASCE/SEI 7-10.

6. **Very High-Seismic Collapse Performance.** The probability of collapse of a very high-seismic archetype is larger than that of the corresponding high-seismic archetype, even when the seismic-force-resisting system is designed for proportionally larger (50 percent greater) seismic forces. As can be seen in Table 6-1, a 50 percent increase in design strength does not result in a 50 percent increase in normalized pushover strength (V_{max}/W) of very high-seismic archetype models. For example, the normalized pushover strength of COM4B ($V_{max}/W = 2.43$) is only about 22 percent larger than that of COM1B ($V_{max}/W = 2.00$).

   Collapse performance of very high-seismic designs was evaluated for MCE_R ground motions ($S_{MS} = 2.25$g) that represent a ground-motion intensity typical of sites relatively close to active faults (an intensity 50 percent greater than that of high-seismic ground motions). The analysis was performed with ground motions recorded at far-field sites, but the amplitudes were scaled up based upon the design parameter of $S_{MS} = 2.25$g.

6.2.2 Brace Configuration Parametric Study

This study compared the response behavior and collapse performance of the two-story (COMB2B) and four-story (COMB3B) steel SCBF baseline archetypes (with super-X bracing) to the response behavior and collapse performance of the same two-story and four-story archetypes re-designed with chevron bracing (COM2B-BC and COM3B-BC, respectively). All four building archetypes were designed for high-seismic loads and modeled with fixed bases (i.e., effects of SSI and foundation flexibility were ignored). Table 6-2 summarizes key model properties and collapse results for the COM2B and COM3B archetype models with and without modified bracing.

Table 6-2 Summary of Key Properties and Collapse Results of Brace Configuration Parametric Study Archetype Models

Archetype ID	Model Properties				Collapse Results				Benchmark Collapse Probability (%)
	No. of Stories	T_1 (sec)	Strength		Drift Ratio*		CMR_{3D}	P[COL|MCE_R] (%)	
			Ω	V_{max}/W	Roof	First Story			
High-Seismic (S_{MS} = 1.5g) Baseline Archetypes Models (Super-X Bracing)									
COM2B	2	0.27	6.0	1.01	0.033	0.051	1.87	3.4	0 to 5
COM3B	4	0.47	3.9	0.66	0.032	0.065	1.83	6.0	0 to 5
High-Seismic (S_{MS} = 1.5g) Archetypes Models with Chevron Bracing									
COM2B-BC	2	0.28	5.3	0.93	0.022	0.042	1.55	8.3	0 to 5
COM3B-BC	4	0.44	4.6	0.79	0.013	0.037	1.25	21	0 to 5

* Median drift ratio at incipient collapse.

The overall findings of the brace configuration parametric study include the following:

1. **Collapse Failure Mode.** The collapse failure mode of the building archetypes with chevron bracing is the same as that of the baseline archetypes with super-X bracing (i.e., sidesway collapse due to P-delta failure of the first story).

2. **Collapse Probabilities.** The MCE_R collapse probability calculated for the two-story building archetype with chevron bracing is comparable to that of the two-story baseline archetype with super-X bracing and is consistent with the benchmark collapse rate, as shown in Table 6-2. The MCE_R collapse probability calculated for the four-story building archetype with chevron bracing is significantly greater than that of the four-story baseline archetype with super-X bracing and is not consistent with the benchmark collapse rate due to a lower displacement capacity of chevron bracing at incipient collapse, as discussed in Section 5.3.2.

3. **Collapse Trend with Height.** The probability of collapse of baseline archetypes with either super-X or chevron bracing increases with height (and longer archetype model period, T_1), all else being equal. Again, this trend is most likely due to differences in building archetype normalized pushover strength (V_{max}/W), which tends to decrease with height, and P-delta collapse of the first story, which becomes more critical with height.

6.2.3 No Redundancy Parametric Study

This study compared the response behavior and collapse performance of the two-story steel SCBF baseline building archetype (i.e., with a "redundant" configuration of two bays of bracing on each side of the archetype) to the response behavior and collapse performance of the same two-story archetype re-designed to have only one bay of bracing on each side (i.e., a "non-redundant" configuration requiring 30 percent larger design brace forces from earthquake loads). Both redundant and non-redundant building archetypes were designed for high-seismic loads and modeled with fixed bases. Table 6-3 summarizes key model properties and collapse results for the redundant (COM2B) and non-redundant (COM2B-NR) archetypes models.

Table 6-3 Summary of Key Properties and Collapse Results of No Redundancy Parametric Study Archetype Models

Archetype ID	Model Properties				Collapse Results				Benchmark Collapse Probability (%)
	No. of Stories	T_1 (sec)	Strength		Drift Ratio*		CMR_{3D}	P[COL | MCE_R] (%)	
			Ω	V_{max}/W	Roof	First Story			
High-Seismic (S_{MS} = 1.5g) Baseline Archetype Model (Redundant Bracing)									
COM2B	2	0.27	6.0	1.01	0.033	0.051	1.87	3.4	0 to 5
High-Seismic (S_{MS} = 1.5g) Archetype Model (Non-Redundant Bracing)									
COM2B-NR	2	0.33	3.8	0.69	0.027	0.045	1.39	11	0 to 5

* Median drift ratio at incipient collapse.

The overall findings of the no redundancy parametric study include the following:

1. **Collapse Failure Mode.** The collapse failure mode of the non-redundant two-story building archetype is the same as that of the two-story redundant (baseline) building archetype (i.e., sidesway collapse due to P-delta failure of the first story).

2. **Collapse Probabilities.** The MCE_R collapse probability calculated for the non-redundant two-story building archetype (with only a single bay of bracing on each side) is significantly greater than that of the redundant two-story baseline archetype (with two bays of bracing on each side) and is not consistent with the benchmark collapse rate, as shown in Table 6-3, due to significantly lower pushover strength (despite being designed for 30 percent larger brace forces from earthquake loads), as explained in Section 5.4.2.

3. **Collapse Trend with Strength.** The higher probability of collapse of the non-redundant archetype than that of the redundant archetype is consistent with the pushover strength of the non-redundant archetype being lower than that of the redundant archetype model (i.e., the lower pushover strength, the worse the collapse performance).

6.2.4 Soil-Structure Interaction and Foundation Flexibility Parametric Study

This study investigated the effects of soil-structure interaction (SSI) and foundation flexibility by: (1) modeling a distributed set of discrete nonlinear soil springs and dampers below flexible foundation elements; and (2) performing dynamic analysis with FEMA P-695 earthquake records filtered to reduce response at very short periods (i.e., due to kinematic interaction).

For this study, the two-story and four-story baseline archetypes were modeled with two sets of nonlinear soil springs and dampers representing stiff soil site conditions (COM2B-SS1) and soft soil site conditions (COM2B-SS2).

For two-story archetypes modeled with nonlinear spring and dampers, collapse analyses were performed using earthquake records modified for kinematic interaction (i.e., filtered records) as well as the standard set of (unfiltered) FEMA P-695 earthquake records.

Table 6-4 summarizes key model properties and collapse results for archetype models with fixed bases (baseline models) and archetype models with flexible foundations that incorporate SSI effects.

Table 6-4 Summary of Key Properties and Collapse Results of SSI and Foundation Flexibility Parametric Study Archetype Models

Archetype ID	Model Properties				Collapse Results				Benchmark Collapse Probability (%)
	No. of Stories	T_1 (sec)	Strength		Drift Ratio*		CMR_{3D}	P[COL | MCE_R] (%)	
			Ω	V_{max}/W	Roof	First Story			
High-Seismic (S_{MS} = 1.5g) Baseline Archetype Models (Rigid Foundation)									
COM2B	2	0.27	6.0	1.01	0.033	0.051	1.87	3.4	0 to 5
COM3B	4	0.46	3.9	0.66	0.032	0.065	1.83	6.0	0 to 5
High-Seismic (S_{MS} = 1.5g) Archetype Models with Flexible Foundation – Stiff Soil									
COM2B-SS1	2	0.31	2.4	0.40	0.083	0.083	2.32	1.2	0 to 5
COM3B-SS1	4	0.66	1.3	0.23	0.086	0.086	2.12	1.8	0 to 5
High-Seismic (S_{MS} = 1.5g) Archetype Models with Flexible Foundation – Soft Soil									
COM2B-SS2	2	0.88	2.3	0.39	0.091	0.096	2.15	2.3	0 to 5
COM3B-SS2	4	1.19	1.5	0.26	0.094	0.092	2.22	1.8	0 to 5
High-Seismic (S_{MS} = 1.5g) Archetype Models with Flexible Foundation – Unfiltered records									
COM2B-SS1	2	0.31	2.4	0.40	0.082	0.083	2.30	1.3	0 to 5
COM2B-SS2	2	0.32	2.3	0.39	0.092	0.097	2.13	2.3	0 to 5

* Median drift ratio at incipient collapse.

The overall findings of the SSI and foundation flexibility parametric study include the following:

1. **Collapse Failure Mode.** Simulated (computed) collapse of the building archetypes incorporating SSI effects and foundation flexibility is due to rocking and uplift of the foundations below braced frames, rather than P-delta failure of first-story framing (i.e., the failure mode of the baseline models with fixed bases). Rocking and uplift of foundations results in similar values of displacement at each story, as indicated by similar

values of roof and first-story drift ratios at the point of incipient collapse (Table 6-4).

2. **Collapse Probabilities.** The MCE_R collapse probabilities of the archetypes incorporating SSI and foundation flexibility are similarly low, but consistently less than, those of the corresponding two-story and four-story baseline archetypes with fixed bases and consistent with benchmark collapse rates, as shown in Table 6-4. The MCE_R collapse probabilities of the two-story archetypes evaluated using filtered earthquake records are essentially the same as those of the two-story archetypes evaluated using unfiltered earthquake records (i.e., foundation flexibility, rather than kinematic interaction, governs archetype model collapse performance).

3. **Nonlinear Static (Pushover) Response.** The nonlinear static (pushover) curves of variant building archetypes with flexible foundations and incorporating SSI effects were found to have significantly lower initial stiffnesses and pushover strengths, in particular for archetype models representing soft site conditions (COM2B-SS2 and COM3B-SS2). Lower pushover strengths for archetypes with flexible foundations and incorporating SSI effects were due to their foundations reaching full strength before the bracing could reach full strength.

4. **Elastic Model Periods.** The elastic model periods of the variant building archetypes with flexible foundations and incorporating SSI effects were found to be significantly longer than those of the corresponding baseline models with fixed bases, in particular for archetypes representing soft site conditions (COM2B-SS2 and COM3B-SS2), which have periods well beyond the approximate limit of 0.5 seconds used in this report to define short-period buildings.

6.2.5 No Reserve Moment Frame Parametric Study

This study compared the response behavior and collapse performance of the two-story baseline building archetype (i.e., with inherent reserve moment-frame capacity provided by gusset plates at beam-to-column connections and column-base connections) to the response behavior and collapse performance of the same two-story archetype (denoted as COM2B-NMF) modified to eliminate reserve moment capacity (i.e., no moment-frame capacity at beam-to-column and column-base connections).

Table 6-5 summarizes key model properties and collapse results for archetype models with reserve moment capacity (baseline model) and without reserve moment capacity.

Table 6-5 Summary of Key Properties and Collapse Results of No Reserve Moment-Frame Capacity Parametric Study Archetype Models

Archetype ID	Model Properties				Collapse Results				Benchmark Collapse Probability (%)
	No. of Stories	T_1 (sec)	Strength		Drift Ratio*		CMR_{3D}	P[COL | MCE_R] (%)	
			Ω	V_{max}/W	Roof	First Story			
High-Seismic (S_{MS} = 1.5g) Baseline Archetype Model (Reserve Moment Capacity)									
COM2B	2	0.27	6.0	1.01	0.033	0.051	1.87	3.4	0 to 5
High-Seismic (S_{MS} = 1.5g) Archetype Model without Reserve Moment Capacity									
COM2B-NMF	2	0.27	5.1	0.86	0.043	0.047	1.80	4.1	0 to 5

* Median drift ratio at incipient collapse.

The overall findings of the no reserve moment frame parametric study include the following:

1. **Collapse Failure Mode.** The collapse failure mode of the two-story building archetype without reserve moment-frame capacity is similar to that of the two-story baseline archetype with inherent reserve moment-frame capacity. However, removing the reserve moment-frame capacity within the braced frames reduces the stiffness of the upper story and results in more uniform drift demand. This is unique to the super-X configuration, where large gusset-plate connections are at the top of the second story but not the first story.

2. **Collapse Probabilities.** The MCE_R collapse probability calculated for the two-story building archetype without reserve moment-frame capacity is slightly greater than, but essentially the same as, that of the two-story baseline archetype with inherent reserve moment-frame capacity, as shown in Table 6-5.

3. **Collapse Trend with Strength.** The similarity of the MCE_R collapse probabilities of the two-story building archetypes with and without reserve moment-frame capacity is consistent with the similarity of the strengths of these two archetype models. The archetype model without reserve moment capacity is still relatively strong (e.g., $\Omega = 5.1$) and lack of reserve moment-frame capacity in a weaker steel SCBF system would be expected to have a more significant influence on collapse performance.

6.3 Conclusions and Recommendations

Prior FEMA P-695 collapse performance studies on a variety of structural systems over a range of periods have suggested that, for systems with design periods less than about 0.5 seconds, the probability of collapse given MCE_R ground motions increases significantly as the design period decreases. Trends in observed earthquake damage of short-period buildings, however, do not support the high collapse probabilities predicted by numerical analysis. The apparent discrepancy between analytical prediction of collapse performance and the opinions and observations of structural engineers has been designated the *short-period building seismic performance paradox*.

With improved numerical modeling and representative steel SCBF building archetypes, this study has shown that MCE_R collapse probabilities decrease as the design period decreases, which is a reversal of the trend observed in prior FEMA P-695 studies. Further, numerical analyses of short-period steel SCBF buildings designed and evaluated for high-seismic loads (S_{MS} = 1.5g), resulted in low collapse probabilities for MCE_R ground motions, consistent with the collapse rates inferred by the observed performance of low-rise buildings in past earthquakes (e.g., red tag data from the 1994 Northridge earthquake). As a result, this study has solved the short-period building seismic performance paradox for steel SCBF systems.

Numerical investigations conducted in this study provide valuable insights into the collapse performance of steel SCBF buildings that should be of importance to seismic-code-development committees, engineering practitioners, and researchers. In the sections that follow, results from this study are compared to a prior FEMA P-695 study on steel SCBF building archetypes, and recommendations are provided in the following areas:

- Improved Seismic Design Codes and Standards
- Advanced Seismic Design and Analysis Practice
- Enhanced Modeling and Testing

6.3.1 Comparison with Previous FEMA P-695 Collapse Probability Study

Key model properties and collapse results of a previous study of archetype models of short-period steel SCBF buildings, as reported in NIST GCR 10-917-8, are summarized in Table 6-6. The NIST GCR 10-917-8 study evaluated collapse performance for two-story, three-story, six-story, twelve-story, and sixteen-story heights of steel SCBF building archetypes designed for two FEMA P-695 seismic levels, SDC D_{max} (S_{MS} = 1.5g) and SDC D_{min} (S_{MS} = 0.75g). Only model properties and collapse results for two-story and

three-story steel SCBF archetypes designed and evaluated for S_{MS} = 1.5g (i.e., high-seismic design level) are reported in Table 6-6.

Table 6-6 Summary of Key Properties and Collapse Results of Archetype Models of Previous Study of Steel SCBF Buildings Designed for High-Seismic Loads

Archetype ID	Model Properties					Collapse Results			
	No. of Stories	T (sec)	T_1 (sec)	Strength		Drift Ratio*		CMR	P[COL | MCE_R] (%)
				Ω	V_{max}/W	Roof	First Story		
NIST GCR 10-917-8: High-Seismic (S_{MS} = 1.5g) Archetype Models									
2SCBFDmax	2	0.26	0.40	1.44	0.24	-	≤ 0.10	1.00	35
3SCBFDmax	3	0.49	0.58	1.41	0.23	-	≤ 0.10	1.60	8.6
PG-1SCB	*All*	*0.38*	*0.49*	*1.43*	*0.24*	-	*≤ 0.10*	*1.30*	*17*

* Drift ratios at incipient collapse are not provided in the NIST GCR 10-917-8 report. In that report, the study of steel SCBF building archetypes assumed a story drift ratio of 0.10 for modeling non-simulated collapse failure modes.

Similar information in Table 6-1 through Table 6-5 of this chapter are reported in Table 6-6, noting the following differences:

- The design period, T, (as well as the model period, T_1) is reported (for comparison with collapse probabilities plotted in Figure 1-1 of this report).
- Drift ratios at incipient collapse are not provided in the NIST GCR 10-917-8 report. In that report, the study of steel SCBF building archetypes assumed a story drift ratio of 0.10 for modeling non-simulated collapse failure modes.
- The collapse margin ratio, *CMR*, is based on incremental dynamic analysis of 2D analytical models. 2D (planar) models of braced frames were used in all previous FEMA P-695 studies of steel SCBF building archetypes.

The collapse results plotted in Figure 1-1 of this report for the short-period steel SCBF system represents the average value of the collapse probabilities of the performance group PG-1SCB of the NIST GCR 10-917-8 study (i.e., average collapse probability of 17 percent for an average design period of T = 0.38 seconds). The individual collapse probabilities for the two-story and three-story archetype models are 35 percent and 8.6 percent, respectively, as reported in Table 6-6.

The lower probability of collapse for the three-story archetype model is likely due, at least in part, to its 0.58-second period. The two-story and three-story archetypes were designed for the same value of the seismic coefficient (i.e., C_s = 0.167g), and both archetype models have about the

same overstrength (i.e., about $\Omega = 1.4$). However, at a period of 0.58 seconds, the response level of the FEMA P-695 record set is, on average, about 80 percent of the response level at a period of 0.40 seconds, which is the model period of the two-story archetype. Hence, the FEMA P-695 record set would need to be scaled up proportionally more (i.e., 1.0/0.8 = 1.25) to determine the median collapse level of the three-story archetype model, all else equal.

The explanation for differences in collapse probabilities of the NIST study and those of this study is rooted in the differences in the strength (and possibly the collapse displacement capacity) of the archetype models, as discussed below for two-story archetypes (i.e., the only archetype height common to this study and the previous study).

6.3.2 Comparison with Two-Story Archetype Model Properties and Collapse Performance

The probability of collapse of the COM2B archetype model of this study is about 3.4 percent; whereas the collapse probability of the two-story archetype model (i.e., 2SCBFDmax) of the NIST GCR 10-917-8 study is about 35 percent. The strength of the COM2B model of this study is more than four times that of the 2SCBFDmax model (e.g., $\Omega = 5.96$ as compared to $\Omega = 1.44$). The collapse displacement capacity of the COM2B archetype model (e.g., about 5 percent at the first story) is likely less than that of the 2SCBFDmax archetype model, which could be as much as 10 percent at any story due to the liberal assumption the previous study used to model non-simulated collapse failure modes.

The significant difference in collapse performance is primarily due to the large difference in the strength of the COM2B archetype model of this study and that of the 2SCBFDmax archetype model of the previous study. The source of the strength discrepancy can be attributed to differences in the designs of the two archetypes, which derive from different objectives of each study. In the previous study, the archetypes were intentionally configured and optimized to provide the minimum seismic-force-resisting system necessary to meet the design seismic forces. This resulted in very large and perhaps unrealistic tributary areas for each braced frame. In this study, archetypes were intended to represent more typical, but possibly less optimal, building configurations. As a result, archetypes in this study exhibited significantly greater overstrength and consequently lower collapse probabilities than previous studies.

The collapse performance of the archetypes of this study might reasonably be expected when any of the following conditions, all common for short-period steel SCBF buildings, are met:

- Buildings include more braced frames than are strictly necessary for strength, in order to provide a symmetrical and redundant system.
- Braces have relatively low seismic demand, such that a small incremental change in brace size results in a large relative change in capacity.
- Braces are sized for material availability, economy, or constructability rather than structural strength optimization.
- Braces have relatively low seismic demand and have compression and tension capacities that are significantly different.

6.3.3 Recommendations for Improved Seismic Design Codes and Standards

This section describes topics and provides recommendations considered particularly relevant to seismic-code-development committees, including the Provisions Update Committee of the Building Seismic Safety Council, the ASCE/SEI 7 Seismic Subcommittee, the ASCE/SEI 41 Standards Committee, the AISC Committee for Specifications (Task Committee 9) responsible for development of ANSI/AISC 341, and other steel standards committees. Seismic-code committees have limited resources and recommended studies would, in most cases, require a funded project to develop the requisite technical basis of any proposals to improve existing codes or standards.

Very High-Seismic Collapse Potential. The collapse probabilities of two-story and four-story baseline archetypes of this study designed and evaluated for very high-seismic loads (i.e., 1.5 × high seismic, SDC D_{max}, criteria of FEMA P-695) exceed the 10 percent collapse-safety objective of ASCE/SEI 7 for Risk Category II structures, often by a substantial amount (Figure 6-1). Collapse performance is, in all cases, substantially worse for an archetype designed and evaluated for very high-seismic criteria than the same archetype designed and evaluated for high-seismic criteria (Table 6-1). This trend is largely caused by the lower overstrength of very high-seismic archetypes, which had braces with more efficient designs than those of high-seismic archetypes, due to the limited availability of brace sizes. An increase in the probability of collapse given MCE_R ground motions also was observed in a study documented in FEMA P-695 for reinforced concrete moment frame archetypes. There is a consistent trend of collapse probabilities

exceeding the 10 percent collapse-safety objective of ASCE/SEI 7 in regions of very high seismicity, which is not unique to short-period steel SCBF buildings.

A study is recommended to quantify the potential increase in the conditional probability of collapse given MCE_R ground motions (i.e., above the 10 percent target of ASCE/SEI 7 for Risk Category II structures) and the associated increase in annual probability of collapse of building archetypes of common seismic-force-resisting systems at sites located in regions of very high seismicity (i.e., $S_{MS} \geq 1.5g$).

Design for Rocking Response of Braced Frames on a Flexible Foundation. The parametric study of SSI and foundation flexibility found collapse performance of steel SCBF building archetypes to be governed by large lateral displacements due to rocking of braced frames on flexible foundations (i.e., where rocking occurs before braced frames reach their strength capacities). Observed rocking response behavior was not found to adversely affect collapse performance for the limited number of steel SCBF archetypes investigated by this study but represents an entirely different collapse failure mode from that due to brace failure—the failure mode assumed by seismic design codes and standards that specify seismic demand loads and assumed by design requirements for steel SCBF buildings.

Further study is recommended to first determine if there is a collapse-safety issue due to rocking (i.e., identify steel SCBF configurations, if any, for which collapse performance could be made worse due to rocking) and if so, develop appropriate code changes to remedy the potential collapse-safety deficiency. Second, it is recommended that additional study investigate and determine feasible code changes that would explicitly incorporate rocking response in the design of steel SCBF buildings. New design methods for rocking response would likely need to apply to all seismic-force-resisting systems, not just steel SCBFs.

Deformation Compatibility of Components Not Part of the Seismic-Force-Resisting System. The nonlinear models of steel SCBF building archetypes of this study have large drift displacement capacities (e.g., median first-story drift ratios as large as 10 percent at incipient collapse) that are significantly larger than those currently used for ASCE/SEI 7 to check deformation compatibility of components not part of the seismic-force-resisting system. This is of possible concern because the collapse probabilities determined in this study assume that the gravity system can support gravity loads out to the drift at incipient collapse.

A study is recommended to determine whether current ASCE/SEI 7 provisions for deformation compatibility checks are adequate given the new drift information available from this study.

FEMA P-695 Seismic Criteria Update. The seismic criteria of FEMA P-695 are based on the "Zone 4" seismic criteria of the 1994 version of the *Uniform Building Code* (ICBO, 1994), as embodied in the deterministic-lower-limit seismic criteria of Section 21.2.2 of ASCE/SEI 7-05 (ASCE, 2005). The seismic criteria of FEMA P-695 are out-of-date with respect to the current seismic criteria of ASCE/SEI 7-16 (ASCE, 2016) and the forthcoming ASCE/SEI 7-22, as proposed. At short periods (i.e., the acceleration domain), the seismic criteria of FEMA P-695 are either the same as the deterministic lower limit of ASCE/SEI 7-16 or only about 10 percent less than those proposed for ASCE/SEI 7-22. In the velocity domain (i.e., periods greater than 1.0 second for Site Class D site conditions), the seismic criteria of FEMA P-695 are only about 60 percent of those of ASCE/SEI 7-16 (and somewhat less for ASCE/SEI 7-22, as proposed). Updating the seismic criteria of FEMA P-695 would not significantly affect the collapse evaluation of short-period building archetypes (and the findings of this study of steel SCBF buildings) but could be of importance to the collapse evaluation of taller building archetypes with longer periods.

As per the original "Zone 4" approach of FEMA P-695, all of the ground motions represent "far-field" sites and purposely ignore higher levels of ground shaking typical of sites closer to the fault(s) governing site seismic hazard. Accordingly, FEMA P-695 implicitly permits MCE_R collapse probabilities greater than 10 percent for structures at sites where ground motions are greater than those of the "far-field" SDC D_{max} seismic criteria; whereas, the 10 percent collapse objective of Section 1.3.1.3 (Performance-Based Procedures) and Section 12.2.1.1 (Alternate Structural Systems) of ASCE/SEI 7-16 applies to all sites, regardless of their proximity to fault rupture, noting that the commentary to Section 12.2.1.1 identifies FEMA P-695 as the preferred methodology for verifying compliance with the 10 percent collapse objective. As shown by comparison of the collapse performance of high-seismic and very high-seismic baseline archetype models of this study, very different conclusions could be reached if the MCE_R ground motions greater than those of the "far-field" SDC D_{max} of FEMA P-695 were required for collapse evaluation. The fundamental question is simply: does the 10 percent collapse safety of ASCE/SEI 7-16 apply to buildings at all possible sites or only to those sites that are not "near-source"?

A study is recommended to determine what if any updates to FEMA P-695 should be made to: (1) incorporate current ASCE/SEI 7-16 and forthcoming

ASCE/SEI 7-22 ground-motion criteria; and (2) address the apparent discrepancy between the acceptance criteria of FEMA P-695 and those of Section 12.2.1.1 of ASCE/SEI 7-16.

Redundancy Factor. The parametric study of redundancy (albeit of only one steel SCBF building archetype configuration) found that the redundancy design requirements of Section 12.3.4 of ASCE/SEI 7-10, and by extension ASCE/SEI 7-16, do not affect comparable collapse performance of a "non-redundant" steel SCBF building designed for seismic loads factored by the redundancy factor, $\rho = 1.3$. Contrary to the intent of the design requirements, the strength of the "non-redundant" steel SCBF archetype was less than that of the "redundant" steel SCBF archetype, which adversely affected collapse performance.

Further study is recommended to determine if there is a collapse-safety issue for steel SCBF buildings due to potential shortcomings of current redundancy requirements and, if so, to develop appropriate code changes to remedy the potential collapse-safety deficiency.

Effect of Overstrength. The observed overstrength of the steel SCBFs in this study exceed the ASCE/SEI 7 overstrength factor of two for the system. ANSI/AISC 341 requires capacity design of the brace connections, beams, and columns for the specified brace sizes and expected strengths, helping to mitigate the impact of braces that are considerably stronger than the design seismic loads. However, the diaphragms and collectors are required to be designed for the design seismic loads increased by the ASCE/SEI 7 overstrength factor. This could result in unanticipated diaphragm and collector damage.

6.3.4 Recommendations for Advanced Seismic Design and Analysis Practices

This section describes topics and provides recommendations considered particularly relevant to engineering practitioners, especially those who are interested in performance-based design of new steel SCBF buildings or seismic retrofit of existing steel SCBF buildings. The performance-based-design recommendations may not be practical for implementation by most practitioners and would likely require funded projects to fully develop the requisite methods.

Performance-Based Design Based on Pushover Strength. The archetype models, methods, and results of this study that better represent observed collapse performance may be of interest to practitioners for performance-based design of steel SCBF buildings. The collapse analyses of steel SCBF

building archetypes show a strong correlation between collapse performance and the strength of the archetype model, as determined by nonlinear (static) pushover analysis.

Additional study would be required to develop a complete performance-based design methodology for new buildings, or to augment the current performance-based methods of ASCE/SEI 41 for seismic retrofit of existing buildings.

Performance-Based-Design Criteria. The collapse results of baseline archetype models show strong trends of the combined influence of strength and displacement capacity on collapse performance. Such trends could be used to establish performance-based design criteria for steel SCBF buildings.

Additional study would be required to develop the relationship between the strength, displacement capacity, and collapse performance of steel SCBF buildings considering differences in collapse failure modes (e.g., collapse due to rocking rather than brace failure) and differences in brace configurations of bracing (e.g., super-X bracing, chevron bracing).

Damage and Loss Estimation. The archetype models, methods, and results of this study that better represent observed collapse performance of steel SCBFs may be of interest to practitioners developing estimates of earthquake damage and loss using, for example, the FEMA P-58 technology (FEMA, 2018) or other methods, such as those of the insurance industry. The probability of collapse is an important element of building damage and loss estimation, and the improved models and methods of this study would provide a more reliable characterization of the earthquake collapse risk of steel SCBF buildings.

Best-Practice Design Recommendations. The results of this study show that MCE_R collapse performance can be significantly influenced (and improved) by the following design considerations.

- Drift Capacity of the Gravity System Connections. Beam-column connections of the gravity system should have special detailing to avoid premature failure during large lateral displacements of steel SCBF buildings (i.e., story drift ratios of up to 8 percent). Such detailing should include a minimum gap between the beam flange and column to avoid prying action on these connections.
- Foundation Design for Rocking of Braced Frames. Where braced frames can rock (i.e., foundation uplift can occur before braces yield), the foundation may require special design and detailing to accommodate rocking response of the braced frames above.

- Steel Superstructure Design for Rocking Braced Frames. Where braced frames can rock (i.e. foundation uplift can occur before braces yield), gravity system connections, collectors, and collector connections adjacent to rocking frames must be able to accommodate associated large deformations and rotations.
- Design of Chevron Allowing Yielding Beams. In this study, chevron-type braced frames exhibited detrimental performance associated with a concentration of drift in the first story rather than throughout the height of the braced frame. There is currently a proposal to AISC Task Committee 9 for the next ANSI/AISC 341 provisions that would allow beams in chevron frames to be designed for a smaller vertical unbalanced force. This results in some beam yielding but also improves distribution of drift vertically up the braced frame.
- Diaphragm and Collector Design. Because several factors common to short-period buildings can result in significant overstrength in the braced frames, associated diaphragms and collectors may need to be designed considering the actual overstrength of the vertical elements of the SCBF system.

Best-Practice Analysis Recommendations. The results of this study show that where nonlinear models are used to evaluate the collapse potential of steel SCBF buildings, to reliably calculate the behavior of the structures and the probability of collapse, they should:

- include foundation flexibility and the behavior of the soil through the use of nonlinear soil springs and dampers as required to permit foundation movement and deformation, including uplift and rocking of braced frames above,
- incorporate realistic collapse displacement capacity of the seismic-force-resisting system,
- explicitly model P-delta effects,
- explicitly model brace-connection behavior, including the nonlinear rotation response of gusset-plate connections, and beam-to-column connections within the braced frames, and
- use the end-to-end length of the braces when modeling their nonlinear buckling behavior.

6.3.5 Recommendations for Enhanced Modeling and Testing

This section describes topics and provides recommendations considered particularly relevant to engineers and academics interested in research of steel SCBF buildings. In this context, the recommendations apply to sophisticated modeling of steel SCBF buildings, and testing recommendations apply to monotonic- and cyclic-load and static and dynamic testing of braced-frame assemblies.

Cyclic-Load Testing Protocol. There are a number of available cyclic-load testing protocols that have been used to develop hysteretic backbone characterizations of structural and nonstructural elements of buildings, including the CUREE Publication No. W-02, *Development of a Testing Protocol for Woodframe Structures* (CUREE, 2001), FEMA 461, *Interim Testing Protocols for Determining the Seismic Performance Characteristics of Structural and Nonstructural Components* (FEMA, 2007), and the ANSI/AISC 341 protocols, which are not necessarily appropriate for measuring nonlinear behavior at very large displacements.

Experimental data of steel component and system behavior through collapse are critical for calibration of numerical models, such as those described in this study. Such test data are rare. Test protocols that quantify necessary component- and system-deformation demands through collapse are needed such that experiments can be systematically conducted through the large deformations necessary for collapse simulations. This protocol would also address the need for tests to include quantification of the residual capacities of components after significant deterioration.

Testing of New Brace Materials. The numerical simulations in this work considered ASTM A500 square HSS steel braces. However, new brace materials, including ASTM A1085, are being introduced and could significantly change brace and system behavior. Test data are necessary to examine these differences and understand their potential impacts on collapse performance.

Testing of Column-Base Connections. Column-base connections were found to play a role in the collapse performance of steel SCBFs. There is little experimental data on the performance of typical column-base connections where a brace gusset plate is present under combined flexural- and axial-force demands. Testing programs consisting of realistic connection configurations and loadings should be undertaken.

Testing of Diaphragms, Collectors, and Connections. Overstrength was shown to be large in short-period steel SCBFs. While limited testing on diaphragms and collectors for steel framing exists, that testing does not include demands corresponding to the larger overstrength observed here. Additionally, experimental data investigating the complex interaction between composite floors, shear studs, and collector connections are also lacking.

Shake-Table Testing of Rocking Response (to Collapse). Shake-table testing of full-scale steel SCBF test buildings or braced-frame test assemblies with flexible foundations that permit uplift and realistically capture rocking response would provide valuable insight into the seismic response and collapse performance of steel SCBF buildings.

Further Development of Numerical Component and System Models. All of the testing needs identified above would generate data and an improved physics-based understanding of component and system behavior that would promote the development of new nonlinear models. Such component and system models could be integrated within 3D system models to further the understanding and predication of the seismic performance of steel SCBFs through collapse.

Post-Earthquake Investigation of Foundation Uplift. Following future earthquakes, reconnaissance teams should prioritize investigation of foundation uplift in braced-frame buildings and structures with similarly stiff-and-strong seismic-force-resisting systems. Given the results of this study, it is expected that uplift would occur when SCBFs on strip footings are subjected to even design-level earthquake shaking. Field data to document this phenomenon would be valuable.

Appendix A
Archetype Design Criteria and Details

A.1 Introduction

Appendix A documents the material design criteria and the design details for each of the archetypes. Section A.2 documents the material and design criteria for all the archetypes, and Section A.3 shows the designs for each archetype, including plans, details, and tabulated member properties.

A.2 Design Criteria

A.2.1 Codes

Designs for the steel SCBF archetypes were based on design requirements of ANSI/AISC 360-10 and ANSI/AISC 341-10.

Design loads were based on design requirements of the 2015 IBC and, by reference, ASCE/SEI 7-10.

A.2.2 Materials

Material properties are summarized in Table A-1.

Table A-1 Summary of Material Properties used for Design of Steel SCBF Archetypes

Material	Properties
Wide-Flange Columns and Beams	F_y = 50 ksi, F_u = 65 ksi, ASTM A992
HSS Braces	F_y = 50 ksi, F_u = 62 ksi, ASTM A500 Gr. C
Gusset Plates	F_y = 36 ksi, F_u = 58 ksi, ASTM A36
Base Plates	F_y = 50 ksi, F_u = 65 ksi, ASTM A572
Anchor Rods	F_y = 55 ksi, F_u = 75 ksi, ASTM F1554 F_y = 105 ksi F_u = 125 ksi, ASTM F1554
Weld Electrodes	70 ksi – E70XX
High-Strength Bolts	ASTM F3125 Gr. F1852
Steel Reinforcing	F_y = 60 ksi, ASTM A615
Concrete	f'_c = 4.0 ksi, ASTM C150

A.2.3 Site-Specific Design Criteria

Soil properties were assumed to represent typical West Coast sites as described in Appendix B. Assumed site-specific properties of soils are summarized in Table A-2. For the SSI and foundation flexibility study only, a soft-soil profile was assumed, with a lower bearing pressure. Both stiff- and soft-soil sites were characterized as Site Class D.

Table A-2 Site-Specific Design Criteria used for Design of Steel SCBF Archetypes

Material	Properties
Assumed Site Class	D
Allowable Soil Bearing Pressure (stiff soil)	3000 psf
Allowable Soil Bearing Pressure (soft soil)	1500 psf
Modulus of subgrade reaction (stiff soil)	129 kip / cu ft
Modulus of subgrade reaction (soft soil)	60 kip / cu ft
Minimum Footing Depth	12 in

A.2.4 Gravity Loads

Archetype designs were developed for dead and live loads typical in commercial office buildings. A floor live load of 50 psf plus 15 psf for partitions was used. A dead load of 81 psf and 25 psf, inclusive of the self-weight of the structure, was used at the floor and roof, respectively. The superimposed dead loads included typical allowances for finishes, including mechanical, electrical, plumbing, ceilings, lights, flooring, roofing, and sprinklers. A partition weight of 15 psf was included in the seismic mass calculation per ASCE/SEI 7-10 Section 12.7.2. The dead load of the exterior walls was 10 psf. A 30-foot × 30-foot bay on the roof included 150 psf dead load for mechanical equipment. The seismic weight indicated in Table A-4 was calculated using the above dead loads from the floors, roof, and exterior walls over the footprint of the buildings. Beams and columns were designed using LRFD-load combinations for strength design. Serviceability vibration checks were also made for the floor structures in conformance with *AISC Design Guide 11* (AISC, 2016).

Table A-3 Gravity Loads used for Design of Steel SCBF Archetypes

Building Type	Floor live load + Partition load (psf)	Floor Dead Load (psf)	Roof Dead Load (psf)	Exterior Wall Dead Load (psf)
COM	50 + 15	81	25	10

A.2.5 Building Periods of Vibration

The design period is defined as $T = C_u T_a \geq 0.25$ seconds, in accordance with the analysis requirements of FEMA P-695, where the values of the parameters C_u and T_a are specified by ASCE/SEI 7-10. Calculated periods are summarized in Table A-4

A.2.6 Seismic Design Criteria

Designs were developed for each of the building archetypes with the seismic criteria summarized in Table A-4.

Table A-4 Seismic Criteria used for Design of Steel SCBF Archetypes

Archetype ID	No. of Stories	Seismic Design Criteria			Seismic Weight (k)	Base Shear (k)
		SDC	T^* (sec)	C_s (g)		
Commercial Buildings: High Seismic						
COM1	1	D	0.25	0.167	495	83
COM2	2	D	0.34	0.167	1868	312
COM3	4	D	0.57	0.167	4646	776
Commercial Buildings: Very High Seismic						
COM4	1	E	0.25	0.25	495	124
COM5	2	E	0.34	0.25	1868	468
COM6	4	E	0.57	0.25	4646	1164

* The design period is defined as $T = C_u T_a \geq 0.25$ seconds, in accordance with the requirements of FEMA P-695, where the values of the parameters C_u and T_a are specified by ASCE/SEI 7-10. $T = C_u T_a = 0.2$ seconds for COM1B and COM4B but was taken as 0.25 seconds for design per the requirements of FEMA P-695.

Steel members within the seismic-force-resisting system were designed using LRFD-load combinations and applicable requirements of ANSI/AISC 341. Vertical seismic loading, E_v, indicated in ASCE/SEI 7 Section 12.4, was considered in design of both the steel superstructures and foundations.

A.2.7 Foundation Design at Braced Frames

As discussed in Section 3.5.1, ASCE/SEI 7 Section 12.4 load combinations were used to design the foundations for stability against overturning and allowable bearing pressures. Foundations for all baseline and variant archetypes, except COM3B-SS and COM6B, utilized a continuous footing across the brace-frame width. Foundation lengths at these locations varied from 36 feet to 45 feet. Refer to Figure A-4 through Figure A-12 for dimensions of all foundations in each parametric study. At the designs with a continuous footing across the brace-frame width only, the footing was

designed assuming rigid-body motion of the footing and was allowed to have zero tension in the soil. The equation used was:

$$Q_a = (2/3)P_a / (B \times (L - e)) \quad \text{(A-1)}$$

where:

Q_a = Bearing pressure (ksf)

P_a = Total gravity load on the brace frame, including both columns and foundation weight, at service-level using ASCE/SEI 7 Section 12.4 combinations (kips)

B = Footing width (ft)

L = Footing length (ft)

e = Load eccentricity = M_{ot} / P_a (ft)

M_{ot} = Service-level overturning moment due to ASCE/SEI 7 code-prescribed lateral loads, using Section 12.4 load combinations and Section 12.13.4 reduction in overturning moment

Archetypes COM3B-SS and COM6B both utilized continuous footings around the perimeters of the buildings. For these two archetypes, it was impractical to use the previously described method for calculating the footing dimensions because the large overturning moments would have created very long footings, where the distance between the braced-frame footings would have been minimal. For these archetypes, the footings were designed using a beam-on-elastic-foundation method with soil springs resisting the gravity and lateral overturning forces. Soil spring values used in these archetypes are indicated in Table A-2.

In practice, some engineers use the IBC Alternative Load Combinations, Section 1605.3.2, to size foundations rather than ASCE/SEI 7 Section 12.4 load combinations. The alternative load combinations can lead to smaller foundations. Had the archetype designs used the alternative load combinations, the footings could have reduced in width and length. For the purposes of this study, it was decided to *not* use the IBC alternative load combinations for consistency with the FEMA P-695 load combination recommendations.

A.3 Structural Plans

In the following section, the structural designs for each of the archetypes are documented. The floor and roof framing are identical for all archetypes and are shown only once. Nine unique foundations were designed for the baseline and variant archetypes, including the six baseline archetype

foundations, two foundations using soft soils for SSI and foundation flexibility analysis, and one foundation for the two-story no-redundancy archetype (Figure A-3 through Figure A-9). The foundations for the archetypes with stiff soils used in the SSI and foundation flexibility analysis are the same as their respective baseline foundations and are not repeated in the figures.

The steel member sizes within the braced frames, including braces, beams, column sizes, and gusset parameters, are presented in Table A-5 through Table A-31. Designs for the COM2B-NMF archetype are not listed separately because that archetype is identical in design to the COM2B archetype. As described in Chapter 3, changes were made to modeling assumptions for the purposes of that parametric study.

As discussed in Chapter 3, braces sizes were selected to produce a design demand-to-design capacity ratio (D/C) closest to 1.0, including using HSS shapes that are allowed by code but that may not be readily available or used commonly in practice, including HSS 3 1/2×3 1/2 , HSS 4 1/2×4 1/2 and HSS 5 1/2×5 1/2. Selection of the most efficient brace sizes was done to minimize the inherent overstrength associated with braced-frame systems. In this context, the term "overstrength" has two components. The first is a result of the limited selection of HSS brace sizes that meet the requirements for seismic compactness in ANSI/AISC 341-10. This selection can be further limited to those sections commonly available to fabricators, which often do not include the 1/2-inch sizes. The second component of overstrength results from the fact that pairs of braces in tension and compression are designed to the compression limit state, but ultimately fail in a combination of tensile yielding and post-buckling compression capacity, which is generally greater for slender braces. Both of these are captured in a characterization of overstrength that is defined as the summation of the horizontal component of the expected tensile capacity and post-buckled capacity of all braces in the direction under consideration in relation to the total equivalent-lateral-force (ELF) design base shear. See Table A-32 for a definition of terms and a summary of the overstrength in each archetype. This characterization of "overstrength" is not precisely the same as the overall archetype overstrength presented in Chapter 4 through Chapter 6 and quantified as the overstrength factor, Ω, consistent with the FEMA P-695 procedures.

A.3.1 Framing Plans

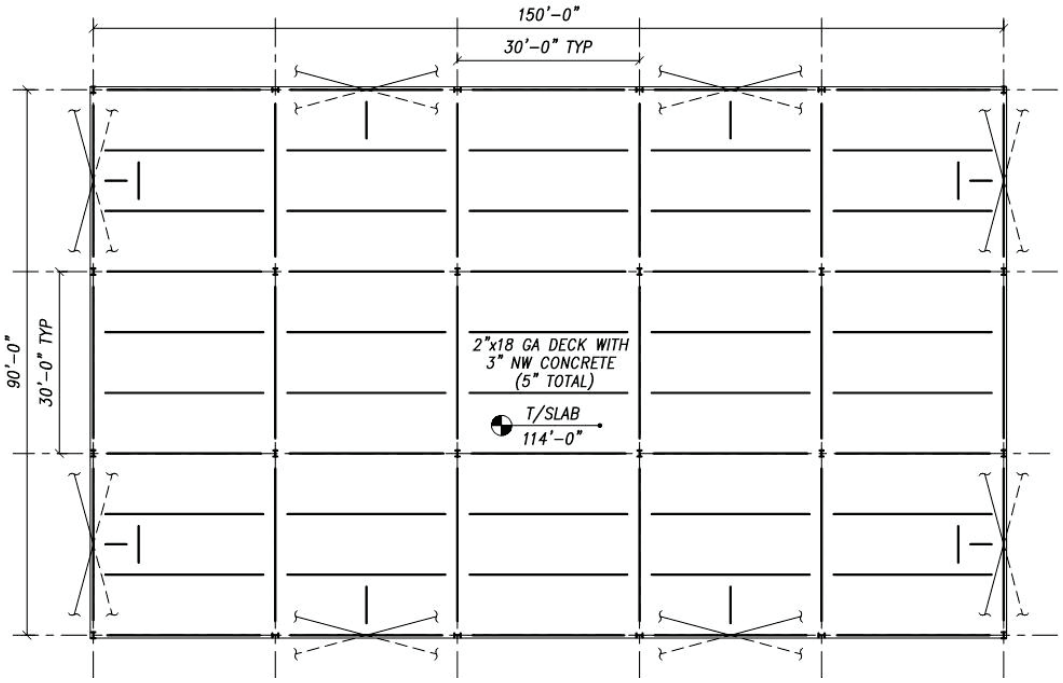

Figure A-1 Overall framing plan without member sizes.

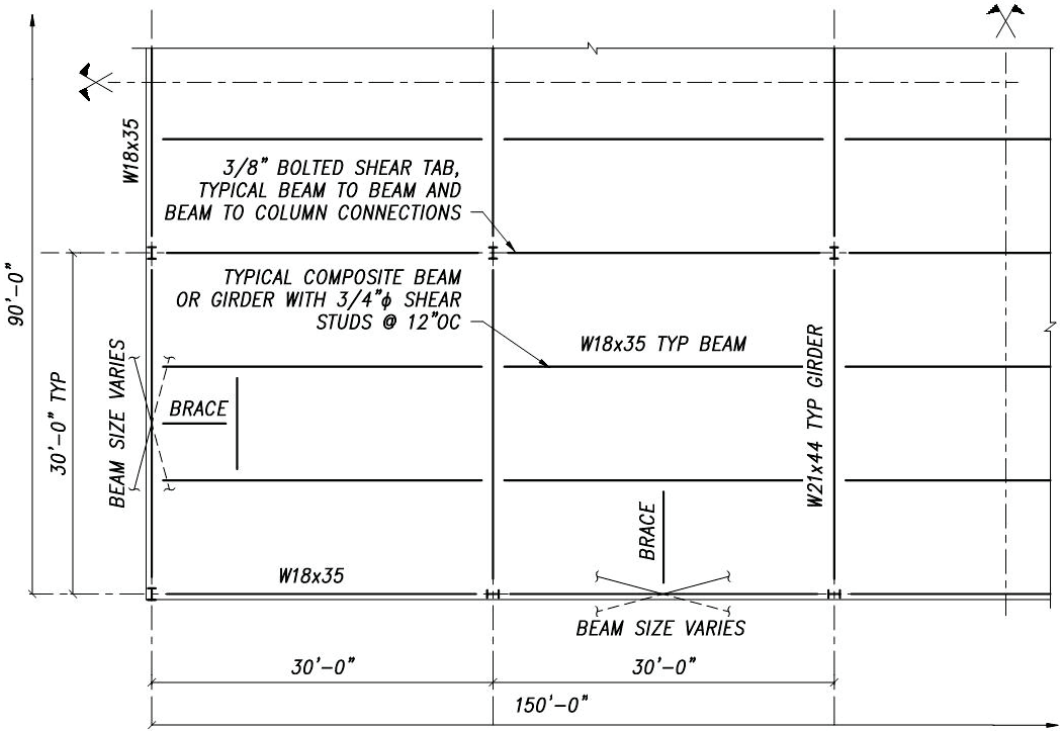

Figure A-2 Typical floor framing plan for COM2B, COM3B, COM5B, COM6B, and their variants. See Table A-5 through Table A-31 for member sizes in braced bays.

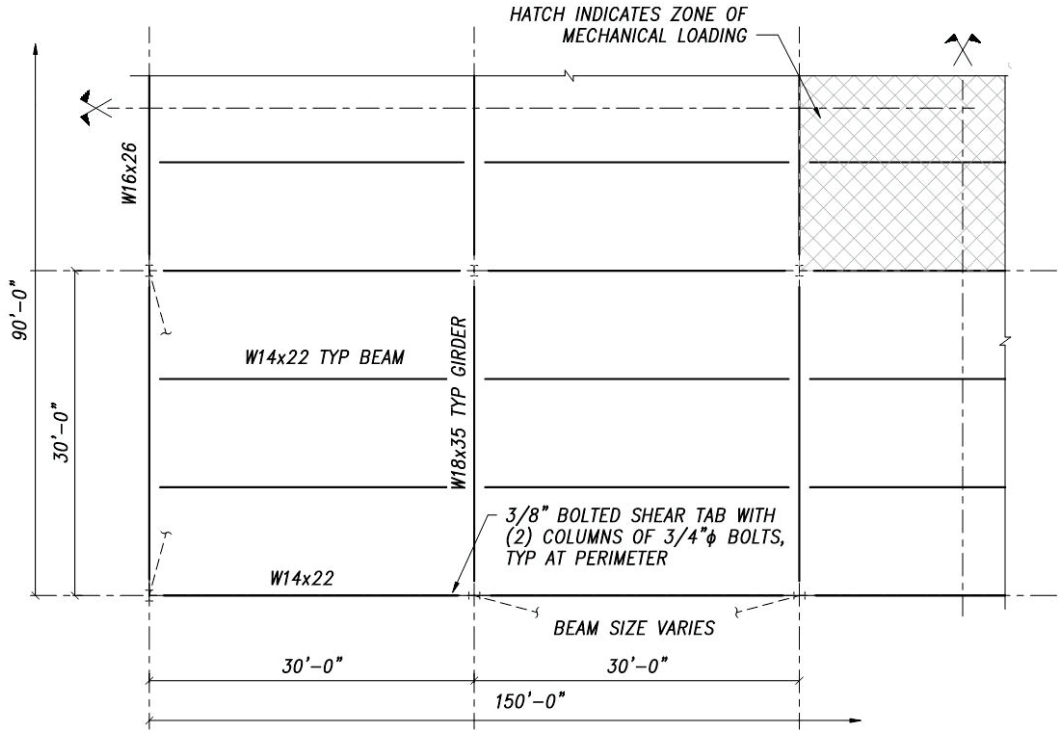

Figure A-3 Typical roof framing plans for all archetypes.

A.3.2 Foundation Plans

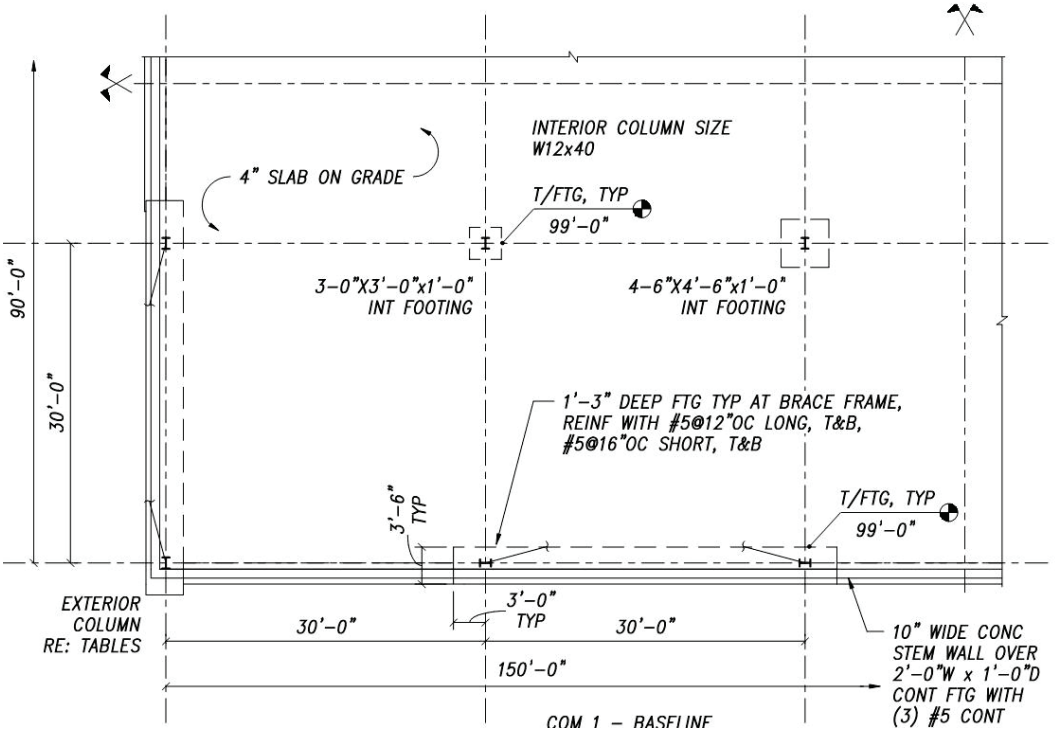

Figure A-4 Foundation plan: COM1B.

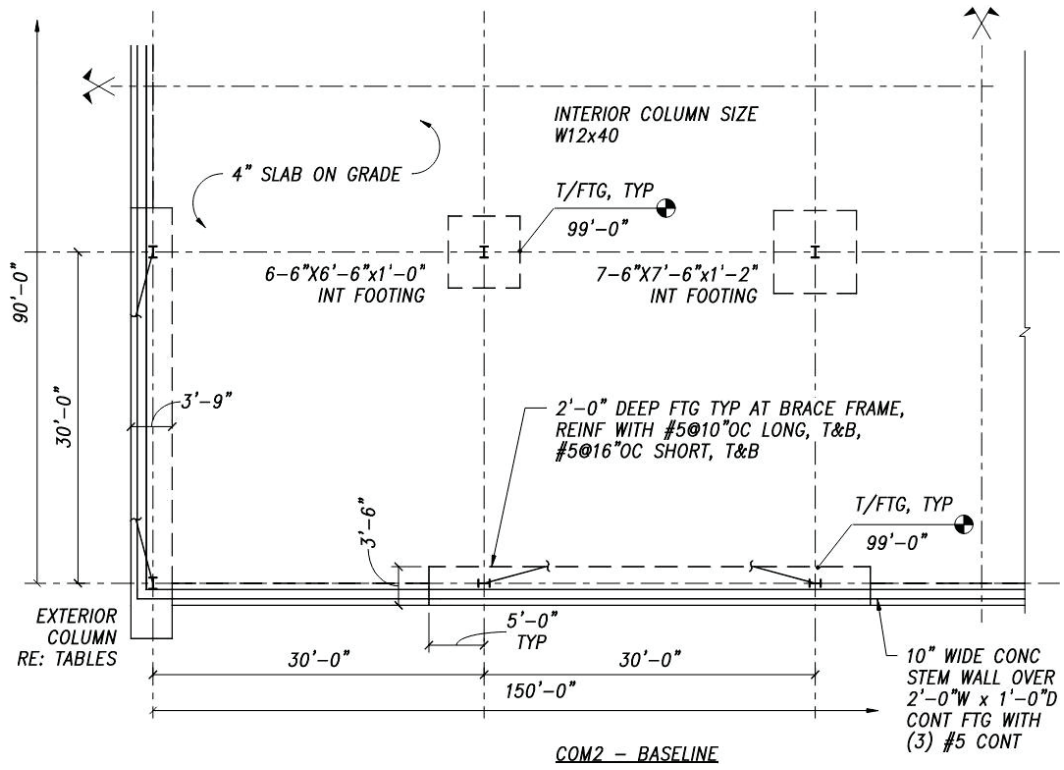

Figure A-5 Foundation plan: COM2B.

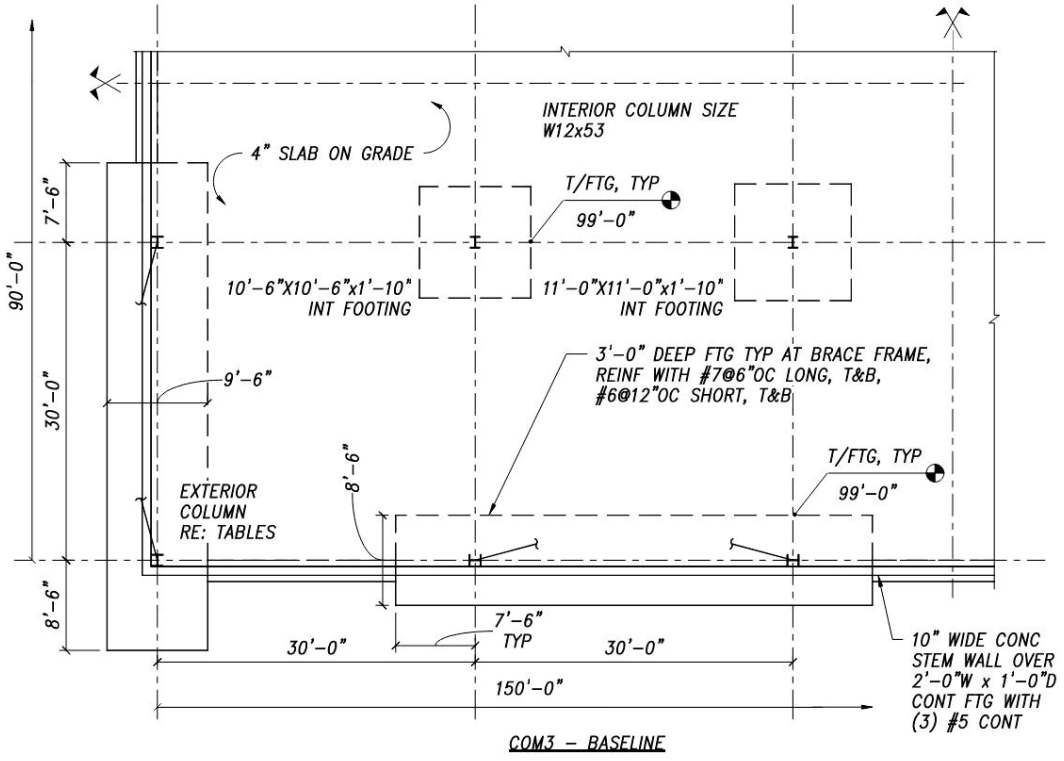

Figure A-6 Foundation plan: COM3B.

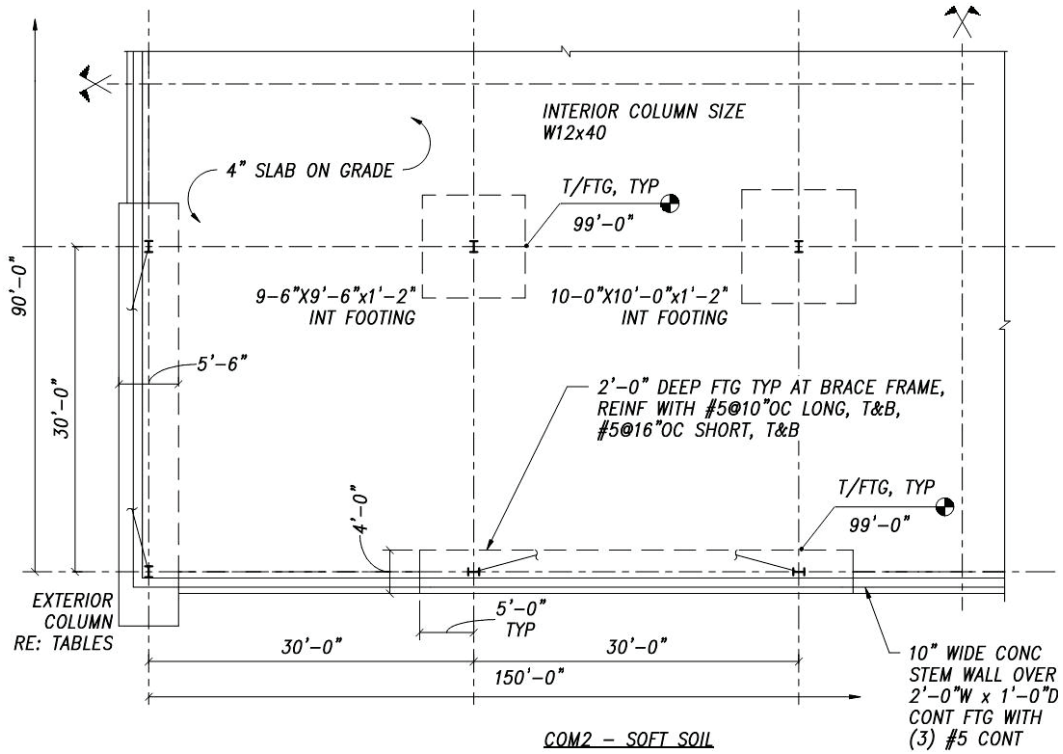

Figure A-7 Foundation plan: COM2B-SS with soft soil.

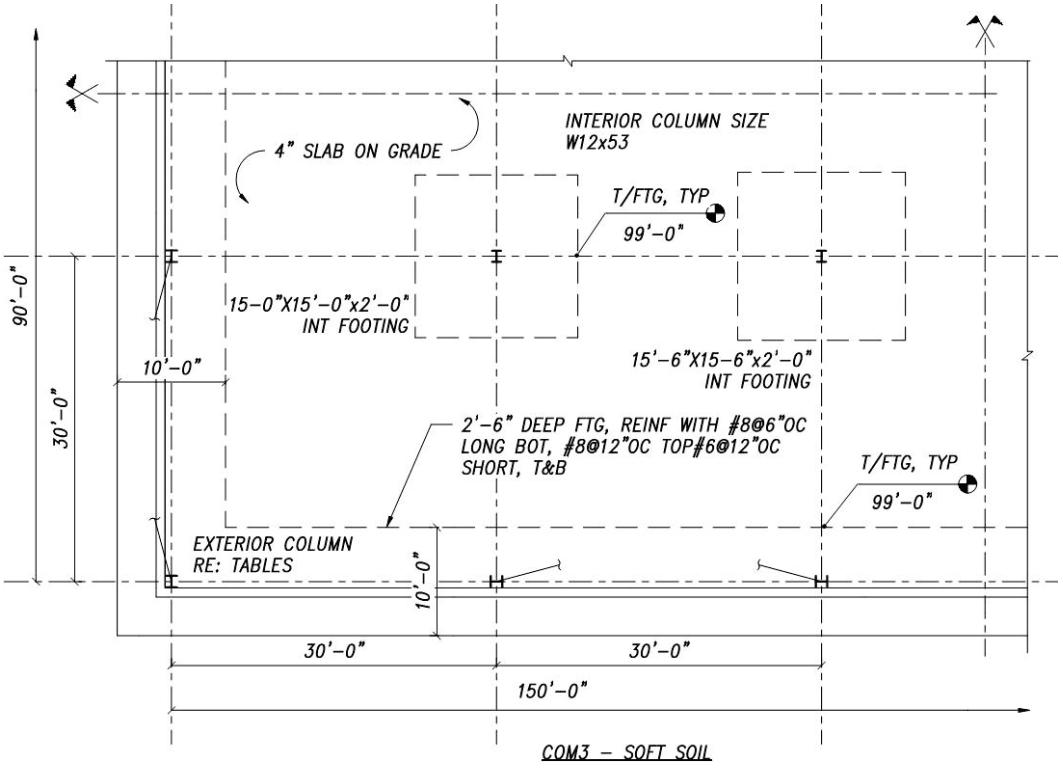

Figure A-8 Foundation plan: COM3B-SS with soft soil.

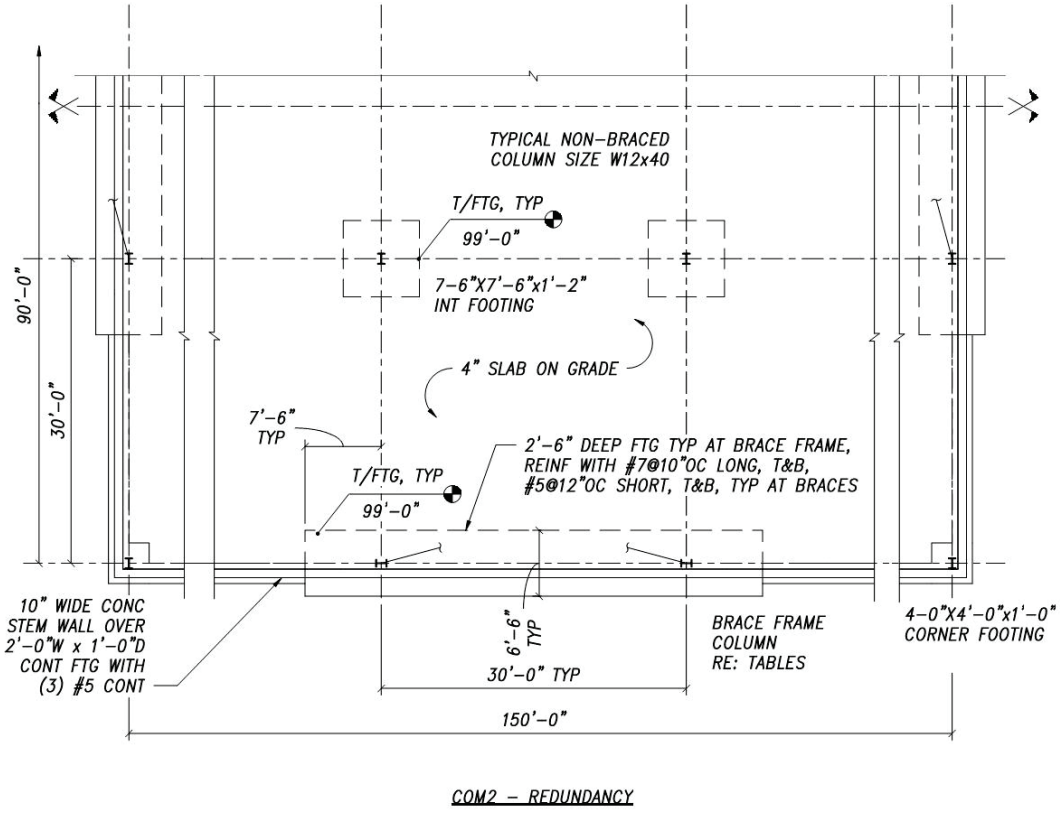

Figure A-9 Foundation plan: COM2B-NR.

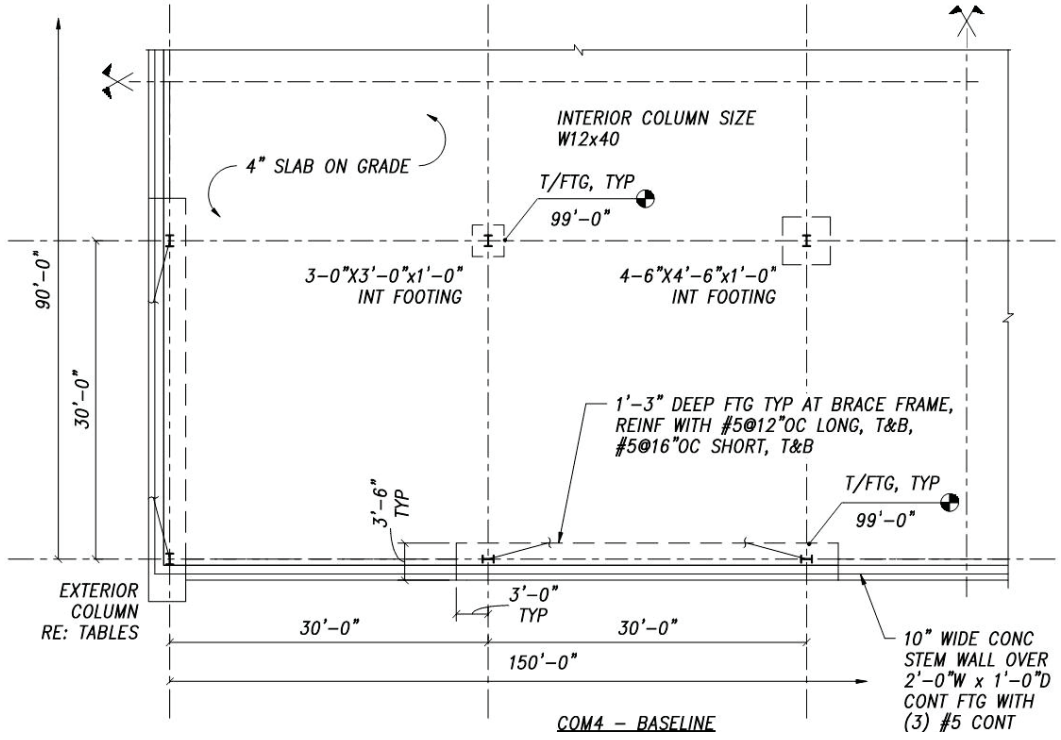

Figure A-10 Foundation plan: COM4B.

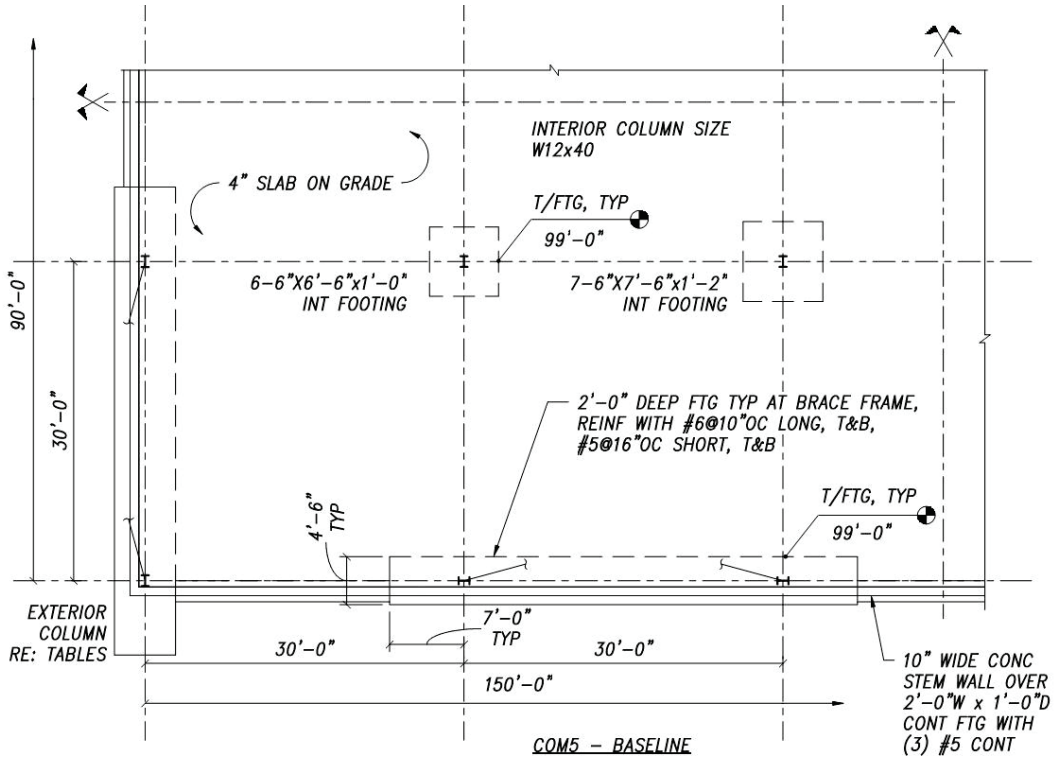

Figure A-11 Foundation plan: COM5B.

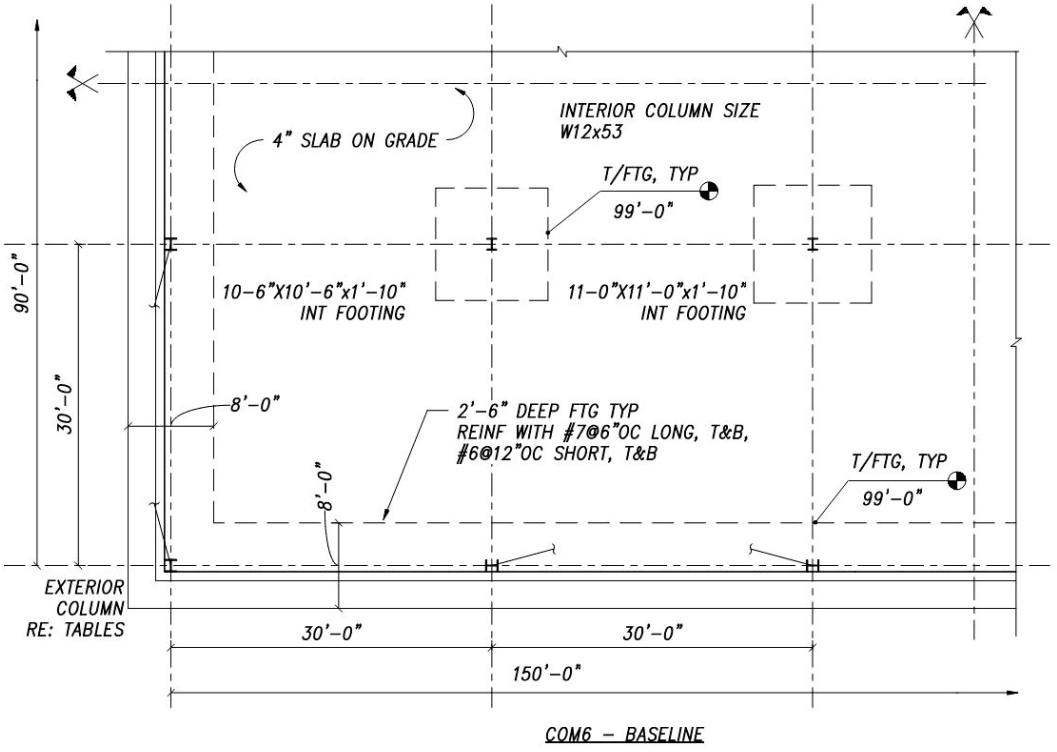

Figure A-12 Foundation plan: COM6B.

A.3.3 Braced Frame and Gusset Details

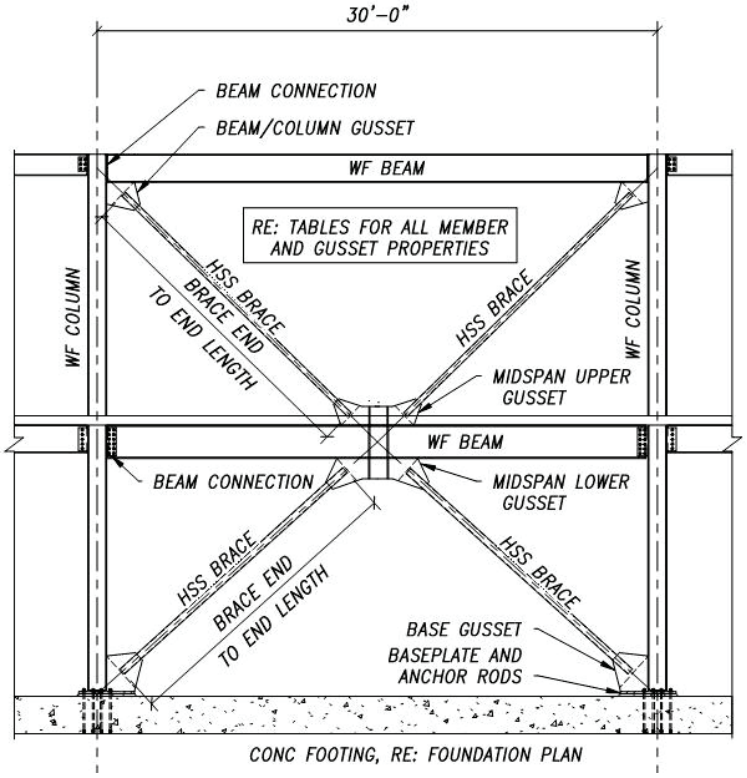

Figure A-13 Example braced frame elevation.

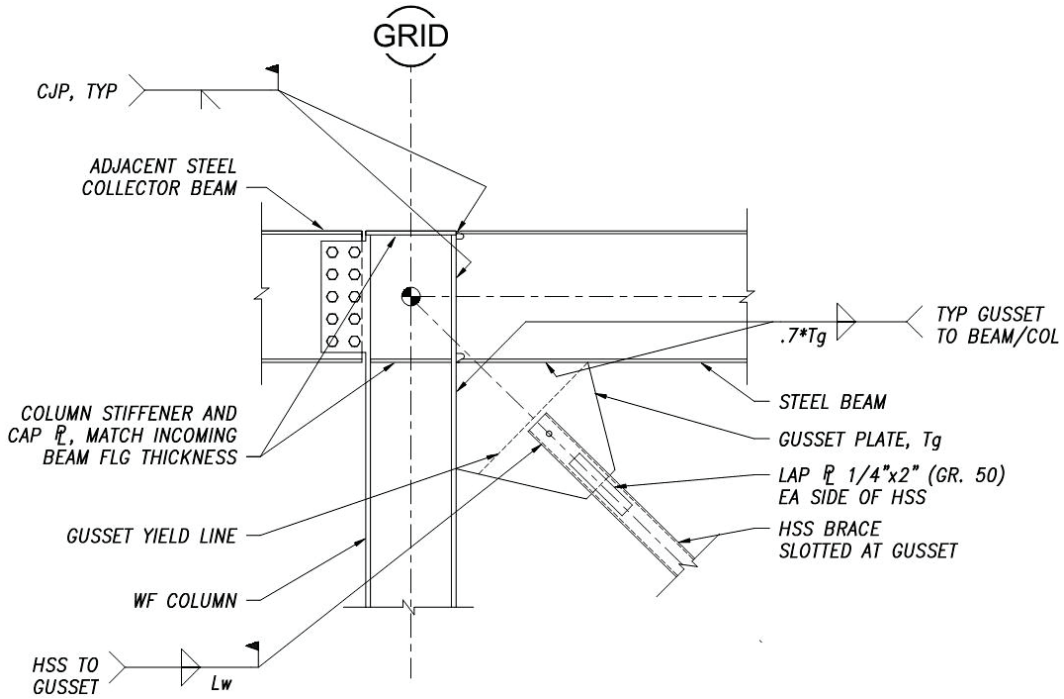

Figure A-14 Beam/column/brace gusset connection—annotated detail. This detail applies to all archetype configurations, see Figure A-15 and tabulated data in Table A-5 through Table A-31 for data pertinent to each archetype.

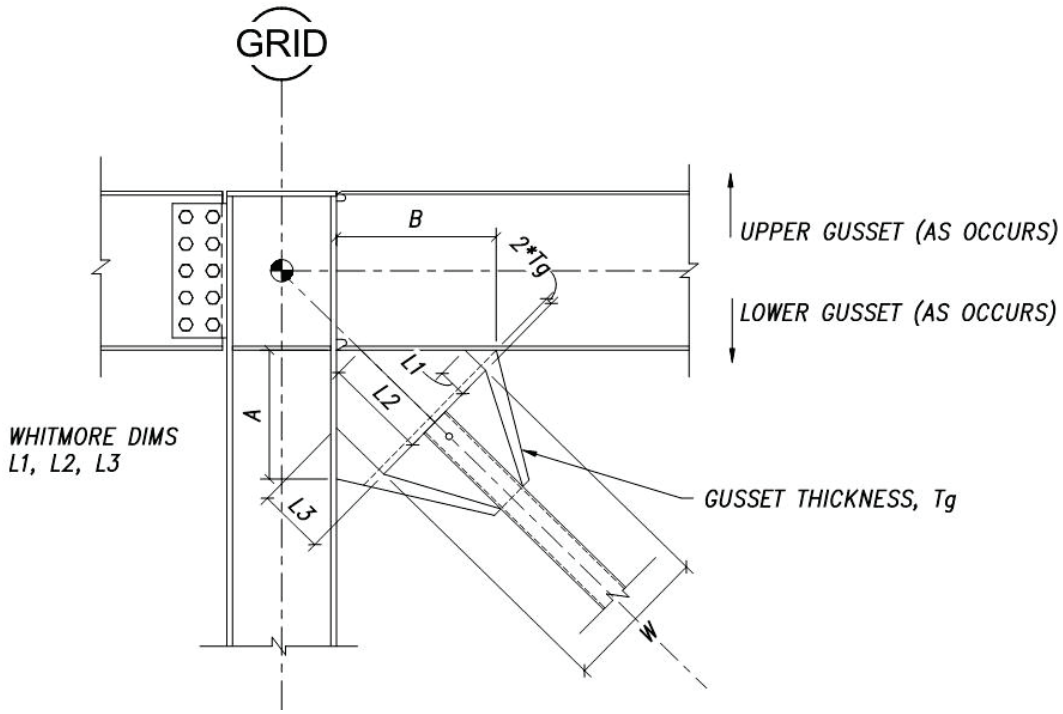

Figure A-15 Beam/column/brace gusset connection—tabulated gusset properties. See Table A-5 through Table A-31 for member sizes in braced bays.

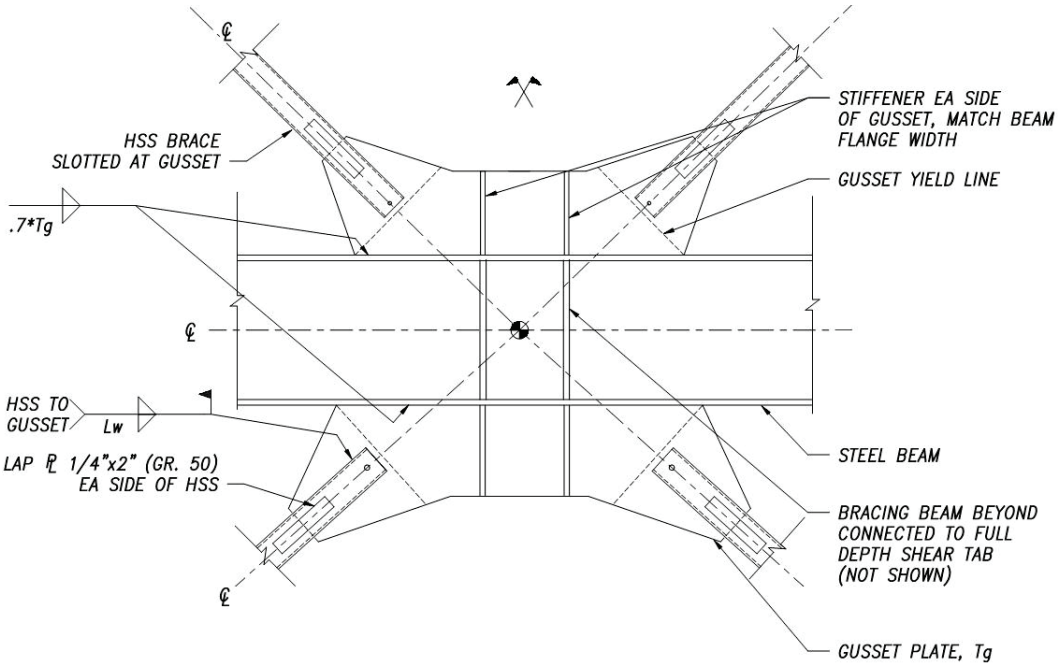

Figure A-16 Midspan gusset connection—annotated detail. This detail applies to all archetype configurations, see Figure A-17 and tabulated data in Table A-5 through Table A-31 for data pertinent to each archetype.

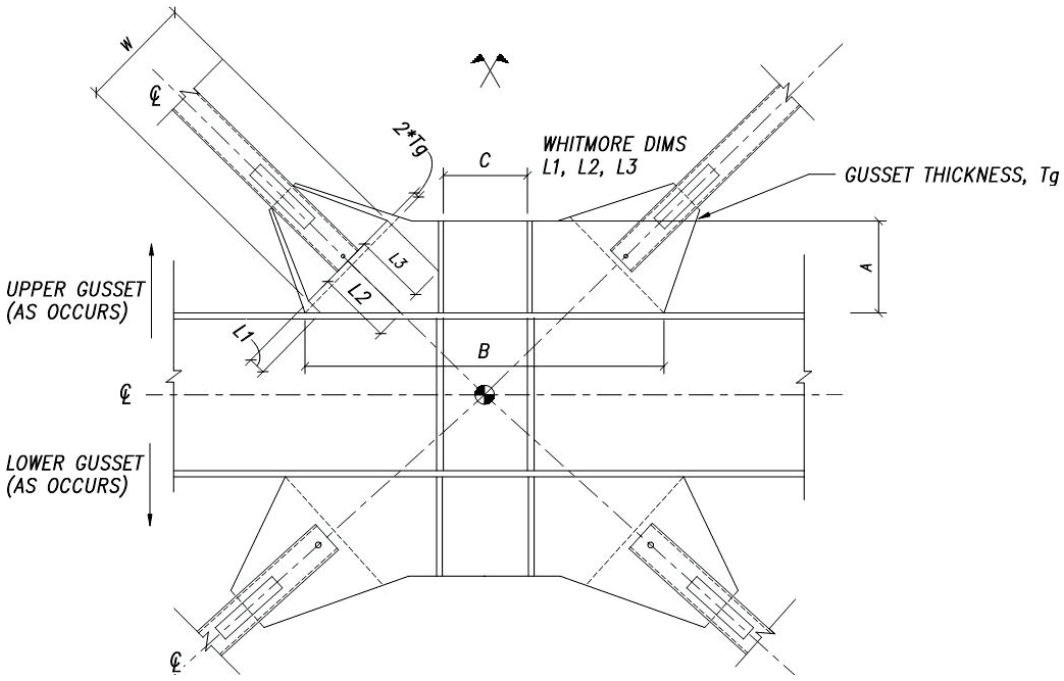

Figure A-17 Midspan gusset connection—tabulated gusset properties. See Table A-5 through Table A-31 for member sizes in braced bays.

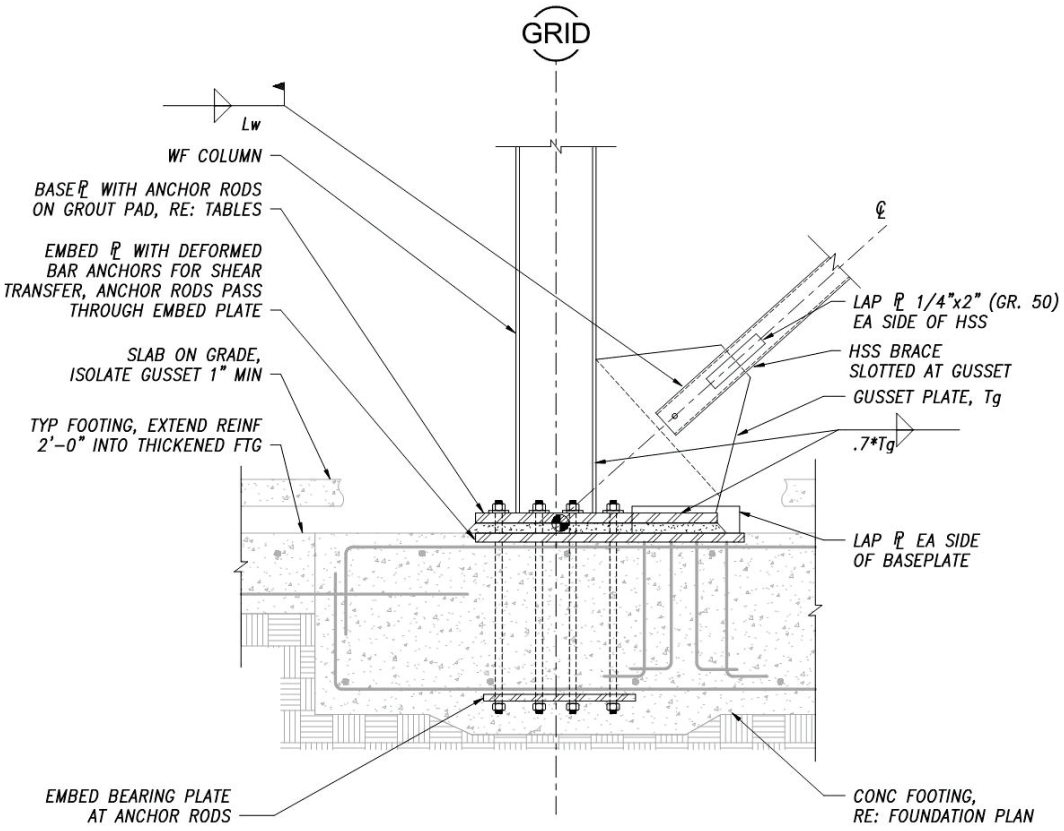

Figure A-18 Base gusset connection—annotated detail. This detail applies to all archetype configurations, see Figure A-19 and tabulated data in Table A-5 through Table A-31 for data pertinent to each archetype.

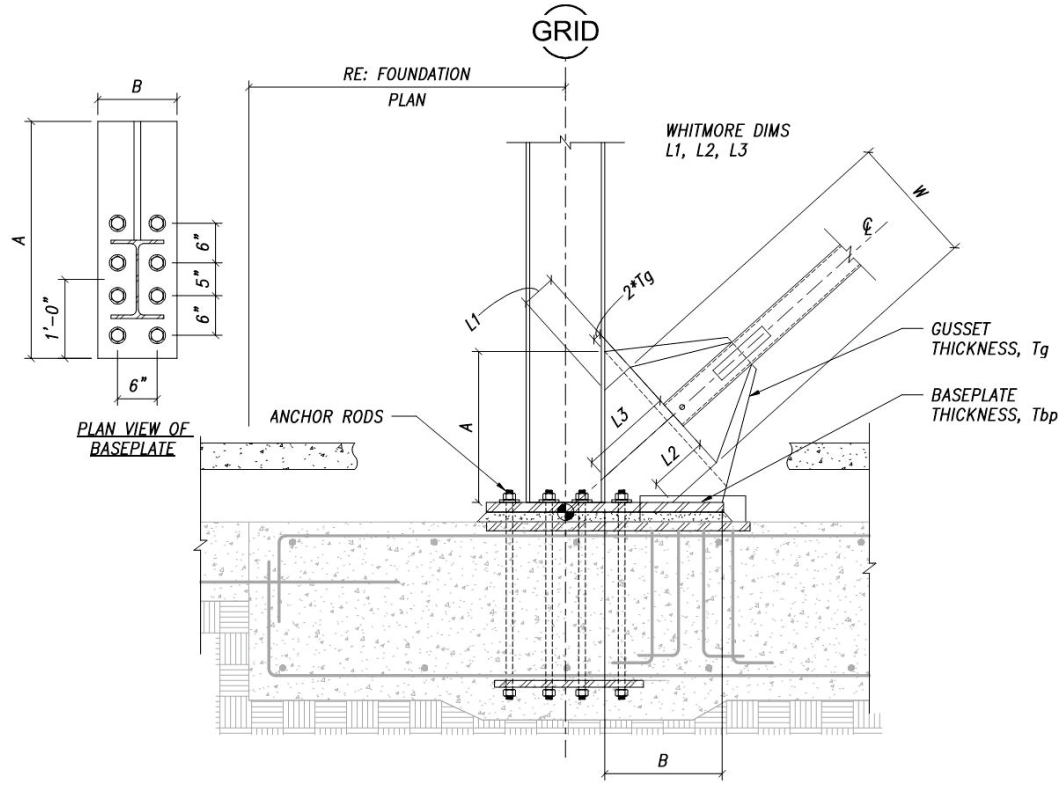

Figure A-19 Base gusset connection—tabulated gusset properties. See Table A-5 through Table A-31 for member sizes in braced bays.

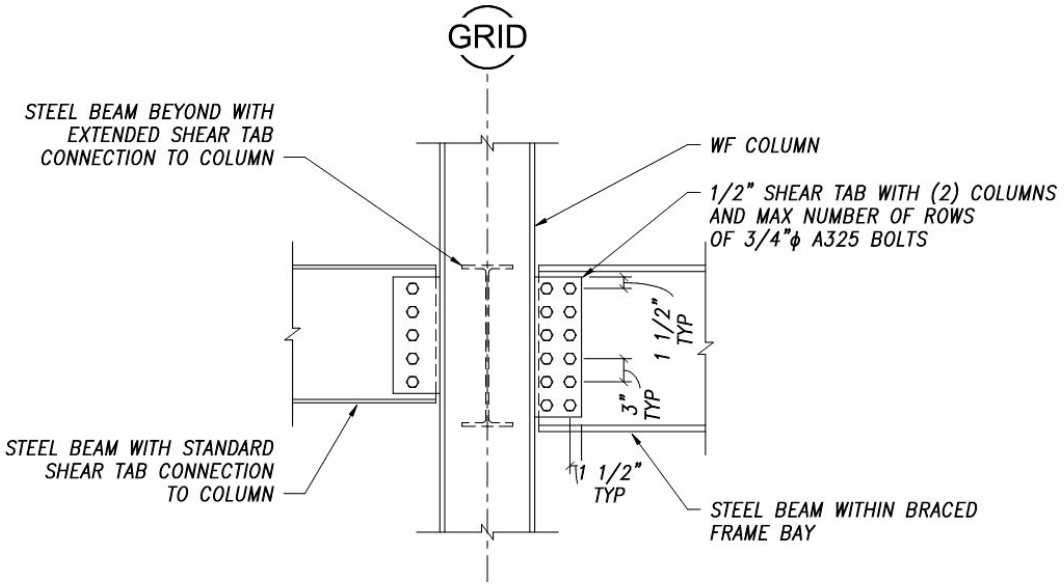

Figure A-20 Midspan beam connection at column.

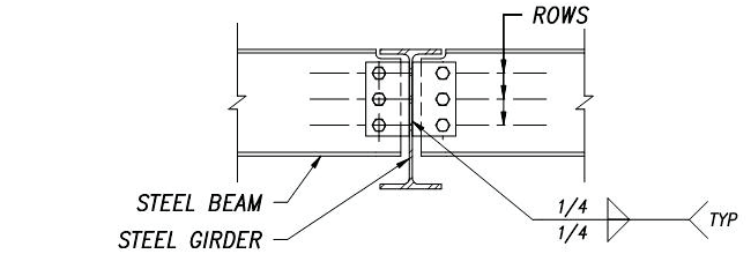

SHEAR TAB TO WF GIRDER

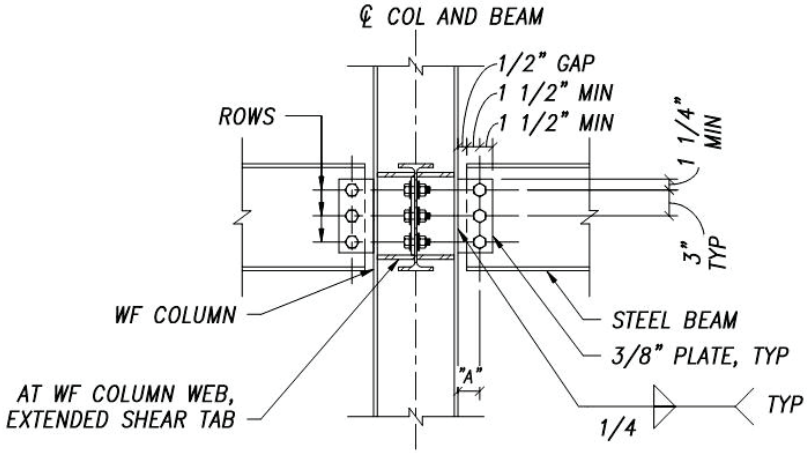

SHEAR TAB TO WF COLUMN

MEMBER DEPTH	ROWS OF BOLTS	MAX COPE DEPTH (in)	MAX COPE LENGTH (in)	CAPACITY (K) "A"<=3"		
				NO COPE	SINGLE COPE	DOUBLE COPE
W14	3	1.5	4	44	42	39
W16	4	1.5	5	63	61	50
W18	5	1.5	5	82	80	80
W21	6	1.5	5.5	89	84	84
W24	7	2	6	108	84	84

NOTES:
1. CAPACITIES ARE BASED ON AISC 360–10, LOAD AND RESISTANCE FACTORED DESIGN (LRFD).
2. HOLES IN SHEAR TAB MAY BE EITHER STANDARD OR SHORT–SLOT HOLES.
3. 3/4"ϕ A325N BOLTS E70XX ELECTRODES Fy=36 KSI TABS Fy=50 KSI BEAMS, GIRDERS, AND COLUMNS

Figure A-21 Typical shear-tab connections at gravity members.

A.3.4 Tabulated Data for Member Sizes and Gusset Properties

Table A-5 through Table A-31 provide the designs of the steel SCBF brace frames for all baseline and variant archetype designs. Tables reference member sizes and gusset parameters indicated on previous figures.

Table A-5 Member Properties Within Braced Bay: COM1B

Location	Brace Size and D/C Ratio	Brace End to End Length	Column Size	Beam Size	Beam Connection
Roof – 1st Floor	HSS 3×3×5/16 D/C = 0.99	16′-6″	W12×50	W27×94	½″ shear tab with (2) cos × (7) rows ¾″ A325 bolts

Note: D/C ratio (Demand-to-Capacity): in this context, the "demand" is the code-specified seismic load effect according to the equivalent-lateral-force procedure in ASCE/SEI 7, and the "capacity" is the governing limit state calculated in accordance with the LRFD provisions of ANSI/AISC 360.

Table A-6 Gusset Properties: COM1B

Location	*Tg* (in)	*W* (in)	*L1* (in)	*L2* (in)	*L3* (in)	*A* (in)	*B* (in)	*Lw* (in)	*C* (in)
Midspan Gusset									
Roof – LG	3/8	16.5	1.25	10	13.5	12	54	12	11
Base Gusset									
Base	1/2	15.5	1	8.25	5.75	16	13	12	NA

Note:

LG / UG = Upper Gusset or Lower Gusset
W = Whitmore Width
A = Gusset Height
Lw = Brace Lap Length
Tg = Gusset Thickness
L1, *L2*, *L3* = Whitmore Lengths
B = Gusset Width
C = Stiffener Width

Table A-7 Baseplate Properties: COM1B

Baseplate Thickness, Tbp (in)	Anchor Rods	Baseplate Length, *A* (in)	Baseplate Width, *B* (in)
1	(4) 1″ Gr. 55	31	12

Table A-8 Member Properties Within Braced Bay: COM2B

Location	Brace Size and D/C Ratio	Brace End to End Length	Column Size	Beam Size	Beam Connection
Roof – 2nd Floor	HSS 3 1/2×3 1/2×1/4 D/C = 0.74	16′-10″	W12×50	W18×46	CJP moment connection
2nd Floor – 1st Floor	HSS 4 1/2×4 1/2×3/8 D/C = 0.86	16′-0″	W12×50	W21×101	½″ shear tab with (2) cos × (6) rows ¾″ A325 bolts

Note: D/C ratio (Demand-to-Capacity): in this context, the "demand" is the code-specified seismic load effect according to the equivalent-lateral-force procedure in ASCE/SEI 7, and the "capacity" is the governing limit state calculated in accordance with the LRFD provisions of ANSI/AISC 360.

Table A-9 Gusset Properties: COM2B

Location	*Tg* (in)	*W* (in)	*L1* (in)	*L2* (in)	*L3* (in)	*A* (in)	*B* (in)	*Lw* (in)	*C* (in)
Beam / Column Gusset									
Roof – LG	3/8	16	3.5	11.5	7.5	14	17.5	11	NA
Midspan Gusset									
2nd Floor – UG	3/8	16	1.5	9.5	9.5	12	47	11	11
2nd Floor – LG	5/8	18.5	2.25	15	12.5	13	52	16	11
Base Gusset									
Base	5/8	19.5	5.25	14	9	23	19	16	NA

Note:

LG / UG = Upper Gusset or Lower Gusset
W = Whitmore Width
A = Gusset Height
Lw = Brace Lap Length
Tg = Gusset Thickness
L1, *L2*, *L3* = Whitmore Lengths
B = Gusset Width
C = Stiffener Width

Table A-10 Baseplate Properties: COM2B

Baseplate Thickness, Tbp (in)	Anchor Rods	Baseplate Length, *A* (in)	Baseplate Width, *B* (in)
1	(8) 1″ Gr. 55	37	12

Table A-11 Member Properties Within Braced Bay: COM3B

Location	Brace Size and D/C Ratio	Brace End to End Length	Column Size	Beam Size	Beam Connection
Roof – 4th Floor	HSS 3 1/2×3 1/2×5/16 D/C = 0.79	16′-11″	W12×50	W18×46	CJP moment connection
4th Floor – 3rd Floor	HSS 5×5×3/8 D/C = 0.94	16′-0″	W12×50	W21×101	½″ shear tab with (2) cos × (6) rows ¾″ A325 bolts
3rd Floor – 2nd Floor	HSS 5×5×1/2 D/C = 0.87	15′-8″	W12×96	W18×60	CJP moment connection
2nd Floor – 1st Floor	HSS 6×6×1/2 D/C = 0.71	14′-11″	W12×96	W18×76	½″ shear tab with (2) cos × (5) rows ¾″ A325 bolts

Note: D/C ratio (Demand-to-Capacity): in this context, the "demand" is the code-specified seismic load effect according to the equivalent-lateral-force procedure in ASCE/SEI 7, and the "capacity" is the governing limit state calculated in accordance with the LRFD provisions of ANSI/AISC 360.

Table A-12 Gusset Properties: COM3B

Location	*Tg* (in)	*W* (in)	*L1* (in)	*L2* (in)	*L3* (in)	*A* (in)	*B* (in)	*Lw* (in)	*C* (in)
Beam / Column Gusset									
Roof – LG	1/2	16.5	1.5	9.5	6.5	11	15	11	NA
3rd Floor – UG	5/8	22	1.75	8	13.5	15.5	20	15	NA
3rd Floor – LG	5/8	25.5	1.75	15.5	8	18	23	19	NA
Midspan Gusset									
4th Floor – UG	1/2	16	1.5	9.5	8.5	11	46	11	11
4th Floor – LG	5/8	22	1.75	13.5	8	15	53.5	15	11
2nd Floor – UG	5/8	25.5	1.75	15.5	8.5	18	59	19	11
2nd Floor – LG	3/4	33	2.25	20.5	10.5	24	71	24	11
Base Gusset									
Base	3/4	33.5	8	21.5	6	33	19	24	NA

Note:

LG / UG = Upper Gusset or Lower Gusset
W = Whitmore Width
A = Gusset Height
Lw = Brace Lap Length
Tg = Gusset Thickness
L1, *L2*, *L3* = Whitmore Lengths
B = Gusset Width
C = Stiffener Width

Table A-13 Baseplate Properties: COM3B

Baseplate Thickness, Tbp (in)	Anchor Rods	Baseplate Length, *A* (in)	Baseplate Width, *B* (in)
2 1/4	(8) 1 3/8″ Gr. 55	48	16

Table A-14 Member Properties Within Braced Bay: COM4

Location	Brace Size and D/C Ratio	Brace End to End Length	Column Size	Beam Size	Beam Connection
Roof – 1st	HSS 3 1/2× 3 1/2×5/16 D/C = 0.80	16′-4″	W12×50	W27×114	½″ Shear tab with (2) cos × (7) rows ¾″ A325 Bolts

Note: D/C ratio (Demand-to-Capacity): in this context, the "demand" is the code-specified seismic load effect according to the equivalent-lateral-force procedure in ASCE/SEI 7, and the "capacity" is the governing limit state calculated in accordance with the LRFD provisions of ANSI/AISC 360.

Table A-15 Gusset Properties: COM4B

Location	*Tg* (in)	*W* (in)	*L1* (in)	*L2* (in)	*L3* (in)	*A* (in)	*B* (in)	*Lw* (in)	*C* (in)
Midspan Gusset									
Roof – LG	1/2	16	1.5	10	14	12	52	11	11
Base Gusset									
Base	1/2	15	2	9.5	7.5	15.5	16	11	NA

Note:

LG / UG = Upper Gusset or Lower Gusset
W = Whitmore Width
A = Gusset Height
Lw = Brace Lap Length
Tg = Gusset Thickness
L1, *L2*, *L3* = Whitmore Lengths
B = Gusset Width
C = Stiffener Width

Table A-16 Baseplate Properties: COM4B

Baseplate Thickness, Tbp (in)	Anchor Rods	Baseplate Length, *A* (in)	Baseplate Width, *B* (in)
1	(8) 1″ Gr. 55	34	12

Table A-17 Member Properties Within Braced Bay: COM5B

Location	Brace Size and D/C Ratio	Brace End to End Length	Column Size	Beam Size	Beam Connection
Roof – 2nd Floor	HSS 3 1/2×3 1/2×3/8 D/C = 0.87	16′-6″	W12×50	W18×60	CJP moment connection
2nd Floor – 1st Floor	HSS 5×5×3/8 D/C = 0.86	15′-9″	W12×50	W21×73	½″ shear tab with (2) cos × (6) rows ¾″ A325 bolts

Note: D/C ratio (Demand-to-Capacity): in this context, the "demand" is the code-specified seismic load effect according to the equivalent-lateral-force procedure in ASCE/SEI 7, and the "capacity" is the governing limit state calculated in accordance with the LRFD provisions of ANSI/AISC 360.

Table A-18 Gusset Properties: COM5B

Location	*Tg* (in)	*W* (in)	*L1* (in)	*L2* (in)	*L3* (in)	*A* (in)	*B* (in)	*Lw* (in)	*C* (in)
Beam / Column Gusset									
Roof – LG	1/2	17	5	13.5	10	13.5	18	12	NA
Midspan Gusset									
2ND Floor – UG	1/2	17	2.5	11	10	12	50	12	11
2nd Floor – LG	5/8	22	1.75	14	12	15	58	15	11
Base Gusset									
Base	5/8	22	5.5	15.5	9	22	22	15	NA

Note:

LG / UG = Upper Gusset or Lower Gusset
W = Whitmore Width
A = Gusset Height
Lw = Brace Lap Length
Tg = Gusset Thickness
L1, *L2*, *L3* = Whitmore Lengths
B = Gusset Width
C = Stiffener Width

Table A-19 Baseplate Properties: COM5B

Baseplate Thickness, Tbp (in)	Anchor Rods	Baseplate Length, *A* (in)	Baseplate Width, *B* (in)
1 ¼	(8) 1″ Gr. 55	40	12

Table A-20 Member Properties Within Braced Bay: COM6B

Location	Brace Size and D/C Ratio	Brace End to End Length	Column Size	Beam Size	Beam Connection
Roof – 4th Floor	HSS 4×4×5/16 D/C = 0.77	16′-10″	W12×50	W18×60	CJP moment connection
4th Floor – 3rd Floor	HSS 5 1/2× 5 1/2 ×3/8 D/C = 0.94	15′-6″	W12×50	W21×101	½″ shear tab with (2) cos × (6) rows ¾″ A325 bolts
3rd Floor – 2nd Floor	HSS 6×6×1/2 D/C = 0.76	14′-10″	W12×96	W18×65	CJP moment connection
2nd Floor – 1st Floor	HSS 6×6×1/2 D/C = 0.96	14′-11″	W12×96	W18×50	½″ shear tab with (2) cos × (5) rows ¾″ A325 bolts

Note: D/C ratio (Demand-to-Capacity): in this context, the "demand" is the code-specified seismic load effect according to the equivalent-lateral-force procedure in ASCE/SEI 7, and the "capacity" is the governing limit state calculated in accordance with the LRFD provisions of ANSI/AISC 360.

Table A-21 Gusset Properties: COM6B

Location	*Tg* (in)	*W* (in)	*L1* (in)	*L2* (in)	*L3* (in)	*A* (in)	*B* (in)	*Lw* (in)	*C* (in)
Beam / Column Gusset									
Roof – LG	1/2	16.5	1.75	10.5	7	12	16	11	NA
3rd Floor – UG	5/8	23	2	14	8.5	16	21	16	NA
3rd Floor – LG	5/8	33	2.5	20.5	9.5	24.5	29.5	24	NA
Midspan Gusset									
4th Floor – UG	1/2	16.5	2	11	9	12	49	11	11
4th Floor – LG	5/8	24	2	15	11	16	60	16	11
2nd Floor – UG	5/8	33.5	4	22	10.5	24	71	24	11
2nd Floor – LG	3/4	33	2.5	20.5	10.5	24	71	24	11
Base Gusset									
Base	3/4	33.5	8	21.5	6	33	30	24	NA

Note:

LG / UG = Upper Gusset or Lower Gusset
W = Whitmore Width
A = Gusset Height
Lw = Brace Lap Length
Tg = Gusset Thickness
L1, *L2*, *L3* = Whitmore Lengths
B = Gusset Width
C = Stiffener Width

Table A-22 Baseplate Properties: COM6B

Baseplate Thickness, Tbp (in)	Anchor Rods	Baseplate Length, *A* (in)	Baseplate Width, *B* (in)
2 1/4	(8) 1 1/2″ Gr. 55	48	16

Table A-23 Member Properties Within Braced Bay: COM2B-BC

Location	Brace Size and D/C Ratio	Brace End to End Length	Column Size	Beam Size	Beam Connection
Roof – 2nd Floor	HSS 3 1/2× 3 1/2×5/16 D/C = 0.82	16′-0″	W12×50	W27×114	½″ shear tab with (2) cos × (7) rows ¾″ A325 bolts
2nd Floor – 1st Floor	HSS 4 1/2× 4 1/2×5/16 D/C = 0.96	15′-8″	W12×50	W27×146	CJP moment connection

Note: D/C ratio (Demand-to-Capacity): in this context, the "demand" is the code-specified seismic load effect according to the equivalent-lateral-force procedure in ASCE/SEI 7, and the "capacity" is the governing limit state calculated in accordance with the LRFD provisions of ANSI/AISC 360.

Table A-24 Gusset Properties: COM2B-BC

Location	*Tg* (in)	*W* (in)	*L1* (in)	*L2* (in)	*L3* (in)	*A* (in)	*B* (in)	*Lw* (in)	*C* (in)
Beam / Column Gusset									
2nd Floor - UG	1/2	14.5	2	9.5	14	8	19	11	NA
Midspan Gusset									
Roof – LG	1/2	14.5	1.5	9.5	13	10	50	11	11
2nd Floor – LG	5/8	16.5	1.75	11	16	12	56	11	11
Base Gusset									
Base	5/8	17	2.25	12	6	20	18	11	NA

Note:

LG / UG = Upper Gusset or Lower Gusset
W = Whitmore Width
A = Gusset Height
Lw = Brace Lap Length
Tg = Gusset Thickness
L1, *L2*, *L3* = Whitmore Lengths
B = Gusset Width
C = Stiffener Width

Table A-25 Baseplate Properties: COM2B-BC

Baseplate Thickness, Tbp (in)	Anchor Rods	Baseplate Length, *A* (in)	Baseplate Width, *B* (in)
1	(8) 1″ Gr. 55	36	12

Table A-26 Member Properties Within Braced Bay: COM3B-BC

Location	Brace Size and D/C Ratio	Brace End to End Length	Column Size	Beam Size	Beam Connection
Roof – 4th Floor	HSS 3 1/2× 3 1/2×5/16 D/C = 0.91	16′-0″	W12×50	W27×114	½″ shear tab with (2) cos × (7) rows ¾″ A325 bolts
4th Floor – 3rd Floor	HSS 5×5×3/8 D/C = 0.91	14′-9″	W12×50	W27×178	CJP moment connection
3rd Floor – 2nd Floor	HSS 5×5×1/2 D/C = 0.84	13′-11″	W12×96	W30×191	CJP moment connection
2nd Floor – 1st Floor	HSS 5×5×1/2 D/C = 0.93	13′-1″	W12×96	W30×191	CJP moment connection

Note: D/C ratio (Demand-to-Capacity): in this context, the "demand" is the code-specified seismic load effect according to the equivalent-lateral-force procedure in ASCE/SEI 7, and the "capacity" is the governing limit state calculated in accordance with the LRFD provisions of ANSI/AISC 360.

Table A-27 Gusset Properties: COM3B-BC

Location	*Tg* (in)	*W* (in)	*L1* (in)	*L2* (in)	*L3* (in)	*A* (in)	*B* (in)	*Lw* (in)	*C* (in)
Beam / Column Gusset									
4th Floor – LG	1/2	16	1.5	9.5	13.5	9	20	11	NA
3rd Floor – UG	5/8	22	2	13.5	17	14	27	14	NA
2nd Floor – UG	5/8	26.5	2.5	17	18.5	19	31	19	NA
Midspan Gusset									
Roof – LG	1/2	16	1.25	9.5	13	10	52	11	11
4th Floor – LG	5/8	22	2	14	15	15	64	15	11
3rd Floor – LG	5/8	26.5	2.5	17	18.5	19	77	19	11
2nd Floor – LG	5/8	26.6	1.5	17.5	20.5	18	78	19	11
Base Gusset									
Base	5/8	26.5	8.75	20.5	10	26	30	19	NA

Note:

LG / UG = Upper Gusset or Lower Gusset
W = Whitmore Width
A = Gusset Height
Lw = Brace Lap Length
Tg = Gusset Thickness
L1, *L2*, *L3* = Whitmore Lengths
B = Gusset Width
C = Stiffener Width

Table A-28 Baseplate Properties: COM3B-BC

Baseplate Thickness, Tbp (in)	Anchor Rods	Baseplate Length, *A* (in)	Baseplate Width, *B* (in)
2 1/4	(8) 1 3/8″ Gr. 55	37	16

Table A-29 Member Properties Within Braced Bay: COM2B-NR

Location	Brace Size and D/C Ratio	Brace End to End Length	Column Size	Beam Size	Beam Connection
Roof – 2nd Floor	HSS 4 1/2× 4 1/2×5/16 D/C = 0.74	16′-8″	W12×50	W18×55	CJP moment connection
2nd Floor – 1st Floor	HSS 5 1/2× 5 1/2×3/8 D/C = 0.97	15′-3″	W12×50	W21×83	½″ shear tab with (2) cos × (6) rows ¾″ A325 bolts

Note: D/C ratio (Demand-to-Capacity): in this context, the "demand" is the code-specified seismic load effect according to the equivalent-lateral-force procedure in ASCE/SEI 7, and the "capacity" is the governing limit state calculated in accordance with the LRFD provisions of ANSI/AISC 360.

Table A-30 Gusset Properties: COM2B-NR

Location	*Tg* (in)	*W* (in)	*L1* (in)	*L2* (in)	*L3* (in)	*A* (in)	*B* (in)	*Lw* (in)	*C* (in)
Beam / Column Gusset									
Roof – LG	5/8	16.5	4	12	8.5	15	18	11	NA
Midspan Gusset									
2ND Floor – UG	5/8	16.5	2	10.5	9	10	47	11	11
2nd Floor – LG	5/8	24	2.25	15	12.5	18	52	16	11
Base Gusset									
Base	5/8	24	8.25	19	12	24	25	16	NA

Note:

LG / UG = Upper Gusset or Lower Gusset
W = Whitmore Width
A = Gusset Height
Lw = Brace Lap Length
Tg = Gusset Thickness
L1, *L2*, *L3* = Whitmore Lengths
B = Gusset Width
C = Stiffener Width

Table A-31 Baseplate Properties: COM2B-NR

Baseplate Thickness, Tbp (in)	Anchor Rods	Baseplate Length, *A* (in)	Baseplate Width, *B* (in)
1 1/4	(8) 1 1/8″ Gr. 55	43	12

Table A-32 Overstrength of Steel SCBF System by Story

Archetype ID Type	V_s (kips)	Story	Brace Size at Story X	V_b (kips)	V_b/V_s
COM1B	83	1	HSS 3×3×5/16	584	7
COM2B	312	1	HSS 4 1/2×4 1/2×3/8	1153	3.7
	128	2	HSS 3 1/2×3 1/2×1/4	580	4.5
COM3B	776	1	HSS 6×6×1/2	2211	2.9
	672	2	HSS 5×5×1/2	1672	2.5
	460	3	HSS 5×5×3/8	1316	2.9
	147	4	HSS 3 1/2×3 1/2×5/16	696	4.7
COM4B	124	1	HSS 3 1/2×3 1/2×5/16	713	5.8
COM5B	468	1	HSS 5×5×3/8	1337	2.9
	192	2	HSS 3 1/2×3 1/2×3/8	813	4.2
COM6B	1164	1	HSS 6×6×1/2	2211	1.9
	1008	2	HSS 6×6/1/2	2184	2.2
	690	3	HSS 5 1/2×5 1/2×3/8	1507	2.2
	221	4	HSS 4×4×5/16	830	3.8
COM2B-NR	312	1	HSS 5 1/2×5 1/2×3/8	767	2.5
	128	2	HSS 4 1/2×4 1/2×5/16	484	3.8
COM2B-BC	312	1	HSS 4 1/2×4 1/2×5/16	993	3.2
	128	2	HSS 3 1/2×3 1/2×5/16	707	5.5
COM3B-BC	776	1	HSS 5×5×1/2	1762	2.3
	672	2	HSS 5×5×1/2	1715	2.6
	460	3	HSS 5×5/3/8	1340	2.9
	147	4	HSS 3 1/2×3 1/2×5/16	707	4.8

Note: In this context, "overstrength" is defined as the summation of the horizontal component of the expected tensile capacity and post-buckled capacity of all braces in the direction under consideration in relation to the total equivalent-lateral-force-design base shear.

V_s = Total story shear at level X

V_b = Total horizontal expected brace frame capacity at story X = $(R_y \times F_y \times A_g + 0.3 \times 1.14 \times F_{cr} \times A_g)(\cos \theta) \times$ number of braced bays

F_y = Specified minimum yield stress, ksi

R_y = Ratio of expected yield stress to the specified minimum yield stress, F_y

A_g = Gross area of member, in^2

F_{cr} = Buckling stress for the section as determined by analysis, ksi

V_b/V_s = "Overstrength" see note

Appendix B

Development of Soil Springs, Soil Dampers, and Frequency-Modified Ground-Motion Records for the SSI Parametric Study

B.1 Introduction

This appendix introduces soil-structure interaction (SSI) theory and documents the means and methods used to develop soil springs, soil dampers, and frequency-modified ground-motion records that are used in the SSI and foundation flexibility parametric study. More information about the implementation of the parameters and the results of the parametric study can be found in Chapter 4 and Chapter 5, respectively.

B.2 Background and Theory

The coupled response to ground movement of a structure and its foundation soil is identified here as soil-structure interaction. SSI is a complex phenomenon with a large body of literature. NIST GCR 12-917-21 (NIST, 2012b) synthesized the current state-of-the-art understanding of SSI effects and guidance on modeling techniques based on that knowledge. FEMA P-1050*, NEHRP Recommended Seismic Provisions for New Buildings and Other Structures* (FEMA, 2015b), includes guidance on seismic design procedures including the effects of SSI. This appendix briefly introduces the physical effects of seismic SSI on a building system and summarizes some of the principal analysis methods as they relate to this study.

B.2.1 Inertial-Interaction Effects

Inertial interaction is caused by the inertia of the structure mass, which, during dynamic loading, imposes shear and moment loads on the foundation. These loads must then be supported by the surrounding soil and, due to soil flexibility, cause foundation translation and rotation.

The default case for the analysis of structural response is the *fixed-base* condition, where the foundation and supporting soil are assumed to be perfectly rigid. The *flexible-base* condition includes the deformation of the soil and

foundation. The soil flexibility increases the overall flexibility of the building system, resulting in a lengthening of the fundamental period. As is well known from spectral acceleration diagrams, the energy content of an earthquake varies with frequency. Significant period lengthening will impact the seismic demand on the structure, as spectral acceleration is often used to estimate base shear for an elastic response of a structure. In general, for structures with short fundamental periods, period lengthening will cause an increase in spectral acceleration, whereas for structures with long periods, spectral acceleration decreases with period lengthening. The change in the flexibility of the system can also change the load and deformation distribution within the structure and foundation, the effects of which are often complicated.

In addition to changing flexibility, inertial interaction also provides two mechanisms for energy dissipation: (1) radiation damping; and (2) hysteretic or material damping. Radiation damping is caused by energy being radiated away from the foundation, out into the surrounding soil during vibration cycles. Hysteretic damping is caused by internal energy dissipation within the soil material. The increase in damping due to these inertial interaction effects will tend to decrease response of a flexible-base structure.

Soil stiffness and damping are parameterized as impedance functions, which are theoretically known to be frequency dependent. Stiffness can be described as a spring coefficient, k, and damping can be given as a damping ratio, β. Translational stiffness is relatively constant with frequency, whereas rotational stiffness decreases and damping increases with increasing frequency.

B.2.2 Kinematic-Interaction Effects

In addition to inertial-interaction effects described above, SSI also changes the ground motions in the vicinity of the soil-structure system. The ground motions that would occur without the existence of the structure are known as free-field ground motions. The presence of the relatively stiff foundation, which imposes loads on the soil, changes the ground motions near the structure. Ground motions that include the altering effects of SSI are known as Foundation Input Motions.

Kinematic interaction includes the phenomenon known as base-slab averaging, where the natural spatial variation in the free-field ground motions throughout the area occupied by the structure must be averaged due to the stiffness of the foundation. The spatial variation in ground motions includes both a deterministic component due to wave-passage effects and a stochastic component due to natural seismic wave-path complexities. Kinematic interaction also includes effects due to foundation embedment, which are not

discussed here in detail due to the shallow foundation depths of the building prototypes selected for this study.

Kinematic-interaction effects are estimated using transfer functions between the free-field ground motion and the foundation input motion. Semi-empirical models for the transfer function indicate that the foundation input motion will be smaller than the free-field motion at high frequencies, and they are predicted to be the same at low frequencies.

B.3 Representative Field Sites

Two soil sites with differing soil conditions were selected for the SSI study. The sites vary in terms of site class, which was classified based on shear-wave velocity in the upper 30 meters (V_{s30}), per FEMA P-1050. The soft site was selected to be near the site class D/E boundary, with a target V_{s30} = 180 m/s (591 ft/s). The stiff site was selected to be near the site class C/D boundary, with a target V_{s30} = 360 m/s (1181 ft/s). More information about the conditions at the selected sites is given below.

B.3.1 Soft Site

The soft site was selected to be near the site class D/E boundary, with a target V_{s30} = 180 m/s (591 ft/s). The Imperial Valley Wildlife Liquefaction (WLA) site was selected as a representative site. The site consists of unsaturated soft clay near the soil surface. The shear-wave-velocity profile is documented in Star et al. (2015). The estimated V_{s30} at WLA is 183 m/s (600 ft/s). A simplified assumed shear-wave profile of the site is taken to be V_s = 100 m/s (328 ft/s) from surface to 3 m (10 ft) below the surface, V_s = 140 m/s (459 ft/s) from 3 m to 5 m (10 ft to 16 ft) below the surface, V_s = 170 m/s (558 ft/s) from 5 m to 12 m (16 ft to 39 ft) below the surface, and V_s = 230 m/s (755 ft/s) more than 12 m (39 ft) below the surface. Undrained shear strength of the soil was estimated as 32 kPa (668 lbs/ft^2). Poisson's ratio for the soil was estimated to be 0.45, and the unit weight was estimated to be 16 kN/m^3 (103 lbs/ft^3). At large strains, the shear modulus of the soil reduces from the maximum elastic value. The effective reduction factor for shear modulus was estimated to be 0.6.

B.3.2 Stiff Site

The stiff soil site was selected to be near the site class C/D boundary, with a target V_{s30} = 360 m/s (1181 ft/s). The Cholame Parkfield 12W site was selected as a representative site. The site consists of dense sands near the soil surface. The shear-wave-velocity profile is documented in Thompson et al. (2010). Based on shear-wave velocity data, V_{s30} is estimated to be 354 m/s (1161 ft/s). A simplified, assumed shear-wave profile of the site is taken to

be V_s = 295 m/s (968 ft/s) from surface to 1 m (3.3 ft) below the surface, V_s = 310 m/s (1017 ft/s) from 1 m to 2 m (3.3 ft to 6.6 ft) below the surface, V_s = 315 m/s (1033 ft/s) from 2 m to 10 m (6.6 ft to 33 ft) below the surface, V_s = 335 m/s (1099 ft/s) from 10 m to 15 m (33 ft to 49 ft) below the surface, V_s = 370 m/s (1214 ft/s) from 15 m to 20 m (49 ft to 66 ft) below the surface, and V_s = 415 m/s (1362 ft/s) more than 20 m (66 ft) below the surface. The friction angle of the soil was estimated to be 40 degrees, Poisson's ratio was estimated to be 0.35, and the unit weight of the soil was estimated to be 19 kN/m^3 (122 lbs/ft^3). At large strains, the shear modulus of the soil reduces from the maximum elastic value. The effective reduction factor for shear modulus was estimated to be 0.8.

B.4 Foundation Springs and Dampers

B.4.1 Development of the Foundation Impedances

This section summarizes the development of the foundation impedance functions (springs and dampers) for the COM2B and COM3B designs for the soft and stiff soil sites.

As described in Section 3.5.1, the foundation system for the COM2B and COM3B designs consist of shallow spread footings with a slab-on-grade. Figure B-1(a) shows the layout of the footing structures in the COM2B design for soft and stiff soil and for the COM3B design for stiff soil. The springs and dampers were developed for four different foundation types, under the East-West (E/W) exterior strip foundations, under the North-South (N/S) exterior strip foundations, and under the small and large interior isolated footings. The soil-foundation springs and dampers were not included for the slab-on-grade.

Figure B-1(b) shows the layout of the footing structures in the COM3B design for soft soil. For this configuration, springs and dampers were developed for four different foundation types, under the long E/W exterior strip foundations, under the shorter N/S exterior strip foundations, and under the small and large interior isolated footings. The soil-foundation springs and dampers were not included for the slab-on-grade.

For all foundations located along the exterior of the structure (i.e., the E/W and N/S strip foundations), springs and dampers were developed at nodes located at a 5-foot spacing along the center line of each foundation. Three springs and parallel dampers control translation in the two horizontal (subscripts x, z) directions and one vertical (subscript y) direction. Rotation of the foundation in the in-plane direction is controlled by the vertical springs. Rotational springs (notated with the subscripts xx and zz) control

the out-of-plane rotation. Figure B-2 shows a cross section through a single node of a foundation, with the vertical and horizontal translation springs and out-of-plane rotational springs and dampers shown. The spring controlling translation along the length of the foundation is not shown.

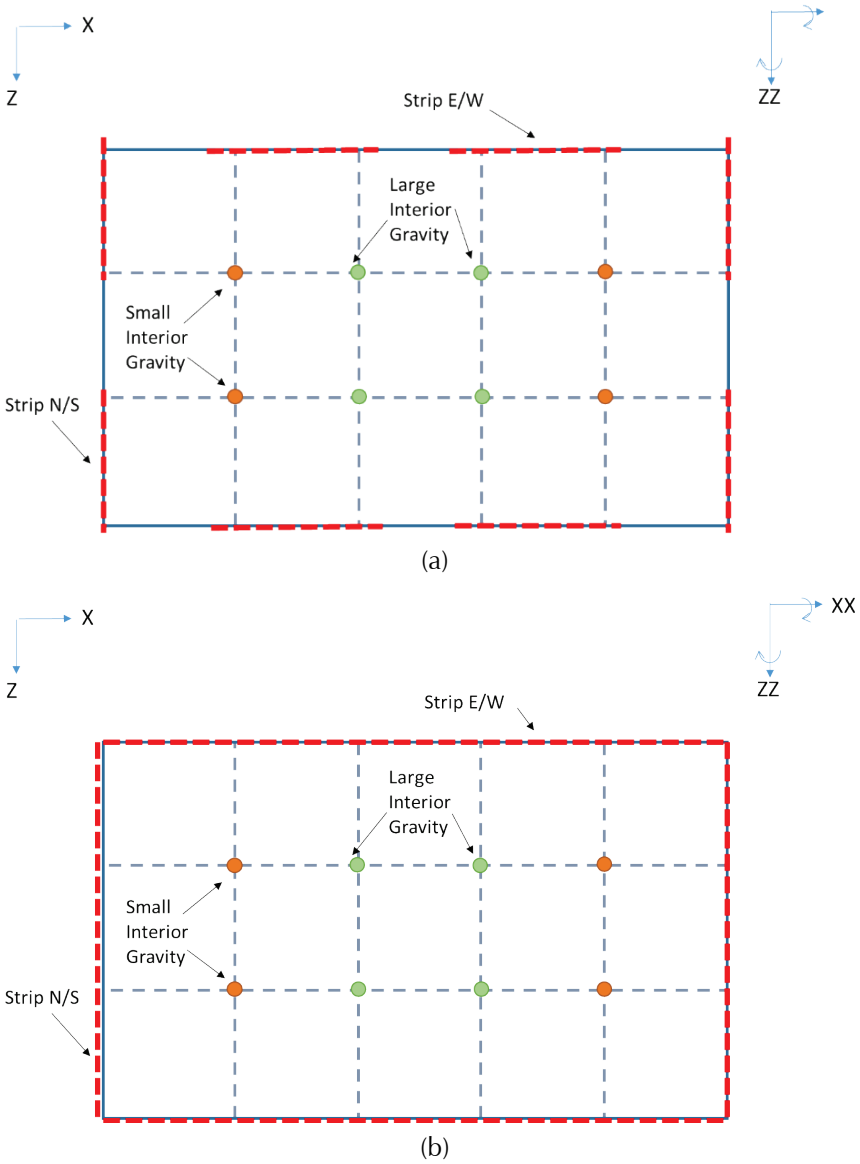

Figure B-1 Layout of modeled footings for SSI study: (a) COM2B soft and stiff sites and COM3B stiff site and (b) COM3B soft site.

For each interior footing, the foundation spring stiffness and damping values were developed as lumped impedance values, located at a single node under the center of the square foundations. Five springs and parallel dampers control translation in two horizontal (subscripts x, z) directions and one vertical (subscript y) direction and rotations about the x and z axes (notated with the subscripts xx and zz).

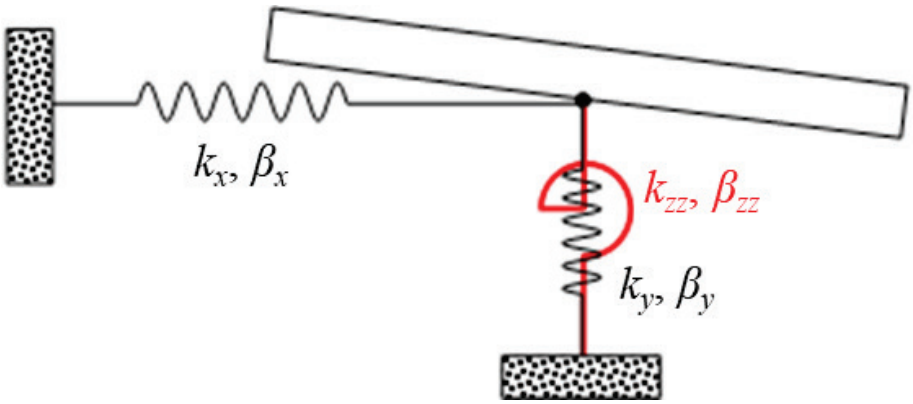

Figure B-2 Cross section through a single node of a foundation showing translational and rotational springs and dampers.

Foundation impedance functions are dependent on the foundation dimensions. Detailed foundation plans for COM2B and COM3B are provided in Section A.3.2. The foundation dimensions in the X- and Z-directions used for the calculation of foundation impedances for each footing type are given in Table B-1 and Table B-2. Note that these dimensions are equivalent to 2*L* and 2*B* used in NIST (2012b) and FEMA P-1050. Determining the foundation dimensions for the square and rectangular foundations is straightforward. The foundation dimensions for the L-shaped wall is estimated based on an equivalent foundation with a moment of inertia matching that of the actual foundation.

Table B-1 shows the foundation dimensions for the COM2B soft and stiff sites as being equivalent, and this assumption was used in the calculation of the spring and damper properties reported in Table B-3 and Table B-4. However, the final designs for these two cases were in fact different, as shown in Appendix A. The final designs for the COM2B soft site were larger than those for the COM2B stiff site. By using smaller footings than the final designs in the calculation of the spring and damper properties, the SSI and foundation flexibility analysis done for the COM2B soft site behaved in a more flexible manner than it otherwise would have with spring and damper properties based on larger foundation dimensions. However, it was determined that the overall collapse response behavior was unlikely to have changed appreciably had the spring and damper properties been based on the final designs. Thus, the COM2B soft site model was not re-run with updated spring and damper properties, and instead the response results reported in Chapter 5 are based on spring and damper properties reported in this appendix, which assume that the COM2B soft and stiff sites have equivalent foundation dimensions.

Table B-1 X and Z Dimensions for Calculation of Foundation Springs and Dampers for COM2B Soft and Stiff Sites and COM3B Stiff Site

Footing Type	COM2B Soft and Stiff Sites	COM3B Stiff Site
E/W Strip	40′ × 3.5′	45′ × 8.5′
N/S Strip	3.7′ × 40′	9.5′ × 46′
Large Interior Isolated	7.5′ × 7.5′	11′ × 11′
Small Interior Isolated	6.5′ × 6.5′	10.5′ × 10.5′

Table B-2 X and Z Dimensions for Calculation of Foundation Springs and Dampers for COM3B Soft Site

Footing Type	COM3 Soft Site
Long E/W Strip	150′ × 10′
Short N/S Strip	10′ × 90′
Large Interior Isolated	15.5′ × 15.5′
Small Interior Isolated	15′ × 15′

The average effective shear-wave velocity of the soil under each foundation is used, along with the density of the soil, to estimate the small-strain shear modulus, G_0. As described in NIST (2012b), the effective depth interval for calculating the shear-wave velocity depends on the size of the foundation and the spring orientation. For the translations and vertical springs, the effective depth is equal to the half-dimension of an equivalent square foundation with an area matching the actual foundation. For the rotational springs, it is equal to the half-dimension of an equivalent square foundation matching the moment of inertia of the actual foundation. The small-strain shear modulus is reduced by the strain reduction factors given in Section B.3 to get a modulus appropriate for estimating springs and dampers for each footing type.

Foundation impedance values in the vertical, translational, and rotational directions were calculated using equations by Pais and Kausel (1988) for a rigid surface foundation, as given in Table 2-2a of NIST (2012b) for surface foundations. The foundation impedance values are divided by the number of nodes in order to determine the final spring stiffness values. This approach, when applied to the vertical stiffness values, tends to underestimate the in-plane rotational stiffness of the foundation system compared to that predicted using the lumped impedance value. As capturing the rotational stiffness is considered more important to the behavior of the system compared to vertical translation, factors are used to increase the stiffness of the vertical springs across the extent of the foundation, in order to better match the rotational

behavior. In order to model radiation damping from rocking, a lumped rocking damper value at the center of the foundation was calculated.

The impedance springs and dampers calculated using Pais and Kausel (1988) equations, as given in Table 2-2a of NIST (2012b), are frequency dependent. However, due to the limitations of the modeling software, implementing frequency dependent springs and dampers was not possible. Following NIST (2012b), a single frequency value was selected corresponding to the first-mode, flexible-base period of the system, approximately 0.47 seconds and 0.28 seconds for COM2B soft and stiff sites, respectively, and 0.60 seconds for COM3B.

The ultimate capacity of the translational stiffness springs, $K_{x,capacity}$ and $K_{z,capacity}$, are controlled by the strength of the soil. The clay at the soft site was estimated to have an undrained soil-foundation interface strength of 32 kPa (668 lbs/ft^2). The sand at the surface of the stiff site generates a friction angle between the soil and foundation of 40 degrees (friction ratio of 0.83). For all sites, strain hardening of 15 percent was included to account for additional sliding resistance due to passive pressure on foundation elements.

The capacity of the vertical springs, $K_{y,capacity}$, are controlled by the unfactored bearing capacity of the foundation. The vertical springs have no tension capacity and thus zero resistance to foundation uplift. Strain hardening of 15 percent was included. The in-plane rotational springs capacity, $K_{ip,capacity}$, is naturally controlled by the uplift and bearing capacity of the vertical springs and does not need to be explicitly modeled. The out-of-plane rotational springs, $K_{oop,capacity}$, were set to be elastic with no limiting capacity.

Radiation damping is presented in terms of damping ratio percentages, β. Calculated spring and damper values for the COM2B soft and stiff sites and COM3B soft and stiff sites are reported in Table B-3 to Table B-6.

Table B-3 Spring and Damper Properties per Node for COM2B Soft Site

Footing Type	Translation-X	Translation-Z	Vertical-Y	Rotation-ZZ	Rotation-XX
E/W Strip	$K_x = 9.1\times10^2$ kips/ft $K_{x,capacity} = 10$ kips $\beta_x = 7.1\%$	$K_z = 1.1\times10^3$ kips/ft $K_{z,capacity} = 10$ kips $\beta_z = 5.7\%$	$K_y = 1.7\times10^3$ kips/ft $K_{y,capacity} = 53$ kips	$\beta_{zz} = 0.44\%$	$K_{xx} = 8.7\times10^3$ kip-ft/rad $\beta_{xx} = 0.01\%$
N/S Strip	$K_x = 1.2\times10^3$ kips/ft $K_{x,capacity} = 11$ kips $\beta_x = 6.0\%$	$K_z = 9.4\times10^2$ kips/ft $K_{z,capacity} = 11$ kips $\beta_z = 7.4\%$	$K_y = 1.8\times10^3$ kips/ft $K_{y,capacity} = 57$ kips	$K_{zz} = 1.0\times10^4$ kip-ft/rad $\beta_{zz} = 0.01\%$	$\beta_{xx} = 0.40\%$
Large Interior Isolated	$K_x = 4.6\times10^3$ kips/ft $K_{x,capacity} = 38$ kips $\beta_x = 5.1\%$	$K_z = 4.6\times10^3$ kips/ft $K_{z,capacity} = 38$ kips $\beta_z = 5.1\%$	$K_y = 6.5\times10^3$ kips/ft $K_{y,capacity} = 226$ kips $\beta_y = 8.9\%$	$K_{zz} = 7.8\times10^4$ kip-ft/rad $\beta_{zz} = 0.05\%$	$K_{xx} = 7.8\times10^4$ kip-ft/rad $\beta_{xx} = 0.05\%$
Small Interior Isolated	$K_x = 3.9\times10^3$ kips/ft $K_{x,capacity} = 28$ kips $\beta_x = 4.4\%$	$K_z = 3.9\times10^3$ kips/ft $K_{z,capacity} = 28$ kips $\beta_z = 4.4\%$	$K_y = 5.7\times10^3$ kips/ft $K_{y,capacity} = 170$ kips $\beta_y = 7.7\%$	$K_{zz} = 5.1\times10^4$ kip-ft/rad $\beta_{zz} = 0.03\%$	$K_{xx} = 5.1\times10^4$ kip-ft/rad $\beta_{xx} = 0.03\%$

Table B-4 Spring and Damper Properties per Node for COM2B Stiff Site

Footing Type	Translation-X	Translation-Z	Vertical-Y	Rotation-ZZ	Rotation-XX
E/W Strip	$K_x = 1.2\times10^4$ kips/ft $\beta_x = 4.1\%$	$K_z = 1.5\times10^4$ kips/ft $\beta_z = 3.4\%$	$K_y = 2.0\times10^4$ kips/ft $K_{y,capacity} = 988$ kips	$\beta_{zz} = 0.07\%$	$K_{xx} = 1.0\times10^5$ kip-ft/rad $\beta_{xx} = 0.001\%$
N/S Strip	$K_x = 1.6\times10^4$ kips/ft $\beta_x = 3.5\%$	$K_z = 1.3\times10^4$ kips/ft $\beta_z = 4.3\%$	$K_y = 2.2\times10^4$ kips/ft $K_{y,capacity} = 1061$ kips	$K_{zz} = 1.2\times10^5$ kip-ft/rad $\beta_{zz} = 0.001\%$	$\beta_{xx} = 0.07\%$
Large Interior Isolated	$K_x = 6.2\times10^4$ kips/ft $\beta_x = 3.0\%$	$K_z = 6.2\times10^4$ kips/ft $\beta_z = 3.0\%$	$K_y = 8.0\times10^4$ kips/ft $K_{y,capacity} = 4386$ kips $\beta_y = 4.8\%$	$K_{zz} = 9.6\times10^5$ kip-ft/rad $\beta_{zz} = 0.01\%$	$K_{xx} = 9.6\times10^5$ kip-ft/rad $\beta_{xx} = 0.01\%$
Small Interior Isolated	$K_x = 5.1\times10^4$ kips/ft $\beta_x = 2.7\%$	$K_z = 5.1\times10^4$ kips/ft $\beta_z = 2.7\%$	$K_y = 6.6\times10^4$ kips/ft $K_{y,capacity} = 3254$ kips $\beta_y = 4.3\%$	$K_{zz} = 5.9\times10^5$ kip-ft/rad $\beta_{zz} = 0.01\%$	$K_{xx} = 5.9\times10^5$ kip-ft/rad $\beta_{xx} = 0.01\%$

Table B-5 Spring and Damper Properties per Node for COM3B Soft Site

Footing Type	Translation-X	Translation-Z	Vertical-Y	Rotation-ZZ	Rotation-XX
Long E/W Strip	$K_x = 1.1x10^3$ kips/ft $K_{x,capacity} = 32$ kips $\beta_x = 15.7\%$	$K_z = 2.4x10^3$ kips/ft $K_{z,capacity} = 32$ kips $\beta_z = 12.4\%$	$K_y = 2.0x10^3$ kips/ft $K_{y,capacity} = 187$ kips	$\beta_{zz} = 5.1\%$	$K_{xx} = 1.2x10^5$ kip-ft/rad $\beta_{xx} = 0.04\%$
Short N/S Strip	$K_x = 1.6x10^3$ kips/ft $K_{x,capacity} = 32$ kips $\beta_x = 10.6\%$	$K_z = 1.4x10^3$ kips/ft $K_{z,capacity} = 32$ kips $\beta_z = 12.8\%$	$K_y = 2.6x10^3$ kips/ft $K_{y,capacity} = 185$ kips	$K_{zz} = 1.1x10^5$ kip-ft/rad $\beta_{zz} = 0.04\%$	$\beta_{xx} = 2.2\%$
Large Interior Isolated	$K_x = 9.4x10^3$ kips/ft $K_{x,capacity} = 161$ kips $\beta_x = 8.3\%$	$K_z = 9.4x10^3$ kips/ft $K_{z,capacity} = 161$ kips $\beta_z = 8.3\%$	$K_y = 1.4x10^4$ kips/ft $K_{y,capacity} = 1040$ kips $\beta_y = 14.5\%$	$K_{zz} = 6.8x10^5$ kip-ft/rad $\beta_{zz} = 0.20\%$	$K_{xx} = 6.8x10^5$ kip-ft/rad $\beta_{xx} = 0.20\%$
Small Interior Isolated	$K_x = 3.9x10^3$ kips/ft $K_{x,capacity} = 28$ kips $\beta_x = 4.4\%$	$K_z = 3.9x10^3$ kips/ft $K_{z,capacity} = 28$ kips $\beta_z = 4.4\%$	$K_y = 5.7x10^3$ kips/ft $K_{y,capacity} = 170$ kips $\beta_y = 7.7\%$	$K_{zz} = 6.2x10^5$ kip-ft/rad $\beta_{zz} = 0.17\%$	$K_{xx} = 6.2x10^5$ kip-ft/rad $\beta_{xx} = 0.17\%$

Table B-6 Spring and Damper Properties per Node for COM3B Stiff Site

Footing Type	Translation-X	Translation-Z	Vertical-Y	Rotation-ZZ	Rotation-XX
E/W Strip	$K_x = 1.7\times10^4$ kips/ft $\beta_x = 3.5\%$	$K_z = 2.0\times10^4$ kips/ft $\beta_z = 3.0\%$	$K_y = 4.2\times10^4$ kips/ft $K_{y,capacity} = 3500$ kips	$\beta_{zz} = 0.03\%$	$K_{xx} = 6.2\times10^5$ kip-ft/rad $\beta_{xx} = 0.001\%$
N/S Strip	$K_x = 2.1\times10^4$ kips/ft $\beta_x = 3.3\%$	$K_z = 1.8\times10^4$ kips/ft $\beta_z = 3.8\%$	$K_y = 4.6\times10^4$ kips/ft $K_{y,capacity} = 4350$ kips	$K_{zz} = 8.1\times10^5$ kip-ft/rad $\beta_{zz} = 0.002\%$	$\beta_{xx} = 0.04\%$
Large Interior Isolated	$K_x = 9.1\times10^4$ kips/ft $\beta_x = 2.1\%$	$K_z = 9.1\times10^4$ kips/ft $\beta_z = 2.1\%$	$K_y = 1.2\times10^5$ kips/ft $K_{y,capacity} = 8880$ kips $\beta_y = 3.4\%$	$K_{zz} = 3.0\times10^6$ kip-ft/rad $\beta_{zz} = 0.002\%$	$K_{xx} = 3.0\times10^6$ kip-ft/rad $\beta_{xx} = 0.002\%$
Small Interior Isolated	$K_x = 8.7\times10^4$ kips/ft $\beta_x = 2.0\%$	$K_z = 8.7\times10^4$ kips/ft $\beta_z = 2.0\%$	$K_y = 1.1\times10^5$ kips/ft $K_{y,capacity} = 7880$ kips $\beta_y = 3.2\%$	$K_{zz} = 2.6\times10^6$ kip-ft/rad $\beta_{zz} = 0.002\%$	$K_{xx} = 2.6\times10^6$ kip-ft/rad $\beta_{xx} = 0.002\%$

B.4.2 Spring and Damper Example Calculations

The soil-foundation spring and damper values are calculated individually for each foundation configuration at each soil site. In the following calculations, the E/W strip foundation of the COM2B stiff site is shown an example case, including the calculations necessary to compute the stiffness and damping parameters:

1. Determine the effective shear modulus

Where soil profiles are non-uniform, it is necessary to determine an effective shear modulus to use for impedance calculations. As described in NIST (2012b), the first step is to calculate the effective depth intervals, z_p, based on the foundation plan area, A, for translations, and based on foundation moments of inertia, I_x and I_z, for rotation of the foundation:

$$\textit{Horizontal}\ (x,z)\text{: } z_p^{A} = \sqrt{A/4} = 5.91 \text{ ft}$$

$$\textit{Rotation}\ (zz)\text{: } z_{p,zz}^{I} = \sqrt[4]{I_z} = 10.89 \text{ ft} \qquad \text{NIST (2012b) Eq. 2-18 (b-c)}$$

$$\textit{Rotation}\ (xx)\text{: } z_{p,xx}^{I} = \sqrt[4]{I_x} = 3.22 \text{ ft}$$

The average shear-wave velocity over the effective depths is calculated:

$$V_{s,avg} = \frac{z_p}{\sum_{i=1}^{n}\left(\Delta z_i \Big/ \left(V_s(z)\right)_i\right)} \qquad \text{NIST (2012b) Eq. 2-18 (a)}$$

$$V_{s,\,avg,\,horiz} = 990 \text{ ft/s}$$

$$V_{s,\,avg,\,zz} = 990 \text{ ft/s}$$

$$V_{s,\,avg,\,xx} = 968 \text{ ft/s}$$

where Δz_p and $(V_s(z))_i$ are the thickness and the velocity of discretized layers of the soil profile.

The product of the density, ρ, and the square of the shear-wave velocity gives the small strain shear modulus. At large strains, the effective shear modulus, G_{eff}, of the soil reduces from the small-strain value. The effective reduction factor for shear modulus was estimated to be 0.8.

$$G_{eff,\,horiz} = 0.8 \times \rho \times V_{s,avg,horiz}^2 = 2.97 \times 10^6 \text{ lb/ft}^2$$

$$G_{eff,\,zz} = 0.8 \times \rho \times V_{s,avg,zz}^2 = 2.97 \times 10^6 \text{ lb/ft}^2$$

$$G_{eff,\,xx} = 0.8 \times \rho \times V_{s,avg,xx}^2 = 2.82 \times 10^6 \text{ lb/ft}^2$$

2. Calculate the static spring stiffness

Pais and Kausel (1988) equations for a rigid surface foundation, as given in Table 2-2a of NIST (2012b), were used to estimate the static spring stiffnesses for the five degrees of freedom described in Section B.4.1. The inputs to these equations are the foundation length ($2L$ = 40 feet) and width ($2B$ = 3.5 feet), Poisson's ratio of the soil (v = 0.35), and the shear moduli determined in Step 1 of these example calculations. The full equations are not reproduced here for brevity. Calculated static spring stiffnesses are:

$$K_{x,static} = 1.1\times10^5 \text{ kips/ft}$$

$$K_{z,static} = 1.4\times10^5 \text{ kips/ft}$$

$$K_{zz,static} = 3.0\times10^7 \text{ kip-ft/rad}$$

$$K_{xx,static} = 9.1\times10^5 \text{ kip-ft/rad}$$

$$K_{y,static} = 1.7\times10^5 \text{ kips/ft}$$

3. Determine the dynamic modifiers and damper values

Dynamic spring modifiers (α) and damper values (β) are frequency dependent. First, the dimensionless frequency is calculated:

$$a_o = \omega B / V_s \qquad \text{NIST (2012b) Eq. 2-15}$$

where ω is angular frequency. In order to be compatible with the time-domain analysis used by the modeling software, a single value of angular frequency corresponding to the first-mode period of the undamaged COM2 soil-structure system (approximately 0.28 seconds) is selected.

A single value of α and β is then calculated for each of the five degrees of freedom using Pais and Kausel (1988) equations, as given in Table 2-3a of NIST (2012b). The input parameters for these calculations are the dimensionless frequency, the foundation dimensions L and B, the static spring stiffnesses determined in Step 2 of these example calculations, the shear moduli determined in Step 1 of these example calculations, and Poisson's ratio of the soil. The calculated dynamic spring modifiers and damper values are:

$\alpha_x = 1.00$	$\beta_x = 4.16\%$
$\alpha_z = 1.00$	$\beta_z = 3.37\%$
$\alpha_{zz} = 0.999$	$\beta_{zz} = 0.07\%$
$\alpha_{xx} = 1.00$	$\beta_{xx} = 0.001\%$
$\alpha_y = 0.997$	$\beta_y = 5.82\%$

The modifiers are multiplied by the static stiffnesses to get the final stiffness values:

$$K_x = \alpha_x \times K_{x,static} = 1.1\times10^5 \text{ kips/ft}$$

$$K_z = \alpha_z \times K_{z,static} = 1.4\times10^5 \text{ kips/ft}$$

$$K_{zz} = \alpha_{zz} \times K_{zz,static} = 3.0\times10^7 \text{ kip-ft/rad}$$

$$K_{xx} = \alpha_{xx} \times K_{xx,static} = 9.1\times10^5 \text{ kip-ft/rad}$$

$$K_y = \alpha_y \times K_{y,static} = 1.7\times10^5 \text{ kips/ft}$$

4. Determine the spring capacities

The capacity of the horizontal translation springs is dependent on the friction angle of the soil ($\phi' = 40$ degrees) and varies depending on the vertical foundation load (V) according to the equation:

$$K_{z,capacity} = V \times \tan\phi'$$

The vertical spring capacity is calculated using Meyerhoff's bearing capacity equation. Vesic's bearing capacity factors (N_q, N_γ) were used with Hansen's shape (F_{qs}, $F_{\gamma s}$) and depth (F_{qd}, $F_{\gamma d}$) factors. See, for example, Coduto et al. (2015) for bearing capacity equations. The input parameters for these calculations are the unit weight of the soil (γ), the dimensions of the foundation, and the friction angle of the soil. In the bearing capacity equation below, the width of the foundation is parameterized as $2B$, as in the NIST (2012b) report and the steps above, although it is more commonly reported in the literature as B. A factor of safety (FS) of 1 was applied to the bearing capacity.

$$K_{y,capacity} = \frac{Q_{ult}}{FS} = \left(D\gamma N_q F_{qs} F_{qd} + \frac{(2B)}{2}\gamma N_\gamma F_{\gamma s} F_{\gamma d} \right) \times L \times B / FS = 5.8 \times 10^3 \text{ kips}$$

where the depth (D) of the foundation is 2 feet.

5. Determine the distributed spring properties

The calculated foundation impedances and capacities are divided by the number of nodes (N) to get the nodal spring value. The spring nodes are located every 5 feet along the centerline of the foundation. That means that there are 9 nodes along the 40-foot-long foundation.

The rotational stiffness, K_{zz}, is taken as null because the distributed vertical spring stiffness, K_y, will provide the stiffness against rotation. The vertical nodal spring stiffness is modified by stiffness factor, $R_{k,zz}$, to produce an equivalent rotational stiffness.

$$R_{k,zz} = \frac{K_{zz}}{\left(\frac{K_y}{N}\right)\sum_{i=1}^{N}\left(d_i^2\right)} = 1.08$$

where d_i is the distance of each node from the center of the foundation.

Per node, the updated spring stiffness properties are:

$$K_x = K_x/N = 1.2\times10^4 \text{ kip/ft}$$

$$K_z = K_z/N = 1.5\times10^4 \text{ kip/ft}$$

$$K_{zz} = —$$

$$K_{xx} = K_{xx}/N = 1.0\times10^5 \text{ kip-ft/rad}$$

$$K_y = K_y \times R_{k,zz}/N = 2.0\times10^4 \text{ kip/ft}$$

$$K_{y,capacity} = K_{y,capacity}/N = 988 \text{ kips}$$

B.5 Frequency-Modified Ground-Motion Records

Kinematic-interaction effects are modeled using modified ground motions, known as the foundation input motions (FIM). This section discusses the modification of the suite of ground motions to account for kinematic-interaction effects.

The ratio of FIM and free-field ground motion in the frequency domain is presented as a transfer function, H_u. The period-dependent transfer function, H_u, is calculated using semi-empirical equations, as in NIST (2012b) Equation 3-3 and Equation 3-4. It is dependent on a parameter κ_a, the dimensions of the foundation, and the shear-wave velocity of the soil. The overall dimensions of the structure in plan view (150 feet × 90 feet) were selected for calculating H_u, and the embedment was assumed to be negligible. The foundation parameter κ_a is calculated using the semi-empirical model by Kim and Stewart (2003), as given in NIST (2012b) Equation 3-5, based on the shear-wave velocity of the soil at the surface of the site, reduced by the effective reduction factor for shear modulus, which is estimated to be 0.8 for the stiff site and 0.6 for the soft site. Figure B-3 shows the calculated transfer functions for the soft and stiff sites.

The calculation of the FIM is achieved by converting the free-field ground motion to the Fourier domain. The frequency-dependent transfer function is then applied, and the ground motions are converted back to the time domain for use in the SSI and foundation flexibility modeling. The Matlab Fast Fourier Transform (FFT) function was used for the calculations. This process was applied to all motions in both horizontal directions for the suite of ground motions used in the SSI and foundation flexibility modeling.

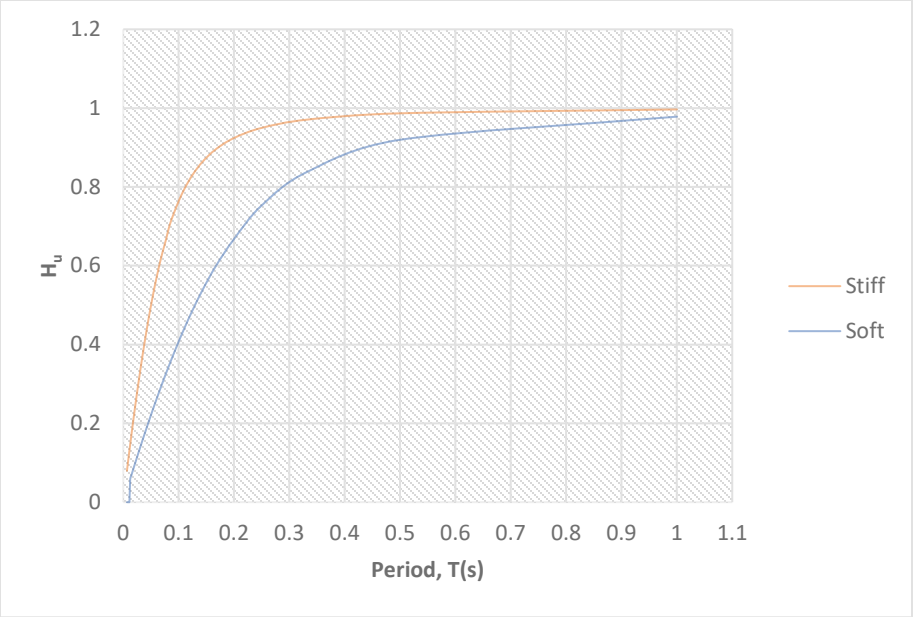

Figure B-3 Transfer function for soft and stiff sites.

Appendix C

Archive of Peak Response Calculations

C.1 Peak Response Parameters Archived for Each Model

Response parameters of interest (stripe statistics) were post-processed and archived at each intensity stripe to determine the peak response for each archetype. For each archetype, an Excel spreadsheet containing these response parameters for each IDA and all intensity stripes was generated and archived. The names of the archive files for each archetype are listed in Table C-1. See Chapter 4, Table 4-3 for a list of the specific response parameters that were archived. The archives for all stripe statistics are available at https://femap2139.atcouncil.org.

Table C-1 Peak Response Archive Files for Short-Period Steel SCBF Building Archetypes

Archetype ID	No. of Stories	Seismic Region	Parametric Study	Peak Response Archive Files
COM1B	1	High	Baseline	Stripe_Statistics_ATC116_S_COM1B
COM2B	2	High	Baseline	Stripe_Statistics_ATC116_S_COM2B
COM2B-SS	2	High	SSI/Foundation Flexibility*	Stripe_Statistics_ATC116_S_COM2B-SS1 Stripe_Statistics_ATC116_S_COM2B-SS2 Stripe_Statistics_ATC116_S_COM2B-SS1-Unfiltered Stripe_Statistics_ATC116_S_COM2B-SS2-Unfiltered
COM2B-NR	2	High	No Redundancy	Stripe_Statistics_ATC116_S_COM2B-NR
COM2B-BC	2	High	Brace Configuration	Stripe_Statistics_ATC116_S_COM2B-BC
COM2B-NMF	2	High	No Reserve Moment Frame	Stripe_Statistics_ATC116_S_COM2B-NMF
COM3B	4	High	Baseline	Stripe_Statistics_S_ATC116_COM3B
COM3B-SS	4	High	SSI/Foundation Flexibility	Stripe_Statistics_ATC116_S_COM2B-SS1 Stripe_Statistics_ATC116_S_COM2B-SS2
COM3B-BC	4	High	Brace Configuration	Stripe_Statistics_ATC116_S_COM3B-BC
COM4B	1	Very High	Baseline	Stripe_Statistics_ATC116_S_COM4B
COM5B	2	Very High	Baseline	Stripe_Statistics_ATC116_S_COM5B
COM6B	4	Very High	Baseline	Stripe_Statistics_ATC116_S_COM6B

* Soft and stiff sites with unfiltered and filtered ground motions.

References

AIJ, 1995a, *Preliminary Reconnaissance Report of the 1995 Hyogoken-Nanbu Earthquake*, English Edition, Architectural Institute of Japan, Tokyo, Japan.

AIJ, 1995b, *Reconnaissance Report on Damage to Steel Building Structures Observed from the 1995 Hyogoken-Nanbu (Hanshin /Awaji) Earthquake*, Japanese Edition with Abridged English Edition, Steel Committee of Kinki Branch, Architectural Institute of Japan, Tokyo, Japan.

AISC, 2010a, *Specification for Structural Steel Buildings*, ANSI/AISC 360-10, American Institute of Steel Construction, Chicago, Illinois.

AISC, 2010b, *Seismic Provisions for Structural Steel Buildings*, ANSI/AISC 341-10, American Institute of Steel Construction, Chicago, Illinois.

AISC, 2011, *Steel Construction Manual*, 14th Ed., American Institute of Steel Construction, Chicago, Illinois.

AISC, 2016, *Vibrations of Steel-Framed Structural Systems Due to Human Activity, Second Edition*, AISC Design Guide 11, American Institute of Steel Construction, Chicago, Illinois.

ASCE, 2005, *Minimum Design Loads for Buildings and Other Structures*, ASCE/SEI 7-05, American Society of Civil Engineers, Reston, Virginia.

ASCE, 2007, *Seismic Rehabilitation of Existing Buildings*, ASCE/SEI 41-06, American Society of Civil Engineers, Reston, Virginia.

ASCE, 2010, *Minimum Design Loads for Buildings and Other Structures*, ASCE/SEI 7-10, American Society of Civil Engineers, Reston, Virginia.

ASCE, 2016, *Minimum Design Loads and Associated Criteria for Buildings and Other Structures*, ASCE/SEI 7-16, American Society of Civil Engineers, Reston, Virginia.

ASCE, 2017, *Seismic Evaluation and Retrofit of Existing Buildings*, ASCE/SEI 41-17, American Society of Civil Engineers, Reston, Virginia.

ATC, 1989, *Procedures for Postearthquake Safety Evaluation of Buildings*, ATC-20, Applied Technology Council, Redwood City, California.

ATC, 2005, *Field Manual: Postearthquake Safety Evaluation of Buildings Second Edition*, ATC-20-1, Applied Technology Council, Redwood City, California.

ATC, 2015, *Roadmap for Solutions to the Issue of Short Period Building Performance*, ATC-116 Report, Applied Technology Council, Redwood City, California.

Bruneau, M., Uang, C.M., and Sabelli, R., 2011, *Ductile Design of Steel Structures*, 2nd Ed., McGraw-Hill, New York, New York.

CEN, 2004, *Eurocode 8: Design of Structures for Earthquake Resistance - Part 1: General Rules, Seismic Actions and Rules for Buildings*, European Committee for Standardization, Brussels, Belgium.

Chopra, A.K., and McKenna, F., 2016, "Modeling viscous damping in nonlinear response history analysis of buildings for earthquake excitation," *Earthquake Engineering and Structural Dynamics*, Vol. 45, No. 2, pp. 193-211.

Coduto, D.P., Kitch, W.A., and Yeung, M-C.R., 2015, *Foundation Design: Principles and Practices*, 3rd Ed., Pearson, New York, New York.

CUREE, 2001, *Development of a Testing Protocol for Woodframe Structures*, CUREE Publication No. W-02, Consortium of Universities for Research in Earthquake Engineering, Richmond, California.

EERI, 1978, *Reconnaissance Report, Miyagi-Ken-oki, Japan Earthquake, June 12, 1978*, Earthquake Engineering Research Institute, Oakland, California.

FEMA, 2006, *Techniques for the Seismic Rehabilitation of Existing Buildings*, FEMA 547, prepared by Rutherford & Chekene Consulting Engineering for the National Institute of Standards and Technology and the Federal Emergency Management Agency, Washington, D.C.

FEMA, 2007, *Interim Testing Protocols for Determining the Seismic Performance Characteristics of Structural and Nonstructural Components*, FEMA 461, prepared by the Applied Technology Council for the Federal Emergency Management Agency, Washington, D.C.

FEMA, 2009a, *NEHRP Recommended Seismic Provisions for New Buildings and Other Structures*, FEMA P-750, prepared by the Building Seismic Safety Council of the National Institute of Building Sciences for the Federal Emergency Management Agency, Washington, D.C.

FEMA, 2009b, *Quantification of Building Seismic Performance Factors*, FEMA P-695, prepared by the Applied Technology Council for the Federal Emergency Management Agency, Washington, D.C.

FEMA, 2015a, *Rapid Visual Screening of Buildings for Potential Seismic Hazards: A Handbook*, 3rd Ed., FEMA P-154, prepared by the Applied Technology Council for the Federal Emergency Management Agency, Washington, D.C.

FEMA, 2015b, *NEHRP Recommended Seismic Provisions for New Buildings and Other Structures*, FEMA P-1050, prepared by the Building Seismic Safety Council of the National Institute of Building Sciences for the Federal Emergency Management Agency, Washington, D.C.

FEMA, 2018, *Seismic Performance Assessment of Buildings, Volume 1 – Methodology*, 2nd Ed., FEMA P-58-1, prepared by the Applied Technology Council for the Federal Emergency Management Agency, Washington, D.C.

FEMA, 2020a, *Short-Period Building Collapse Performance and Recommendations for Improving Seismic Design, Volume 1 – Overarching Findings, Conclusions, and Recommendations*, FEMA P-2139-1, prepared by the Applied Technology Council for the Federal Emergency Management Agency, Washington, D.C.

FEMA, 2020b, *Short-Period Building Collapse Performance and Recommendations for Improving Seismic Design, Volume 2 – Study of One-to-Four Wood Light-Frame Buildings*, FEMA P-2139-2, prepared by the Applied Technology Council for the Federal Emergency Management Agency, Washington, D.C.

FEMA, 2020c, *Short-Period Building Collapse Performance and Recommendations for Improving Seismic Design, Volume 3 – Study of One-to-Four Story Special Reinforced Masonry Shear Wall Buildings*, FEMA P-2139-3, prepared by the Applied Technology Council for the Federal Emergency Management Agency, Washington, D.C.

Hsiao, P-C., Lehman, D.E., and Roeder, C.W., 2012, "Improved analysis model for special concentrically braced frames," *Journal of Constructional Steel Research*, Vol. 73, pp 80-94.

Hsiao, P-C., Lehman, D.E., and Roeder, C.W., 2013a, "A model to simulate special concentrically braced frames beyond brace fracture," *Earthquake Engineering and Structural Dynamics*, Vol. 42, No. 2, pp. 183-200.

Hsiao, P-C., Lehman, D.E., and Roeder, C.W., 2013b, "Evaluation of response modification coefficient and collapse potential of SCBFs," *Earthquake Engineering and Structural Dynamics*, Vol. 42, No. 10, pp. 1547-1564.

ICBO, 1988, *Uniform Building Code*, 1988 Ed., International Conference of Building Officials, Whittier, California.

ICBO, 1994, *Uniform Building Code*, 1994 Ed., International Conference of Building Officials, Whittier, California.

ICC, 2015, *International Building Code*, International Code Council, Washington, D.C.

Kato B., Tanaka A., Yamanouchi H., 1980, "A field work investigation of steel building damage due to the 1978 Miyagiken-Oki earthquake," *Proceedings of the 7th World Conference on Earthquake Engineering*, Istanbul, Turkey.

Kim, S. and Stewart, J.P., 2003, "Kinematic soil-structure interaction from strong motion recordings," *Journal of Geotechnical and Geoenvironmental Engineering*, Vol. 129, No. 4, pp. 323-335.

Kircher, C.A., Whitman, R.V., Holmes, W.T., 2006, "HAZUS earthquake loss estimation methods," *Natural Hazards Review*, Vol. 7, No. 2, pp. 45-59.

Krawinkler, H., Anderson, J.C., and Bertero, V.V., 1996, "Northridge earthquake of January 17, 1994: Reconnaissance report, Part 2," *Earthquake Spectra*, Vol. 11, Suppl. C, pp. 25-47.

Lignos, D.G., Hartloper, A.R., Elkady, A., Deierlein, G.G., and Hamburger, R., 2019, "Proposed updates to the ASCE 41 nonlinear modeling parameters for wide-flange steel columns in support of performance-based seismic engineering," *Journal of Structural Engineering*, Vol. 145, No. 9.

Liu, J., and Astaneh-Asl, A., 2004, "Moment-rotation parameter for composite shear tab connections," *Journal of Structural Engineering*, Vol. 130, No. 9, pp. 1371-1380.

Lumpkin, E.J., Hsiao, P-C., Roeder, C.W., Lehman, D.E., Tsai, C-Y., Wu, A-C., Wei, C-Y., and Tsai, K-C., 2012, "Investigation of the seismic

response of multi-story braced frames," *Journal of Constructional Steel Research*, Vol. 77, pp. 131-144.

Mazzoni, S., McKenna, F., Scott, M.H., and Fenves, G.L., 2006, *OpenSees Command Language Manual*, University of California, Berkeley, California.

Miranda, E., and Bertero, V.V., 1994, "Evaluation of strength reduction factors for earthquake-resistant design," *Earthquake Spectra*, Vol. 10, No. 2, pp. 357-379.

NIST, 2010, *Evaluation of the FEMA P-695 Methodology for Quantification of Building Seismic Performance Factors*, NIST GCR 10-917-8, prepared by the NEHRP Consultants Joint Venture, a partnership of the Applied Technology Council and the Consortium for Universities for Research in Earthquake Engineering, for the National Institute of Standards and Technology, Gaithersburg, Maryland.

NIST, 2012a, *Tentative Framework for Development of Advanced Seismic Design Criteria for New Buildings*, NIST GCR 12-917-20, prepared by the NEHRP Consultants Joint Venture, a partnership of the Applied Technology Council and the Consortium for Universities for Research in Earthquake Engineering, for the National Institute of Standards and Technology, Gaithersburg, Maryland.

NIST, 2012b, *Soil-Structure Interaction for Building Structures*, NIST GCR 12-917-21, prepared by the NEHRP Consultants Joint Venture, a partnership of the Applied Technology Council and the Consortium for Universities for Research in Earthquake Engineering, for the National Institute of Standards and Technology, Gaithersburg, Maryland.

NIST, 2017, *Guidelines for Nonlinear Structural Analysis for Design of Buildings: Part IIa—Steel Moment Frames*, NIST GCR 17-917-46v2, prepared by the Applied Technology Council for the National Institute of Standards and Technology, Gaithersburg, Maryland.

NOAA, 1973, *San Fernando, California, Earthquake of February 9, 1971*, National Oceanic and Atmospheric Administration, Washington, D.C.

OES, 1995, *The Northridge Earthquake of January 17, 1994: Report of Data Collection and Analysis, Part A: Damage and Inventory Data*, The Governor's Office of Emergency Services of the State of California, Sacramento, California.

OES, 1997, *The Northridge Earthquake of January 17, 1994: Report of Data Collection and Analysis, Part B: Analysis and Trends*, Governor's Office of Emergency Services of the State of California, Sacramento, California.

Pais, A., and Kausel, K., 1988, "Approximate formulas for dynamic stiffnesses of rigid foundations," *Soil Dynamics and Earthquake Engineering*, Vol. 7, No.4, pp. 213-227.

Roeder, C.W., Lumpkin, E.J., and Lehman, D.E., 2011, "A balanced design procedure for special concentrically braced frame connections," *Journal of Constructional Steel Research*, Vol. 67, No. 11, pp. 1760-1772.

Roeder, C.W., Lumpkin, E.J., and Lehman, D.E., 2012, "Seismic performance assessment of concentrically braced steel frames," *Earthquake Spectra*, Vol. 28, No. 2., pp. 709-727.

Roeder, C.W., Sen, A.D., Terpstra, C., Ibarra, S.M., Liu, R., Lehman, D.E., and Berman, J.W., 2019, "Effect of beam yielding on chevron braced frames," *Journal of Constructional Steel Research*, Vol. 159, pp. 428-441.

Roeder, C.W., Sen, A.D., Asada, H., Ibarra, S.M., Lehman, D.E., Berman, J.W., Tsai, K.C., Tsai, C.Y., Wu, A.C., Wang, K.J., and Liu, R., in press, "Inelastic behavior and seismic design of multistory chevron-braced frames with yielding beams," *Journal of Constructional Steel Research*, https://doi.org/10.1016/j.jcsr.2019.105817.

Sabelli, R., Roeder, C.W., and Hajjar, J.F., 2013, *Seismic Design of Steel Special Concentrically Braced Frame Systems: A Guide for Practicing Engineers*, NEHRP Seismic Design Technical Brief No. 8, NIST GCR 13-917-24, produced by the NEHRP Consultants Joint Venture, a partnership of the Applied Technology Council and the Consortium of Universities for Research in Earthquake Engineering, for the National Institute of Standards and Technology, Gaithersburg, Maryland.

Sen, A.D., Roeder, C.W., Berman, J.W., Lehman, D.E., Li, C.H., Wu, A.C., and Tsai, K.C., 2016, "Experimental investigation of chevron concentrically braced frames with yielding beams," *Journal of Structural Engineering*, Vol. 142, No. 12.

Sen, A.D., Roeder, C.W., Lehman, D.E., and Berman, J.W., 2019, "Nonlinear modeling of concentrically braced frames," *Journal of Constructional Steel Research*, Vol. 157, pp. 103-120.

Simpson, B.G., Mahin, S.A., and Lai, J-W., 2017, *Experimental Investigation of the Behavior of Vintage and Retrofit Concentrically Braced Steel Frames under Cyclic Loading*, PEER Report No. 2017/12, Pacific Earthquake Engineering Research Center, University of California, Berkeley, Berkeley, California.

Star, L.M., Givens, M.J., Nigbor, R.L., and Stewart, J.P., 2015, "Field-testing of structure on shallow foundation to evaluate soil-structure interaction effects," *Earthquake Spectra*, Vol. 31, No. 4, pp. 2511-2534.

Tanaka, A., Morita, K., and Yamanouchi, H., 1980, "Damage of braced steel frames due to the 1978 Miyagiken-Oki earthquake," *Proceedings of the 7th World Conference on Earthquake Engineering*, Istanbul, Turkey.

Thompson, E.M., Kayen, R.E., Carkin, B., and Tanaka, H., 2010, *Surface-Wave Site Characterization at 52 Strong-Motion Recording Stations Affected by the Parkfield, California, M6.0 Earthquake of 28 September 2004*, Open-File Report 2010-1168, U.S. Geological Survey, Reston, Virginia.

Tremblay, R., Filiatrault, A., Bruneau, M., Nakashima, M., Prion, H.G.L., and DeVall, R., 1996, "Seismic design of steel buildings: Lessons from the 1995 Hyogo-ken Nanbu earthquake," *Canadian Journal of Civil Engineering*, Vol. 23, No. 3, pp. 727-756.

Tremblay, R., Filiatrault, A., Timler, P., and Bruneau, M., 1995, "Performance of steel structures during the 1994 Northridge earthquake," *Canadian Journal of Civil Engineering*, Vol. 22, No. 2, pp. 338-360.

Uriz, P., and Mahin, S.A., 2008, *Toward Earthquake-Resistant Design of Concentrically Braced Steel-Frame Structures*, PEER Report 2008/08, Pacific Earthquake Engineering Research Center, University of California, Berkeley, Berkeley, California.

Veletsos, A.S., and Newmark, N.M., 1960, "Effect of inelastic behavior on the response of simple systems to earthquake motion," *Proceedings of the 2nd World Conference on Earthquake Engineering*, Tokyo, Japan, Vol. 2, pp. 895-912.

Project Participants

Federal Emergency Management Agency

Mai (Mike) Tong (Project Officer)
Federal Emergency Management Agency
500 C Street, SW, Room 416
Washington, DC 20472

Robert D. Hanson (Technical Advisor)
Federal Emergency Management Agency
5885 Dunabbey Loop
Dublin, Ohio 43017

Applied Technology Council

Jon A. Heintz (Project Executive)
Applied Technology Council
201 Redwood Shores Parkway, Suite 240
Redwood City, California 94065

Scott D. Schiff (Associate Project Manager)
Applied Technology Council
201 Redwood Shores Parkway, Suite 240
Redwood City, California 94065

Justin Moresco (Project Manager)
Applied Technology Council
201 Redwood Shores Parkway, Suite 240
Redwood City, California 94065

Project Technical Committee

Charles A. Kircher (Project Technical Director)
Kircher & Associates
1121 San Antonio Road, Suite D-202
Palo Alto, California 94303

Jeffrey W. Berman
University of Washington
Dept. of Civil & Environmental Engineering
201 More Hall, Box 352700
Seattle, Washington 98195

Kelly Cobeen
Wiss, Janney, Elstner Associates, Inc.
2000 Powell Street, Suite 1650
Emeryville, California 94608

J. Daniel Dolan
Washington State University
Department of Civil and Environmental Engineering
P.O. Box 642910
Pullman, Washington 99164

Andre Filiatrault
University at Buffalo
Department of Civil, Structural and Environmental Engineering
134 Ketter Hall
Buffalo, New York 14260

James R. Harris
J. R. Harris & Company
1175 Sherman Street, Suite 2000
Denver, Colorado 80203

Gregory Kingsley
KL&A, Inc.
1717 Washington Avenue, Suite 100
Golden, Colorado 80401

Dawn Lehman
University of Washington
Dept. of Civil & Environmental Engineering
201 More Hall, Box 352700
Seattle, Washington 98195

Weichiang Pang
Clemson University
Glenn Department of Civil Engineering
312 Lowry Hall
Clemson, South Carolina 29634

P. Benson Shing
University of California, San Diego
Department of Structural Engineering
9500 Gilman Drive
La Jolla, California 92093

Project Review Panel

Anthony Court (ATC Board Contact)
A.B. Court & Associates
4340 Hawk Street
San Diego, California 92103

Onder Kustu
OAK Structural (retired)
P.O. Box 2074
Danville, California 94526

William T. Holmes
Structural Engineer
2600 La Cuesta Avenue
Oakland, California 94611

James O. Malley
Degenkolb Engineers
375 Beale Street, Suite 500
San Francisco, California 94105

Larry Kruth
American Institute of Steel Construction
130 E. Randolph Street, Suite 2000
Chicago, Illinois 60601

Steve Pryor
Simpson Strong-Tie
5956 W. Las Positas Boulevard
Pleasanton, California 94588

Soil-Structure Interaction Working Group

Lisa Star
California State University, Long Beach
Department of Civil Engineering and Construction Engineering Management
1250 Bellflower Boulevard
Long Beach, California 90840

Jonathan P. Stewart
University of California, Los Angeles
Department of Civil and Environmental Engineering
5731 Boelter Hall
Los Angeles, California 90095

Steel Working Group

Alex Stone
KL&A, Inc.
1717 Washington Avenue, Suite 100
Golden, Colorado 80401

Sarah Wichman
University of Washington
Dept. of Civil & Environmental Engineering
201 More Hall, Box 352700
Seattle, Washington 98195

Steel Workshop Participants

David Bonneville
Degenkolb Engineers
1300 Clay Street, 9th Floor
Oakland, California 94612

Greg Deierlein
Stanford University
Department of Civil and Environmental Engineering
Blume Earthquake Engineering Center
Stanford, California 94305

Rick Drake
Fluor Enterprises
3 Polaris Way
Aliso Viejo, California 92698

Matt Eatherton
Virginia Tech
Civil and Environmental Engineering (MC 0105)
Patton Hall Room 105A
750 Drillfield Drive
Blackburg, Virginia 24061

Michael Givens
Group Delta Consultants
900 Wilshire Boulevard, 19th Floor
Los Angeles, California 90017

Steve Harris
Simpson Gumpertz & Heger
100 Pine Street, Suite 1600
San Francisco, California 94111

John Hooper
Magnusson Klemencic Associates
1301 Fifth Avenue, Suite 3200
Seattle, Washington 98101

Walterio Lopez
Rutherford & Chekene
375 Beale Street, Suite 310
San Francisco, California 94105

Bonnie Manley
American Iron and Steel Institute
41 Tucker Road
Norfolk, Massachusetts 02081

Pat McManus
Martin/Martin
1600 Specht Point Road, Suite 117
Fort Collins, Colorado 80525

John Rolfes
CSD Structural Engineers
8989 N Port Washington Road
Milwaukee, Wisconsin 53217

Rafael Sabelli
Walter P Moore
595 Market Street, Suite 2130
San Francisco, California 94105

Tom Sabol
University of California, Los Angeles
BOX 951593, 5713 Boelter Hall
Los Angeles, California 90095

Barbara Simpson
Oregon State University
340 Owen Hall
Corvallis, Oregon 97331

Robert Tremblay
Ecole Polytechnique of Montreal
Department of Civil, Geological, and Mining Engineering
P.O. Box 6079, St. Downtown
Montreal, Quebec H3C 3A7
Canada

Chia-Ming Uang
University of California, San Diego
Department of Structural Engineering
La Jolla, California 92093

Lydell Wiebe
McMaster University
Department of Civil Engineering
1280 Main Street West, JHE 301
Hamilton, Ontario L8S 4L7
Canada

FEMA

FEMA P-2139-4